

**GENERALIZED DYNAMIC AVERAGE MODELING OF LINE-COMMUTATED
CONVERTER SYSTEMS IN TRANSIENT SIMULATION PROGRAMS**

by

Sina Chiniforoosh

B.Sc., Shiraz University, 2005

M. Sc., Sharif University of Technology, 2007

A THESIS SUBMITTED IN PARTIAL FULFILLMENT OF
THE REQUIREMENTS FOR THE DEGREE OF

DOCTOR OF PHILOSOPHY

in

THE FACULTY OF GRADUATE STUDIES

(Electrical and Computer Engineering)

THE UNIVERSITY OF BRITISH COLUMBIA

(Vancouver)

April 2012

© Sina Chiniforoosh, 2012

Abstract

Power electronic converters are used in a wide range of applications as well as being the enabling technology for interfacing the alternative energy resources and many loads in modern power systems. The methodology of developing the so-called dynamic average-value models (AVMs) for such converters is based on averaging the variables (currents and voltages) within a switching interval resulting in numerically efficient models that are much more suitable than the detailed switching models for system-level studies as well as numerical linearization and the respective small-signal analysis. However, the AVMs available in the literature for line-commutated converters have several limitations such as neglecting the effects of losses, being only valid in certain operational modes and under balanced excitation, as well as employing a simplified representation of the multi-phase transformer in high-pulse-count converters. Moreover, a unified AVM methodology for high-pulse-count converters has not yet been established.

In this thesis, a generalized AVM methodology is developed for voltage-source- and rotating-machine-fed multi-pulse line-commutated converters for both classes of transient simulation software packages, i.e., state-variable-based and nodal-analysis-based electromagnetic transient program (EMTP) type. The previously-developed AVM approaches, i.e., analytical and parametric, are extended to the EMTP-type programs, and the indirect and direct methods of interfacing the models with external circuit-network are introduced and compared. For the machine-converter systems, the effects of machine and bridge losses are taken into account in the new AVM. Finally, a generalized dynamic AVM methodology is developed for high-pulse-count converters based on the parametric approach. An effective multi-phase transformer model is developed in transformed ($qd0$) and phase (abc) variables. An efficient transformer model is also developed, which accurately represents the multi-phase transformer using an equivalent three-phase formulation. The

proposed generalized AVM remains valid for all operational modes under balanced and unbalanced excitation. This model is employed for AVM implementation in state-variable-based and EMTP-type programs. Extensive simulation and experimental studies are carried out on several example systems in order to compare the developed AVMs against the detailed and previously-developed average models in time- and frequency-domains. The results demonstrate the great accuracy of the proposed AVMs and a significant improvement compared to the previously-developed models.

Preface

The research results presented in this thesis have been partly published, accepted for publication, or ready for submission as several journal articles and publications in conference proceedings. In all publications, I was responsible for developing the models, conducting the simulation and experimental studies, compiling the results and conclusions, as well as preparing the manuscripts. My research supervisor, Dr. Juri Jatskevich, has provided supervisory comments and corrections during the process of modeling, conducting the studies, and writing the manuscripts, which I have accommodated in the final manuscripts. The other co-authors have also provided comments, suggestions, and constructive feedback.

A version of Chapters 1 and 2 has been published:

S. Chiniforoosh, J. Jatskevich, *et al.*, “Definitions and applications of dynamic average models for analysis of power systems,” *IEEE Transactions on Power Delivery*, vol. 25, no. 4, pp. 2655-2669, Oct. 2010.

A version of Chapter 3 has been published:

S. Chiniforoosh, A. Davoudi, and J. Jatskevich, “Averaged-circuit modeling of line-commutated rectifiers for transient simulation programs,” in *Proc. IEEE International Symposium on Circuits and Systems (ISCAS '10)*, Paris, France, May-Jun. 2010.

A version of Chapter 3 is ready for submission:

S. Chiniforoosh, H. Atighechi, and J. Jatskevich, “Directly-interfaced dynamic average models for representing line-commutated rectifier systems in EMTP-type programs,” to be submitted.

A version of Chapters 1, 2, and 4 has been published:

S. Chiniforoosh, H. Atighechi, A. Davoudi, J. Jatskevich, *et al.*, “Dynamic average modeling of front-end diode rectifier loads considering discontinuous conduction mode and unbalanced operation,” *IEEE Transactions on Power Delivery*, vol. 27, no. 1, pp. 421-429, Jan. 2012.

A version of Chapters 1, 2, and 4 is ready for submission:

S. Chiniforoosh, H. Atighechi, and J. Jatskevich, “Steady-state and dynamic impedance of front-end diode rectifier loads as predicted by dynamic average-value models,” to be submitted.

A version of Chapter 5 has been accepted for publication:

S. Chiniforoosh, A. Davoudi, P. Alaeinovin, and J. Jatskevich, “Dynamic modelling and characterisation of vehicular power system considering alternator iron core and rectifier losses,” to appear in *IET Electrical Systems in Transportation*, 2012, 25 pages, (Manuscript ID:EST-2011-0031.R1).

A version of Chapter 6 is ready for submission:

S. Chiniforoosh, H. Atighechi, and J. Jatskevich, “Generalized dynamic average modeling of high-pulse-count rectifier systems in transient simulation programs,” to be submitted.

Table of Contents

Abstract.....	ii
Preface.....	iv
Table of Contents	vi
List of Tables	x
List of Figures.....	xi
Acknowledgements	xviii
Dedication	xx
Chapter 1: Introduction	1
1.1 Motivation.....	1
1.2 Literature Review.....	3
1.2.1 Three-Phase (Six-Pulse) Converter Models.....	7
1.2.2 High-Pulse-Count Converter Models	8
1.3 Research Objectives and Anticipated Impact	10
1.4 Thesis Organization	13
Chapter 2: Dynamic Average Modeling in State-Variable-Based Simulators.....	15
2.1 State-Variable-Based Simulators	15
2.2 Detailed Analysis	18
2.3 Dynamic Average Modeling.....	22
2.3.1 Analytical Approach	22
2.3.1.1 Classical Reduced-Order Model (AVM-1).....	25
2.3.1.2 Improved Reduced-Order Model (AVM-2).....	26
2.3.2 Parametric Approach	27
2.4 Implementation of the AVMs in SV-Based Programs	28
2.5 Small-Signal Frequency-Domain Analysis.....	29

Chapter 3: Dynamic AVM Formulation for EMTP-Type Solution.....	33
3.1 Electro-Magnetic Transient Programs	33
3.2 Detailed Analysis	35
3.3 Dynamic Average Modeling.....	40
3.3.1 Analytical AVM for EMTP-type Solution	40
3.3.2 Indirectly-Interfaced Analytical Average-Value Model (IIAAVM)	43
3.3.3 Directly-Interfaced Analytical Average-Value Model (DIAAVM)	45
3.3.3.1 Direct Interface in qd Variables	47
3.3.3.2 Direct Interface in abc Variables.....	50
3.3.4 Parametric AVM for EMTP-Type Solution	53
3.4 Example of AVM Implementation in PSCAD/EMTDC	55
3.5 Comparison of Direct and Indirect Interfacing Methods.....	57
Chapter 4: AVM Verification in SV-Based and EMTP-Type programs	62
4.1 Example Micro-Wind Turbine Generator System.....	62
4.1.1 Large-Signal Time-Domain Analysis.....	63
4.1.2 Small-Signal Frequency-Domain Analysis.....	64
4.2 Example 3-Phase (6-Pulse) Front-End Rectifier system	66
4.2.1 Steady-State Time Domain Analysis.....	67
4.2.1.1 Operation in DCM	67
4.2.1.2 Operation in CCM.....	69
4.2.2 Dynamic Performance under Balanced Conditions.....	71
4.2.2.1 Balanced Operation in DCM	71
4.2.2.2 Balanced Operation in CCM.....	72
4.2.3 Dynamic Performance under Unbalanced Conditions.....	76
4.2.3.1 Unbalanced Operation in DCM	76
4.2.3.2 Unbalanced Operation in CCM	78

4.2.4	System Impedance Analysis	81
4.2.4.1	Steady-State Analysis	81
4.2.4.2	Small-Signal Frequency-Domain Analysis.....	83
4.2.5	Conclusion	87
Chapter 5: Inclusion of Losses in Machine-Fed Converter Systems		88
5.1	Introduction.....	88
5.2	Example Vehicular Power System Architecture.....	89
5.3	System Detailed Model.....	91
5.3.1	Representation of Rotational Losses.....	93
5.3.2	Verification of Detailed Model.....	95
5.3.3	Battery Model	97
5.4	System Dynamic Average-Value Modeling	98
5.4.1	Alternator Model in Transformed qd Coordinates and Variables.....	98
5.4.2	Average-Value Modeling of Non-Ideal Rectifier	101
5.5	Case Studies	104
Chapter 6: Generalized Dynamic AVM for High-Pulse-Count Converters		110
6.1	Introduction.....	110
6.2	High-Pulse-Count Converter System Structures	110
6.3	Multi-Phase Transformer Modeling	115
6.3.1	Original Interconnected Transformer Model	115
6.3.2	Analytically-Derived Equivalent Compacted Transformer Model.....	121
6.3.3	Round Shifted Equivalent Model.....	126
6.3.4	Compensation for Asymmetric Leakages	133
6.4	Detailed Analysis	134
6.4.1	Detailed Analysis using Uncompensated Transformer Models.....	135
6.4.2	Detailed Analysis using Compensated Transformer Models.....	139

6.4.3	Operational Mode Analysis	144
6.5	Dynamic Average Modeling.....	151
6.5.1	Reduced-Order Analytical AVM.....	151
6.5.2	Generalized Dynamic Average Modeling Methodology	152
6.5.2.1	Generalized Transformer Model in Transformed Variables.....	153
6.5.2.2	Generalized Rectifier Model.....	159
6.5.2.3	Implementation in SV-Based Simulators.....	160
6.5.3	Generalized Model with Collapsed Transformer.....	161
6.5.4	Implementation in EMTP-Type Programs.....	164
6.6	Model Verification in Time Domain	170
6.6.1	Steady-State Analysis	170
6.6.2	Transient Analysis under Balanced Conditions.....	171
6.6.3	Transient Analysis under Unbalanced Conditions.....	182
6.7	Model Verification in Frequency Domain.....	188
Chapter 7: Conclusions and Future Work		192
7.1	Conclusions and Contributions	192
7.2	Future Work	196
References.....		198
Appendices.....		208
Appendix A Parameters of the Six-Pulse Converter Example Systems		208
A.1	Parameters of the 6-Pulse Converter System Considered in Section 3.5	208
A.2	Parameters of the Micro-Wind Turbine System Considered in Chapter 4	208
A.3	Parameters of the Front-End Rectifier System Considered in Chapter 4	208
A.4	Parameters of the Vehicular Power System Considered in Chapter 5.....	209
Appendix B Parameters of the 18-Pulse Example System Considered in Chapter 6		210

List of Tables

Table 1.1	Dynamic average models of the three-phase (six-pulse) rectifier systems.....	8
Table 1.2	Dynamic models of high-pulse-count converter systems.....	9
Table 2.1	Operational modes of the conventional 3-phase (6-pulse) rectifier.....	20
Table 4.1	Maximum values of the dc bus voltage and current for different system topologies.....	69
Table 4.2	Steady-state values of the dc bus voltage and current predicted by various models in DCM.....	69
Table 4.3	Steady-state values of the dc bus voltage and current predicted by various models in CCM-1.....	70
Table 4.4	System eigenvalues predicted by different models in DCM and CCM-1.	74
Table 4.5	Comparison of simulation time steps of different models.....	81
Table 4.6	System input impedance in DCM and CCM-1.....	83
Table 6.1	Operational modes of the conventional 9-phase (18-pulse) rectifier.....	147
Table 6.2	Eigenvalues of the 18-pulse rectifier system (without dc capacitor).....	178
Table 6.3	Eigenvalues of the 18-pulse rectifier system with dc capacitor.....	182
Table 6.4	Comparison of simulation time steps for different models.....	188

List of Figures

Figure 1.1	Typical configurations of multi-pulse line-commutated rectifier systems.....	4
Figure 2.1	Flowchart of a typical variable-step state-variable-based solver.	17
Figure 2.2	Simplified circuit diagram of a typical three phase front-end rectifier load system.	18
Figure 2.3	Typical current and voltage waveforms of the six-pulse rectifier: (a) operation in DCM; and (b) operation in CCM.....	20
Figure 2.4	(a) Relationship among the variables in the converter and arbitrary reference frames; and (b) Typical waveforms and the respective transformed waveforms in converter reference frame.	24
Figure 2.5	Block diagrams of AVM implementations in SV-based simulators: (a) analytically-derived (AVM-1 and AVM-2); and (b) parametric (PAVM).	28
Figure 2.6	System-level impedance-based representation of subsystems interconnected through an ac-dc converter.....	29
Figure 3.1	Flowchart of a typical nodal-analysis-based solver.....	34
Figure 3.2	Topological variations of the ac side impedance in a typical three phase front-end rectifier load system (a) series impedance (b) general network with series and parallel branches.	36
Figure 3.3	Three-phase currents at the bridge terminals for DCM and CCM operation: (a) without shunt filters; and (b) with shunt filters.....	37
Figure 3.4	Three-phase ac currents of the system at the input source terminals in presence of the shunt filters for DCM and CCM operations.	37
Figure 3.5	Circuit diagram of the AVM described by (3-6)-(3.8), (3-20), (3-21).	43
Figure 3.6	Circuit diagram of the IIAAVM using PSCAD-like approach.	44
Figure 3.7	Circuit diagram of the DIAAVM in qd variables.	49

Figure 3.8	Equivalent circuit diagram of the DIAVM in abc variables.	52
Figure 3.9	Indirectly-interfaced parametric average-value model.....	55
Figure 3.10	Example of IIPAVM implemented in PSCAD: (a) PAVM block together with controllable sources and interfacing ports; and (b) AVM module interfaced with external ac and dc subsystems.....	56
Figure 3.11	DC bus waveforms predicted by the models with $50\mu s$ time step.....	59
Figure 3.12	Input phase current predicted by the models with $50\mu s$ time step.....	59
Figure 3.13	DC bus waveforms predicted by the models with $500\mu s$ time step.....	60
Figure 3.14	Input phase current predicted by the models with $500\mu s$ time step.....	60
Figure 3.15	Input phase current predicted by the models with $1000\mu s$ time step.	61
Figure 4.1	Example PMSG micro-wind turbine generator system.....	62
Figure 4.2	Waveforms of the example PMSG micro-wind turbine generator system.....	64
Figure 4.3	Speed-to-output-voltage transfer function for the example micro-wind turbine system.	65
Figure 4.4	(a) Regulation characteristic of the system without ac input filter with dc capacitor; and (b) Magnified view showing the performance of models in DCM region.....	68
Figure 4.5	Regulation characteristic of the system in CCM operation as predicted by different models.	70
Figure 4.6	Transient response of the six-pulse rectifier system in DCM predicted by different models.	72
Figure 4.7	Transient response of the rectifier system with ac filter and without the dc capacitor predicted by different models.....	74
Figure 4.8	Transient response of the six-pulse rectifier system with dc capacitor in CCM predicted by different models.	75
Figure 4.9	Transient response of the rectifier system to a change in ac voltages, leading to unbalanced operation in DCM, as observed in the ac currents predicted by various models.	77

Figure 4.10	Transient response of the rectifier system to a change in ac voltages, leading to unbalanced operation in DCM, as observed in the dc bus predicted by various models.....	78
Figure 4.11	Transient response of the rectifier system to a change in ac voltages, leading to unbalanced operation in CCM, as observed in the ac currents predicted by various models.	79
Figure 4.12	Transient response of the rectifier system to a change in ac voltages, leading to unbalanced operation in CCM, as observed in the dc bus predicted by various models.....	80
Figure 4.13	Phasor diagrams representing unbalanced operation: (a) asymmetric input voltages, (b) positive sequence, (c) negative sequence, and (d) zero sequence components.	82
Figure 4.14	Dc-side impedance Z_{dc} (top) and ac- side impedance Z_{qq} (bottom) of the rectifier system in CCM-1 with input ac filter but without dc capacitor predicted by different models.....	85
Figure 4.15	AC-side impedance Z_{qq} (top) and Z_{qd} (bottom) of the rectifier system in CCM-1 with input ac filter and dc capacitor predicted by different models.	86
Figure 5.1	A typical vehicular electric power system and its power conversion chain.....	90
Figure 5.2	A circuit diagram for automotive alternator-rectifier-battery systems (top) with a typical voltage regulator-exciter (bottom).	92
Figure 5.3	Measured and simulated detailed responses to speed increase observed in the dc and ac sides.	96
Figure 5.4	Equivalent circuits of the considered alternator model in q and d axes.	100
Figure 5.5	Parametric functions considering ideal and non-ideal rectifier diodes.	103
Figure 5.6	Block diagram of the overall combined model depicting subsystems and their inputs and outputs.	105
Figure 5.7	System response to the increase in alternator speed as predicted by the detailed and average-value models under fixed excitation.....	105

Figure 5.8	Input speed, excitation (field) current and the dc bus voltage predicted by the detailed and the average-value models when the system uses the voltage regulator-exciter.	106
Figure 5.9	System response during the engine acceleration from 950 rpm to 4000 rpm predicted by the detailed and proposed average-value models.....	108
Figure 5.10	System transfer function from the field (excitation) voltage to the dc bus voltage predicted by the detailed and average-value models.....	109
Figure 6.1	Classification of high-pulse-count rectifier systems.	111
Figure 6.2	Typical 9-phase (18-pulse) rectifier example system topology considered in this Chapter.....	113
Figure 6.3	Typical 3- to 9-phase transformer structure for the 18-pulse rectifier example system.	114
Figure 6.4	Phasor diagrams of the primary and secondary voltages for the 3-to-9-phase transformer of Figure 6.3.....	115
Figure 6.5	Equivalent round transformer model depicting three-phase primary winding set and the equivalent secondary segments.	128
Figure 6.6	The k – th set of extended secondary windings is replaced by its shifted equivalent in the fictitious round equivalent transformer model.	130
Figure 6.7	Fictitious round shifted equivalent transformer model.	132
Figure 6.8	Initialization and steady state of the 18-pulse example system as seen at the dc bus and ac primary side currents predicted by various transformer models.....	137
Figure 6.9	Initialization and steady state of the 18-pulse example system as seen at the secondary side currents predicted by various transformer models.	138
Figure 6.10	Initialization and steady state of the 18-pulse example system as seen in the dc bus and ac primary side currents as predicted by compensated transformer models.	140

Figure 6.11	Initialization and steady state of the 18-pulse example system as seen in the ac secondary side currents as predicted by compensated transformer models.....	141
Figure 6.12	Comparison of the 18-pulse example system response as seen in the dc bus and ac primary side currents as predicted by symmetric and asymmetric transformer models.	142
Figure 6.13	Comparison of the 18-pulse example system response as seen in the ac secondary side currents as predicted by symmetric and asymmetric transformer models. ..	143
Figure 6.14	Nine-phase ac currents of the 18-pulse converter in DCM-type modes (Modes 1-4).....	145
Figure 6.15	Nine-phase ac currents of the 18-pulse converter in CCM-type modes (Modes 5-11).....	146
Figure 6.16	Equivalent circuit of the generalized transformer model in transformed qd0 variables.	158
Figure 6.17	Block diagram of the generalized AVM implementation in SV-based simulators.....	161
Figure 6.18	Equivalent circuit of the collapsed transformer model in transformed qd0 variables.	162
Figure 6.19	Block diagram of the generalized collapsed AVM implementation in SV-based simulators.....	164
Figure 6.20	Equivalent circuit of the collapsed transformer model in phase (<i>abc</i>) variables.	166
Figure 6.21	Example of the generalized dynamic AVM implementation in PSCAD: (a) details of the PAVM module; and (b) details of the equivalent-collapsed transformer model.	168

Figure 6.22	Example of the generalized dynamic AVM implementation in PSCAD: (a) interfacing the PAVM and transformer blocks; and (b) AVM module with external ac and dc subsystems.	169
Figure 6.23	Regulation characteristic of the 18-pulse rectifier system as predicted by various models.	171
Figure 6.24	Transient response of the 18-pulse rectifier system (without dc filter capacitor) within Mode 5 (7-6 valve) as predicted by various models.....	174
Figure 6.25	Transient response of the 18-pulse rectifier system (without dc filter capacitor) during a transient from Mode 5 (7-6 valve) to Mode 10 (9-valve) predicted by various models.	175
Figure 6.26	Response of the 18-pulse rectifier system (without dc filter capacitor) primary and secondary currents during a transient from Mode 5 (7-6 valve) to Mode 10 (9-valve) as predicted by the detailed and proposed GAVM models.....	176
Figure 6.27	Response of the 18-pulse rectifier system (without dc filter capacitor) secondary voltages during a transient from Mode 5 (7-6 valve) to Mode 10 (9-valve) as predicted by the detailed and proposed GAVM models.....	177
Figure 6.28	Transient response of the 18-pulse rectifier system during a transient from Mode 5 (7-6 valve) to Mode 1 (4-2 valve) in th presence of dc filter capacitor as predicted by various models.	179
Figure 6.29	Transient response of the 18-pulse rectifier system primary and secondary currents during a transition from Mode 5 (7-6 valve) to Mode 1 (4-2 valve) in the presence of dc capacitor as predicted by detailed and proposed GAVM models.....	180
Figure 6.30	Zoomed-in view of the 18-pulse rectifier system primary and secondary currents during Mode 1 (4-2 valve) operation in the presence of dc capacitor as predicted by detailed and proposed GAVM models.....	181

Figure 6.31	Transient response of the 18-pulse rectifier system to a change in the input voltage leading to unbalanced operation in ac side as predicted by various models.....	184
Figure 6.32	Response of the 18-pulse rectifier system primary and secondary currents during a transient leading to unbalanced operation as predicted by detailed and proposed GAVM models.....	185
Figure 6.33	Response of the 18-pulse rectifier system primary and secondary currents in transformed qd0 variables during a transient leading to unbalanced operation as predicted by detailed and proposed GAVM models.....	186
Figure 6.34	Impedance Z_{dc} of the 18-pulse rectifier at dc side in Mode 5 (7-6 valve) without dc capacitor as predicted by various models.	190
Figure 6.35	Impedance Z_{qq} of the 18-pulse rectifier at the ac side in Mode 10 (9-valve) without dc capacitor as predicted by the detailed and proposed GAVM models.....	190
Figure 6.36	Impedance Z_{qq} of the 18-pulse rectifier at the ac side in Mode 5 (7-6 valve) in presence of the dc capacitor as predicted by various models.	191

Acknowledgements

I would like to express my deepest gratitude to my research supervisor, Dr. Juri Jatskevich, for his great vision, immense inspiration, tremendous help, generous support, and endless patience throughout my PhD program. This research was made possible by his continuous encouragement, constant supervision, and invaluable feedback. The financial support for this research was made possible through the Natural Science and Engineering Research Council (NSERC) Discovery Grant entitled “Modelling and Analysis of Power Electronic and Energy Conversion Systems” and the Discovery Accelerator Supplement Grant entitled “Enabling Next Generation of Transient Simulation Programs” lead by Dr. Juri Jatskevich as a sole principle investigator.

Special thanks are also owed to the members of my research supervisory committee, Drs. Hermann Dommel and Jose Marti for their help and valuable guidance, and to Drs. William Dunford, Shahriar Mirabbasi, Yusuf Altintas, and Wilsun Xu for being on my examining committee and dedicating their valuable expertise and time.

I have received enormous help from all my colleagues and fellow graduate students in the Electric Power and Energy Systems research group at UBC through the years, for which I would like to express my sincere gratitude and appreciation. Particularly, I thank Ali Davoudi and Liwei Wang who have been very inspiring, and have set a great example of dedication and research productivity for me. I would also like to thank Pooya Alaeinovin, Hamid Atighechi, and Mehrdad Chapariha for our countless discussions on various research topics and student life in general. Many thanks also go to Amir Rasuli, Mehmet Sucu, Tom De Rybel, Michael Wrinch, Marcelo Tomim, Arvind Singh, Nathan Ozog, Leon Max Vargas, and all former and current members of the Electric Power and Energy Systems research group at UBC. I would also like to thank all the staff at the Department of Electrical and Computer Engineering and the Faculty of Graduate Studies.

Finally, I would like to thank my family and friends for their continuous moral support, and their contribution to making my life a pleasant experience. My Mother's love and support have always been with me even though she was, at times, thousands of miles away. I thank Sally for her love, patience, and for always being there for me. I thank Ehsan Azadi Yazdi, Maziar Eghbalnia, Mahdi Salehi, Bruce Krayenhoff, and all my friends for the wonderful times I spent with them and the tremendous delight they have brought to my life.

Dedication

This thesis, which is by no means a miracle, is dedicated to *Sally* for showing me that miracles are possible in life.

And to my mother, *Laleh Chiniforoosh* whose love and support have pervaded the years of my life.

And to the memory of my beloved father, *Bahman Chiniforoosh*, whose words of wisdom have been a great motivation for me.

Chapter 1: Introduction

1.1 Motivation

The recent developments in power systems have been inextricably linked with integration of renewable and clean energy resources and the associated enabling power-electronic-based technology. Power electronic converters are increasingly employed in the power systems with the development of Smart Energy Grid and interfacing of a large number of Independent Power Producers (IPPs) and Distributed Energy Resources (DERs). Power electronic converters are also utilized in a variety of applications such as High Voltage DC (HVDC) transmission systems, high-power dc supplies, excitation systems of large electric generators, as well as vehicular, naval, and aircraft power systems, etc. Design and analysis of all these modern electrical energy systems extensively relies on modeling and simulation of the power-electronic-based systems with switching components. The procedures for design and analysis of such complex systems typically involve a large number of computer studies in time and frequency domains.

Various simulation software packages are commercially available and may be used for modeling the power-electronic-based systems considering all the switching details. These software packages may be generally classified into State-Variable-based (SV-based) [1]-[7] and Nodal-Analysis-based (NA-based) languages [8]-[12]. The Electro-Magnetic Transient Program (EMTP) [8] and many commonly used EMTP-type packages are also based on the nodal or modified nodal equations. With the development of modern simulation tools, the detailed models of power-electronic-based systems, where the switching of all devices is implemented, may be readily implemented in both SV- and NA-based simulation packages.

It is therefore possible to develop models of larger systems from a number of smaller subsystems/modules that can be used for the simulation of system transients. However, the detailed switching models are computationally expensive, and result in a significant increase of the required computing time, which in turn limits the size of the system that can be practically implemented in a given package. In addition, the detailed models are discontinuous due to inherent switching, and hence are not directly suitable for linearization and small-signal frequency-domain characterization, e.g., obtaining impedance characteristics and input-output transfer functions. These characteristics are important in assessing the stability of power-electronic-based systems and design of corresponding controllers [13], [14]. Extracting these characteristics from the detailed switching model of the system is possible only through the traditional frequency-sweep method or similar techniques [15], [16], which become extremely time-consuming and challenging especially at low frequencies.

These challenges have led to development of the so-called dynamic Average-Value Models (AVMs) which approximate the original system by “neglecting” or “averaging” the effects of fast switching within a prototypical switching interval. The switching effects, i.e., ripples, are often undesirable and small, and do not have a significant effect on longer-term dynamics of the system. The resulting average-value models, therefore, make a useful tool for predicting the slower dynamics of the system below the switching frequency. These models are computationally efficient and could run orders of magnitudes faster than the original switching models, leading to the possibility of efficient system-level simulations and studies. Additionally, since AVMs are time-invariant, they can be numerically linearized about any desired operating point for small-signal analysis, i.e., obtaining local transfer functions and impedances. Obtaining such characteristics from the AVMs is then almost instantaneous in many SV-based simulators, e.g., [4].

Dynamic average models have been successfully used for modeling of vehicular [17], [18] and naval [14], [19] electric power systems as well as the distributed dc power systems of aircraft [20], [21] and spacecraft [22]–[24]. Average-value modeling has also been often applied to variable speed wind energy systems [25]–[32] where the machines are typically interfaced with the grid using the power electronic converters. The need for efficient dynamic AVMs is drastically increasing with the development of the modern power systems and its many components that are interface through power electronics. In order to promote research in this area and disseminate results in the power engineering community, the IEEE Task Force on Dynamic Average Modeling has been assembled under the Working Group on Modeling and Analysis of System Transients Using Digital Programs. The research objectives of this thesis are in line with the overall goals of this Task Force.

1.2 Literature Review

For the purpose of this thesis, the high power converters that are commonly encountered in utility applications may be divided into Pulse-Width Modulated (PWM) and the line-commutated converters. This particular research is focused on multi-pulse line-commutated rectifiers which have typical configuration as depicted in Figure 1.1. Depending on the application, the source may be a distribution feeder (or transformer) as in Case I, or a rotating machine (generator) as in Cases II and III. In the simplest case of the conventional three-phase (six-pulse) line-commutated rectifiers, the three-phase ac subsystem may also include an ac filter network which feeds a single three-phase bridge rectifier composed of six diodes. The single rectifier then feeds a dc system (load) through an optional dc filter network. For the converters that are composed of multiple sets of three-phase bridges, the 3-phase/n-phase transformer and possible interconnection/Inter-Phase Transformer (IPT) may be used as depicted in Figure 1.1.

Configurations similar to Figure 1.1 are commonly used as the input stage in low- to medium-power variable frequency drives (VFDs) and motor loads that are widely used in industrial and commercial applications [33]-[39]. These loads are often referred to as the front-end rectifier loads [40], [41], and may appear in large numbers in industrial facilities [42], distributed generation [43], as well as vehicular power systems [44]. The ac filter network may take various configurations depending on application and cost constraints, wherein passive or active filters may be considered to reduce the harmonics. Commonly used passive filters include series choke inductors and shunt filters that are tuned to lower harmonics (typically 5th and 7th) [45], [46].

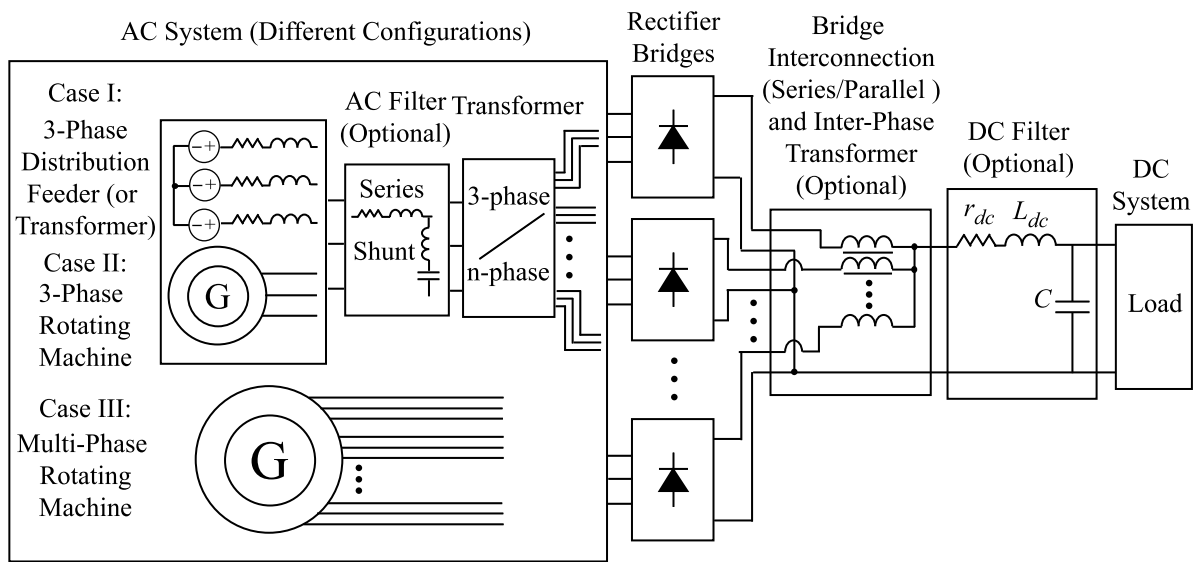


Figure 1.1 Typical configurations of multi-pulse line-commutated rectifier systems.

Converters with higher pulse count (e.g. 12-, 18-, and 24-pulse configurations) are also widely used in industrial applications, electric systems of aircrafts, ships, distributed generation systems, etc. [47]-[49]. High-pulse-count converters are generally considered to improve the quality of the output dc voltage as well as the current at the input ac terminals. These converters may also be used to improve the reliability of systems whenever such

property is important. As illustrated in Figure 1.1, higher-pulse-count converters may be fed from a distribution feeder (or transformer) or an electric machine. The use of a 3-to-n-phase transformer is inevitable in the first case where the converter is fed from a typically three-phase power network. In the case of a machine-fed high-pulse-count converter, instead of using a multi-phase transformer (as in Case II), the multi-phase voltages may be directly produced by the means of multi-phase machine windings [50], i.e., Case III in Figure 1.1. In all the above cases, additional ac filtering may also be employed, if desired, but it is often not required due to the presence of transformer and/or electric machine. Each of the multiple three-phase output sets of the ac subsystem are fed into a diode bridge. At the dc side, the bridges may be generally interconnected using various configurations, e.g., series, parallel, or a combination, with or without an inter-phase transformer. Similar to the case of six-pulse converter, the rectifier ultimately feeds a dc subsystem (load) through an optional dc filter network.

The objective of average-value modeling is to replace the discontinuous switching cells, the rectifier sub-circuits, with continuous circuit elements and dependent sources that reproduce the averaged behavior of the switching cell within a prototypical switching interval. Dynamic AVMs for line-commutated converters have been generally developed using two main approaches, i.e., analytical [50]-[68] and parametric [69]-[74].

In analytical approach, the system equations are mathematically derived, and the network variables are then averaged over a prototypical switching interval [51]. The first challenge in deriving the AVMs analytically is the existence of the so-called operational modes, e.g., Continuous Conduction Modes (CCM) and Discontinuous Conduction Mode (DCM). In general, an operational mode is defined by a sequence of repeated topologies determined by periodic changes of switches in steady-state operation. The changes in load conditions would lead to a change in the topologies and hence the mode of operation. Therefore, operational modes are functions of the loading/operating conditions. Also, the shapes of the current and

voltage waveforms may vary significantly in different operational modes. Thus, deriving the AVMs requires knowledge of the operational modes and the boundary conditions for which the respective averages will be valid. In many cases, the converter might be designed to operate in a certain operational mode in steady-state. Most of the analytically-derived AVMs therefore assume a certain operational mode (typically only one mode) [50], [51], [53]-[59], [63]-[68]. However, in order to accurately predict the transients, the average models should be developed for all possible operational modes. Therefore, there will be an AVM for each operational mode that is in the range of interest. Such models can then be “switched” as the system changes the modes, which makes this approach additionally challenging. In more complicated configurations such as 12-pulse or 18-pulse converters (Figure 1.1), the number and complexity of operational modes significantly increases [62], [75] making the analytical approach of deriving the correct average-value equations even more challenging and less tractable.

Using the analytical approach, it is also generally difficult to establish closed-form explicit equations that describe the system of complicated configurations, e.g., machine-fed converter systems (Figure 1.1 Cases II and III) [53]–[55]. In many cases, the final model is implicit and would require iterative solution. In addition to the above challenges, the analytical derivation of AVMs becomes cumbersome or impractical when the model includes parasitics of semiconductor switches, losses or magnetic saturation of electric machinery, etc.

To overcome the challenges of the analytical average-value modeling, the parametric approaches have evolved [69]-[74]. In these approaches, a proper state model AVM structure is first defined, and the parameters of the AVM are then extracted numerically from a detailed switch-level model of the system, or possibly a hardware prototype, using methods similar to the “black-box” approach. For this purpose, the averaging concept is numerically applied in order to extract appropriate model parameters. Although establishing the dynamic average-value models using parametric approach requires a detailed model of the system,

once established properly, the AVM is valid for a wide range of operating conditions and possibly all desired operational modes. Moreover, this approach may be systematically extended to other converters/configurations, and accounting for the losses and parasitics becomes more practical compared to the analytical approach.

1.2.1 Three-Phase (Six-Pulse) Converter Models

Various models for the six-pulse converter system have been presented in the literature. Several models that are of particular interest to this research are listed in Table 1.1 together with the features of each model. A great deal of contribution has been made in this field by the research group at Purdue University wherein analytically-derived AVMs have been formulated for voltage-source- [51] and machine-fed [52]–[55] converters. The AVM for this system is typically considered for CCM-1 mode of operation. The model [51], for example, is valid in one mode (i.e. CCM-1) and neglects the resistance on the ac side. Subsequent effort has been made by the research group at Virginia Polytechnic Institute and State University (Virginia Tech) [65], [66] to include the ac side resistance and improve the model dynamics. A constant parameter AVM has been also developed for machine-fed converter in a collaborative work involving the same research group [69]. A particular case of three-phase rectifier feeding constant-voltage loads has been addressed in collaborative work at Massachusetts Institute of Technology (MIT) and the University of Wisconsin-Madison [57], [58], and subsequent collaboration of the research groups at the University of Belgrade and the Swiss Federal Institute of Technology Zurich (ETH) [59].

The development of parametric approach is owed largely to the contributions of the research group at the University of British Columbia (UBC) [70], [71], [72]. The model proposed in [70] relates the averaged dc and ac variables through the parametric algebraic functions that are established numerically for the desired range of operation and modes. A

transient study may be carried out using a detailed model of the system from which the parametric functions are readily calculated numerically [71].

Table 1.1 Dynamic average models of the three-phase (six-pulse) rectifier systems.

Models	Steady-State/ Dynamic	Dynamic Order (Full/ Reduced)	DCM, CCMs (1, 2, 3)	AC Filter (r_{ac}, L_{ac})	DC Filter (r_{dc}, L_{dc}, C)	Variable AC Inductance (Yes / No)
[51]	Dynamic	Reduced	CCM 1	L_{ac}	r_{dc}, L_{dc}, C	No
[57], [58]	Dynamic	Reduced	CCM 2	r_{ac}, L_{ac}	C	No
[59]	Dynamic	Reduced	CCM 2	L_{ac}	C	No
[65], [66]	Dynamic	Reduced	CCM 1	r_{ac}, L_{ac}	r_{dc}, L_{dc}, C	No
[53]	Steady-State	N/A	CCM 1	-	r_{dc}, L_{dc}, C	Yes
[54]	Dynamic	Reduced	CCM 1	-	r_{dc}, L_{dc}, C	Yes
[55], [56]	Dynamic	Reduced	CCM 1	-	C	Yes
[69]	Dynamic	Full	CCM 1	-	C	Yes
[52]	Dynamic	Reduced	CCMs 1, 2, 3	-	r_{dc}, L_{dc}, C	Yes
[70], [71], [72]	Dynamic	Full	CCMs 1, 2, 3	-	r_{dc}, L_{dc}, C	Yes

1.2.2 High-Pulse-Count Converter Models

Several most relevant models of high-pulse-count converters available in the literature, together with their main properties, are summarized in Table 1.2. Most often, the number of pulses is considered to be a multiple of three, e.g., 12-, 18-, and 24-pulse configurations, wherein the system is constructed by several three-phase subsets as depicted in Figure 1.1. However, unusual cases are also encountered, such as the 5-phase (10-pulse) configuration considered in [60], [61]. In the above research, conducted at the University of Missouri-Rolla, extensive analytical effort has been required for derivation of analytical AVMs for all operational modes in both cases of voltage-source- and machine-fed converter systems. However, considering the amount of effort required in [60], such analysis does not seem practical for higher-pulse-count systems with significantly more operational modes.

Generally, as the number of pulses increases, the number and complexity of the operational modes will significantly increase. This makes analytical average-value modeling of the high-pulse-count converters very challenging in general. Typically, only the most common mode of operation is considered. In many cases, additional assumptions and/or approximations are employed in order to simplify the model derivation. A common assumption is the idealized operation of the multi-phase transformer in voltage-source-fed converters.

Table 1.2 Dynamic models of high-pulse-count converter systems.

Models	Pulse Count	Detailed/ Analytical AVM/ Parametric AVM	AC Subsystem (Voltage Source/ Rotating Machine)	Dynamic Order (Full /Reduced)	Single Mode / Multi Mode	Transformer Dynamics (Yes, No)
[60], [61]	10-pulse	Detailed and Analytical AVM	Voltage Source and Rotating Machine	Reduced	Multi Mode	No
[47], [76], [77], [78]	12-pulse	Detailed	Voltage Source	Full	Multi Mode	Yes
[62]	12-pulse	Analytical AVM	Voltage Source	Reduced	Multi Mode	No
[63], [64]	12-pulse	Analytical AVM	Voltage Source	Reduced	Single Mode	No
[73]-[75]	12-pulse	Detailed	Rotating Machine	Full	Multi Mode	N/A
[50]	12-pulse	Analytical AVM	Rotating Machine	Reduced	Single Mode	N/A
[73]	12-pulse	Parametric AVM	Rotating Machine	Full	Multi Mode	N/A
[74]	12-pulse	Parametric AVM	Rotating Machine	Full	Multi Mode	N/A
[48], [77], [78]	18-pulse	Detailed	Voltage Source	Full	Multi Mode	Yes
[65]-[68]	18-pulse	Analytical AVM	Voltage Source	Reduced	Single Mode	No
[49], [79]	24-pulse	Detailed	Voltage Source	Full	Multi Mode	Yes

Analytically-derived AVMs for the 6-phase (12-Pulse) voltage-source- and machine-fed converter systems have been developed for common operating conditions in [62]-[64] and [50], respectively. Similar to the case of a 6-pulse converter, in many cases the analysis is limited to only one mode of operation. In [63], [64], to facilitate the derivation, it is additionally assumed that the duration of commutation interval (angle) is small, resulting in an approximate model for a single operating mode. The phase-shifting transformer is also assumed ideal, i.e., the dynamics, magnetizing current, losses, etc. are neglected. Reference [62], however, derives averaged dc side equations for the 12-pulse voltage-source-fed system, in all modes of operations, together with the respective boundary conditions.

Obtaining these results required extensive analytical effort. Parametric approach has been considered in [73], [74] for 12-pulse machine-converter systems in an attempt to include a range of operating conditions, and reduce the extent of analytical effort. For the 18-pulse configuration, a reduced-order analytical AVM has been formulated and evaluated in [65]-[68].

1.3 Research Objectives and Anticipated Impact

All above-mentioned average models developed for the line-commutated converters have been reported to provide acceptable results in particular cases investigated therein. In general, however, each model has several limitations. A unified and generalized dynamic AVM methodology for high-pulse-count converters has not been established prior to this thesis. Moreover, the dynamic AVMs available in the literature [50]-[74] have been formulated for the SV-based approach, wherein the discretization of the state equations is done automatically at the system level. These models, therefore, may not be readily implementable in the EMTP-type solution [8], where the discretization is performed at the branch/component level. As these software packages are increasingly used for simulation of power-electronic-based systems, integration of AVMs into these packages is very desirable to achieve efficient simulation of system transients. Developing the AVMs for implementation in these programs is more challenging and has not yet received the needed attention.

The ultimate goal of this research is to develop a generalized methodology that can be readily applied to an arbitrary high-pulse-count system (Figure 1.1), in order to develop an accurate and full-order dynamic average representation of the system in both SV- and NA-based simulators. The first steps toward this goal include addressing the fundamental shortcomings of the six-pulse converter AVMs. Therefore, this thesis has the following

research objectives for the six-pulse voltage-source-fed, six-pulse machine-fed, and high-pulse-count converter systems:

Objective 1: Development of the AVMs for EMTP-type solution

Extension of the analytical and parametric approaches to the EMTP-type solution is the first objective of this thesis. For this purpose, indirect and direct methods of interfacing the developed AVMs with the external EMTP circuit network are developed and compared. The performance of the developed AVMs is then investigated and compared in a wide range of operating conditions including DCM and CCM operation, as well as under unbalanced excitation. The dynamic model of front-end rectifiers with unbalanced input voltages is particularly desirable when studying single-phase faults and unbalance voltage sags [80].

Objective 2: Including the effects of machine and rectifier losses

In development of AVMs, the switches are typically assumed ideal [50]-[64], [70]-[74], and the effects of machine losses are neglected [50], [52]-[56], [60], [61], [69]-[74]. The effects of diode and machine losses are particularly important in low voltage applications such as vehicular power systems that operate at 12-14 V dc. Taking these effects into account is the second objective of this research.

Objective 3: Developing the generalized high-pulse-count AVM methodology

For high-pulse-count converters, the existing models have been derived for one particular configuration depicted in Figure 1.1. The third objective of this research is to develop a unified and generalized AVM methodology for all configurations of the high-pulse-count converter systems. Achieving this objective requires the following steps:

(a) Accurate full-order representation of a multi-phase transformer

The steady-state and dynamic effects of the multi-phase transformer have been fully or partially neglected in the AVMs available in the literature [62]-[68]. The transformer is typically assumed to instantaneously convert the three-phase input voltages to a set of multi-phase voltages that are equal in magnitude and evenly shifted in phase. Due to neglecting parts of the system dynamics, the final model then has a reduced-order formulation. In some cases, [65], in order to improve the accuracy of the model, artificial equivalent leakage inductances and resistances have been computed and placed at the secondary side in series with the ideal multi-phase voltage source. Such oversimplified representation of the transformer ignores important effects such as magnetizing current and dynamics of the transformer. An accurate full-order representation of a multi-phase transformer is required for the generalized AVM methodology.

(b) AVM validity in all operational modes and under unbalanced conditions

In the available AVMs for high-pulse-count systems, the operation is usually limited to one mode only [50], [62]-[68], [73], [74]. Moreover, all these models have been derived under the assumption of a balanced excitation [50], [60]-[68], and therefore are not suitable to investigate the system performance under any asymmetric faults. It is therefore very desirable to have a generalized AVM methodology that would be valid in all operational modes as well as under unbalanced conditions.

Accomplishment of the Objectives 1 through 3 would enable accurate and accelerated simulation of power systems that include a large number of power-electronic-based converters and modules. With the development of Smart Energy Grids, the need for rapid and efficient simulation of such systems is continuously increasing. It is envisioned that such dynamic models may be readily implemented in the future generations of both SV-based and

EMTP-type simulation programs as standard built-in library components and models. While conducting transient simulation of large power systems, for each power-electronic-based subsystem, the user would then have an option to choose the dynamic average equivalent instead of the detailed switch-level model. Employing these models for representing the power electronic components will result in significant gains in simulation speeds, set the stage for the new generation of transient simulation tools with enhanced features and capabilities, and enable new computer-aided design tools, etc. Such tools would be used by thousands of researchers and engineers throughout the world saving them countless hours of precious time.

1.4 Thesis Organization

This thesis is organized as follows: In Chapter 2, implementation of analytical and parametric AVMs in SV-based programs is considered. This Chapter sets the stage for the discussions in Chapter 3, wherein the AVMs are formulated specifically for implementation in the EMTP-type software packages. Both approaches of constructing the average models, i.e., analytical and parametric, are considered. Two methods for interfacing the developed AVMs with the external circuit-network, i.e., indirect and direct methods, are introduced and compared.

In Chapter 4, the performance of developed models in SV-based and NA-based simulators is investigated and compared under various operating conditions including light and heavy loading (DCM and CCM) as well as balanced and unbalanced ac side. For this purpose, a front-end rectifier example system is considered.

In Chapter 5, the effects of parasitics and machine losses are taken into account while developing the AVM for machine-fed six-pulse converter systems. An example vehicular power system is considered in this Chapter. A thorough analysis is performed on this system to demonstrate the effects of losses and effectiveness of the new AVM in predicting the

entire power conversion chain. It is demonstrated that the results predicted by the proposed AVM provide an excellent match with the experimental set-up and those of the detailed switching model. A significant improvement in accuracy compared to the previously-developed state-of-the-art AVM is also demonstrated.

In Chapter 6, a generalized methodology is developed for dynamic average modeling of high-pulse-count converter systems in SV-based and NA-based simulators. An example 400Hz aircraft power system with an 18-pulse topology is considered to demonstrate the new methodology. The proposed methodology is general and could be readily applied to an arbitrary high-pulse-count system where the number of phases is a multiple of three. The steady-state and dynamic effects of transformer are completely taken into account as well as the negative and zero sequence components for unbalanced operation. For this purpose, a generalized transformer model is developed in transformed (qd) and phase (abc) variables that can be used in AVMs. The effectiveness of the developed methodology is demonstrated through extensive simulation studies in time and frequency domains including asymmetric faults.

Finally, in Chapter 7, the conclusions are drawn. The research contributions are also summarized and related to the original objectives of this thesis. The path for future research is then outlined and related to the present efforts undertaken by the UBC's Electric Power and Energy Systems research group.

Chapter 2: Dynamic Average Modeling in State-Variable-Based Simulators

2.1 State-Variable-Based Simulators

State Variable (SV) approach is frequently used for analysis of dynamic systems including electric power systems. The examples of software packages include ACSL [1], Easy5 [2], Eurostag [3], and the well-known MATLAB\Simulink [4]. There are also more specialized tools such as SimPowerSystems (SPS) [5], PLECS [6], and ASMG [7], etc., that come with circuit interfaces and built-in libraries for simulation of transients in power and power-electronic modules [81]. Internally, the program engine assembles system of differential and/or differential algebraic equations (DAEs) that constitute the state-variable-based model of the overall system. Depending upon the features of a given program, the DAEs may be converted into a first-order system of differential equations (ODE) as

$$\begin{aligned} \dot{\mathbf{x}} &= \mathbf{f}(\mathbf{x}, \mathbf{u}, t) \\ \mathbf{y} &= \mathbf{g}(\mathbf{x}, \mathbf{u}, t) \end{aligned} \quad (2.1)$$

where \mathbf{x} , \mathbf{u} , and \mathbf{y} denote the vectors of state variables, inputs, and outputs, respectively. Whenever appropriate, the linear time invariant part of the system/circuit may then be represented using a more compact state-space equation:

$$\begin{aligned} \dot{\mathbf{x}} &= \mathbf{Ax} + \mathbf{Bu} \\ \mathbf{y} &= \mathbf{Cx} + \mathbf{Du} \end{aligned} \quad (2.2)$$

where \mathbf{A} , \mathbf{B} , \mathbf{C} , and \mathbf{D} are the so-called state-space matrices that are computed for the given topology and parameters of the linear circuit. In some tools, for example SimPowerSystems [5], the circuit part is directly implemented in the form of (2.2), whereas the remaining part of the system e.g. control blocks, mechanical subsystem, etc. are in a more general form (2.1).

The time-domain transient responses are then calculated numerically by integrating the state-space equations (2.1), (2.2) using either fixed- or variable-step ODE solvers embedded in the SV program. The formulations (2.1), (2.2) also contain very useful information about the system's dynamical modes which is often utilized together with numerical linearization for the frequency-domain characterization and design of controllers.

The SV-based programs, unlike EMTP-type simulators, allow the use of variable-step integration (solvers) wherein the step-size is dynamically adjusted to satisfy the local accuracy constraints. Figure 2.1 shows a typical time-stepping flowchart of the SV-based programs. As usual, after initialization the program estimates the size for the first time step and the simulation enters the major time-stepping loop. This step-size is limited between the user-defined minimum and maximum values of Δt_{\min} and Δt_{\max} , respectively. In the next step, the state vector \mathbf{x}_{n+1} is computed together with an error function estimate \mathbf{r} and the vector of output variables \mathbf{y}_{n+1} . The local accuracy of the solution in each time-step is assessed based on the value of this error function. Typically, the user can also specify the absolute and relative error tolerances. If the error estimate \mathbf{r} exceeds either of the tolerances, the time-step is reduced (for example to a half of the previous Δt) and the solver attempts the solution again. To accurately handle the switching discontinuities, the algorithm also computes a special vector of event variables \mathbf{e}_{n+1} . These variables are monitored at each time step for zero-crossing. A topological change in the system is detected whenever one of the variables in \mathbf{e}_{n+1} changes the sign within the time step. If this condition is detected, the

time step is reduced and the solution iterates inside the minor time-stepping loop to precisely locate the zero-crossing. After that, the equations are updated accordingly and the simulation proceeds. Hence, very frequent switching will result in more iterations and effective reduction of the time step. This may lead to significant increase in the computation time especially when a large number of switches are present in the network or a high frequency switching is taking place.

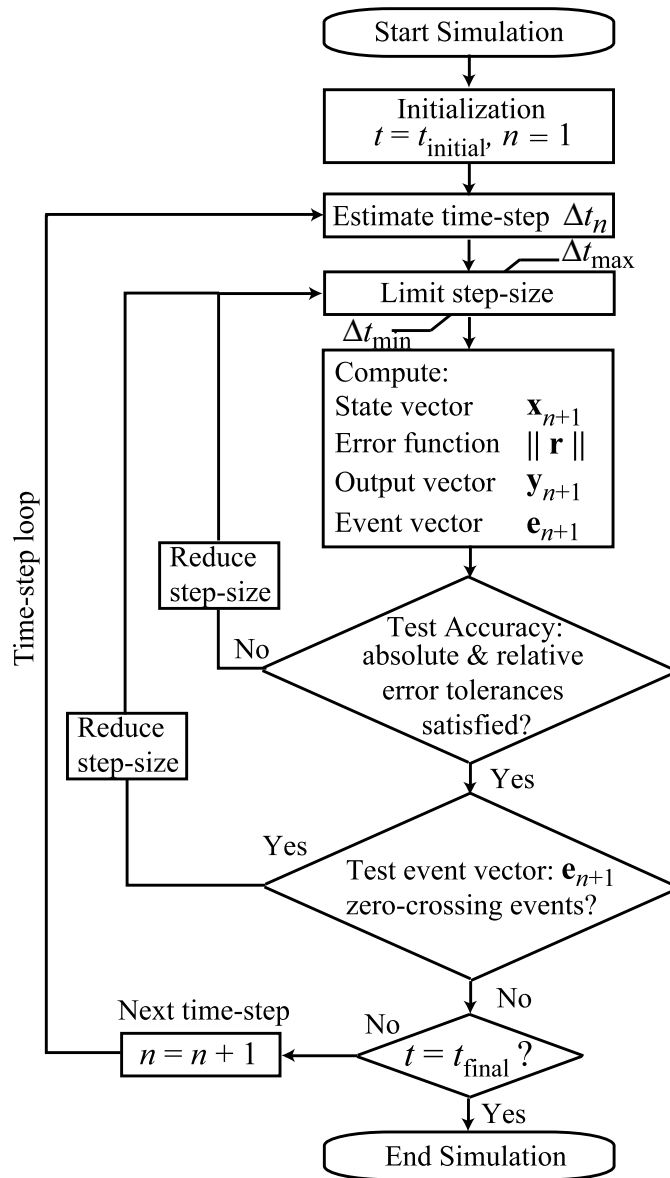


Figure 2.1 Flowchart of a typical variable-step state-variable-based solver.

2.2 Detailed Analysis

Let us start the discussion from a simple case of three-phase (six-pulse) converter system depicted in Figure 2.2, wherein a series filter inductor is considered at the ac side. Topological variations in this system, such as including/excluding the filters at the ac/dc sides, significantly affect the rectifier operation leading to discontinuous (DCM) and continuous (CCM) conduction modes commonly encountered in practical applications. In the simplified circuit diagram of Figure 2.2, the ac network is represented by its Thevenin equivalent voltages, e_{abc_s} and the series resistance and inductance, r_{th} , L_{th} . The impedance of the optional series ac filter is represented by r_{ac} , L_{ac} , and the combined equivalent impedance of the ac subsystem is denoted by r_s , L_s . It should be noted that if the system is fed from a synchronous generator (Figure 1.1 Case II), the machine may be represented using the voltage-behind-reactance formulation [82]–[84] which results in a circuit similar to Figure 2.2 (but possibly with coupled and/or variable equivalent inductances).

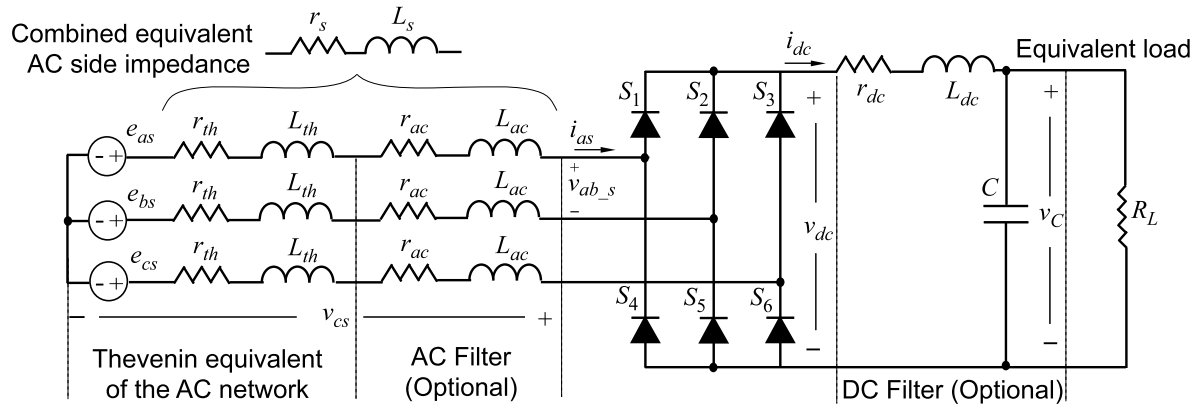


Figure 2.2 Simplified circuit diagram of a typical three phase front-end rectifier load system.

In Figure 2.2, the dc filter, represented by r_{dc} , L_{dc} , C , is also optional and may be partially present in the system. In many cases, such as battery charging [85], [86] and variable-speed-drive applications [40], [41], the dc filter inductor may be omitted whereas

the capacitor is included to smooth the dc bus voltage. In such cases, the ac filter inductor must often be included in order to reduce ac side current harmonics. To represent an equivalent energy dissipating load on the dc side in Figure 2.2, a simple resistor, R_L , is connected to the dc bus [85], [87], [88].

In order to study the performance of the front-end rectifier load system of Figure 2.2, the system detailed model, wherein switching of all diodes is represented, maybe readily built in many SV-based simulators. In this system, a discontinuous conduction mode (DCM) operation is typically observed at light load. This mode is frequently encountered in the front-end rectifiers of low- to medium power variable frequency drives [87], [89], where the ac filter is often not used (or is very small) but there is a large capacitor on the dc bus. The corresponding waveforms are illustrated in Figure 2.3 (a). If the angular frequency of the ac source is denoted by ω_e , there exist six equal switching intervals, T_s , within a single electrical cycle defined by $T_{cycle} = 2\pi/\omega_e$. In DCM, each switching interval is then divided into two subintervals. During the conduction subinterval, t_{cond} , two diodes are conducting and two of the phases carry the dc bus current in opposite directions. At some point, the line-to-line voltage in these two phases becomes smaller than the dc bus voltage and the current reaches zero and remains zero for the rest of the interval – hence discontinuous mode. This subinterval is denoted by t_{dcm} in Figure 2.3 (a). During t_{dcm} , all diodes are off. The dc load is, in the meanwhile, being fed from the dc capacitor as observed in the dc bus voltage waveform v_{dc} . The switching pattern in DCM is therefore 2-0.

If the combined value of the source and ac filter inductances becomes sufficiently large [87], [90], or the load on the dc bus is sufficiently increased, the dc bus current becomes continuous – hence continuous mode. In this case, as the load varies from a light load to a short circuit, three different switching patterns can be observed resulting in three distinct continuous conduction modes (CCM) of operation [91]. The corresponding waveforms of the

phase currents and the dc bus voltage are shown in Figure 2.3 (b). The operational modes are summarized in Table 2.1 together with the conduction pattern and the commutation angle.

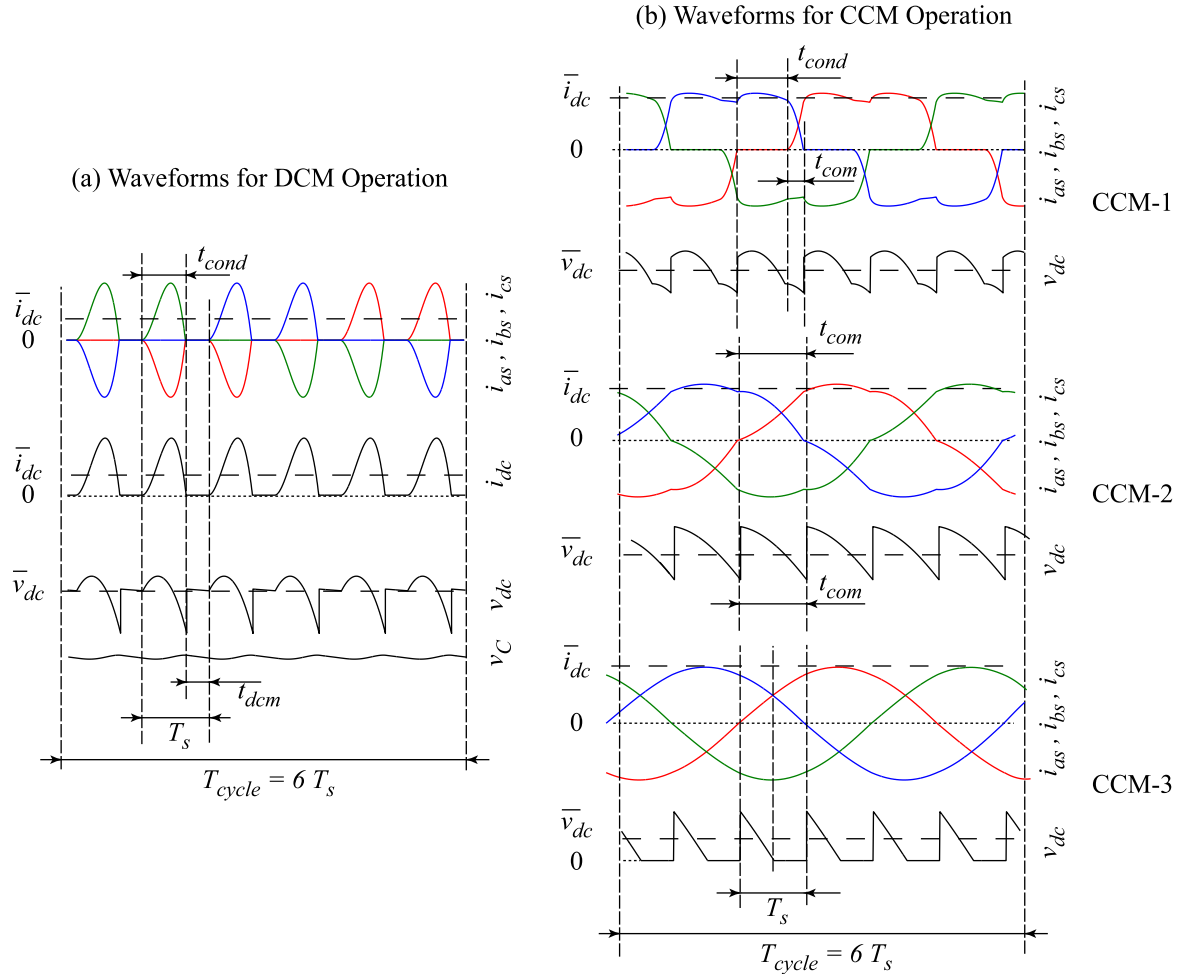


Figure 2.3 Typical current and voltage waveforms of the six-pulse rectifier: (a) operation in DCM; and (b) operation in CCM.

Table 2.1 Operational modes of the conventional 3-phase (6-pulse) rectifier.

Operational Modes	Conduction Pattern	Commutation Angle
DCM	2-0	$\mu = 0^\circ$
CCM-1	2-3	$0^\circ < \mu < 60^\circ$
CCM-2	3	$\mu = 60^\circ$
CCM-3	3-4	$60^\circ < \mu < 120^\circ$

Within CCM-1 [see Figure 2.3 (b), top plot], each switching interval is divided into two subintervals referred to as commutation and conduction [51]. During the conduction subinterval, t_{cond} , only two diodes conduct; whereas during the commutation subinterval, t_{com} , corresponding to the commutation angle $\mu = \omega_e \cdot t_{com}$, the current is being switched from one phase to another; and three diodes conduct. Therefore, a conduction pattern of 2-3 diodes is observed within each 60 electrical degrees, and $0^\circ < \mu < 60^\circ$.

The mode CCM-2 [see Figure 2.3 (b), middle plot], may be achieved by further increasing the load current. In this mode, the commutation angle μ increases and reaches 60 degrees resulting in disappearance of the conduction subinterval. Consequently, there will be three diodes carrying current throughout the switching intervals. Hence, the conduction pattern becomes just 3 (or 3-3).

If the load current is further increased, the commutation angle μ starts to increase resulting in the third mode, CCM-3 [see Figure 2.3 (b), bottom plot]. This changes the switching pattern to 3-4 conducting diodes. Note that this mode contains a topology with 4 simultaneously conducting diodes, which temporarily short-circuits the output as observed in Figure 2.3 (b), (bottom plot). This last mode rarely occurs in practical systems, but may be encountered in rotating machines and brushless exciters with very large inductances [52].

Certain variations in the topology of Figure 2.2 may prevent the occurrence of some operational modes. For instance, without the dc filter inductor, the CCM-3 mode cannot occur and the system could hence only operate in DCM, CCM-1 or CCM-2. Observing the phase currents in DCM depicted in Figure 2.3 (a), it can be concluded that such currents will inject significant harmonics into the network. To avoid operation in DCM, medium and large drives with front-end rectifiers often install additional ac filters (series inductors and shunt filters) to shift the operation to CCM-1 or CCM-2.

2.3 Dynamic Average Modeling

2.3.1 Analytical Approach

In analytical approach, system equations are mathematically derived, and the network variables are then averaged over a prototypical switching interval [51]. The fast averaging over a prototypical switching interval T_s is typically defined as

$$\bar{f} = \frac{1}{T_s} \int_{t-T_s}^t f(\tau) d\tau, \quad (2.3)$$

where f is a network variable, e.g., voltage or current, t is a scalar to denote time, and \bar{f} is the so-called fast average of f .

As observed in the waveforms of Figure 2.3, in steady-state, the variables on the dc side, e.g., i_{dc} , v_{dc} consist of a constant average value superimposed by some ripple due to switching, which often necessitates the use of large capacitors on the dc link. The averaging concept (2.3) may then be directly applied to the dc variables in the system. However, for ac variables, using the above equation evidently does not yield the desired result. Instead, the ac variables first have to be transformed using an appropriate synchronously rotating $qd0$ reference frame [51]. The transformation of a three-phase network variable f (i.e., voltage or current) from phase domain (abc) to an arbitrary $qd0$ reference frame is accomplished using the transformation matrix \mathbf{K} as [51]

$$\mathbf{f}_{qd0} = \mathbf{K} \mathbf{f}_{abc}, \quad (2.4)$$

$$\mathbf{f}_{qd0} = [f_q \quad f_d \quad f_0]^T, \quad (2.5)$$

$$\mathbf{f}_{abc} = [f_a \quad f_b \quad f_c]^T, \quad (2.6)$$

$$\mathbf{K} = \frac{2}{3} \begin{bmatrix} \cos \theta & \cos\left(\theta - \frac{2\pi}{3}\right) & \cos\left(\theta + \frac{2\pi}{3}\right) \\ \sin \theta & \sin\left(\theta - \frac{2\pi}{3}\right) & \sin\left(\theta + \frac{2\pi}{3}\right) \\ \frac{1}{2} & \frac{1}{2} & \frac{1}{2} \end{bmatrix}. \quad (2.7)$$

The angle θ denotes the instantaneous angle of the reference frame which is expressed as

$$\theta = \omega t + \theta_{a0}, \quad (2.8)$$

in terms of the reference frame angular frequency ω and initial angle θ_{a0} . To convert $qd0$ variables back to abc , the inverse transformation may be employed [51]:

$$\mathbf{K}^{-1} = \begin{bmatrix} \cos \theta & \sin \theta & 1 \\ \cos\left(\theta - \frac{2\pi}{3}\right) & \sin\left(\theta - \frac{2\pi}{3}\right) & 1 \\ \cos\left(\theta + \frac{2\pi}{3}\right) & \sin\left(\theta + \frac{2\pi}{3}\right) & 1 \end{bmatrix}. \quad (2.9)$$

In a balanced system, the zero sequence is not present and the third element in (2.5) is hence equal to zero. Also, sometimes the zero sequence is prevented by the system topology as in Figure 2.2, wherein the bridge rectifier only sees the line voltages, and the neutral point of the source appears floating. In such cases, the order of the transformation is reduced to two, and the reference frame is simply referred to as qd reference frame.

In a synchronously rotating reference frame, by definition, the angular frequency of the reference frame ω is equal to that of the ac source ω_e . The so-called converter reference frame [51], a particular case, is typically chosen to facilitate the analysis. In this synchronous reference frame, the reference frame angle θ is aligned with the angle of phase a voltage at the bridge terminal. In this case, due to mathematical properties of the transformation, the d -axis component of the transformed voltages will be zero as depicted in Figure 2.4 (a). The relationship between the voltages in the converter and arbitrary reference frames may be written as [51]

$$\begin{bmatrix} v_{qs}^c \\ 0 \end{bmatrix} = \begin{bmatrix} \cos(\phi_c) & \sin(\phi_c) \\ -\sin(\phi_c) & \cos(\phi_c) \end{bmatrix} \begin{bmatrix} v_{qs}^a \\ v_{ds}^a \end{bmatrix}. \quad (2.10)$$

In the above equation, the superscripts c and a have been used to denote the variables expressed in the converter and arbitrary reference frames, respectively. Throughout this thesis, the converter reference frame will be the default reference frame of choice. Hence, for compactness of the equations, the superscript c may at times be dropped. The angle between the converter and arbitrary reference frames may also be deduced from Figure 2.4 (a) as [51]

$$\phi_c = \tan^{-1} \left(\frac{v_{ds}^a}{v_{qs}^a} \right). \quad (2.11)$$

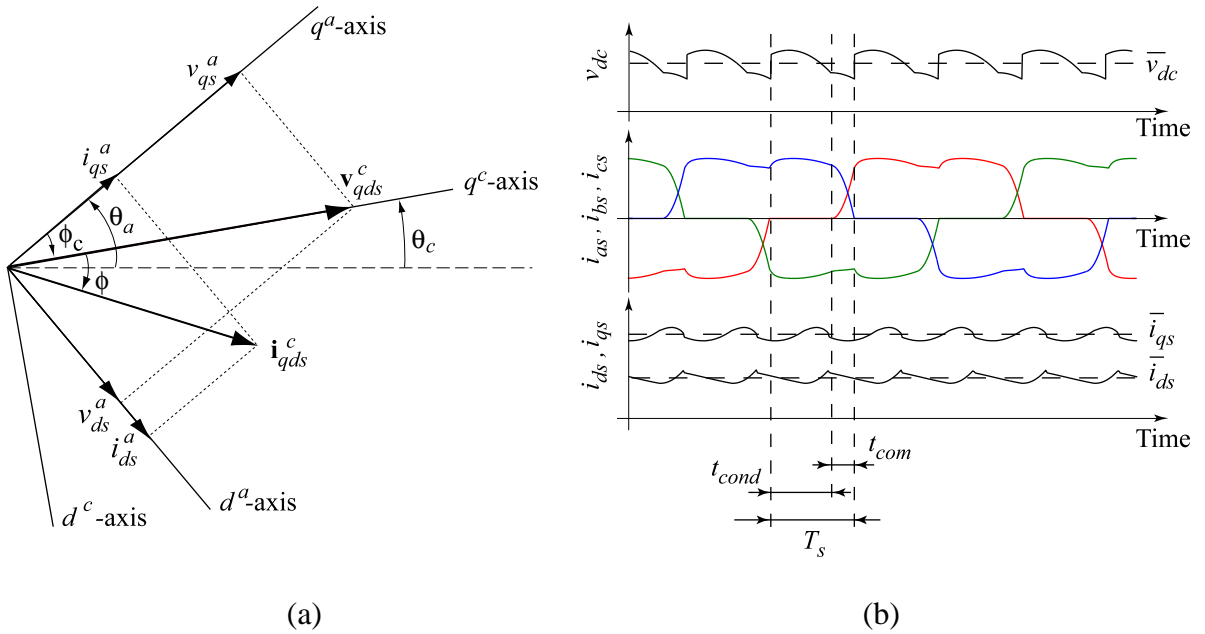


Figure 2.4 (a) Relationship among the variables in the converter and arbitrary reference frames; and (b) Typical waveforms and the respective transformed waveforms in converter reference frame.

The waveforms of the 6-pulse rectifier system for CCM-1 operation together with the transformed ac currents in the converter reference frame have been illustrated in Figure 2.4

(b). As seen in this figure, the resulting qd currents in steady-state are composed of a constant (dc) component and a superimposed ripple, quite similar to the dc bus voltage waveform, which allows averaging of these variables according to (2.3). The averaging of these variables using (2.3) removes the switching ripple but preserves the slower (dc) variations of the transformed variables.

2.3.1.1 Classical Reduced-Order Model (AVM-1)

In the classical model [51], the state equation describing the dynamics of the dc bus current is formulated as

$$\frac{d\bar{i}_{dc}}{dt} = \frac{\frac{3\sqrt{3}}{\pi}\sqrt{2}E - \left(\frac{3}{\pi}\omega_e L_s + r_{dc}\right)\bar{i}_{dc} - \bar{v}_C}{2L_s + L_{dc}}, \quad (2.12)$$

where E is the rms value of the phase voltage, and \bar{v}_C is the average dc filter capacitor voltage. To establish the average q – and d – axes components of the phase currents, the dc current is assumed constant and equal to its average value during the switching interval. Due to this assumption, the current dynamics disappear resulting in a reduced-order model. The phase currents are then expressed during conduction and commutation subintervals, and are averaged, respectively. The result of this procedure yields the following equations:

$$\begin{aligned} \bar{i}_{qs,com}^c &= \frac{-2\sqrt{3}}{\pi}\bar{i}_{dc} \left[\sin\left(\mu - \frac{5\pi}{6}\right) + \sin\left(\frac{5\pi}{6}\right) \right] \\ &\quad - \frac{3}{\pi}\frac{\sqrt{2}E}{\omega_e L_s}(\cos\mu - 1) + \frac{3}{4\pi}\frac{\sqrt{2}E}{\omega_e L_s}(\cos(2\mu) - 1), \end{aligned} \quad (2.13)$$

$$\begin{aligned} \bar{i}_{ds,com}^c &= \frac{-2\sqrt{3}}{\pi}\bar{i}_{dc} \left[\cos\left(\frac{5\pi}{6}\right) - \cos\left(\mu - \frac{5\pi}{6}\right) \right] \\ &\quad - \frac{3}{\pi}\frac{\sqrt{2}E}{\omega_e L_s}\sin\mu + \frac{3}{4\pi}\frac{\sqrt{2}E}{\omega_e L_s}(\sin(2\mu) + 2\mu), \end{aligned} \quad (2.14)$$

$$\bar{i}_{qs,cond}^c = \frac{-2\sqrt{3}}{\pi} \bar{i}_{dc} \left[\sin\left(\frac{7\pi}{6}\right) - \sin\left(\mu + \frac{5\pi}{6}\right) \right], \quad (2.15)$$

$$\bar{i}_{ds,cond}^c = \frac{-2\sqrt{3}}{\pi} \bar{i}_{dc} \left[\cos\left(\mu + \frac{5\pi}{6}\right) - \cos\left(\frac{7\pi}{6}\right) \right], \quad (2.16)$$

The final averaged ac side currents are obtained as

$$\bar{i}_{qs}^c = \bar{i}_{qs,com}^c + \bar{i}_{qs,cond}^c, \quad (2.17)$$

$$\bar{i}_{ds}^c = \bar{i}_{ds,com}^c + \bar{i}_{ds,cond}^c, \quad (2.18)$$

Finally, the commutation angle is expressed as

$$\mu = \cos^{-1} \left(1 - \frac{\sqrt{2} \omega_e L_s}{\sqrt{3} E} \bar{i}_{dc} \right). \quad (2.19)$$

The model defined by (2.12)–(2.19) is referred to as AVM-1.

2.3.1.2 Improved Reduced-Order Model (AVM-2)

A similar model has been derived in [65], where instead of assuming a constant value for the dc current during the switching interval, this current is assumed to change as

$$i_{dc}(\theta) = i_{dc0} + k \cdot \left(\theta - \frac{\mu}{2} \right), \quad (2.20)$$

where i_{dc0} is the average value of i_{dc} during the commutation period, and k is the derivative $di_{dc}/d\theta_e$ during this period of time. The effect of ac side resistance has been also partly taken into account. The resulting model has the following form:

$$\left[\frac{\frac{\pi}{3} - \mu + \frac{3\mu^2}{4\pi}}{\omega_e} r_s + \frac{4\pi - 3\mu}{2\pi} L_s + \frac{\frac{\pi}{3} - \mu}{2\omega_e} r_{dc} + L_{dc} \right] \frac{di_{dc}}{dt} \quad (2.21)$$

$$= \frac{3\sqrt{3}}{\pi} \sqrt{2} E \left(1 - \frac{r_s}{\omega_e L_s} \frac{\mu - \sin \mu}{2} \right) - \left(\frac{2\pi - 3\mu}{\pi} r_s + \frac{3}{\pi} \omega_e L_s + r_{dc} \right) i_{dc0} - v_C,$$

$$\bar{i}_{qs}^c = -\frac{2\sqrt{3}}{\pi} i_{dc0} \cos \mu + \frac{\sqrt{3}}{\pi} k \left(-\sin \mu + \frac{\pi}{3} \right) + \frac{3}{\pi} \frac{\sqrt{2}E}{\omega_e L_s} \left(\cos \mu - \frac{\cos(2\mu)}{4} - \frac{3}{4} \right), \quad (2.22)$$

$$\bar{i}_{ds}^c = -\frac{2\sqrt{3}}{\pi} i_{dc0} \sin \mu + \frac{\sqrt{3}}{\pi} k \left(\cos \mu + \frac{3 - \sqrt{3}\pi}{3} \right) + \frac{3}{\pi} \frac{\sqrt{2}E}{\omega_e L_s} \left(\sin \mu - \frac{\sin(2\mu)}{4} - \frac{\mu}{2} \right). \quad (2.23)$$

The model defined by (2.20)–(2.23) is referred to as AVM-2. This model uses the same commutation angle formulation expressed by (2.19).

2.3.2 Parametric Approach

In the parametric model [70], the rectifier switching cell is considered as an algebraic block that relates the dc voltage and current \bar{v}_{dc} , \bar{i}_{dc} to the ac voltages and currents $\bar{\mathbf{v}}_{qds}^c$ and $\bar{\mathbf{i}}_{qds}^c$ through the respective parametric functions as

$$\left\| \bar{\mathbf{v}}_{qds}^c \right\| = \alpha(\cdot) \bar{v}_{dc}, \quad (2.24)$$

$$\bar{i}_{dc} = \beta(\cdot) \left\| \bar{\mathbf{i}}_{qds}^c \right\|, \quad (2.25)$$

where $\alpha(\cdot)$ and $\beta(\cdot)$ are algebraic functions of the loading conditions. To complete this model, the angle between the vectors $\bar{\mathbf{v}}_{qds}^c$ and $\bar{\mathbf{i}}_{qds}^c$ is calculated based on Figure 2.4 (a) as

$$\phi(\cdot) = \tan^{-1} \left(\frac{\bar{i}_{ds}^a}{\bar{i}_{qs}^a} \right) - \tan^{-1} \left(\frac{\bar{v}_{ds}^a}{\bar{v}_{qs}^a} \right). \quad (2.26)$$

Deriving closed-form analytical expressions for $\alpha(\cdot)$, $\beta(\cdot)$, and $\phi(\cdot)$ is impractical. Instead, these functions may be extracted using the simulation and expressed in terms of dynamic impedance of the switching cell defined as

$$z = \frac{\bar{v}_{dc}}{\left\| \bar{\mathbf{i}}_{qds}^c \right\|}. \quad (2.27)$$

The model based on (2.24)–(2.27) is referred to as PAVM.

2.4 Implementation of the AVMs in SV-Based Programs

Both analytical (AVM-1 [51] and AVM-2 [65]) and parametric (PAVM [70]) AVMs for the three-phase line-commutated rectifier have been formulated as state models. Block diagrams for the final implementations of these approaches are depicted in Figure 2.5 (a) and (b), respectively. These AVMs are straightforward to implement in SV-based simulators using the respective dependent sources and a set of differential and/or algebraic equations that relate the dc and transformed ac variables.

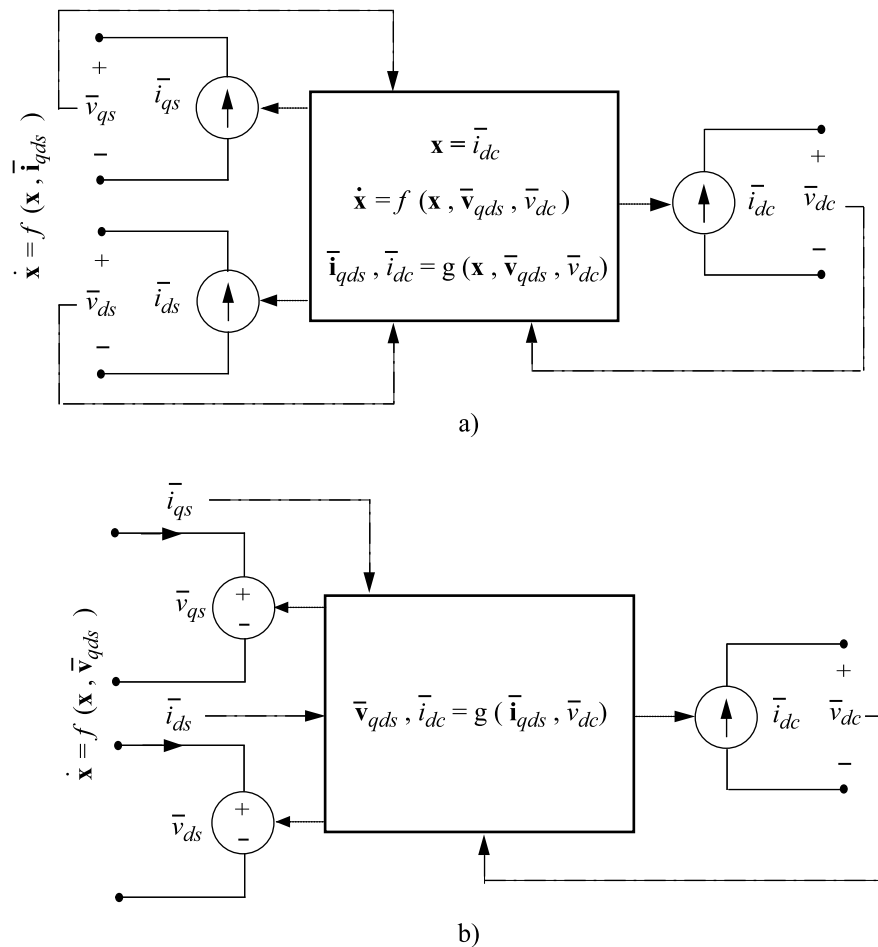


Figure 2.5 Block diagrams of AVM implementations in SV-based simulators: (a) analytically-derived (AVM-1 and AVM-2); and (b) parametric (PAVM).

2.5 Small-Signal Frequency-Domain Analysis

In addition to time-domain studies, the detailed and dynamic average models of line-commutated converters are frequently used for small-signal frequency-domain analysis. To illustrate the small-signal impedance-based analysis of the ac-dc converters [14], [92]–[97], let us first consider the general case of a controlled ac-dc converter connected between System 1 and System 2 as shown in Figure 2.6. The control input (denoted by d) may be the firing angle, for instance, in thyristor controlled converters, or the duty cycle in PWM converters. This converter is first assumed to be operating in a steady-state determined by the fixed control input $d = D$ and a set of balanced ac input voltages. Averaged over a switching interval, the dc variables i_{dc} , v_{dc} will then have constant quiescent values I_{dc} , V_{dc} , respectively, that define the operating point. If the input voltages are kept intact, and a small-signal perturbation \hat{d} , much smaller in amplitude compared to the quiescent value d , is superimposed on the control input, the control-to-output transfer function of the converter $H(s)$ may then be defined as

$$H(s) = \frac{\hat{v}_{dc}(s)}{\hat{d}(s)}, \quad (2.28)$$

where \hat{v}_{dc} is the small-signal perturbation around the average output dc voltage V_{dc} due to the changes in the control input \hat{d} .

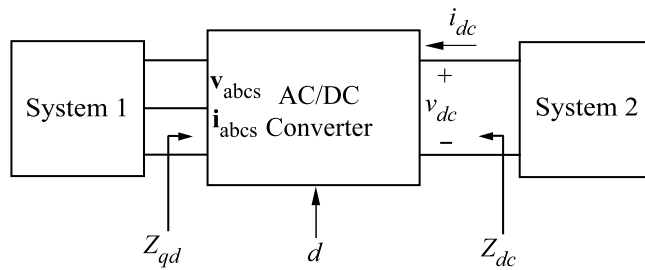


Figure 2.6 System-level impedance-based representation of subsystems interconnected through an ac-dc converter.

Next, the control input is assumed to be kept constant ($d = D$), and a small-signal perturbation is then considered around the quiescent operating point caused by, for instance, the small-signal voltage \hat{v}_{dc} injected at the dc bus. In uncontrolled line-commutated converters, the small-signal perturbation at the dc bus may be implemented in practice by means of a resistor that is frequently switched on and off at the dc bus [54]. This small-signal injection is going to introduce a small perturbation in other network variables about their quiescent operating points. The small-signal output impedance looking from the dc side may then be expressed as

$$Z_{dc}(s) = \frac{\hat{v}_{dc}(s)}{\hat{i}_{dc}(s)}, \quad (2.29)$$

where \hat{i}_{dc} is the small-signal perturbation around I_{dc} caused by the injected signal. The frequency of the injection signal may be slowly swept in the desired frequency range and in each point the magnitude and phase of the impedance are obtained based on (2.29).

The impedance looking from the dc side is essentially the impedance of System 1 as mapped through the switching cell of the ac-dc converter to the dc side; and is determined by the converter and the three phase ac System 1. Therefore, the impedance Z_{dc} will not only depend on the dynamics of System 1 but also the properties of the switching converter itself, e.g., switching strategy, modulation, controls, mode of operation, etc.

Evaluating impedance of the system looking from the ac side requires special consideration because the ac variables are inherently time-variant even in steady state. To extend the impedance-based approach to the ac systems, the ac variables have to be viewed in a system of coordinates where they appear constant in steady state. This extension has been made in [14], where this approach was developed for the stability analysis of ac-dc electric power systems. Therefore, the physical variables on the ac side, \mathbf{v}_{abcs} and \mathbf{i}_{abcs} , are transferred into a synchronous reference frame. The resulting variables \mathbf{v}_{qds} and \mathbf{i}_{qds} have

the required property of being constant in steady state. For this reason, the appropriate impedances (as well as the averaging) are expressed in terms of these transformed variables. Specifically, assuming that the system operates in a steady state operating point determined by the external inputs and control signal d , the small-signal perturbations can be applied. Neglecting the zero sequence, there are two axes to be considered for calculating the appropriate impedance on the ac side denoted here by \mathbf{Z}_{qd} . For example, a small-signal perturbation \hat{v}_{qs} is first considered around the steady-state value V_{qs} . The response of the system in terms of currents generally will be seen in both q and d axes, respectively. This will give the first row of the transfer matrix (2.30). Next, a small-signal perturbation \hat{v}_{ds} is considered around V_{ds} . Similarly, the system response in terms of currents will be seen in both axes. Calculating these transfer functions will give the second row of the impedance transfer matrix \mathbf{Z}_{qd} . The final form of impedance transfer matrix is therefore:

$$\mathbf{Z}_{qd} = \begin{bmatrix} Z_{qq} & Z_{qd} \\ Z_{dq} & Z_{dd} \end{bmatrix} = \begin{bmatrix} \left. \frac{\hat{v}_q(s)}{\hat{i}_q(s)} \right|_{\hat{v}_d=0} & \left. \frac{\hat{v}_q(s)}{\hat{i}_d(s)} \right|_{\hat{v}_d=0} \\ \left. \frac{\hat{v}_d(s)}{\hat{i}_q(s)} \right|_{\hat{v}_q=0} & \left. \frac{\hat{v}_d(s)}{\hat{i}_d(s)} \right|_{\hat{v}_q=0} \end{bmatrix}. \quad (2.30)$$

In a SV-based simulator, the dynamic AVM will typically have the form of (2.1). Assuming a small-signal perturbation about the steady-state operating point as

$$\begin{aligned} \mathbf{x} &= \mathbf{X} + \hat{\mathbf{x}} \\ \mathbf{u} &= \mathbf{U} + \hat{\mathbf{u}} \end{aligned}, \quad (2.31)$$

where $\hat{\mathbf{x}}$ and $\hat{\mathbf{u}}$ are small-signal disturbances about the operating point values \mathbf{X} and \mathbf{U} , the linearized equations are then obtained as

$$\begin{aligned} \dot{\hat{\mathbf{x}}} &= \frac{\partial \mathbf{f}(\mathbf{X}, \mathbf{U}, t)}{\partial \mathbf{x}} \hat{\mathbf{x}} + \frac{\partial \mathbf{f}(\mathbf{X}, \mathbf{U}, t)}{\partial \mathbf{u}} \hat{\mathbf{u}} = \hat{\mathbf{A}}\hat{\mathbf{x}} + \hat{\mathbf{B}}\hat{\mathbf{u}} \\ \hat{\mathbf{y}} &= \frac{\partial \mathbf{g}(\mathbf{X}, \mathbf{U}, t)}{\partial \mathbf{x}} \hat{\mathbf{x}} + \frac{\partial \mathbf{g}(\mathbf{X}, \mathbf{U}, t)}{\partial \mathbf{u}} \hat{\mathbf{u}} = \hat{\mathbf{C}}\hat{\mathbf{x}} + \hat{\mathbf{D}}\hat{\mathbf{u}}, \end{aligned} \quad (2.32)$$

which has the form of (2.2). Once the state-space matrices $\hat{\mathbf{A}}$, $\hat{\mathbf{B}}$, $\hat{\mathbf{C}}$, and $\hat{\mathbf{D}}$ of the linearized system are calculated, obtaining any transfer function of the system becomes a straightforward and almost instantaneous procedure. In a very general case, the input-output transfer function matrix $\mathbf{H}(s)$ (considering all inputs and outputs) may be written as

$$\mathbf{H}(s) = \hat{\mathbf{C}}(s\mathbf{I} - \hat{\mathbf{A}})^{-1}\hat{\mathbf{B}} + \hat{\mathbf{D}}. \quad (2.33)$$

In most SV-based simulation packages, e.g., [4], this procedure can be done automatically making a powerful tool for system-level analysis and design of controllers. A subset of (2.33) will then contain any particular transfer function (impedance) (2.28)–(2.30).

Chapter 3: Dynamic AVM Formulation for EMTP-Type Solution

3.1 Electro-Magnetic Transient Programs

The programs based on nodal analysis [8], [98] (or modified nodal analysis) include EMTP-type and Spice-type programs [99]. The underlying solution approach is based on discretizing the differential equations for each circuit component using a particular integration rule. The EMTP [8] uses an implicit trapezoidal rule for discretization and formulating the network nodal equation that has the following general form:

$$\mathbf{G}\mathbf{V}_n = \mathbf{I}_h. \quad (3.1)$$

Here, \mathbf{G} is the network nodal conductance matrix, and the vector \mathbf{I}_h includes the so-called history current sources and independent current sources injected into the nodes. The nodal voltages \mathbf{V}_n are unknown and calculated by solving (3.1) at every time step. As the \mathbf{G} matrix is usually sparse, specially designed techniques such as optimal reordering schemes and partial LU factorization [100], [101] are often used to solve this linear system instead of inverting the matrix \mathbf{G} directly.

In a typical EMTP formulation which uses a fixed time-step Δt , topological changes due to switching events require special consideration since such changes may happen inside a time-step. A trivial solution is to reduce the step size until a sufficient accuracy of solution is achieved. This would result in using very small time steps and increases the computational burden of the overall simulation. Significant effort has been made to design efficient

algorithms for handling switching events [102]-[106]. Such methods typically include interpolation and/or extrapolations within a time step.

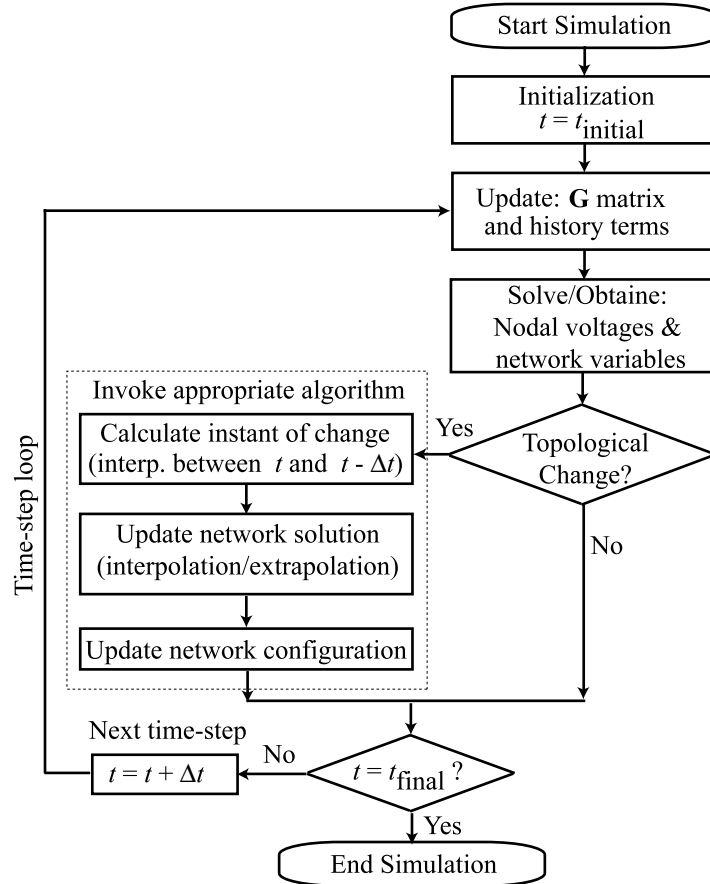


Figure 3.1 Flowchart of a typical nodal-analysis-based solver.

Figure 3.1 shows the time-stepping procedure in a typical EMTP. After the initialization, the simulation enters the major time-stepping loop which continues to execute until the end of simulation when t_{final} is reached. In each time-step, the network \mathbf{G} matrix and history terms are updated as needed, the nodal equations are solved, and the nodal voltages are calculated. At each time step, the network variables are computed to perform the test for the changes in topology. If a change in topology within a given time step is detected (turning on/off of a diode, thyristor, transistor, etc.) the present time step is not accepted and a special

algorithm has to be evoked. A typical algorithm interpolates between the solution points to precisely locate the time instance of the switching event within the time step. Then, the network equation has to be solved considering the shorter subinterval before the switching instance. Thereafter, the system is updated for the new topology and solved again. For re-synchronizing back with the existing time step, several solutions have been proposed in the literature using interpolation/extrapolation [102]–[107]. In many EMTP languages, the so-called Critical Damping Algorithm (CDA) [108], [109] is invoked to suppress the artificial numerical oscillations due to the insufficient damping of the trapezoidal integration. This procedure is then applied whenever there is a switching in the system until the end of simulation.

3.2 Detailed Analysis

In most EMTP-type programs, detailed models of line-commutated rectifier systems may be readily implemented using standard library components. Here, particularly, to demonstrate the effects of the ac side impedance topology on the system performance, a front-end rectifier system is considered with two possible configurations. The corresponding snapshots of the system detailed models implemented in PSCAD/EMTDC [11] are depicted in Figure 3.2 (a) and (b). In Figure 3.2 (a), the impedance on the ac side consists only of a series RL connection. This represents the Thevenin equivalent impedance of the ac power system combined with the optional series choke inductor. If present in the system, the latter typically has the dominant value between the two. In Figure 3.2 (b), a general filter network is considered composed of two series RL connections on both sides of the parallel RLC branches that each represent a shunt filter tuned to a specific harmonic (in this case 5th and 7th). As seen in this figure, when both series and shunt filters are included, the series choke inductor is typically broken into two unequal parts (such as 67% and 33%) and inserted on both sides of the parallel branches [46].

The mode of operation at a fixed given load (for example defined by $R_L = 70 \Omega$ in Figure 3.2) is essentially determined by the value of the equivalent series inductance present on the ac side. In both Figure 3.2 (a) and (b), excluding the additional series choke inductors would then result in an inductance value small enough to force the system into DCM operation under normal loading conditions. The three-phase currents in DCM are shown for both configurations in the top plots of Figure 3.3 (a) and (b).

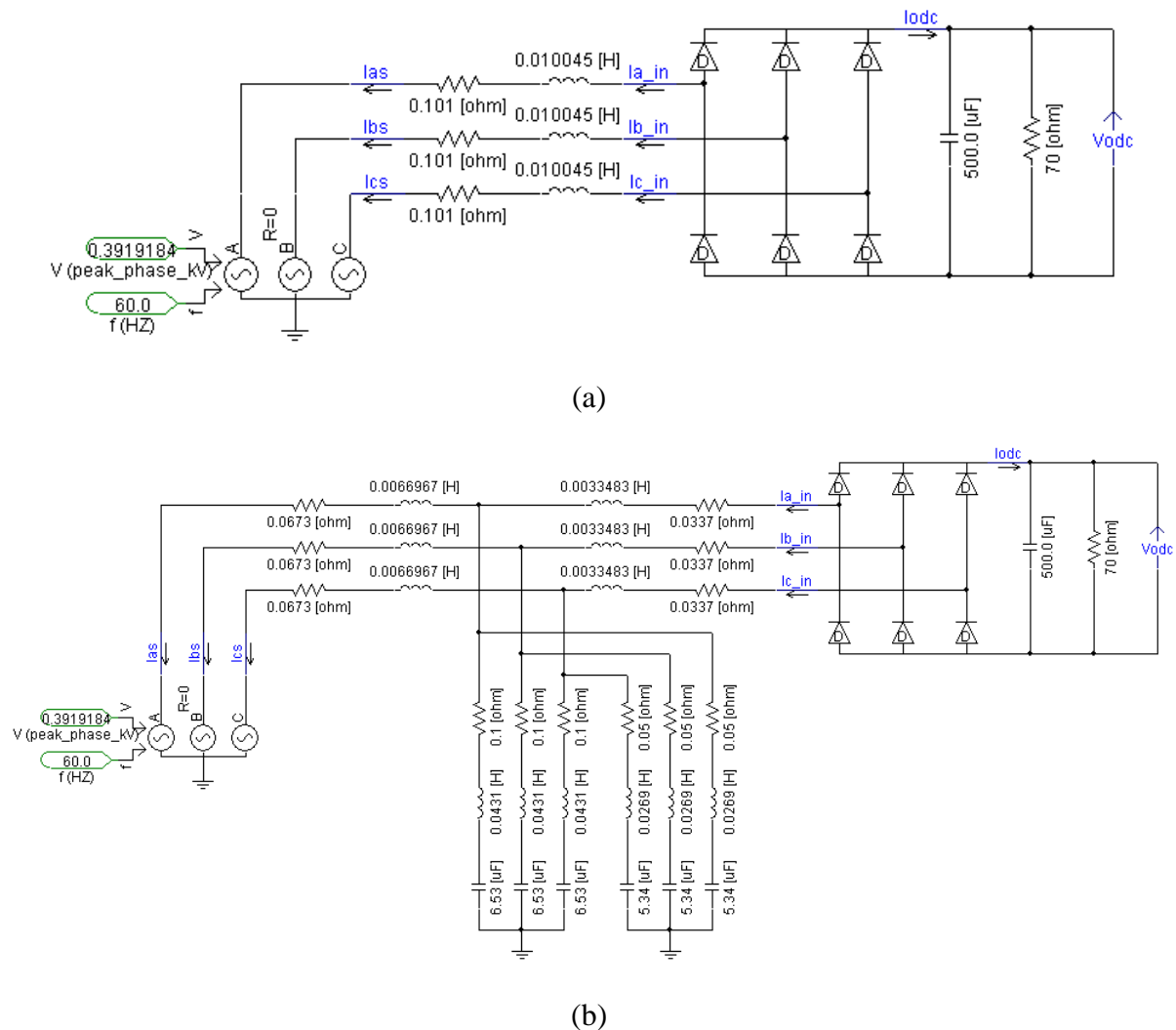


Figure 3.2 Topological variations of the ac side impedance in a typical three phase front-end rectifier load system (a) series impedance (b) general network with series and parallel branches.

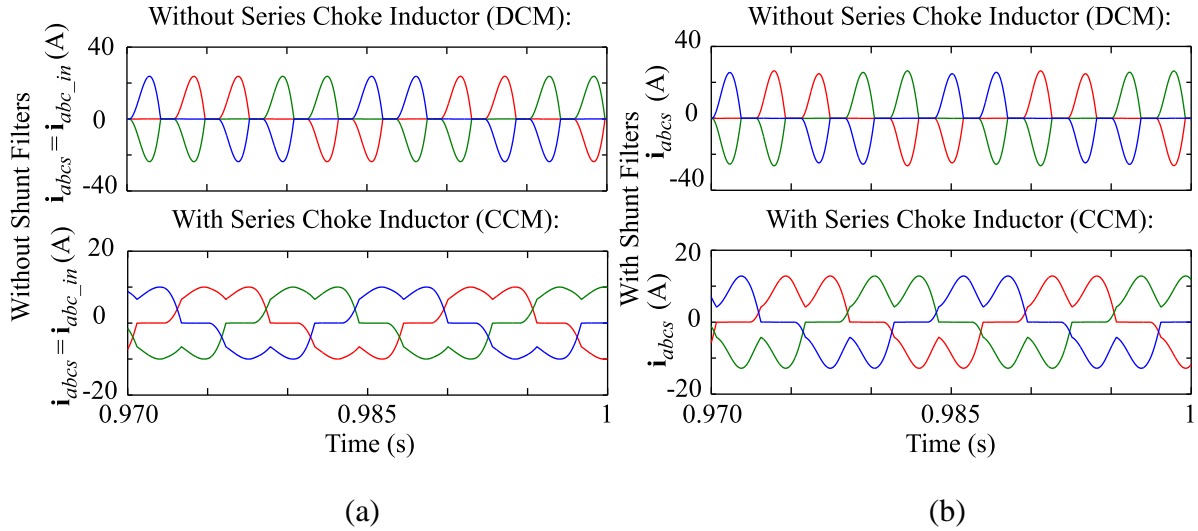


Figure 3.3 Three-phase currents at the bridge terminals for DCM and CCM operation: (a) without shunt filters; and (b) with shunt filters.

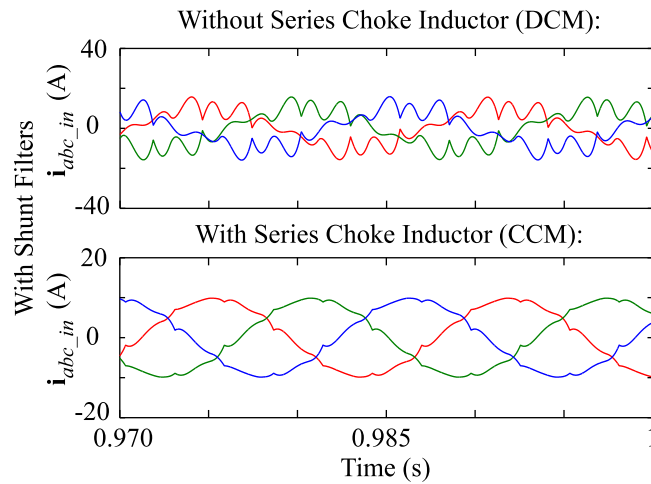


Figure 3.4 Three-phase ac currents of the system at the input source terminals in presence of the shunt filters for DCM and CCM operations.

As dictated by the system topology, the currents at the source and bridge terminals, denoted in Figure 3.2 by i_{abc_s} and i_{abc_in} , are identical in absence of shunt filters, i.e., Figure 3.2 (a). In this case, the high-harmonic-content currents of Figure 3.3 (a) (top plot) are directly fed to the network. In presence of the shunt filters, i.e., Figure 3.2 (b), the source

currents are depicted in Figure 3.4 (top plot). These waveforms show that a somewhat lower harmonic content is achieved in presence of the shunt filters of Figure 3.2 (b). Since these filters are essentially tuned for the 5th and 7th harmonics, their effects on the system operation are normally intended to be minimal except ensuring that the corresponding harmonic content flows through the shunt path instead of the network. The mode of operation and other characteristics of the system are then expected to remain intact as long as the dc load and equivalent series inductive component on the ac side do not vary significantly. The bridge currents are then expected to be almost identical in presence and absence of a well-designed set of shunt filters. This is indeed endorsed by the close agreement observed between the top plots in Figure 3.3 (a) and (b) that have been obtained in the absence and presence of the shunt filters, respectively.

The DCM operation discussed above is most frequently encountered in the front-end rectifiers of the low- to medium power variable frequency drives [87]-[89] where the series ac filter is often not used (or is very small) but there is a large capacitor on the dc bus. This mode is essentially associated with the needle-shape waveforms with high harmonic content that are typically challenging and expensive to filter. As observed in Figure 3.4 (top plot), even in presence of the shunt filters of Figure 3.2 (b), the source current has a seemingly high harmonic content. This problem, of course, can be alleviated using additional shunt filters tuned to the next present harmonics until the desired THD criteria are satisfied. It should be noted, however, that this would further increase the size, cost, and complexity of the already complicated filter network of Figure 3.2 (b).

With the additional series choke inductors, in both configurations of Figure 3.2 (a) and (b), the dc bus current becomes continuous resulting in CCM operation. As the load increases, CCM-1 and CCM-2 operation may both be observed. However, the less common CCM-3 operation is prevented in the configurations of Figure 3.2 (a) and (b) due to the absence of dc link filter inductor as is commonly the case in front-end rectifier variable frequency drives.

The three-phase ac currents for the most common type of CCM operation (CCM-1) corresponding to the same operating point as the previous study ($R_L = 70 \Omega$) are illustrated in Figure 3.3 (a) and (b) (bottom plots) in the absence and presence of the shunt filters, respectively. Comparing these plots to the respective top plots, it is observed that, in both cases, the harmonic contents of the bridge currents automatically reduce to some extent when the system enters CCM. Also, comparing the two bottom plots of Figure 3.3 (a) and (b), it is seen that the bridge currents are essentially similar in absence and presence of the shunt filters, except minor differences in the ripple shape. In the absence of shunt filters, the bridge currents of Figure 3.3 (a) (bottom plot) are directly injected at the source. However, as depicted in Figure 3.4 (bottom plot), the source currents are significantly improved in presence of the shunt filters especially compared to those of the DCM operation (top plot).

In summary, the detailed analysis presented above demonstrates that, on the one hand, the value of the equivalent series inductance on the ac side essentially determines the mode of operation at a given dc load. On the other hand, the effects of the parallel branches (shunt filters) are mainly confined to the currents drawn from the source network which are important in system-level studies concerning the overall performance of the power system. As discussed in the previous Chapter, one crucial step in dynamic average modeling, in general, is relating the ac currents at the bridge terminals to the current injected to the dc bus. This step clearly relies on the mode of operation which determines the shape of the waveforms and hence the values of the respective averages. Therefore, for the purpose of dynamic average modeling, the currents injected to the bridge terminals are of the main interest. From this point of view, the series component of the ac inductance has the dominant impact. The system performance may then be typically investigated for two cases, without and with the series ac inductor filter, regardless of the details of the shunt filter branches.

3.3 Dynamic Average Modeling

As described in the previous Chapter, the AVMs for line-commutated converters based on both analytical and parametric approaches have been formulated as state models. Significant additional effort is required to reformulate the dynamic average models and interface them with the overall circuit network for the EMTP-type solution. In general, both analytical and parametric approaches may be extended to the EMTP-type solution. These extensions are set forth in the next two subsections.

3.3.1 Analytical AVM for EMTP-type Solution

In the circuit of Figure 2.2, if the ac and dc filter inductors together with the diode bridge are considered as the rectifier block, and the input voltage to this block (from the external ac subsystem) is denoted by \bar{v}_{qs} in the converter reference frame, the dynamics of dc bus can be represented by the following state equation [51]:

$$\frac{d\bar{i}_{dc}}{dt} = \frac{\frac{3\sqrt{3}}{\pi}\bar{v}_{qs} - R_{rec}\bar{i}_{dc} - \bar{v}_C}{L_{rec}}. \quad (3.2)$$

Here, the parameters R_{rec} and L_{rec} are defined in terms of the original system parameters as:

$$R_{rec} = r_{dc} + \frac{3}{\pi}L_{ac}\omega_e, \quad L_{rec} = L_{dc} + 2L_{ac}, \quad (3.3)$$

Integrating both sides in (3.2) yields:

$$L_{rec} \int_{t-\Delta t}^t d\bar{i}_{dc} = \int_{t-\Delta t}^t \left(\frac{3\sqrt{3}}{\pi}\bar{v}_{qs} - R_{rec}\bar{i}_{dc} - \bar{v}_C \right) dt, \quad (3.4)$$

where Δt is the chosen integration time step. Next, discretization of (3.4) is carried out using the trapezoidal rule (as commonly done for the EMTP):

$$L_{rec} (\bar{i}_{dc}(t) - \bar{i}_{dc}(t - \Delta t)) = \frac{3\sqrt{3}}{\pi} \frac{\Delta t}{2} (\bar{v}_{qs}(t) + \bar{v}_{qs}(t - \Delta t)) - R_{rec} \frac{\Delta t}{2} (\bar{i}_{dc}(t) + \bar{i}_{dc}(t - \Delta t)) - \frac{\Delta t}{2} (\bar{v}_C(t) + \bar{v}_C(t - \Delta t)) \quad (3.5)$$

Upon rearranging terms, the following equation is obtained:

$$\bar{i}_{dc}(t) = \frac{1}{R_{eq}} \left(\frac{3\sqrt{3}}{\pi} \bar{v}_{qs}(t) - \bar{v}_C(t) \right) + i_{h,dc}(t), \quad (3.6)$$

where R_{eq} is defined as

$$R_{eq} = R_{rec} + \frac{2L_{rec}}{\Delta t}. \quad (3.7)$$

In (3.6), the so-called history term, $i_{h,dc}(t)$, is a function of the network variables at the previous time step. In particular,

$$i_{h,dc}(t) = \left(1 - \frac{2R_{rec}}{R_{eq}} \right) \bar{i}_{dc}(t - \Delta t) + \frac{1}{R_{eq}} \left(\frac{3\sqrt{3}}{\pi} \bar{v}_{qs}(t - \Delta t) - \bar{v}_C(t - \Delta t) \right). \quad (3.8)$$

In the approach set forth in [51], the algebraic equations describing the ac side are obtained by averaging the q - and d -component currents in the commutation and conduction sub-intervals, and combining/adding the result. Omitting the intermediate steps, the result is:

$$\bar{i}_{qs} = \bar{i}_{qs,com} + \bar{i}_{qs,cond}, \quad (3.9)$$

$$\bar{i}_{ds} = \bar{i}_{ds,com} + \bar{i}_{ds,cond}, \quad (3.10)$$

$$\begin{aligned} \bar{i}_{qs,com} &= \frac{-2\sqrt{3}}{\pi} \bar{i}_{dc} \left[\sin\left(\mu - \frac{5\pi}{6}\right) + \sin\left(\frac{5\pi}{6}\right) \right] \\ &\quad - \frac{3\bar{v}_{qs}}{\pi L_{ac} \omega_e} (\cos \mu - 1) - \frac{3\bar{v}_{qs}}{4\pi L_{ac} \omega_e} (1 - \cos(2\mu)), \end{aligned} \quad (3.11)$$

$$\begin{aligned} \bar{i}_{ds,com} = & \frac{-2\sqrt{3}}{\pi} \bar{i}_{dc} \left[\cos\left(\frac{5\pi}{6}\right) - \cos\left(\mu - \frac{5\pi}{6}\right) \right] \\ & - \frac{3\bar{v}_{qs}}{\pi L_{ac}\omega_e} \sin \mu + \frac{3\bar{v}_{qs}}{4\pi L_{ac}\omega_e} (\sin(2\mu) + 2\mu), \end{aligned} \quad (3.12)$$

$$\bar{i}_{qs,cond} = \frac{-2\sqrt{3}}{\pi} \bar{i}_{dc} \left[\sin\left(\frac{7\pi}{6}\right) - \sin\left(\mu + \frac{5\pi}{6}\right) \right] \quad (3.13)$$

$$\bar{i}_{ds,cond} = \frac{-2\sqrt{3}}{\pi} \bar{i}_{dc} \left[\cos\left(\mu + \frac{5\pi}{6}\right) - \cos\left(\frac{7\pi}{6}\right) \right], \quad (3.14)$$

where μ is the so-called commutation angle written as:

$$\mu = \cos^{-1} \left(1 - \frac{\sqrt{2} L_{ac} \omega_e}{\sqrt{3}} \frac{\bar{i}_{dc}}{\bar{v}_{qs}} \right). \quad (3.15)$$

Here, all qd variables are expressed in the converter reference frame. The above equations are first mathematically simplified using trigonometric identities in order to facilitate the next steps in the derivation of the model. After some effort, the simplified expressions for (3.11)-(3.14), are obtained as follows:

$$\bar{i}_{qs,com} = \frac{3}{\pi} \bar{i}_{dc} \sin \mu, \quad (3.16)$$

$$\bar{i}_{ds,com} = \frac{2\sqrt{3}}{\pi} L_{ac} \omega_e \left(\frac{\bar{i}_{dc}^2}{\bar{v}_{qs}} \right) - \frac{3}{2\pi L_{ac} \omega_e} \bar{v}_{qs} \sin \mu + \frac{3}{2\pi L_{ac} \omega_e} \bar{v}_{qs} \mu, \quad (3.17)$$

$$\bar{i}_{qs,cond} = \frac{-3}{\pi} \bar{i}_{dc} \sin \mu - \frac{2}{\pi} L_{ac} \omega_e \left(\frac{\bar{i}_{dc}^2}{\bar{v}_{qs}} \right) + \frac{2\sqrt{3}}{\pi} \bar{i}_{dc}, \quad (3.18)$$

$$\bar{i}_{ds,cond} = \frac{-2\sqrt{3}}{\pi} L_{ac} \omega_e \left(\frac{\bar{i}_{dc}^2}{\bar{v}_{qs}} \right) + \frac{\sqrt{3}}{\pi} \bar{i}_{dc} \sin \mu. \quad (3.19)$$

Substituting the above equations in (3.9) and (3.10) yields the final equations for \bar{i}_{qs} and

\bar{i}_{ds} :

$$\bar{i}_{qs} = \frac{-2}{\pi} L_{ac} \omega_e \left(\frac{\bar{i}_{dc}^2}{\bar{v}_{qs}} \right) + \frac{2\sqrt{3}}{\pi} \bar{i}_{dc}, \quad (3.20)$$

$$\bar{i}_{ds} = \frac{\sqrt{3}}{\pi} \bar{i}_{dc} \sin \mu - \frac{3}{2\pi L_{ac} \omega_e} \bar{v}_{qs} (\sin \mu - \mu). \quad (3.21)$$

3.3.2 Indirectly-Interfaced Analytical Average-Value Model (IIAAVM)

The AVM described by (3.6)-(3.8) and (3-20), (3-21) is of the form depicted in Figure 3.5, where the dc and ac sides have been represented by Norton-equivalent inter-dependent current sources. The presence of these dependent sources, as well as the ac side being represented in qd variables, makes it challenging to implement this model directly in EMTP wherein the ac network is normally represented in phase variables, i.e., abc .

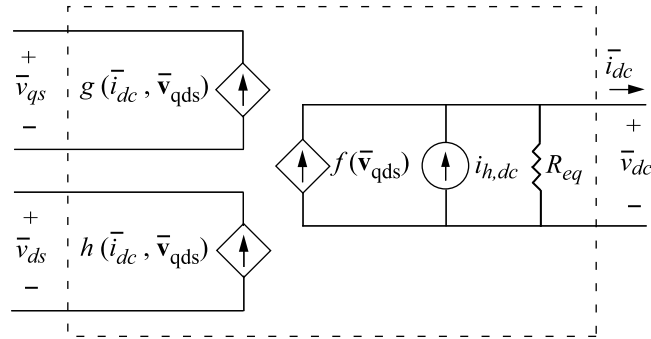


Figure 3.5 Circuit diagram of the AVM described by (3-6)-(3.8), (3-20), (3-21).

Similar to what has been done in interfacing the qd machine models with the abc networks in EMTP; one solution is to introduce a time-step delay between the dc and ac subsystems. This approach is in fact the so-called indirect interfacing [110], [111] of the model with the network. This method of interfacing has been used to interface all the machine models in the PSCAD/EMTDC software [11], [110], [111]. Adopting this method, the ac and dc subsystems become essentially decoupled and the dependent current sources

become independent sources. The values of these sources are calculated, similar to the history sources, according to the solution of the network at the previous time step. Also, since the solution of the network at the previous time steps are readily available, the transformation of the network variables between abc and qd becomes a straightforward operation and the final model is conveniently interfaced with the ac network in abc phase variables (coordinates). In particular, the values of the input three-phase voltages are transformed into the converter reference frame using the appropriate transformation matrix (2.7). The value of the dependent current source at the dc side is then readily obtained as a function of \bar{v}_{qs} . Similarly, the values of the dependent current sources at the ac side are readily obtained using the solution of the network at the previous time step. These current sources are then transformed back to abc applying (2.9), and injected into the ac network as i_{inj_a} , i_{inj_b} , and i_{inj_c} .

However, the time-step delay may cause unfavorable numerical oscillations and convergence problems. To alleviate the problem, the use of an interfacing circuitry has been proposed for the machine models in [111]. A modified circuit includes a resistor r_z and the so-called compensating current source i_{comp} . This circuit is inserted between the ac network and the input port of the AVM in each phase. The final interfacing equivalent circuit of the AVM using this indirect approach is illustrated in Figure 3.6.

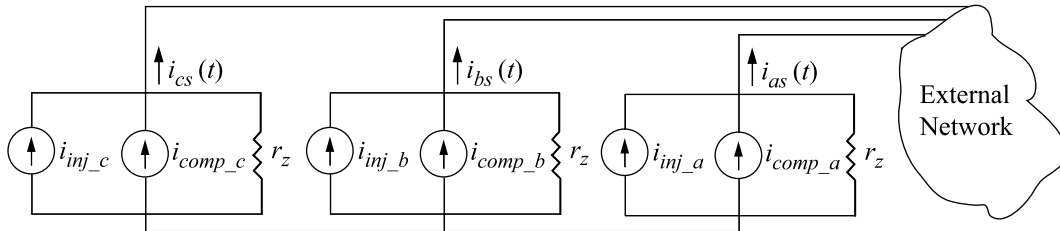


Figure 3.6 Circuit diagram of the IIAVM using PSCAD-like approach.

3.3.3 Directly-Interfaced Analytical Average-Value Model (DIAAVM)

The indirect method of interfacing may lead to reduced accuracy and potential problems with numerical stability of the overall solution especially at larger time steps. This has been demonstrated in [112] for the machine models interfaced using the indirect approaches. It is therefore desirable to achieve a direct interface between the EMTP network and the AVM so that the time-step delay is eliminated and a simultaneous solution of the two subsystems is achieved. This has been set forth in this subsection.

Equations (3.20) and (3.21) describe the qd components of the input ac currents as nonlinear functions of the dc bus current and the qd components of the input ac voltage.

Based on (3.20), (3.21) let us define the following nonlinear functions:

$$f_1(\bar{i}_{dc}, \bar{v}_q) = \frac{\bar{i}_{dc}^2}{\bar{v}_{qs}}, \quad (3.22)$$

$$f_2(\bar{i}_{dc}, \bar{v}_q) = \bar{i}_{dc} \sin \mu, \quad (3.23)$$

$$f_3(\bar{i}_{dc}, \bar{v}_q) = \bar{v}_{qs} \sin \mu, \quad (3.24)$$

$$f_4(\bar{i}_{dc}, \bar{v}_q) = \bar{v}_{qs} \mu, \quad (3.25)$$

where μ itself is, of course, a nonlinear function of \bar{i}_{dc} and \bar{v}_{qs} defined by (3.15). These functions should be first linearized within a time step Δt . For example, the function f_1 at time t may be written as

$$f_1(t) = \left. \frac{\partial f_1}{\partial \bar{i}_{dc}} \right|_{t-\Delta t} \bar{i}_{dc}(t) + \left. \frac{\partial f_1}{\partial \bar{v}_{qs}} \right|_{t-\Delta t} \bar{v}_{qs}(t). \quad (3.26)$$

Using a similar approach, the functions f_1 through f_4 are linearized to have the following form:

$$f_1(t) = A_1 \bar{v}_{qs} + B_1 \bar{i}_{dc}, \quad (3.27)$$

$$f_2(t) = C_2 \bar{v}_{qs} + D_2 \bar{i}_{dc}, \quad (3.28)$$

$$f_3(t) = C_3 \bar{v}_{qs} + D_3 \bar{i}_{dc}, \quad (3.29)$$

$$f_4(t) = C_4 \bar{v}_{qs} + D_4 \bar{i}_{dc}, \quad (3.30)$$

with the coefficients, obtained after extensive effort, as follows:

$$A_1 = -S^2, \quad (3.31)$$

$$B_1 = 2S, \quad (3.32)$$

$$C_2 = \frac{\left(\frac{2}{\sqrt{3}} L_{ac} \omega_e\right) S^3 - S^2}{\sqrt{-S^2 + \frac{\sqrt{3}}{L_{ac} \omega_e} S}}, \quad (3.33)$$

$$D_2 = \frac{3S - \left(\frac{4}{\sqrt{3}} L_{ac} \omega_e\right) S^2}{\sqrt{-S^2 + \frac{\sqrt{3}}{L_{ac} \omega_e} S}}, \quad (3.34)$$

$$C_3 = \frac{S}{\sqrt{-S^2 + \frac{\sqrt{3}}{L_{ac} \omega_e} S}}, \quad (3.35)$$

$$D_3 = \frac{\left(\frac{-2}{\sqrt{3}} L_{ac} \omega_e\right) S + 1}{\sqrt{-S^2 + \frac{\sqrt{3}}{L_{ac} \omega_e} S}}, \quad (3.36)$$

$$C_4 = \mu(t - \Delta t) - \frac{S}{\sqrt{-S^2 + \frac{\sqrt{3}}{L_{ac} \omega_e} S}}, \quad (3.37)$$

$$D_4 = \frac{1}{\sqrt{-S^2 + \frac{\sqrt{3}}{L_{ac} \omega_e} S}}. \quad (3.38)$$

In the above equations the variable S itself is defined as

$$S = \left(\begin{array}{c} \bar{i}_{dc} \\ \bar{v}_{qs} \end{array} \right) \Big|_{t-\Delta t} . \quad (3.39)$$

Substituting (3.27)-(3.39) into (3.20), (3.21), simplifying, and rearranging terms, yields the final linearized equations for qd components of the ac side currents:

$$\bar{i}_{qs} = A \bar{v}_{qs} + B \bar{i}_{dc}, \quad (3.40)$$

$$\bar{i}_{ds} = C \bar{v}_{qs} + D \bar{i}_{dc}, \quad (3.41)$$

with the final coefficients A , B , C , and D defined as

$$A = \frac{2}{\pi} L_{ac} \omega_e S^2, \quad (3.42)$$

$$B = -\frac{4}{\pi} L_{ac} \omega_e S + \frac{2\sqrt{3}}{\pi}, \quad (3.43)$$

$$C = \frac{3\mu(t-\Delta t)}{2\pi L_{ac} \omega_e} + \frac{\frac{2L_{ac} \omega_e S^3 - \frac{\sqrt{3}}{\pi} S^2 - \frac{3}{\pi L_{ac} \omega_e} S}{\sqrt{-S^2 + \frac{\sqrt{3}}{L_{ac} \omega_e} S}}}{}, \quad (3.44)$$

$$D = \frac{-\frac{4}{\pi} L_{ac} \omega_e S^2 + \frac{4\sqrt{3}}{\pi} S}{\sqrt{-S^2 + \frac{\sqrt{3}}{L_{ac} \omega_e} S}}. \quad (3.45)$$

Equations (3.40)-(3.45) together with the discretized dc bus equation (3.6)-(3.8) form the basis for the AVM that may be directly interfaced with the ac network.

3.3.3.1 Direct Interface in qd Variables

Although it is not very common, in some cases, the whole ac network itself may be expressed in qd variables. The direct interfacing of the AVM in this case is simplified. For the sake of completeness, this special case is considered here before the general case of direct

interface in abc variables is discussed. For this purpose, first the discretized dc bus equation (3.6) is rewritten as:

$$\bar{i}_{dc} = E \bar{v}_{qs} + F \bar{v}_C + i_{h,dc}, \quad (3.46)$$

where the new parameters E , and F have been defined as

$$E = \frac{3\sqrt{3}}{\pi R_{eq}}, \quad (3.47)$$

$$F = \frac{-1}{R_{eq}}. \quad (3.48)$$

Substituting (3.46) into (3.40) and (3.41) yields:

$$\bar{i}_{qs} = A' \bar{v}_{qs} + B' \bar{v}_C + i_{h,q}, \quad (3.49)$$

$$\bar{i}_{ds} = C' \bar{v}_{qs} + D' \bar{v}_C + i_{h,d}, \quad (3.50)$$

where the new coefficients and history terms are expressed as

$$A' = A + BE, \quad (3.51)$$

$$B' = BF, \quad (3.52)$$

$$C' = C + DE, \quad (3.53)$$

$$D' = DF, \quad (3.54)$$

$$i_{h,q} = B i_{h,dc}, \quad (3.55)$$

$$i_{h,d} = D i_{h,dc}, \quad (3.56)$$

In all above equations, the ac variables have been expressed in the converter reference frame. As shown in Chapter 1, in this frame, $\bar{v}_{ds} = 0$, and \bar{v}_{qs} can be written, according to (2.10), as

$$\bar{v}_{qs} = v_{qs}^a \cos \phi_c + v_{ds}^a \sin \phi_c, \quad (3.57)$$

where the superscript a denotes variables in the arbitrary reference frame. Also, ϕ_c is the so-called converter angle that defines the position of the converter reference frame q -axis.

Derivation of the directly-interfaced AVM in the arbitrary reference frame requires substitution of (3.57) into (3.46), (3.49), and (3.50), and the subsequent transformation of the ac currents into the arbitrary reference frame. The final model may then be written in the following compact matrix form:

$$\mathbf{G}_{avm-qd} \mathbf{V}_n = \mathbf{I}_{br} - \mathbf{I}_{h-qd}, \quad (3.58)$$

$$\mathbf{G}_{avm-qd} = \begin{bmatrix} F & E \cos \phi_c & E \sin \phi_c \\ B' \cos \phi_c - D' \sin \phi_c & A' \cos^2 \phi_c - \frac{C'}{2} \sin 2\phi_c & \frac{A'}{2} \sin 2\phi_c - C' \sin^2 \phi_c \\ B' \sin \phi_c + D' \cos \phi_c & \frac{A'}{2} \sin 2\phi_c + C' \cos^2 \phi_c & A' \sin^2 \phi_c + \frac{C'}{2} \sin 2\phi_c \end{bmatrix}, \quad (3.59)$$

$$\mathbf{I}_{h-qd} = \begin{bmatrix} i_{h,dc} \\ i_{h,q} \cos \phi_c - i_{h,d} \sin \phi_c \\ i_{h,q} \sin \phi_c + i_{h,d} \cos \phi_c \end{bmatrix}, \quad (3.60)$$

$$\mathbf{V}_n = \begin{bmatrix} \bar{v}_C \\ \bar{v}_{qs}^a \\ \bar{v}_{ds}^a \end{bmatrix}, \mathbf{I}_{br} = \begin{bmatrix} \bar{i}_{dc} \\ \bar{i}_{qs}^a \\ \bar{i}_{ds}^a \end{bmatrix}. \quad (3.61)$$

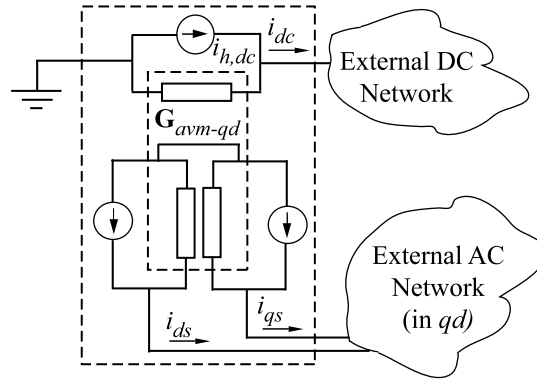


Figure 3.7 Circuit diagram of the DIAAVM in qd variables.

If the external ac network is expressed in qd variables, it can then be directly interfaced with the above model in qd domain as illustrated by the equivalent circuit of Figure 3.7.

This is particularly suitable for the simulation of smaller systems which may include several machine-rectifier modules together with the dc subsystems. Direct interface is conveniently achieved between the AVMs and the machine models expressed in qd variables.

3.3.3.2 Direct Interface in abc Variables

In general, the external ac network is represented in abc phase variables. In order to achieve a direct interface in abc , additional effort is required to transform (3.58) back to the abc phase variables. For this purpose, first, \bar{v}_{qs} is written, employing (2.9), in terms of the phase voltages as

$$\bar{v}_{qs} = \frac{2}{3}(v_{as} \cos \theta_1 + v_{bs} \cos \theta_2 + v_{cs} \cos \theta_3), \quad (3.62)$$

where

$$\theta_1 = \theta_e - \phi_c, \quad (3.63)$$

$$\theta_2 = \theta_e - \phi_c - \frac{2\pi}{3}, \quad (3.64)$$

$$\theta_3 = \theta_e - \phi_c + \frac{2\pi}{3}, \quad (3.65)$$

and θ_e is the electrical angle of the source. Transforming the AVM back to abc variables then includes substitution of (3.62) into (3.46), (3.49), and (3.50), rearranging terms, and finally employing the inverse qd transformation using the transformation matrix (2.9). After some effort, the final model is written in the following compact matrix form:

$$\mathbf{G}_{avm-abc} \mathbf{V}_n = \mathbf{I}_{br} - \mathbf{I}_{h-abc}, \quad (3.66)$$

$$\mathbf{G}_{avm-abc} = \begin{bmatrix} G_{11} & G_{12} & G_{13} & G_{14} \\ G_{21} & G_{22} & G_{23} & G_{24} \\ G_{31} & G_{32} & G_{33} & G_{34} \\ G_{41} & G_{42} & G_{43} & G_{44} \end{bmatrix}, \quad \mathbf{I}_{h-abc} = \begin{bmatrix} i_{h,dc} \\ i_{h,a} \\ i_{h,b} \\ i_{h,c} \end{bmatrix}, \quad (3.67)$$

$$\mathbf{V}_n = \begin{bmatrix} \bar{v}_C \\ v_{as} \\ v_{bs} \\ v_{cs} \end{bmatrix}, \mathbf{I}_{br} = \begin{bmatrix} \bar{i}_{dc} \\ i_a \\ i_b \\ i_c \end{bmatrix}. \quad (3.68)$$

The elements of $\mathbf{G}_{avm-abc}$, and \mathbf{I}_{h-abc} are expressed as

$$G_{11} = F, G_{1m} = \frac{2}{3}E \cos \theta_{m-1}, G_{k1} = B' \cos \theta_{k-1} + D' \sin \theta_{k-1}, \quad m, k = 2, 3, 4, \quad (3.69)$$

$$G_{ij} = \frac{2}{3} \cos \theta_{j-1} (A' \cos \theta_{i-1} + C' \sin \theta_{i-1}), \quad i, j = 2, 3, 4, \quad (3.70)$$

$$i_{h,a} = i_{h,q} \cos \theta_1 + i_{h,d} \sin \theta_1, \quad (3.71)$$

$$i_{h,b} = i_{h,q} \cos \theta_2 + i_{h,d} \sin \theta_2, \quad (3.72)$$

$$i_{h,c} = i_{h,q} \cos \theta_3 + i_{h,d} \sin \theta_3, \quad (3.73)$$

The final AVM (3.66) is expressed as four Norton-equivalent pairs of current source-conductance branches to represent the dc and ac terminals of the converter. The Thevenin equivalent of the developed AVM, if desired, may also be readily obtained by multiplying both sides of (3.66) by $\mathbf{G}_{avm-abc}^{-1}$. This leads to the following equations:

$$\mathbf{V}_n = \mathbf{G}_{avm-abc}^{-1} \mathbf{I}_{br} - \mathbf{e}_{h-abc}, \quad (3.74)$$

$$\mathbf{e}_{h-abc} = \begin{bmatrix} e_{h,dc} \\ e_{h,a} \\ e_{h,b} \\ e_{h,c} \end{bmatrix} = \mathbf{G}_{avm-abc}^{-1} \mathbf{I}_{h-abc}, \quad (3.75)$$

The final equivalent circuit of interfacing the Thevenin equivalent AVM defined by (3.74) is depicted in Figure 3.8.

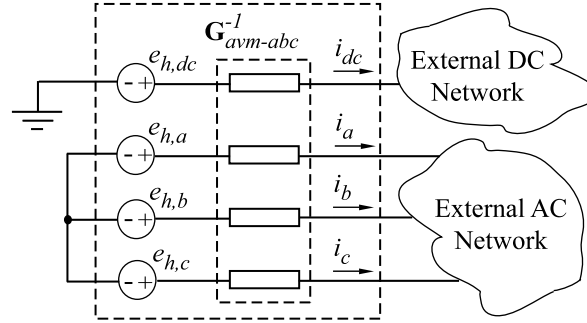


Figure 3.8 Equivalent circuit diagram of the DIAVM in abc variables.

Implementing the AVMs (3.66) and (3.75) are straightforward for EMTP-type solution. However, since the original model was developed in the converter reference frame, the final implementation of the models still requires knowledge of the angle ϕ_c which defines the position of the converter reference frame q -axis. An approximate model may be readily obtained employing the synchronously-rotating reference frame aligned with the source angle instead of the converter reference frame. In many cases, the deviation angle between these two reference frames (due to the impedance connected between the source and the converter) is small and the approximation may be valid for normal operation. If additional accuracy is desired, a simple prediction-correction algorithm may be employed to obtain ϕ_c more precisely.

It should also be noted that, in the final directly-interfaced average model of Figure 3.8, the conductance matrix $\mathbf{G}_{avm-abc}$ may generally change at different time steps due to the nonlinearity of the system. This would typically require triangularization of the system \mathbf{G} matrix which is of course associated with some additional computational time. However, in the EMTP-type software packages, typically the refactorization is performed only on the time-variant portion of the system \mathbf{G} matrix to minimize the computational burden [100], [101]. In general, the additional burden imposed by this step depends on the overall system

and how the EMTP-type software package handles the refactorization of the \mathbf{G} matrix. Further investigation of this effect is therefore outside the scope of this thesis.

3.3.4 Parametric AVM for EMTP-Type Solution

The parametric approach may also be considered for developing AVMs suitable for EMTP-type solution, especially with the intention to alleviate the burden imposed by the extensive mathematical derivations. Similar to the case of analytically-derived AVM, in general, both indirect and direct methods may be used for interfacing the developed model with the EMTP network. However, to avoid laborious mathematical derivations associated with formulating the directly-interfaced parametric average-value model, here, only the indirect method of interfacing is considered to interface the parametric AVM with the network.

According to the approach set forth in [70], parametric functions are considered to relate the dc voltage and current \bar{v}_{dc} , \bar{i}_{dc} to the ac voltages and currents $\bar{\mathbf{v}}_{qds}^c$ and $\bar{\mathbf{i}}_{qds}^c$, and also establish the angle between the vectors $\bar{\mathbf{v}}_{qds}^c$ and $\bar{\mathbf{i}}_{qds}^c$. Based on Figure 2.5 (b), the rectifier block takes the dc bus voltage \bar{v}_{dc} , and the ac currents $\bar{\mathbf{i}}_{qds}^c$ as the input, and provides the dc current \bar{i}_{dc} and ac voltages $\bar{\mathbf{v}}_{qds}^c$ as the output. To formulate and interface the model at dc and ac ports with external circuit networks, the following has to be accomplished. First, rearranging terms in (2.26), the angle δ may be defined as:

$$\delta = \tan^{-1} \left(\frac{\bar{v}_{ds}^a}{\bar{v}_{qs}^a} \right) = \tan^{-1} \left(\frac{\bar{i}_{ds}^a}{\bar{i}_{qs}^a} \right) - \phi(.). \quad (3.76)$$

Next, using (2.24) and (3.76), the ac voltages in arbitrary reference frame may be written as

$$\bar{\mathbf{v}}_{qd0s}^a = \begin{bmatrix} \alpha(\cdot) \bar{v}_{dc} \cos(\delta) \\ \alpha(\cdot) \bar{v}_{dc} \sin(\delta) \\ 0 \end{bmatrix}. \quad (3.77)$$

The third element in the above vector is set to zero because the rectifier sees the line voltages according to the topology of Figure 2.2, hence the zero sequence is not transferred. More general configurations, wherein the zero sequence is also allowed to exist at the ac side, will be considered in Chapter 6. The inverse $qd0$ transformation (2.9) is now applied, and the ac voltages are computed as follows:

$$\mathbf{v}_{abc} = \mathbf{K}^{-1} \begin{bmatrix} \alpha(\cdot) \bar{v}_{dc} \cos(\delta) \\ \alpha(\cdot) \bar{v}_{dc} \sin(\delta) \\ 0 \end{bmatrix}. \quad (3.78)$$

To calculate the dc bus current, the ac phase currents at the input port of the rectifier block first have to be transformed into arbitrary reference frame according to (2.7). Next, using (2.25), the dc bus current is computed as

$$\bar{i}_{dc} = \beta(\cdot) \|\mathbf{K} \mathbf{i}_{abc}\|. \quad (3.79)$$

Using the indirect method of interfacing, the rectifier block may now be interfaced with the circuit networks at the ac and dc ports. For this purpose, the dependent voltage sources are placed at the ac side whose values are calculated according to (3.78) at each time step. A dependent current source is also placed at the dc port whose value is determined according to (3.79). At each time step, the rectifier block uses the dc bus voltage and ac phase currents as the inputs. These values are then employed in the above calculations. Also, the dynamic impedance z , is computed based on the inputs according to

$$z = \frac{\bar{v}_{dc}}{\|\mathbf{K} \mathbf{i}_{abc}\|}. \quad (3.80)$$

The values of parametric functions, corresponding to the operating point defined by z , are then obtained from the pre-stored look-up tables and will be used along with the inputs for

calculating the values of the dependent sources. The final Indirectly-Interfaced Parametric Average-Value Model (IIPAVM) together with the interfacing circuitry is illustrated in Figure 3.9.

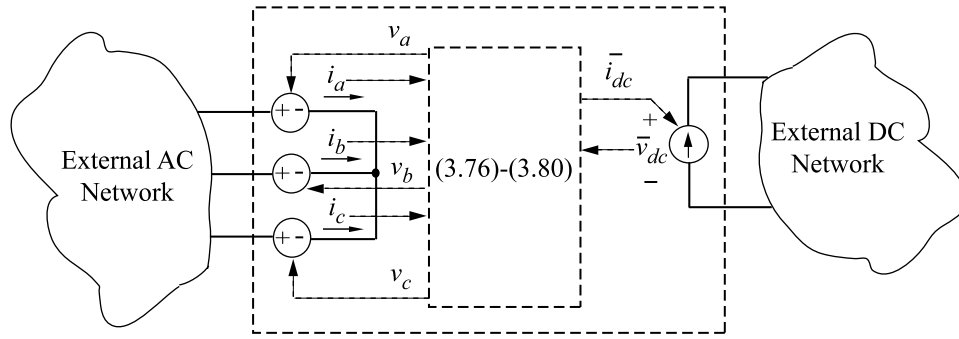
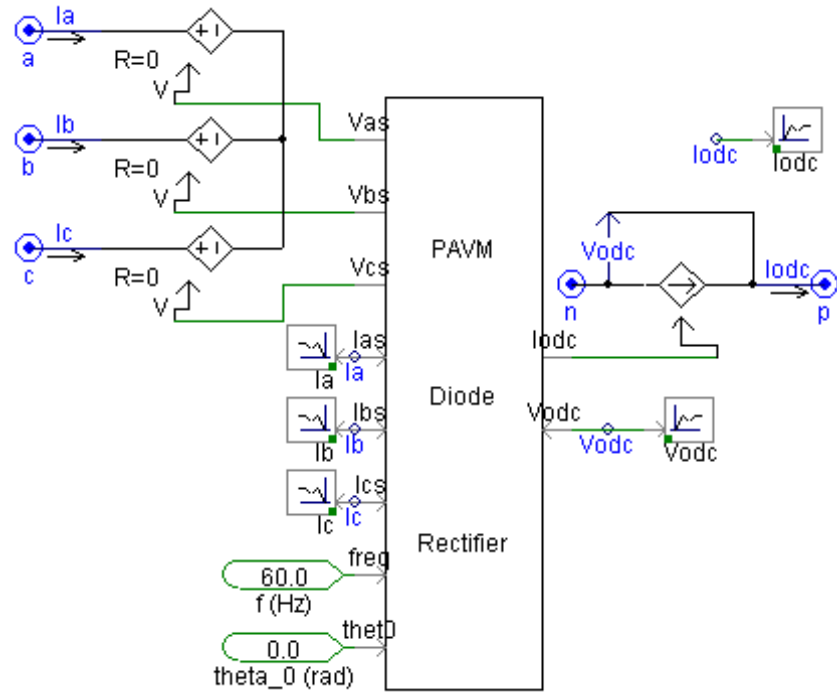


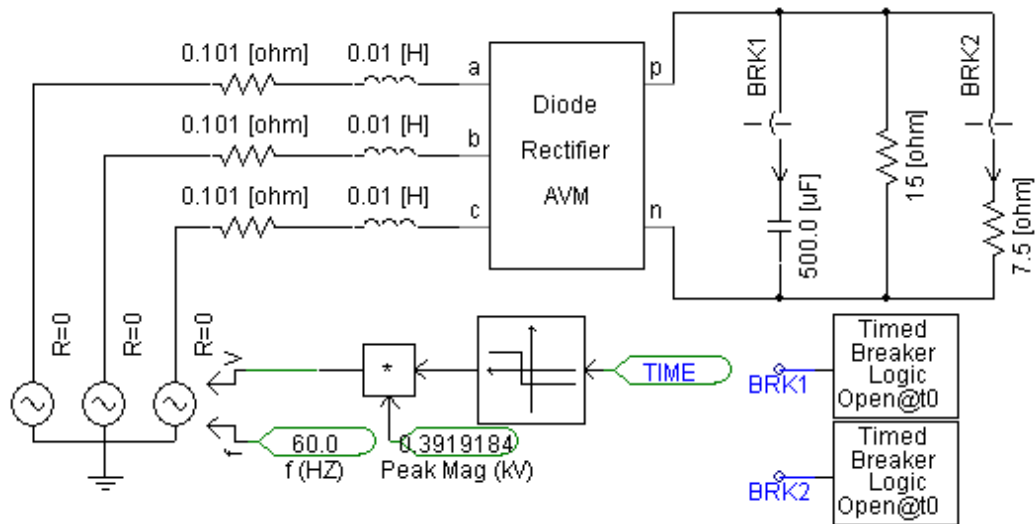
Figure 3.9 Indirectly-interfaced parametric average-value model.

3.4 Example of AVM Implementation in PSCAD/EMTDC

To illustrate the use of AVM in EMTP-type packages, an example implementation of the IIPAVM in PSCAD/EMTDC [11] is shown in Figure 3.10. The block shown in Figure 3.10 (a) contains (3-76)–(3-80) and the transformations between qd and abc coordinates. The subsystem of Figure 3.10 (a) is encapsulated into a single module-block that is then interconnected using its nodes with the external network as shown in Figure 3.10 (b). Such AVM block can then replace the detailed switching rectifier module within a larger ac and dc network (which may include ac filters, e.g. shunt harmonic filters, etc). Figure 3.10 (b) also depicts the timed breaker blocks that are used to implement the system changes for particular transient studies that will be presented in the next Chapter.



(a)



(b)

Figure 3.10 Example of IIPAVM implemented in PSCAD: (a) PAVM block together with controllable sources and interfacing ports; and (b) AVM module interfaced with external ac and dc subsystems.

In the next Chapter, extensive simulation studies will be carried out on the analytical and parametric AVMs developed in Chapters 2 and 3 in both SV-based and EMTP-type simulators. The purpose of these studies is to compare the different AVM implementations in different software packages in terms of predicting the system performance in different operating modes as well as under balanced and unbalanced ac side. Before presenting such thorough analyses, it is useful to further compare the indirect and direct methods of interfacing introduced earlier. This is the purpose of the simulation studies presented in the next section which will conclude the present Chapter.

3.5 Comparison of Direct and Indirect Interfacing Methods

To better demonstrate different properties of the indirectly-interfaced and directly-interfaced AVMs formulated in the previous sections, simulation studies are carried out as follows. For each model, a small integration time-step ($50 \mu\text{s}$) is used first to validate the model against the detailed switch-level reference model of the system. Then, larger integration time steps (0.5 ms and 1 ms) are used to compare the performance of the models.

The detailed (switch-level) model of the system (Figure 2.2) has been implemented in PSCAD/EMTDC [11]. The example system parameters are provided in Appendix A.1. The average-value models are implemented using an EMTP-type algorithm written in Matlab. Initially, at $t = 0$, the system is at zero initial conditions when the three-phase input source is switched on. Then, at $t = 0.02 \text{ s}$, the load resistance is switched from its initial value, $R_{load} = 2 \Omega$, to $R_{load} = 1 \Omega$. Finally, the load resistance is switched back to $R_{load} = 2 \Omega$ at $t = 0.04 \text{ s}$. Figure 3.11 illustrates the waveforms of the dc bus, i_{dc}, v_{dc} , as predicted by the detailed and average-value models. The waveforms of the phase a current i_{as} predicted by the detailed and average-value models are superimposed in Figure 3.12 (a). A magnified view of the first cycle is illustrated in Figure 3.12 (b) for clarity. Studies of Figure 3.11 and

Figure 3.12 are obtained using the typical EMTP time step of $50 \mu s$. As seen in Figure 3.11, provided that the chosen time step is sufficiently small, both methods of interfacing the AVMs lead to convergent results. This is expected as both models have been analytically derived from the same averaged equations. However, as seen in Figure 3.12 (b), the IIAVM has noticeable numerical oscillations at start-up. As explained previously, this is due to the time delay between the ac and dc systems. Except for the start-up oscillations, the above-mentioned figures show that both AVMs can produce acceptable match with the detailed switch-level model of the system, provided that the integration time steps is sufficiently small.

Next, the effect of increasing the time-step size is evaluated. For this purpose, the results of the previous study (Figure 3.11 and Figure 3.12) as predicted by the DIAVM are chosen as the reference solution (labeled as “Ref” in the following figures). The same study is carried out with the time-step of $500 \mu s$, and the results are superimposed in Figure 3.13 and Figure 3.14 with magnified views for clarity. These results demonstrate that the accuracy of the IIAVM somewhat degrades compared to the DIAVM. The error is especially well-pronounced in Fig. Figure 3.13 (b), where IIAVM predicts an out-of-phase response. At the same time, the DIAVM follows the reference with exceptional accuracy even at such a large time step. This numerical behavior of the indirect and direct interfacing methods becomes even more pronounced using a time-step size of $1000 \mu s$, which is shown in Figure 3.15.

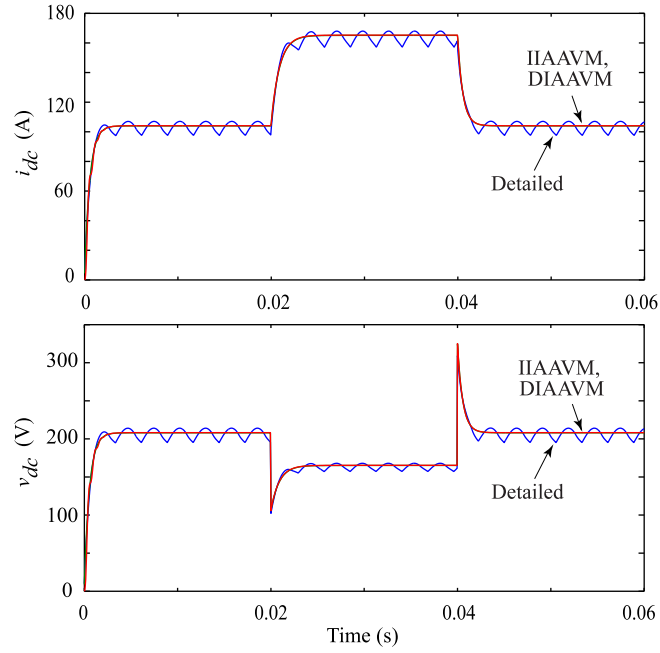


Figure 3.11 DC bus waveforms predicted by the models with $50\mu\text{s}$ time step.

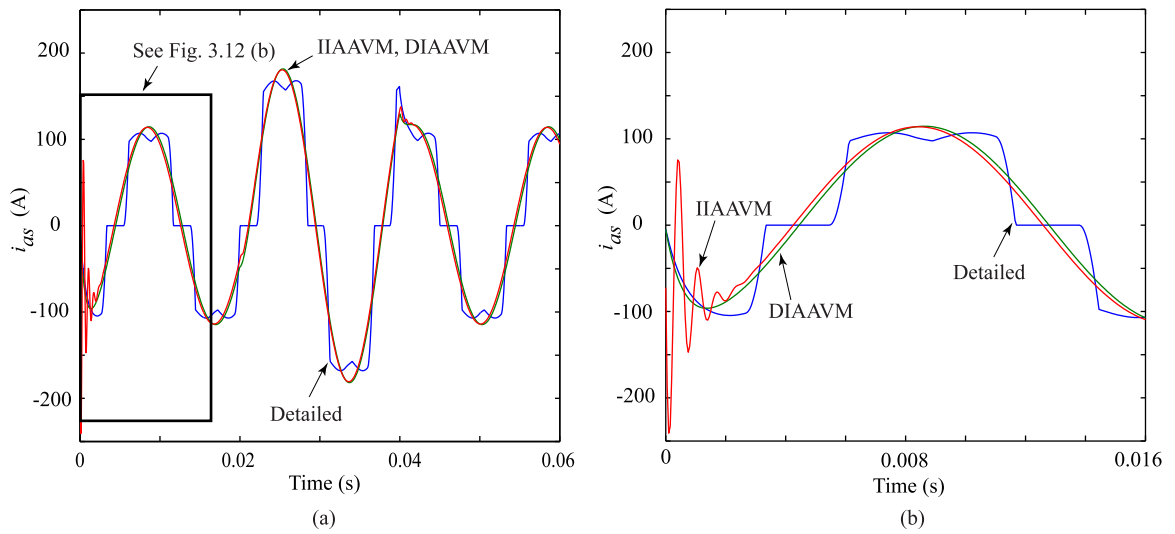


Figure 3.12 Input phase current predicted by the models with $50\mu\text{s}$ time step.

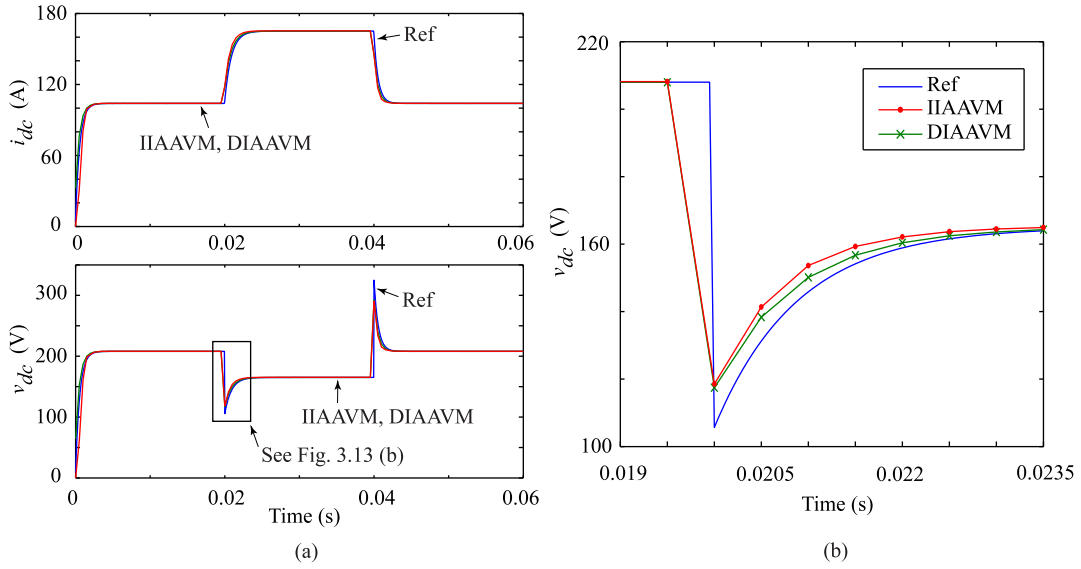


Figure 3.13 DC bus waveforms predicted by the models with $500\mu\text{s}$ time step.

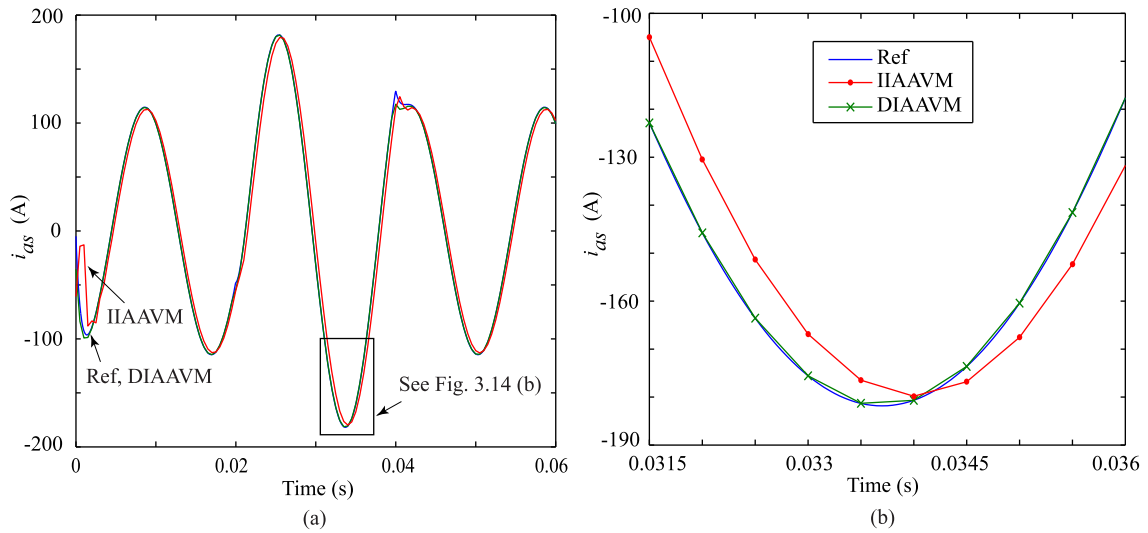


Figure 3.14 Input phase current predicted by the models with $500\mu\text{s}$ time step.

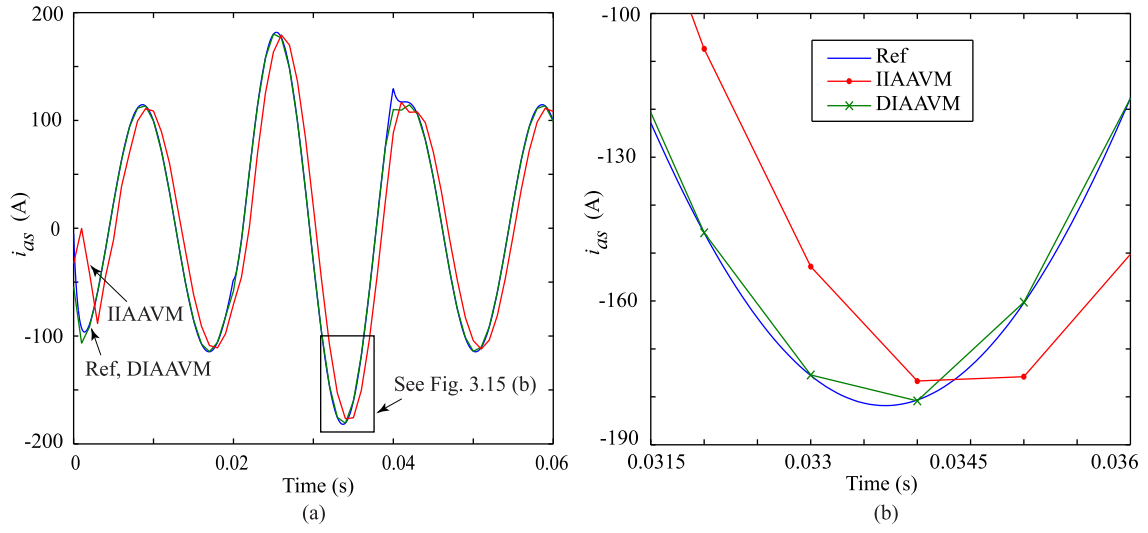


Figure 3.15 Input phase current predicted by the models with $1000\mu s$ time step.

Chapter 4: AVM Verification in SV-Based and EMTP-Type programs

4.1 Example Micro-Wind Turbine Generator System

To demonstrate the properties and benefits of the average-value models, a micro-wind turbine generator system is considered first as depicted in Figure 4.1. The system parameters are summarized in Appendix A.2. Such systems may be used to generate power for telecommunication equipment in the remote areas where an electric grid is not easily accessible.

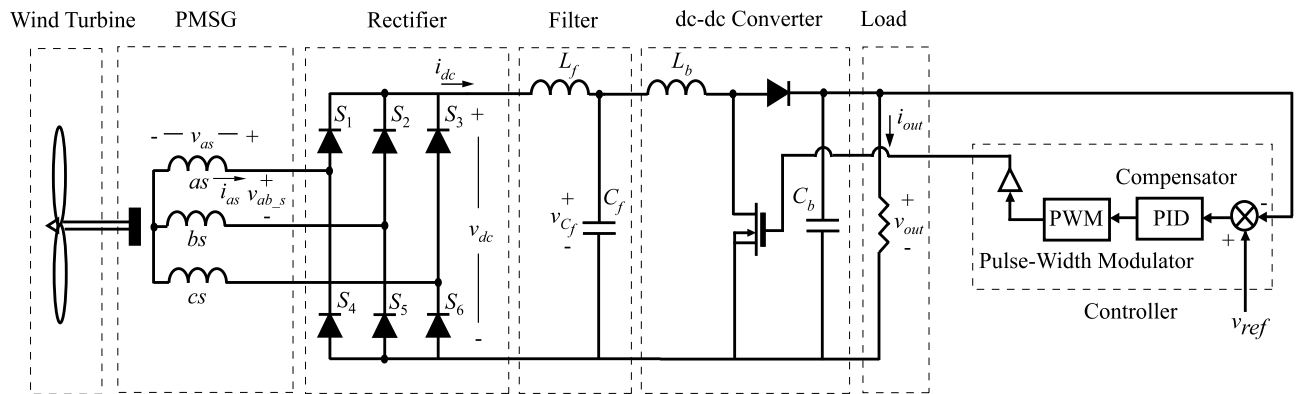


Figure 4.1 Example PMSG micro-wind turbine generator system.

A typical low-cost system consists of a wind turbine coupled to a Permanent Magnet Synchronous Generator (PMSG) through a gearbox. The generator feeds a line-commutated rectifier circuit, followed by an L-C filter, and a dc-dc converter which is connected to the dc bus. The controller adjusts the duty-cycle and regulates the output voltage to the appropriate

level, typically 28V dc. This system contains mechanical components, rotating machine, line-commutated ac-dc converter, dc-dc converter, and a controller; and is therefore considered a suitable example system.

4.1.1 Large-Signal Time-Domain Analysis

The example system is first modeled in detail considering the switching of all diodes and transistor. The average-value model is then developed using the PAVM for the line-commutated converter, and the circuit-averaging [133] for the dc-dc converter. In the computer study considered in this section, the micro-turbine system is subjected to the speed change shown in Figure 4.2 (top plot). The transient responses as observed in the output voltage, output current, dc-link capacitor voltage, and the duty cycle are also shown in Figure 4.2. It is observed that the AVM of the system predicts the behavior of the detailed model with excellent accuracy.

To achieve accurate results for this study using the variable-step solver ODE23 in Matlab/Simulink [4], the detailed model required a total of 386,680 time-steps whereas the AVM results were obtained by only 625 time-steps in total. Relatively small time steps were required in the detailed model in order to capture all the switching events due to high frequency switching of the boost converter as well as the switching of the rectifier diodes. However, the AVM does not have switching and can be executed with much larger time steps. This demonstrates an increase of simulation efficiency of 1,951 times to obtain the results of Figure 4.2.

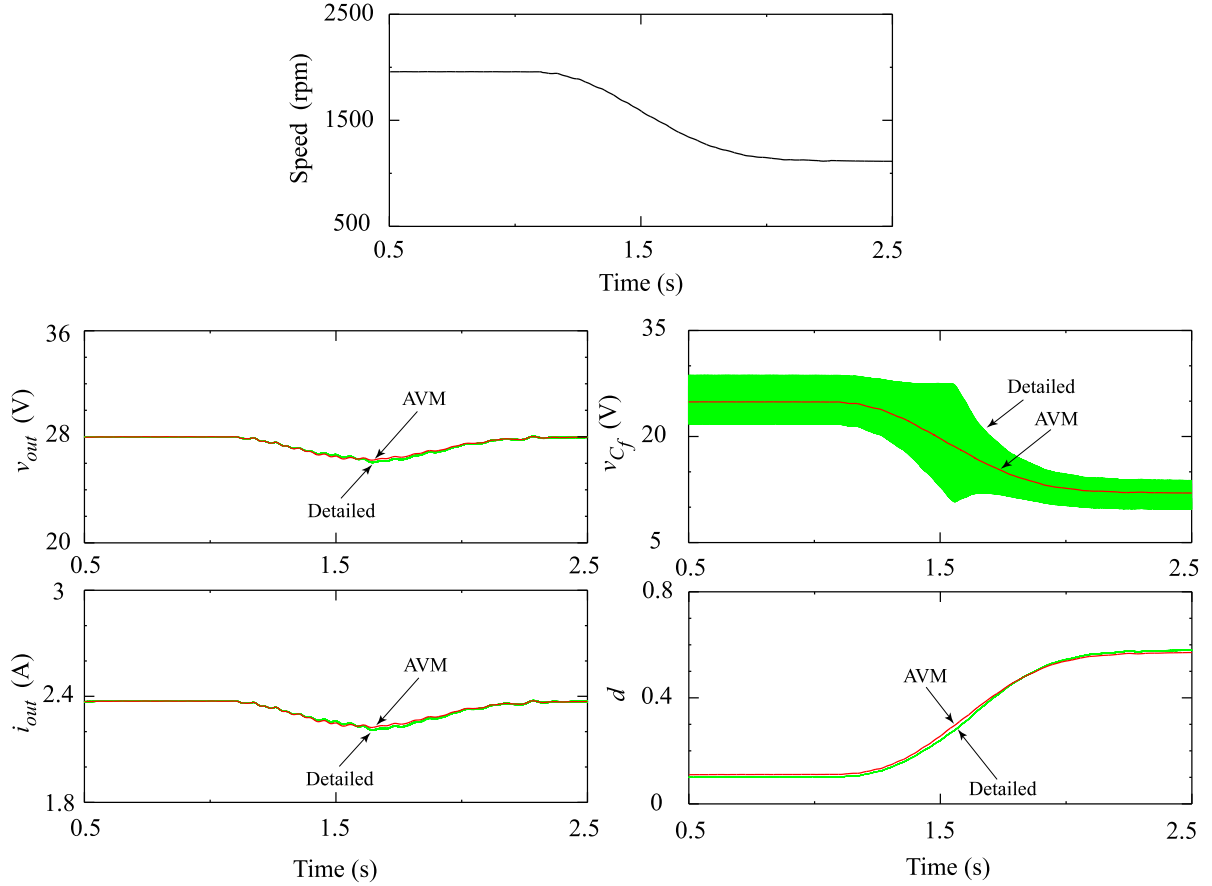


Figure 4.2 Waveforms of the example PMSG micro-wind turbine generator system.

4.1.2 Small-Signal Frequency-Domain Analysis

It is also desired to compare the detailed and average-value models in portraying the small-signal frequency-domain characteristics of the system. For this purpose, a small-signal analysis is performed around the steady-state operating point corresponding to the shaft speed of 1500 rpm. First, the control loop is removed and the duty ratio of the transistor gate signal is fixed to 0.35 to obtain the output voltage of 28 V on the dc bus. The open-loop small-signal input-output transfer function $H(s)$ may then be expressed as

$$H(s) = \frac{\hat{v}_{out}(s)}{\hat{n}(s)}, \quad (4.1)$$

where \hat{v}_{out} is the change in the output dc bus voltage due to the small-signal perturbation \hat{n} in the shaft speed. This transfer function includes the effects of both ac-dc and dc-dc stages of the system; it is useful to designing the controller, but very difficult to derive analytically. It is therefore a suitable measure of comparing the detailed and average-value models. This transfer function has been extracted using both models and the results are superimposed in Figure 4.3. Since the input is the mechanical speed, particularly lower frequency dynamics are of significant importance. Nevertheless, the results in Figure 4.3 are illustrated for up to one-half of the lowest switching frequency present in the system, which corresponds to the diode rectifier stage, (i.e., 300 Hz). As the switching frequency is approached further from this point, it would be normal to observe deviations between the results obtained from the detailed and average-value models. In the whole frequency range depicted in Figure 4.3, however, the results demonstrate an excellent match between the detailed and average-value models.

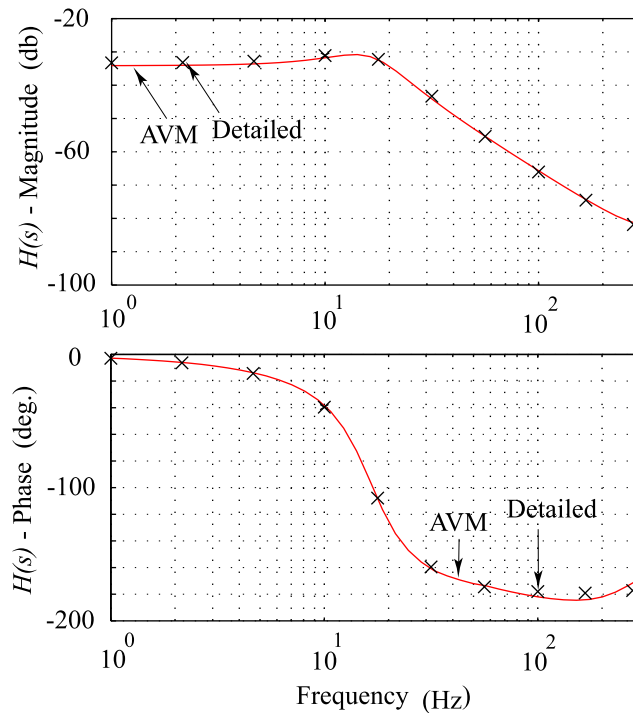


Figure 4.3 Speed-to-output-voltage transfer function for the example micro-wind turbine system.

To obtain the results of the frequency-domain analysis of Figure 4.3 from the detailed model (crosses), the frequency sweep method has been employed which becomes a very time-consuming procedure especially at low frequency. However, the results of Figure 4.3 using the AVM (solid lines) may be produced very rapidly using the automated linearization function offered by Matlab/Simulink [4]. At the same time, the results demonstrate a close agreement between the detailed and average-value models in the whole depicted frequency range.

4.2 Example 3-Phase (6-Pulse) Front-End Rectifier system

Next, a typical medium power frond-end rectifier example system operating at 480V level is considered. The layout of the system topology is similar to Figure 2.2 with the exception that the ac and dc filtering network may take various configurations. The system parameters are summarized in Appendix A.3. Extensive time- and frequency-domain simulation studies are carried out to compare the performance of various models under different operating conditions. Three simulation software packages are chosen to conduct the studies, namely Matlab\Simulink [4], PSCAD/EMTDC [11], and EMTP-RV [12]. These packages have been used to implement the detailed and dynamic average-value models of the system. In general, it is observed that the results predicted by all simulation packages are essentially identical, provided the time step and solver properties have been selected appropriately.

For the analyses presented in this section, in addition to the detailed switch-level models of the system, three dynamic average-value models have been considered based on AVM-1, AVM-2, and PAVM. Regardless of the benefits and challenges of the approaches, all methodologies, if applied correctly, should lead to similar results in predicting the averaged dynamic behavior of the detailed rectifier system below the switching frequency.

The studies that follow consider two topological cases, with and without series filter, and do not consider any shunt filter branches. This choice is based on the conclusions drawn after

the detailed analysis performed in the beginning of Chapter 3. As demonstrated there, if shunt filters are included, the currents drawn from the network are smoother than the bridge currents, since some harmonic content flows through the parallel branches. Other than this, the performance of the system is quite similar in these cases from a dynamic average modeling point of view.

4.2.1 Steady-State Time Domain Analysis

The steady state regulation characteristic provides a suitable measure for comparing the performance of various models under different loading conditions. The regulation characteristics may be obtained by varying the load from open circuit to short circuit and recording the values of the average dc bus voltage and current. These values are denoted by \bar{v}_{dc} and \bar{i}_{dc} , respectively. For the purpose of plotting the regulation characteristics, the voltages and currents are typically normalized by their corresponding maximum values, i.e., open-circuit and short-circuit, as predicted by the detailed model. In order to investigate the operation and performance of various models in DCM and CCM, the considered rectifier system is assumed without and with the series ac inductor filter, respectively.

4.2.1.1 Operation in DCM

Figure 4.4 (a) depicts the regulation characteristics obtained from the detailed and average-value models in the absence of series ac inductor filter and presence of the dc bus capacitor. The calculated values of the short-circuit currents and open-circuit voltages are summarized in Table 4.1. It should be noticed that without the ac filter inductor and only the network Thevenin impedance, the short circuit current would be extremely high, 1982.3A. In practice, the system with such configuration and parameters typically operates at lighter loads (mostly in the DCM or CCM-1) and the operation under heavy load current is impractical. A magnified view of the practical lighter-load region is provided in Figure 4.4 (b). As seen in

this figure, the DCM extends up to the 34.5A of the average dc current. The regulation characteristics predicted by the analytical models, AVM-1 and AVM-2, give a lower voltage and deviate from the one predicted by the detailed switching model. Observing the results in Figure 4.4 (a), it is also evident that the short-circuit current is incorrectly predicted by the analytical models since these models are not valid for heavy-loading conditions in CCM-2 and below. At the same time, the PAVM predicts the same characteristic as the detailed model over the entire region from open to short circuit.

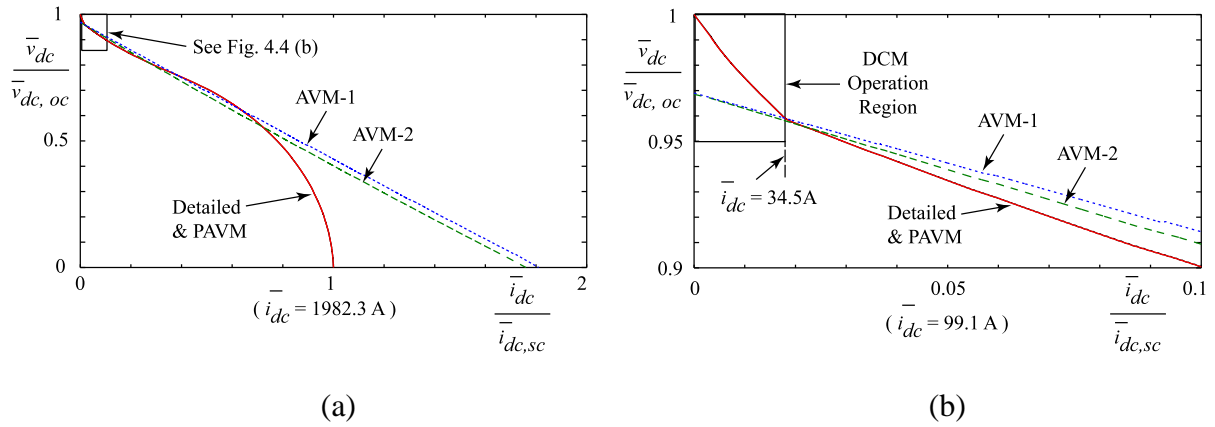


Figure 4.4 (a) Regulation characteristic of the system without ac input filter with dc capacitor; and (b) Magnified view showing the performance of models in DCM region.

To better compare the accuracy attained by the average models, the steady state values of the dc bus voltage and currents calculated by these models are summarized in Table 4.2 for two operating points in DCM. The values computed by the detailed model are assumed as reference. As it can be seen in this table, under heavier load, $R_L = 35 \Omega$, closer to the CCM (but still in DCM), both analytical models AVM-1 and AVM-2 under-estimate the dc voltage and current by about 1.3%. Under a lighter load in DCM, $R_L = 70 \Omega$, the error increases to above 2%, which may still be reasonable for some studies. Note that the error in dc voltage and current is the same since all models assume the same load resistance. At the same time,

the PAVM predicts the steady state dc voltages and current in DCM with extremely good accuracy (up to third digit).

Table 4.1 Maximum values of the dc bus voltage and current for different system topologies.

Configuration	Open-Circuit Voltage, $\bar{v}_{dc,oc}$	Short-Circuit Current, $\bar{i}_{dc,sc}$
Without r_{ac}, L_{ac}	669 V	1982.3 A
With r_{ac}, L_{ac}	648.2 V	98.8 A

Table 4.2 Steady-state values of the dc bus voltage and current predicted by various models in DCM

Models	$R_L = 35 \Omega$	$R_L = 70 \Omega$
Detailed Model (Reference)	$\bar{i}_{dc} = 18.6625 A$ $\bar{v}_{dc} = 653.1879 V$	$\bar{i}_{dc} = 9.4354 A$ $\bar{v}_{dc} = 660.4708 V$
AVM-1	$\bar{i}_{dc} = 18.4260 A$ $\bar{v}_{dc} = 644.9111 V$ <i>error = 1.2672 %</i>	$\bar{i}_{dc} = 9.2366 A$ $\bar{v}_{dc} = 646.5652 V$ <i>error = 2.1070 %</i>
AVM-2	$\bar{i}_{dc} = 18.4160 A$ $\bar{v}_{dc} = 644.5613 V$ <i>error = 1.3208 %</i>	$\bar{i}_{dc} = 9.2341 A$ $\bar{v}_{dc} = 646.3869 V$ <i>error = 2.1335 %</i>
PAVM	$\bar{i}_{dc} = 18.6618 A$ $\bar{v}_{dc} = 653.1625 V$ <i>error = 0.0038 %</i>	$\bar{i}_{dc} = 9.4353 A$ $\bar{v}_{dc} = 660.4708 V$ <i>error = 0.0011 %</i>

4.2.1.2 Operation in CCM

If the series ac inductor filter is added to the system, the value of the short circuit current would become 98.8A as shown in Table 4.1. Moreover, the DCM operation will be limited to a very small region at the extremely light load close to an open circuit at the dc bus. This will also improve the ac current waveforms making them similar to the bottom plot of Figure 3.3 (a) and reducing the harmonic content. Figure 4.5 illustrates the regulation characteristic for this case, wherein the CCM-1 extends to about 35% of the short-circuit dc current and 72% of the open circuit voltage. In this range of CCM-1, which is the most practical range, the characteristics predicted by the analytical models AVM-1 and AVM-2 match very closely the characteristic predicted by the detailed model. The characteristics predicted by analytical

models then start to deviate when the system enters CCM-2, and finally significantly over-estimate the average dc current all the way to the short circuit current which is higher by 180%. However, the PAVM matches the detailed model over the entire region.

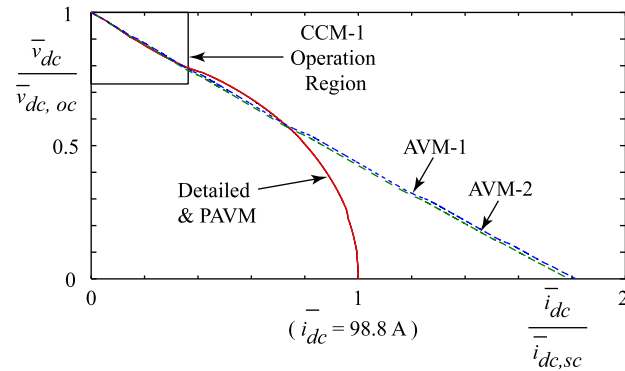


Figure 4.5 Regulation characteristic of the system in CCM operation as predicted by different models.

Table 4.3 Steady-state values of the dc bus voltage and current predicted by various models in CCM-1.

Models	$R_L = 35 \Omega$	$R_L = 70 \Omega$
Detailed model (Reference)	$\bar{i}_{dc} = 16.6247 A$ $\bar{v}_{dc} = 581.8654 V$	$\bar{i}_{dc} = 8.7308 A$ $\bar{v}_{dc} = 611.1575 V$
AVM-1	$\bar{i}_{dc} = 16.7864 A$ $\bar{v}_{dc} = 587.5247 V$ <i>error = 0.9726 %</i>	$\bar{i}_{dc} = 8.8055 A$ $\bar{v}_{dc} = 616.3853 V$ <i>error = 0.8556 %</i>
AVM-2	$\bar{i}_{dc} = 16.7161 A$ $\bar{v}_{dc} = 585.0649 V$ <i>error = 0.5498 %</i>	$\bar{i}_{dc} = 8.7848 A$ $\bar{v}_{dc} = 614.9369 V$ <i>error = 0.6185 %</i>
PAVM	$\bar{i}_{dc} = 16.6442 A$ $\bar{v}_{dc} = 582.5479 V$ <i>error = 0.1173 %</i>	$\bar{i}_{dc} = 8.7864 A$ $\bar{v}_{dc} = 615.0515 V$ <i>error = 0.6368 %</i>

To further compare the accuracy attained by the average models, the steady-state values of the dc bus voltage and currents calculated by these models are summarized in Table 4.3 for two operating points in CCM-1. The values computed by the detailed model are assumed as reference. As seen in this table, under heavier load, $R_L = 35 \Omega$, closer to the CCM-2 (but still in CCM-1), the AVM-1 and AVM-2 over-estimate the dc voltage and current by 0.97%

and 0.55%, respectively. Under a lighter load in CCM-1, $R_L = 70 \Omega$, these errors are still below 1% which is deemed acceptable. The PAVM also predicts the steady state dc voltages and currents in CCM-1 with great accuracy.

4.2.2 Dynamic Performance under Balanced Conditions

4.2.2.1 Balanced Operation in DCM

Next, the rectifier system is assumed to operate without the ac filter but with the dc capacitor as to enable the DCM. In the following study, the system initially operates in steady-state in DCM with load $R_L = 35 \Omega$. At $t = 0.3 \text{ s}$, the load resistance is stepped to $R_L = 70 \Omega$, which forces the system deeper into the DCM operation at a lighter load. The transient responses obtained by the considered detailed and average models are shown in Figure 4.6. The analytical models AVM-1 and AVM-2 predict the dc current and voltage with reasonable accuracy, including the change in operating conditions. The ac current fundamental component is also predicted by these models with sufficient accuracy. The PAVM shows a somewhat higher damping than the other models but a superior prediction of the dc voltage.

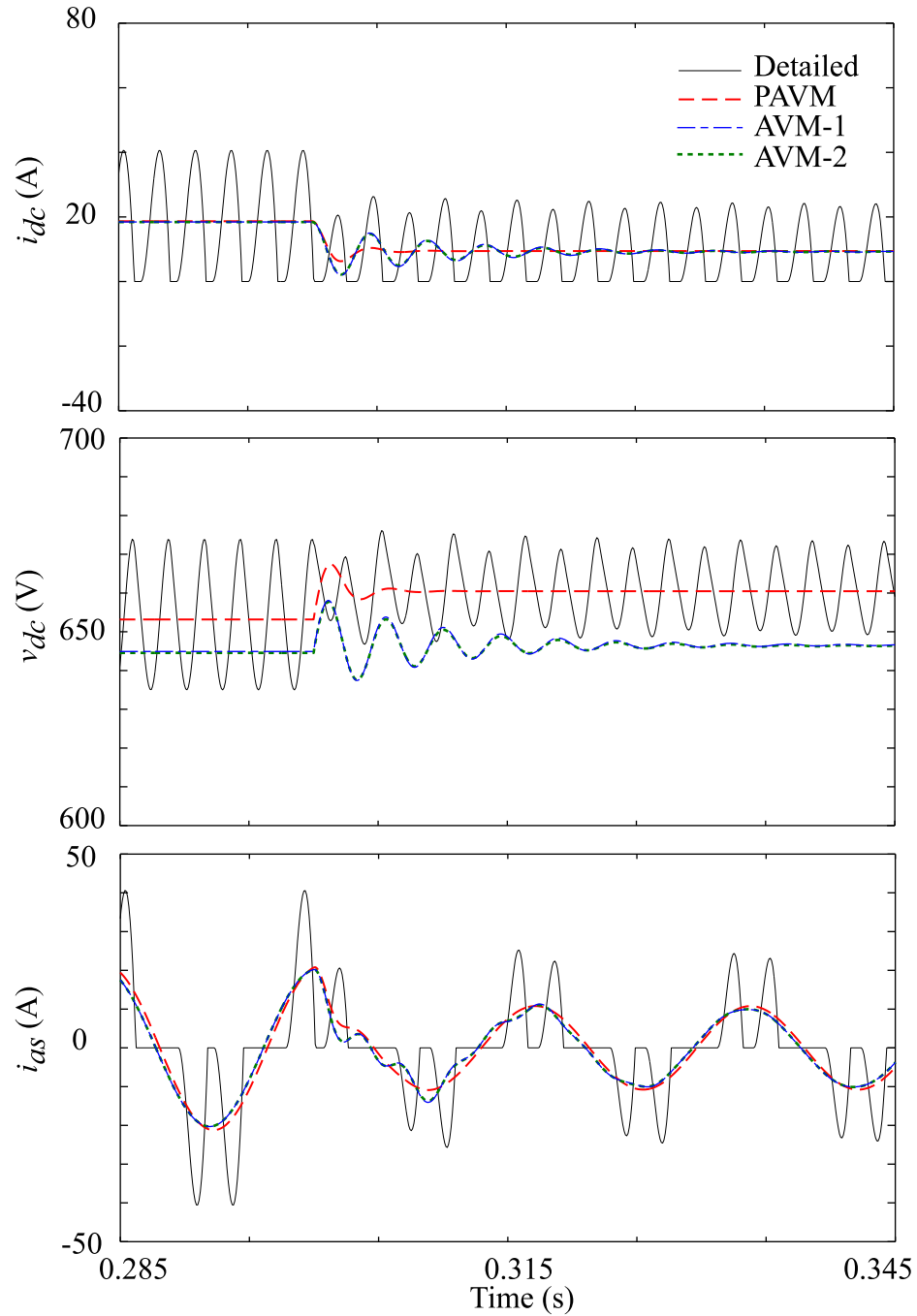


Figure 4.6 Transient response of the six-pulse rectifier system in DCM predicted by different models.

4.2.2.2 Balanced Operation in CCM

First, in order to compare the transient responses of the models, particularly the effects of the model dynamic order (full vs. reduced), the series inductor filter is added to the system

and the dc capacitor is removed from the dc bus. This topology does not allow the dc bus current to become discontinuous and hence prevents the DCM operation. The system will therefore operate in CCM for all loading conditions.

In the next study, the system is assumed to operate initially under a very light load, close to open circuit condition. Then, at $t = 0.3 \text{ s}$, the load resistance is stepped to $R_L = 13.1 \Omega$ which forces the dc bus current to increase. The corresponding transient responses predicted by the detailed and average models are shown in Figure 4.7. As seen in this figure, the new operating point is achieved in CCM-1 and all models predict the new steady state with reasonable accuracy, i.e., the average responses go through the ripple of the waveforms predicted by the detailed model as shown in Figure 4.7. This result is expected and agrees with the steady state analysis presented earlier.

Taking a close look at Figure 4.7, however, it is observed that the responses predicted by the detailed model and PAVM include an overshoot. This overshoot in response is possible because these two models have second order (without the dc capacitor). The AVM-1 and AVM-2, however, are both first-order (reduced-order) models and hence incapable of predicting this effect. These properties are evident from the eigenvalues of the system that have been extracted using numerical linearization and are summarized in Table 4.4 for DCM and CCM operation. In the right column, corresponding to the same operating point as the study of Figure 4.7, it is observed that the AVM-1 and AVM-2 each have the first order corresponding to a real eigenvalue. The PAVM, however, has a pair of complex conjugate eigenvalues corresponding to an underdamped oscillatory transient response. The oscillations are not well observed in Figure 4.7 due to the high damping dictated by the large real part of these eigenvalues. The left column in Table 4.4 corresponds to the DCM operation with the dc filter capacitor that increases the system order by one making the AVM-1 and AVM-2 of the second and the PAVM of the third order.

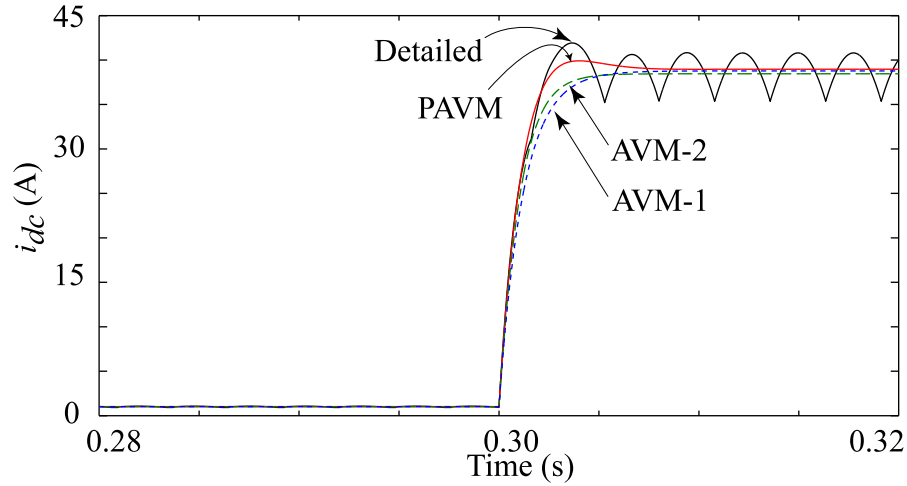


Figure 4.7 Transient response of the rectifier system with ac filter and without the dc capacitor predicted by different models.

Table 4.4 System eigenvalues predicted by different models in DCM and CCM-1.

Model	DCM, $R_L = 35 \Omega$ (w/o ac filter, with dc capacitor)	CCM-1, $R_L = 13.1 \Omega$ (with ac filter, w/o dc capacitor)
PAVM	$-35580,$ $-463.54 \pm 1408.9j$	$-737.8 \pm 529.3j$
AVM-1	$-118.6 \pm 1412.9j$	-1081.8
AVM-2	$-128.9 \pm 1419.6j$	-832.1

Next, to investigate the performance within different modes in CCM operation, the dc capacitor is added to the system. As a result, the order of the system is increased by one. In the following study, the system is assumed to start from zero initial conditions in CCM-1 with the load $R_L = 11.9 \Omega$. At $t = 0.05 s$, the load is stepped to $R_L = 2 \Omega$ forcing the system into the CCM-2. The resulting transient response predicted by various models is shown in Figure 4.8. This figure clearly shows that although AVM-1 and AVM-2 have been derived for CCM-1, their transient response does not exactly follow the dynamic response of the detailed model. This is due to the reduced-order formulation of the models.

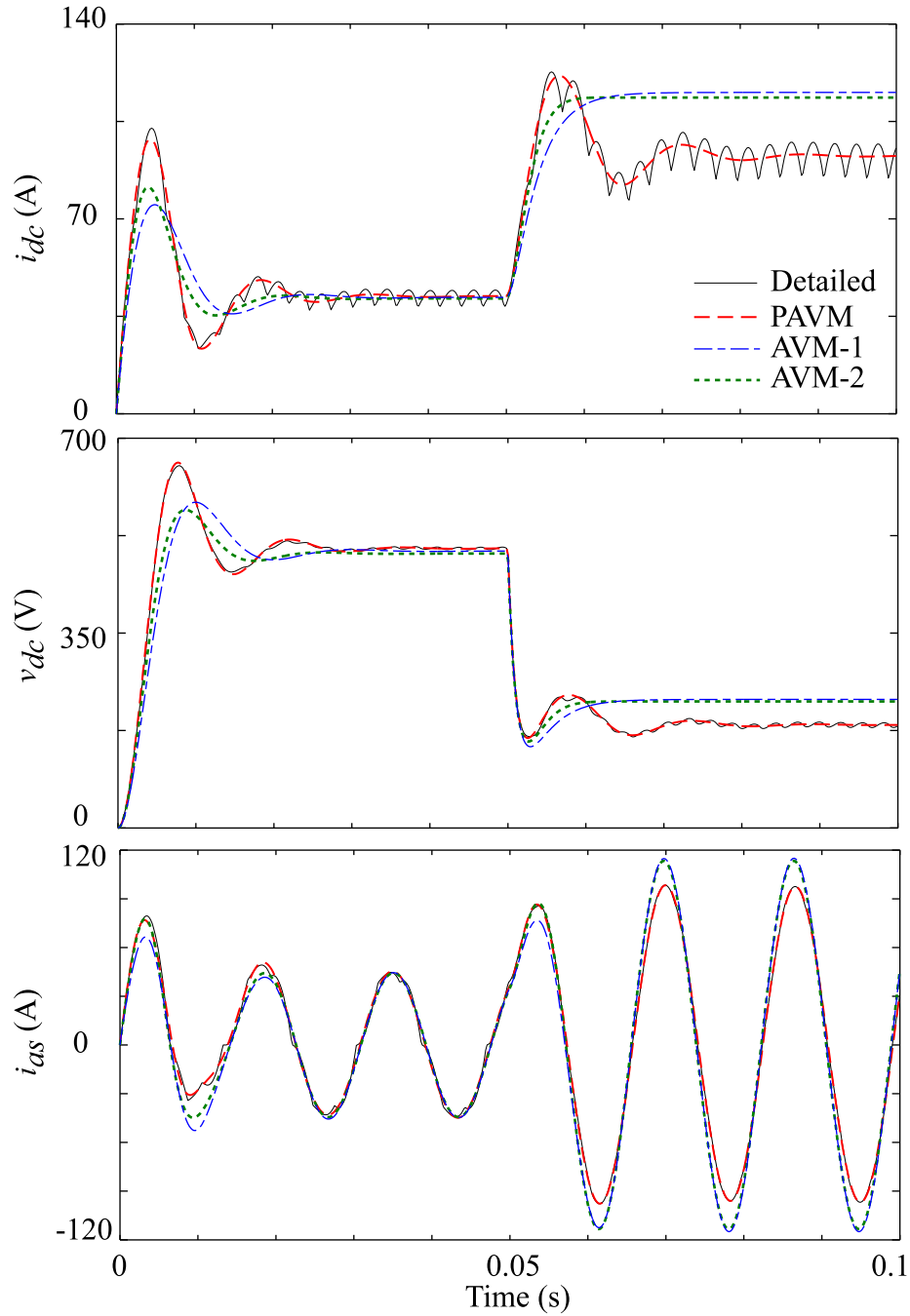


Figure 4.8 Transient response of the six-pulse rectifier system with dc capacitor in CCM predicted by different models.

The improved model AVM-2 indeed predicts the transient slightly better than the classical model AVM-1, but the effects of reduced-order formulation are still visible. The PAVM, due

to full-order formulation, perfectly follows the initialization transient including the overshoot oscillations. At $t = 0.05 \text{ s}$, the rectifier system undergoes another transient and transitions into CCM-2. Both AVM-1 and AVM-2 clearly do not follow this transition very well and predict higher dc voltage and current. This is expected as the models were developed assuming CCM-1 operation. However, the response of the full-order PAVM model is very much consistent with the transient and new steady state predicted by the detailed model since the model has been developed for a range of operating conditions.

4.2.3 Dynamic Performance under Unbalanced Conditions

4.2.3.1 Unbalanced Operation in DCM

For implementing the DCM operation, the ac input filter is removed and the dc capacitor is added to the rectifier system. In the following study, the rectifier system initially operates under a balanced condition with resistive load $R_L = 20 \Omega$. This operating point is close to the boundary between DCM and CCM-1. At $t = 0.08 \text{ s}$, a phase shift of 45 degrees in the c-phase voltage, e_{cs} , is introduced making the three phases asymmetric. This change in input voltage throws the rectifier system into unbalanced operation in DCM. Next, at $t = 0.11 \text{ s}$, the load is stepped to $R_L = 50 \Omega$ making the DCM operation even lighter. The corresponding transient responses, as seen in the ac and dc sides, are shown in Figure 4.9 and Figure 4.10, respectively. As seen in these figures, the heavy asymmetry of the input ac voltages leads to a pronounced change in the conduction pattern of the rectifier diodes, making the ac currents particularly spiky and uneven among the phases. It can be observed in Figure 4.10 that the models AVM-1 and AVM-2 do not predict this condition well by producing larger ripple in dc voltage and current. At the same time, PAVM appears to predict the dc variables with much greater accuracy closely resembling the peaks and fluctuation produced by the detailed simulation of the rectifier system.

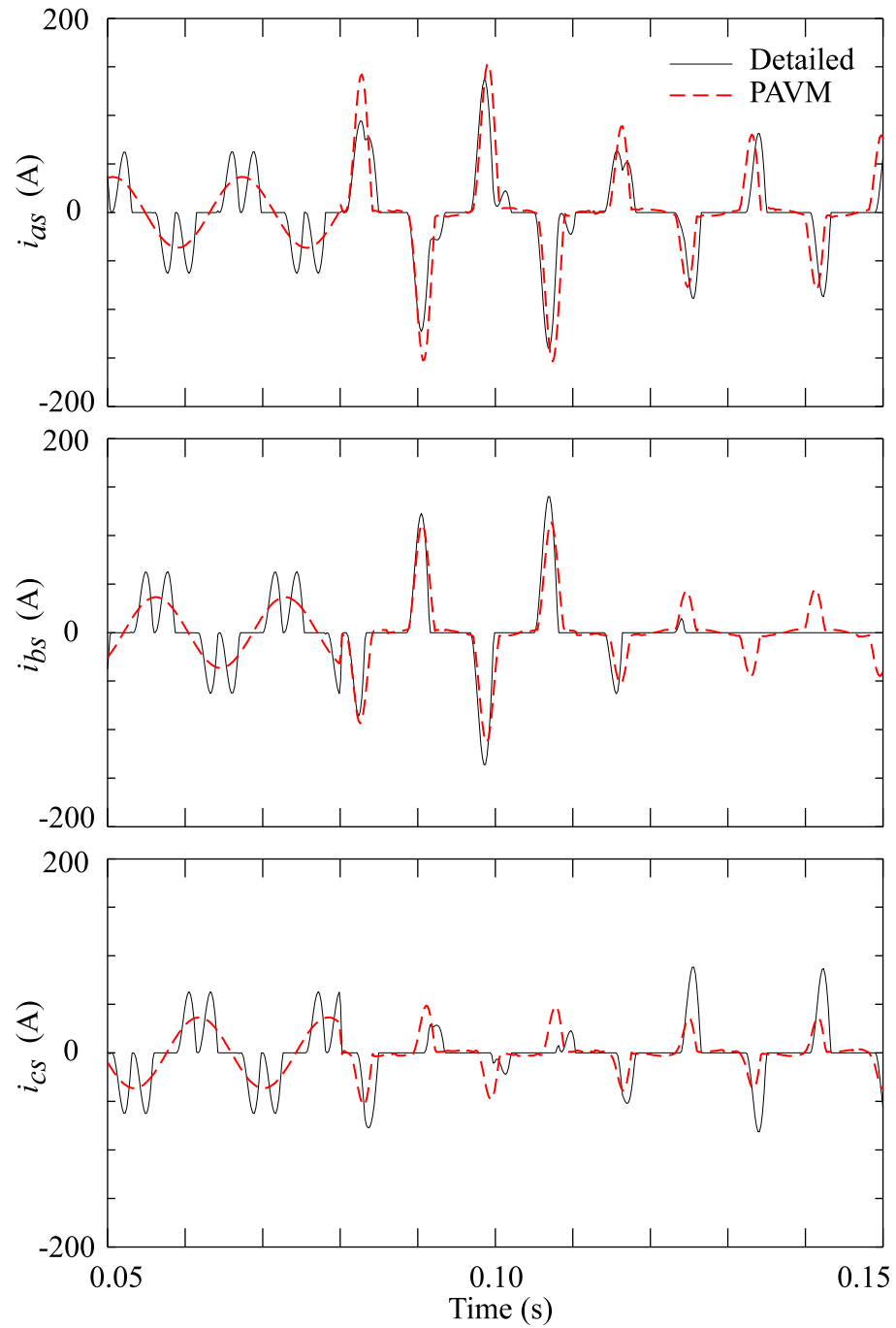


Figure 4.9 Transient response of the rectifier system to a change in ac voltages, leading to unbalanced operation in DCM, as observed in the ac currents predicted by various models.

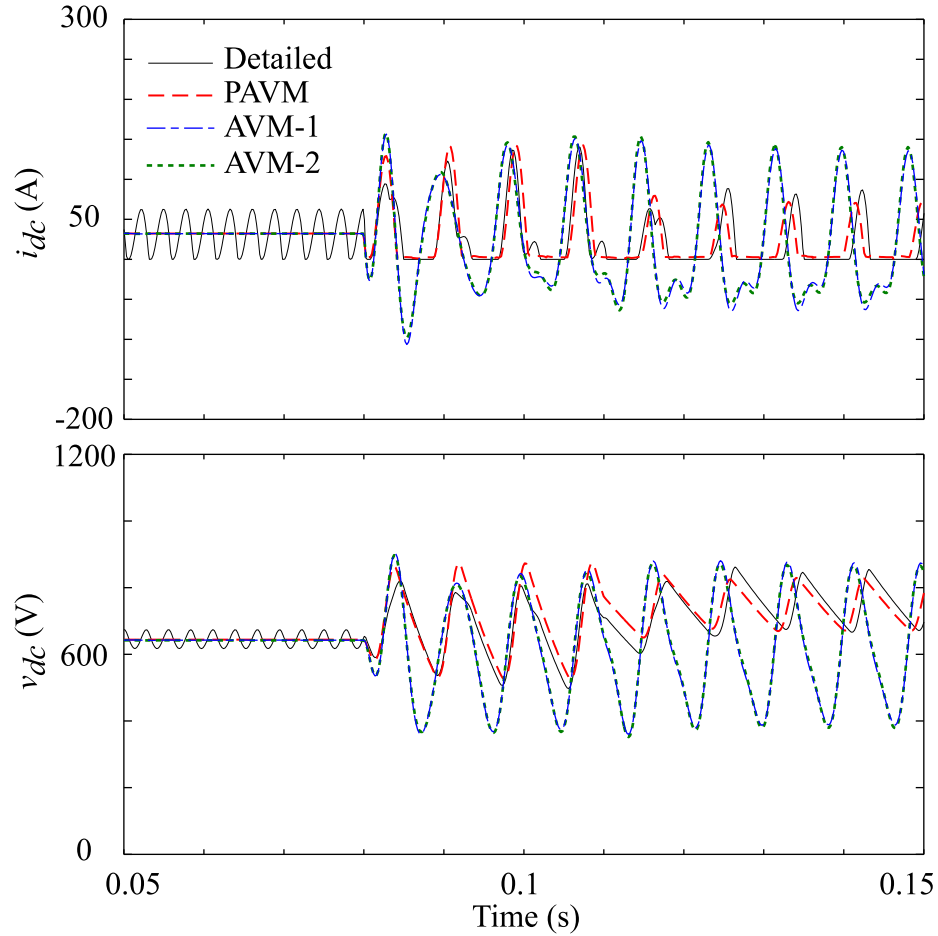


Figure 4.10 Transient response of the rectifier system to a change in ac voltages, leading to unbalanced operation in DCM, as observed in the dc bus predicted by various models.

4.2.3.2 Unbalanced Operation in CCM

To implement the CCM, the input ac filter is added to the system, and the dc capacitor is removed. In the following study, the rectifier is assumed to start in CCM-1 with balanced three-phase source and a resistive load $R_L = 15 \Omega$. At $t = 0.03 \text{ s}$, the magnitude of e_{cs} is reduced by half leading to unbalanced operation among the rectifier phases. Then, at $t = 0.06 \text{ s}$, the load is stepped to $R_L = 5 \Omega$, which changes the mode to CCM-2. The resulting ac phase currents predicted by the models are illustrated in Figure 4.11. The corresponding dc bus current and voltage are shown in Figure 4.12.

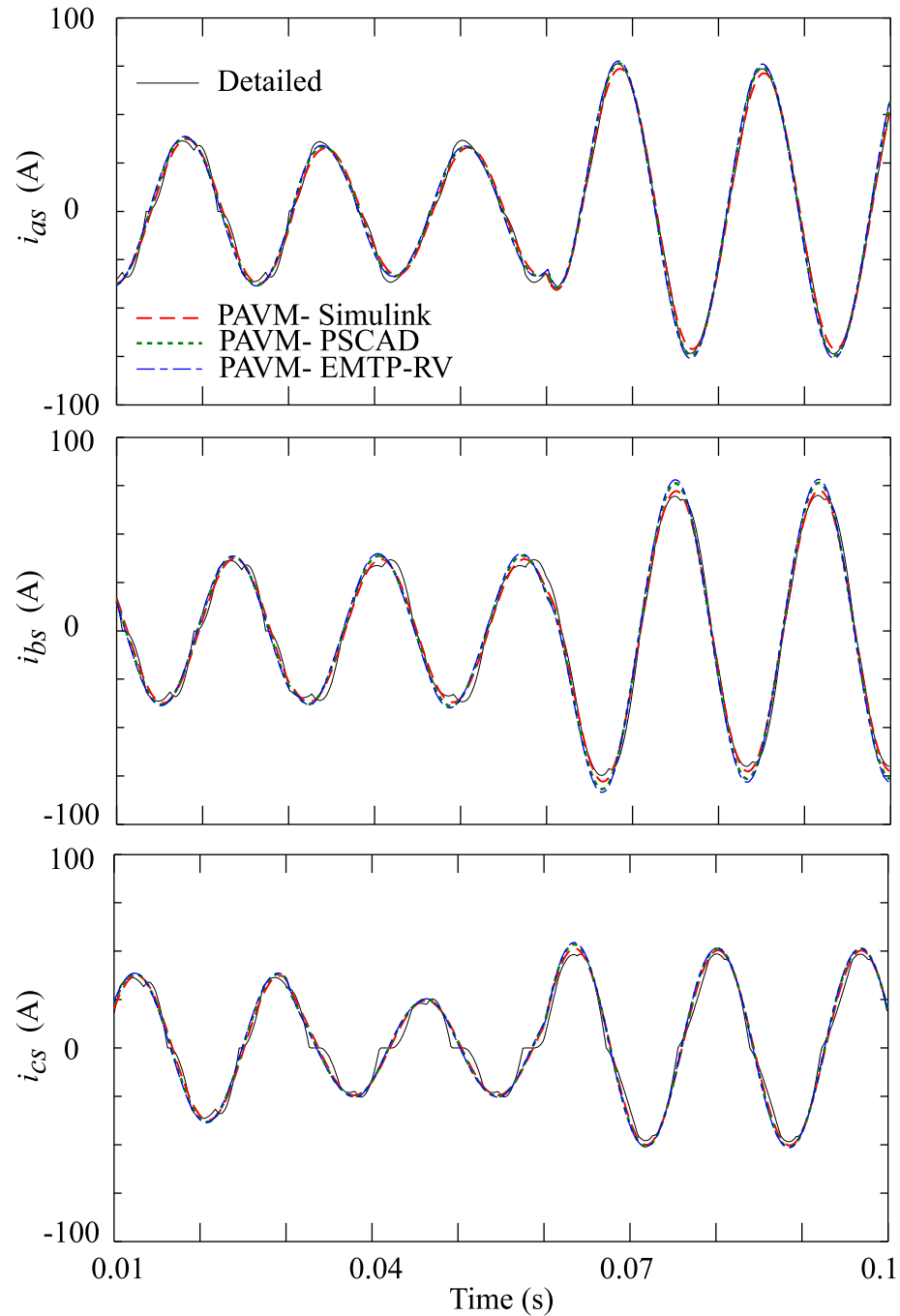


Figure 4.11 Transient response of the rectifier system to a change in ac voltages, leading to unbalanced operation in CCM, as observed in the ac currents predicted by various models.

For clarity of the figures, only the responses of the detailed and PAVM models have been superimposed. The results of PAVM obtained using PSCAD, EMTP-RV, and Simulink are

all superimposed for comparison, and are essentially identical. It is observed that the PAVM predicts the unbalanced operation of the dc and ac variables quite well.

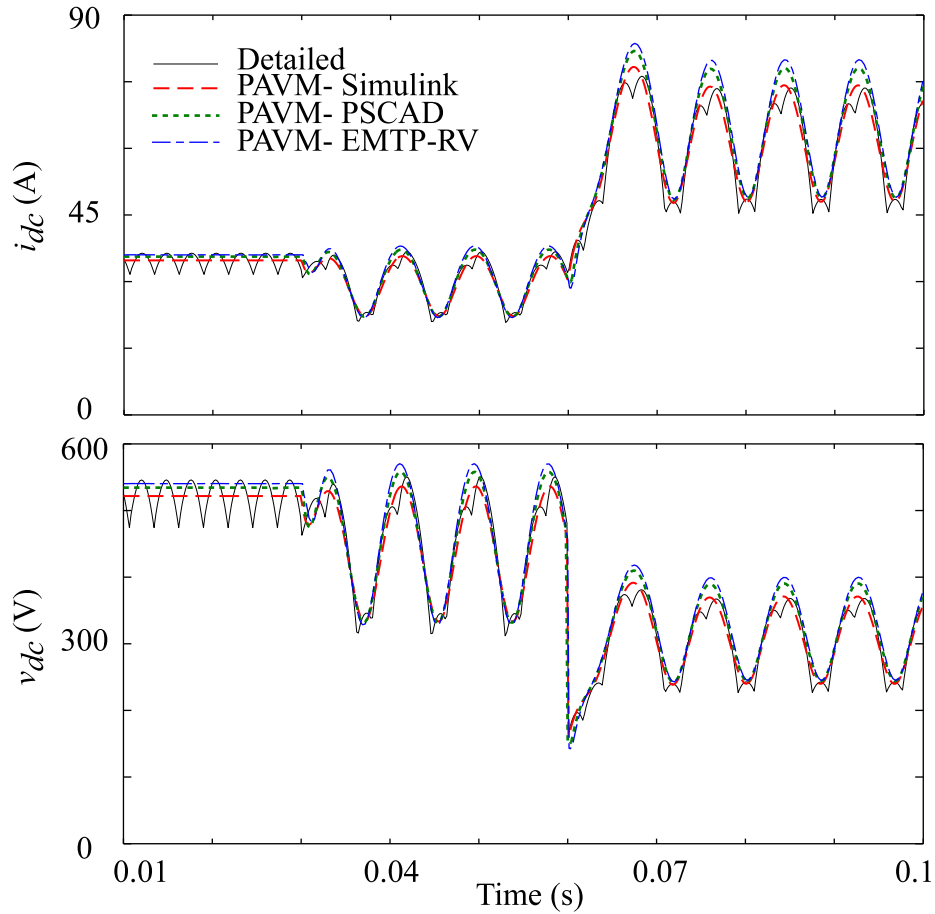


Figure 4.12 Transient response of the rectifier system to a change in ac voltages, leading to unbalanced operation in CCM, as observed in the dc bus predicted by various models.

The time steps needed for simulation by various models in different software packages are also tabulated in order to compare these models in terms of numerical efficiency. The number of time steps taken by the considered models for the study of Figure 4.12 is summarized in Table 4.5. In PSCAD, the detailed model is run using the typical EMTP time step of $50 \mu s$. In Simulink, a variable-step solver ODE15s has been used which dynamically adjusts the time-step size and may therefore require fewer time steps as seen in Table 4.5.

Here, the maximum allowable time step of 1 ms and both absolute and relative tolerances of $1\text{e-}4$ have been used. As seen in Table 4.5, the PAVMs implemented in PSCAD, EMTP-RV, and Simulink require much fewer time steps and are therefore significantly faster than the respective detailed models. For consistency, the PAVM-Simulink model was run with the same solver, ODE15s, step size limits and tolerances as the corresponding detailed model. To obtain a similar result, the PAVM in PSCAD and EMTP-RV had to use a time step of $200\ \mu\text{s}$ and $300\ \mu\text{s}$, respectively.

Table 4.5 Comparison of simulation time steps of different models

Model	Step Size (Δt)	Number of Time Steps
Detailed - PSCAD	$50\ \mu\text{s}$	2,001
Detailed - Simulink	1 ms (max)	1,042
PAVM - PSCAD	$200\ \mu\text{s}$	501
PAVM – EMTP-RV	$300\ \mu\text{s}$	334
PAVM - Simulink	1 ms (max)	247

4.2.4 System Impedance Analysis

4.2.4.1 Steady-State Analysis

Let us first consider the system of Figure 2.2 fed from a balanced three-phase source and operating in a steady-state condition defined by a fixed load resistance R_L . As discussed earlier, the harmonic content of the three-phase currents depends on the mode of operation which is in turn determined by this operating point and the overall equivalent series inductance present at the ac side. Performing a Fourier analysis on these currents and obtaining the fundamental component, the ac input impedance of the system Z_{ac} as seen from the input terminals, may be readily established by dividing the respective phasors of voltage and current.

To investigate the case of unbalanced operation, it is assumed that the magnitude of c-phase source voltage e_{cs} is reduced by half leading to asymmetry among the rectifier phases. The phasor diagrams for the input voltages in this case are depicted in Figure 4.13 (a). Since the input source voltages are known, the respective positive, negative, and zero sequence components may be readily obtained applying the appropriate transformation matrix [113]. The phasor diagrams corresponding to these symmetric components are also depicted in Figure 4.13 (b)-(d). It was clarified earlier that the zero sequence currents will not exist in the system due to topology even though the zero sequence is present in the input phase voltages of Figure 4.13. Under these conditions, the input currents are asymmetric consisting of the positive and negative sequences. The symmetric components of the fundamental currents may be obtained numerically by performing a Fourier analysis. The input impedances of the system corresponding to the positive and negative sequences may then be established from the respective phasors as

$$\left| Z_{ac}^{\pm} \right| = \frac{\left| e_{as}^{\pm} \right|}{\left| i_{as}^{\pm} \right|}, \quad \angle Z_{ac}^{\pm} = \angle e_{as}^{\pm} - \angle i_{as}^{\pm}, \quad (4.2)$$

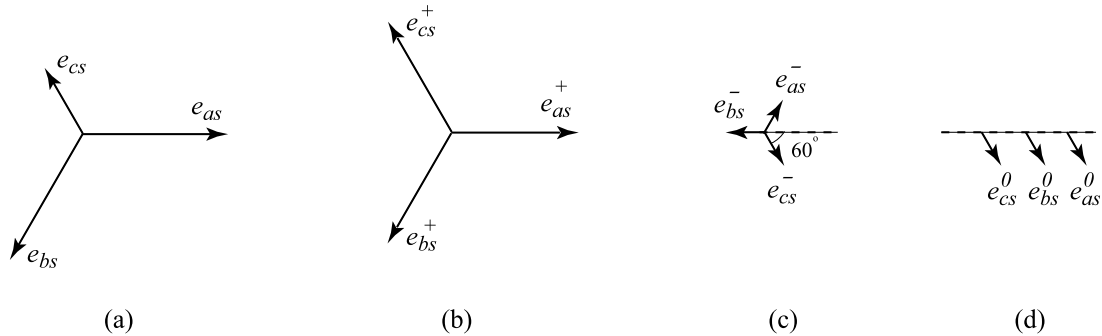


Figure 4.13 Phasor diagrams representing unbalanced operation: (a) asymmetric input voltages, (b) positive sequence, (c) negative sequence, and (d) zero sequence components.

The values of the above impedances have been tabulated in Table 4.6 for balanced and unbalanced operation in DCM and CCM. For DCM operation, the series ac filter inductor is

removed from the system but the dc capacitor is included. For CCM operation with the series ac filter inductor, two separate cases (with and without the dc capacitor) are considered.

Table 4.6 System input impedance in DCM and CCM-1

$R_L = 70 \Omega$	DCM	CCM-1 (with Cap)	CCM-1 (w/o Cap)
Z_{ac}	$36.4 \angle 10.2^\circ \Omega$	$40.8 \angle 18.9^\circ \Omega$	$40.5 \angle 16.9^\circ \Omega$
Z_{ac}^+	$30.4 \angle 5.3^\circ \Omega$	$40 \angle 28.2^\circ \Omega$	$40.5 \angle 16.3^\circ \Omega$
Z_{ac}^-	$6.1 \angle 5.3^\circ \Omega$	$8.9 \angle 34.7^\circ \Omega$	$34.1 \angle 3.5^\circ \Omega$

$R_L = 35 \Omega$	DCM	CCM-1 (with Cap)	CCM-1 (w/o Cap)
Z_{ac}	$18.4 \angle 12.1^\circ \Omega$	$21.6 \angle 24.3^\circ \Omega$	$21.5 \angle 24.1^\circ \Omega$
Z_{ac}^+	$15.4 \angle 1.1^\circ \Omega$	$21.9 \angle 30.1^\circ \Omega$	$21.5 \angle 23.2^\circ \Omega$
Z_{ac}^-	$3.1 \angle 1.1^\circ \Omega$	$5.8 \angle 40.9^\circ \Omega$	$16.8 \angle 7.1^\circ \Omega$

4.2.4.2 Small-Signal Frequency-Domain Analysis

Next, the small-signal output and input impedances as predicted by the average models are compared to the reference (the detailed model). For this purpose, the rectifier system is first assumed to work in the steady state operating point defined by R_L . Based on the discussions of Section 2.5, the small-signal impedance of the system looking into the dc bus is then considered as

$$Z_{dc} = \frac{\hat{v}_{dc}}{-\hat{i}_{dc}}. \quad (4.3)$$

The resulting impedances calculated using different models are shown in Figure 4.14 (top plots) for CCM operation defined by $R_L = 13.1 \Omega$ with the ac inductor filter but without the dc capacitor. For the purpose of extracting this impedance from the detailed model the data points for the magnitude and phase (crosses) have been obtained using the frequency sweep

technique. However, for the average models, the results may be obtained almost instantaneously using the numerical linearization offered by Matlab/Simulink [4]. As expected, all models predict inductive-type impedance, with the analytically-derived reduced-order models AVM-1 and AVM-2 being less accurate than the full-order PAVM.

Extracting the positive and negative sequence impedances looking into the ac terminals and mapping the impedances for various harmonics can be extremely useful for analyzing the impact of the rectifier loads on the ac network, the system stability and power quality [14], [92]-[97]. The necessary considerations for evaluating such small-signal characteristics were discussed in Section 2.5. Adopting that approach, the final 4-by-4 impedance transfer matrix is then defined by (2.30). To give an example, the (1,1) element of the transfer matrix (2.30), the impedance Z_{qq} , has been calculated for all considered models, and the result is shown in Figure 4.14 (bottom plots). As seen in this figure, overall, the system has an inductive-type response with the detailed switching model and the PAVM clearly showing a higher order response and a close agreement as compared to the AVM-1 and AVM-2, which are reduced-order models. This figure also illustrates that the AVM-2 does show an improvement over the classical model AVM-1 especially in predicting the magnitude in the high frequency range.

As discussed earlier, the impedance seen from the ac side, in addition to including the ac input filter, also maps the dc side load impedance as appeared through the rectifier switching cell. This impedance therefore depends not only on dynamics of the load and filters, but also on the operational mode of the rectifier. To demonstrate the effects of the dc side on the ac side impedance, the dc capacitor is added to the rectifier system and the ac side impedances are calculated using the detailed and average models. The impedances Z_{qq} and Z_{qd} , i.e., the first row of the transfer matrix (2.30), are shown in Figure 4.15. The second row impedances are obtained similarly and would essentially reflect the same properties of the modes. The effects of the dc capacitor can be clearly seen in all plots of Figure 4.15. This effect is

particularly pronounced in the range of high frequencies in Z_{qq} . This figure also shows that the full-order PAVM predicts the phase and magnitude of both impedances with great accuracy.

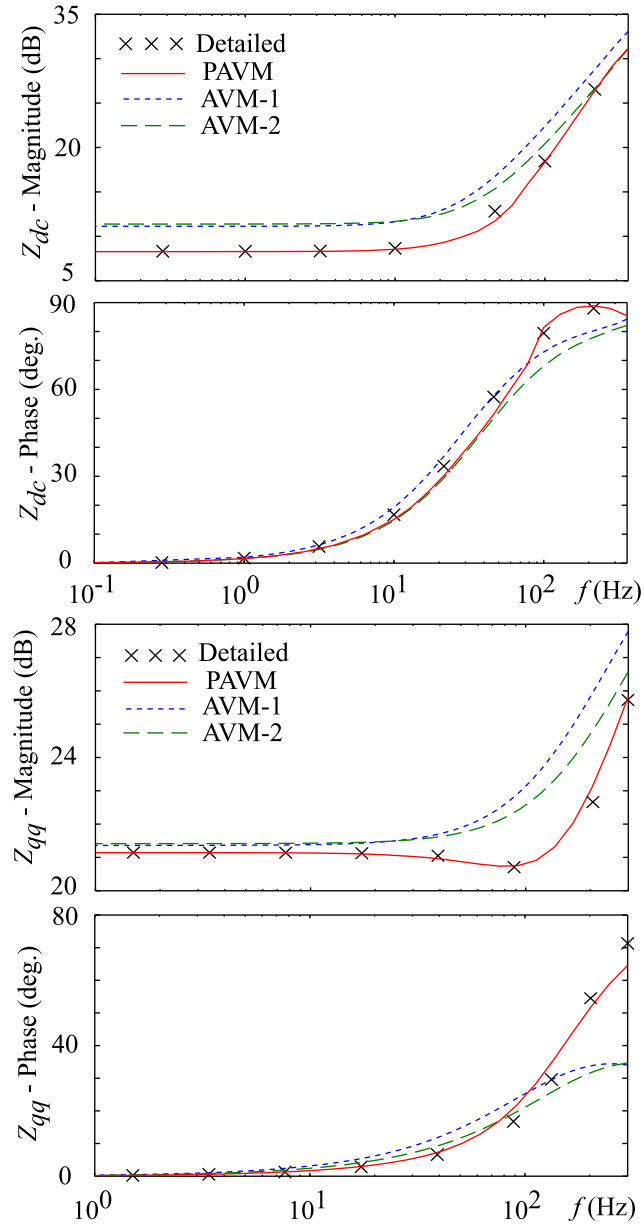


Figure 4.14 Dc-side impedance Z_{dc} (top) and ac- side impedance Z_{qq} (bottom) of the rectifier system in CCM-1 with input ac filter but without dc capacitor predicted by different models.

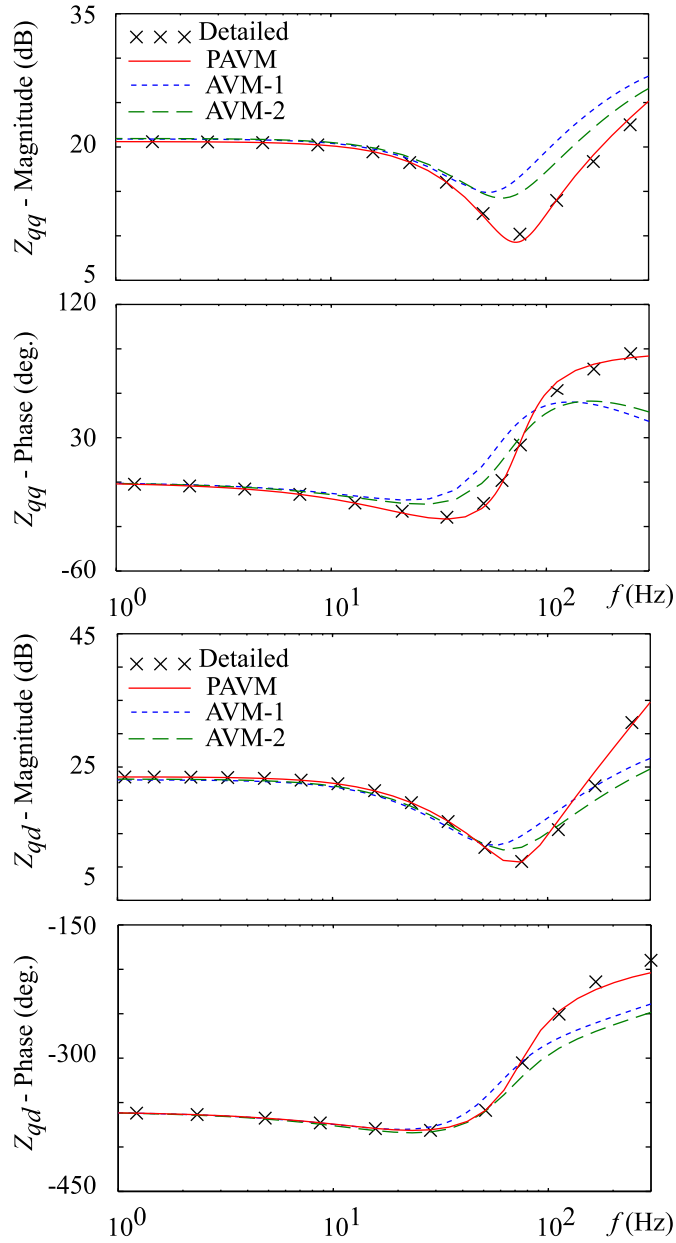


Figure 4.15 AC-side impedance Z_{qq} (top) and Z_{qd} (bottom) of the rectifier system in CCM-1 with input ac filter and dc capacitor predicted by different models.

4.2.5 Conclusion

In this Chapter, the performance of analytical and parametric dynamic average models, implemented in SV-based and NA-based programs, was compared through extensive simulation studies in time and frequency domains under various loading conditions as well as for the cases of balanced and unbalanced excitation. Generally, it is concluded that the results obtained by different software simulation packages are essentially identical, given the time step and other solver properties are appropriately adjusted. Also, it is concluded that, although analytically-derived models AVM-1 and AVM-2 possess reduced dynamic order, they can be effectively used for the transient studies in CCM-1 (and in the vicinity of this mode). The PAVM model is shown to have great accuracy over a much wider range of operating conditions covering both DCM and CCM. It is also demonstrated that such models can accurately predict the small-signal impedance of the system as seen from either ac or dc sides. Based on this conclusion, the parametric approach is considered in next Chapter as the basis for developing a dynamic AVM for machine-fed six-pulse converters taking into account the effects of losses in the diode bridge as well as the machine losses.

Chapter 5: Inclusion of Losses in Machine-Fed Converter Systems

5.1 Introduction

The previous Chapters were focused on the voltage-source-fed line-commutated converter systems (Case I in Figure 1.1) such as the variable frequency drives that are fed from the power network. As discussed in Chapter 1, another category of the line-commutated converter systems is the rotating-machine-fed systems (Cases II and III in Figure 1.1) that are widely encountered in applications such as the distributed generation systems and the electric systems of vehicles.

In the design stages of vehicular power systems, particularly, numerous computer simulations are typically run many times for concept evaluation, prototyping of new power train, design optimization, evaluation of energy and fuel efficiency under various driving conditions, reliability assessment, etc [18]. Accurate dynamic models are then required for large-signal time-domain system-level transient studies as well as small-signal frequency-domain stability analysis and controller design. This becomes a problem, especially when the alternator-rectifier system is just a part of the larger, more complex and diverse vehicular system containing electrical and mechanical components with a wide dynamic range and spread of time scales. Moreover, for multi-objective parameter optimization studies [114], for instance, simulations of such systems may run multiple times (in a loop) and the overall computing time could become quite significant. Therefore, employing dynamic average

models instead of the detailed switching models is extremely beneficial for such analyses conducted on vehicular power systems.

As discussed in Chapter 1, however, the existing average models for machine-converter systems typically neglect the losses in the system. The main sources of losses in such systems are diode conduction losses in the bridge and the machine rotational losses. The effects of these losses are particularly important in lower voltage applications such as vehicular power systems that typically operate at 12-14 V dc. In such cases, the typical diode drops are significant with respect to the output voltage value and their effects are hence pronounced. Moreover, typical car alternators have a low efficiency due their particular structure [115], [116] which demands for appropriate consideration of the machine losses to achieve accurate system modeling.

The focus of this Chapter is the dynamic average modeling for machine-fed converters taking various sources of losses into account. For this purpose, the parametric methodology [70], is extended to include the machine rotational losses as well as the diode bridge conduction losses. First, a brief description of the considered vehicular power system structure is presented. An example vehicular power system is then considered with the parameters provided in Appendix A.4. The detailed and dynamic average modeling of the system including various losses is presented next. The developed models are verified using experimental data and simulation studies.

5.2 Example Vehicular Power System Architecture

The most common mass-produced vehicles are based on the power system architecture shown in Figure 5.1. A typical configuration includes an alternator-rectifier system which is driven by the internal combustion engine (ICE). In most cases, the alternator-rectifier system consists of a synchronous machine with wound field winding and a diode bridge which rectifies the three-phase output voltage to supply the internal electrical system with 12-14 V

dc (or a dual 12- 42 V dc). The rectifier is usually packaged inside the alternator, whereas an LC filter may or may not be included. Since the engine speed varies over a wide range, the field current is adjusted, by means of a closed-loop voltage regulator, to obtain the desired voltage level. This system supplies power to the automotive dc subsystems and energy storage elements (e.g., batteries [117]), as depicted in Figure 5.1.

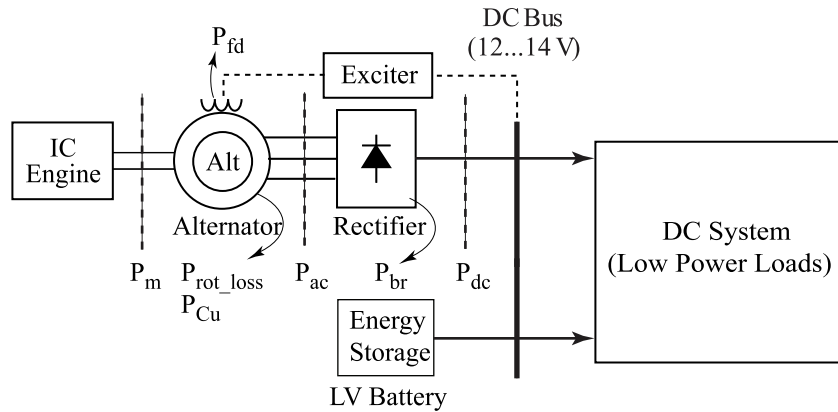


Figure 5.1 A typical vehicular electric power system and its power conversion chain.

The claw-pole, also known as “Lundell”, alternator is the most common type of synchronous machine in automotive applications. This alternator is similar to standard wound rotor synchronous machine in functionality but has a different internal structure. Concentrated stator windings (1 slot/pole/ phase) are also used to minimize cost. The claw-type rotor geometry and concentrated stator windings lead to voltage and/or current harmonics. Precise dynamic characterization of Lundell machines conventionally relies on the detailed finite element (FE) analysis [118]-[120] or the magnetic equivalent circuits (MEC) [121] (which is not available in commonly used simulation packages), both of which are computationally very expensive [122]. As a compromise between model complexity and computational efficiency, a fourth-order coupled-circuit model of a claw-pole alternator has been proposed in [123], where harmonic effects introduced by rotor saliency, concentrated

stator windings and stator slots, as well as magnetic saturation [124] have been included. The resulting model is shown to be more accurate but still considerably complicated compared to standard models of synchronous machines [51].

For simulation of automotive alternator-rectifier systems, and particularly from a system-level point of view, accurate representation of the alternator structural details may be of less interest. Therefore, the standard synchronous machine models in physical (abc) variables, that are numerically efficient and considerably less complicated, may be used to provide a reasonable accuracy. However, due to their special structure, the 14V Lundell alternator/diode-rectifier systems are well known to have a relatively low efficiency [115], [116] and the amount of iron core losses is particularly significant in such machines. To achieve accurate system modeling, appropriate representation of the losses present in the system is then of critical importance.

In the next sections, detailed and dynamic average modeling of the claw-pole Lundell alternator-based automotive power system systems is performed with the special focus on effectively including the effects of the losses in order to accurately predict the power chain in the system.

5.3 System Detailed Model

In the vehicular power system of Figure 5.1, the power conversion chain from input mechanical power, P_m at the alternator shaft, to output electric power, P_{dc} at the dc bus, is also illustrated. As shown in this figure, the important losses in the alternator include the stator copper loss, P_{Cu} , combined rotational and core loss, P_{rot_loss} , and the excitation (field) winding loss P_{fd} . Other types of loss in the alternator include mechanical losses (friction, windage effect, etc.) as well as the stray losses which may be challenging to quantify independently. The approach used in this Chapter lumps these losses into the

rotational losses while characterizing the losses in the alternator. Therefore, all these rotational, stray, and iron core losses of the alternator are combined and represented by P_{rot_loss} in Figure 5.1. Finally, the difference between the electrical power at the ac and dc terminals, denoted by P_{ac} and P_{dc} respectively, is equal to the diode bridge conduction loss denoted by P_{br} .

A circuit diagram of the alternator-rectifier-battery system of Figure 5.1 is depicted in Fig. 2 (top). The assumed voltage regulator-exciter, Fig. 2 (bottom), is used to regulate the dc voltage through the field excitation adjustment. The system parameters are summarized in Appendix A.4. In detailed model, the alternator synchronous machine is represented in terms of physical (abc) variables.

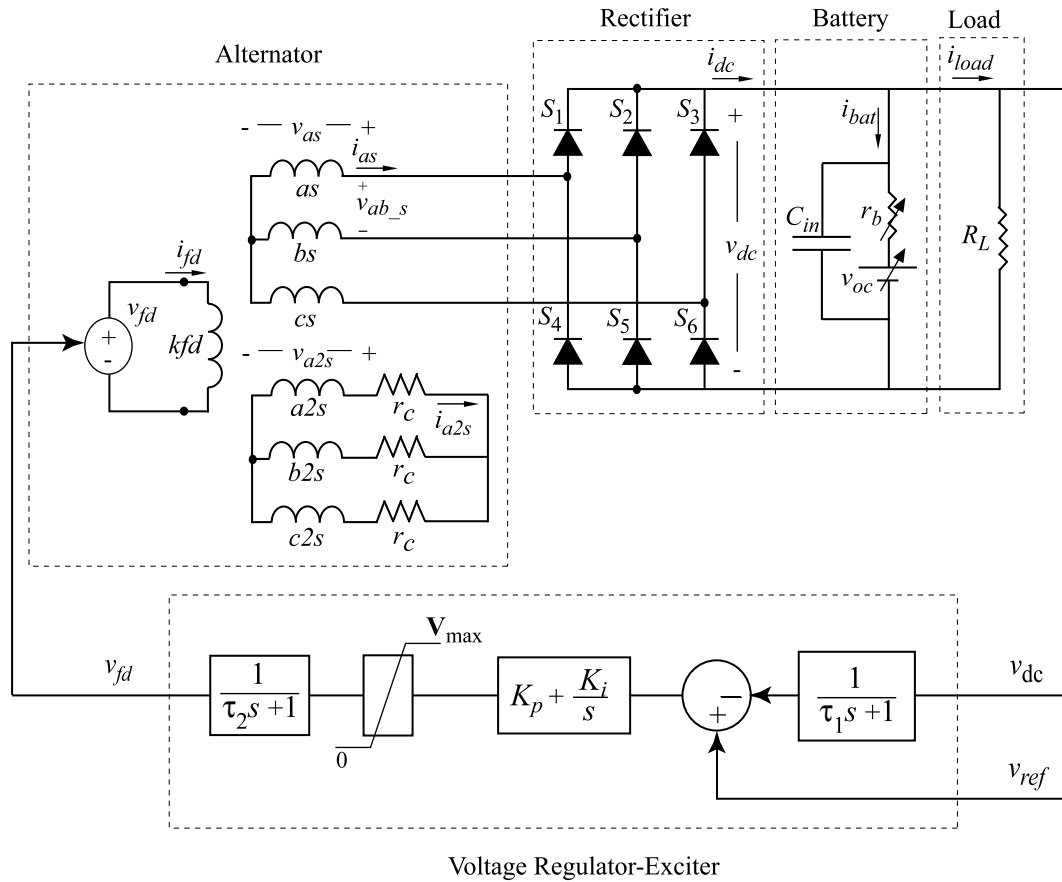


Figure 5.2 A circuit diagram for automotive alternator-rectifier-battery systems (top) with a typical voltage regulator-exciter (bottom).

5.3.1 Representation of Rotational Losses

To represent the iron core losses, which have resistive nature (due to eddy currents) and are significant in this type of machine, the approach considered here consists of introducing an additional short-circuited three-phase windings ($abc2$) to the stator side such that its resistance r_c would dissipate the real power. The machine model therefore becomes similar to a six-phase synchronous machine model [125] with one set of windings short circuited. The classical representation of iron losses typically uses a single resistor that can only represent the losses at one particular frequency of operation. Including an additional set of winding, however, allows for inclusion of losses over a range of frequencies. Using the curve-fitting techniques, the winding parameters may be then obtained such that the loss characteristics predicted by the model would match the actual loss characteristics over a wide range of frequencies. The adopted concept is similar to using RL ladder network in order to model the core losses over a range of frequencies in magnetic and electric equivalent circuits [126], [127].

Since the purpose of this additional winding is to represent the losses, its angular displacement is not relevant. Without loss of generality, the winding $abc2$ is then assumed to be in the same angular position as the main stator winding abc . This choice of the winding location significantly simplifies magnetic coupling among the windings making it easier to determine the corresponding parameters.

The parameters of additional winding $abc2$ are calculated based on the experimental measurements of the alternator losses. To measure the losses, a variable-speed dc machine is employed as a prime mover while the alternator stator terminals are kept open-circuited. For a fixed excitation current of $i_{fd} = 2A$, the open-circuit stator phase voltage and the mechanical torque on the shaft are measured while the shaft speed is varied. The corresponding measured losses are summarized in Appendix A.4. As mentioned earlier, this

measurement combines the rotational, stray, and iron core loss into a single lumped loss characteristic. Since the stator back emf voltages induced in winding $abc2s$ vary linearly with speed, the variation of losses with respect to the back emf is quite similar in shape to the variation of losses with respect to the shaft speed. In particular, the measured characteristic is then approximated by a quadratic expression as

$$P_{rot_loss}(E_a) = \frac{E_a^2}{r_c}, \quad (5.1)$$

where E_a is the back-emf induced in the additional winding $abc2s$. Since the additional windings $abc2s$ are similar to the stator windings abc , their back emf are equal to the open-circuit stator voltages. The value of r_c is then obtained using the least square curve-fitting method to achieve the best fit for the measured loss characteristic (5.1). The result is given in Appendix A.4.

The final machine model in phase coordinates is then described by the corresponding voltage, flux linkage and torque equations as

$$\begin{bmatrix} \mathbf{v}_{abc} \\ \mathbf{v}_{abc2s} = \mathbf{0} \\ v_{fd} \end{bmatrix} = \begin{bmatrix} \mathbf{r}_s & 0 & 0 \\ 0 & \mathbf{r}_c & 0 \\ 0 & 0 & r_{fd} \end{bmatrix} \begin{bmatrix} -\mathbf{i}_{abc} \\ -\mathbf{i}_{abc2s} \\ i_{fd} \end{bmatrix} + \frac{d}{dt} \begin{bmatrix} \boldsymbol{\lambda}_{abc} \\ \boldsymbol{\lambda}_{abc2s} \\ \lambda_{fd} \end{bmatrix}, \quad (5.2)$$

$$\begin{bmatrix} \boldsymbol{\lambda}_{abc} \\ \boldsymbol{\lambda}_{abc2s} \\ \lambda_{fd} \end{bmatrix} = \begin{bmatrix} \mathbf{L}_s & \mathbf{L}_{s1s2} & \mathbf{L}_{sr}(\theta_r) \\ \mathbf{L}_{s1s2} & \mathbf{L}_s & \mathbf{L}_{sr}(\theta_r) \\ \mathbf{L}_{rs}(\theta_r) & \mathbf{L}_{rs}(\theta_r) & L_{fd} \end{bmatrix} \begin{bmatrix} -\mathbf{i}_{abc} \\ -\mathbf{i}_{abc2s} \\ i_{fd} \end{bmatrix}, \quad (5.3)$$

$$T_e = \left(\frac{P}{2} \right) (\mathbf{i}_{abc} + \mathbf{i}_{abc2s})^T \frac{\partial}{\partial \theta_r} [\mathbf{L}'_{sr}(\theta_r)] i'_{fd}, \quad (5.4)$$

where \mathbf{v}_{abc} , \mathbf{i}_{abc} and $\boldsymbol{\lambda}_{abc}$ are the stator phase voltage, current and flux linkage vectors, and v_{fd} , i_{fd} and λ_{fd} are rotor-winding voltage, current and flux linkage, respectively.

Also, \mathbf{v}_{abc2s} , \mathbf{i}_{abc2s} and $\boldsymbol{\lambda}_{abc2s}$ are the voltage, current and flux linkage of the second set

of stator winding. The diagonal matrices \mathbf{r}_s and \mathbf{r}_c contain the stator winding resistance and the resistance corresponding to the combined losses, respectively. The field winding resistance and inductance are denoted by r_{fd} and L_{fd} . Matrices \mathbf{L}_s and $\mathbf{L}_{sr}(\theta_r)$ represent the stator winding self- and mutual-inductances and the stator-to-rotor mutual inductances respectively. The angle θ_r denotes the rotor position. The detailed expressions for these inductance matrices may be found in [51]. Note that since the additional stator winding is chosen to have the same angular displacement as the regular stator windings, the inductance matrix is considerably simplified compared to a six-phase synchronous machine with shifted sets of windings [125]. Matrix \mathbf{L}_{s1s2} contains the mutual inductances between the two sets of stator windings and may be expressed similarly. Such a choice of winding displacement also simplifies the expression for electromagnetic torque (5.4). In (5.4), P denotes the number of poles. In $\mathbf{L}'_{sr}(\theta_r)$ and i'_{fd} , all quantities are referred to the stator side.

5.3.2 Verification of Detailed Model

Next, the detailed model of the alternator-rectifier system is experimentally verified. For this purpose, the field winding is supplied with a constant dc source of $v_{fd} = 6.4 V$, and a resistive load, $R_L = 11.5 \Omega$, is directly connected to the dc bus. A dc machine, with adjustable speed, is coupled to the alternator to emulate the changes in engine speed. A transient study is carried out in which the alternator speed is varied as shown in Figure 5.3 (top plot). The recorded speed waveform is also used as the synchronous machine speed in the detailed model simulation studies.

The resulting measured and predicted dc bus voltage, v_{dc} as well as measured and simulated waveforms of the stator phase current, i_{as} , and stator line-to-line voltage, v_{ab_s} , are illustrated in Figure 5.3. For better comparison between the measured and simulated

waveforms, the dc bus voltages, v_{dc} , and stator currents, i_{as} , are superimposed and a zoomed-in view is also provided in Figure 5.3 (two bottom plots). An excellent match between corresponding waveforms in Figure 5.3 implies a good accuracy of the detailed model, which is considered acceptable for the purpose of dynamic average modeling methodology presented in the later sections.

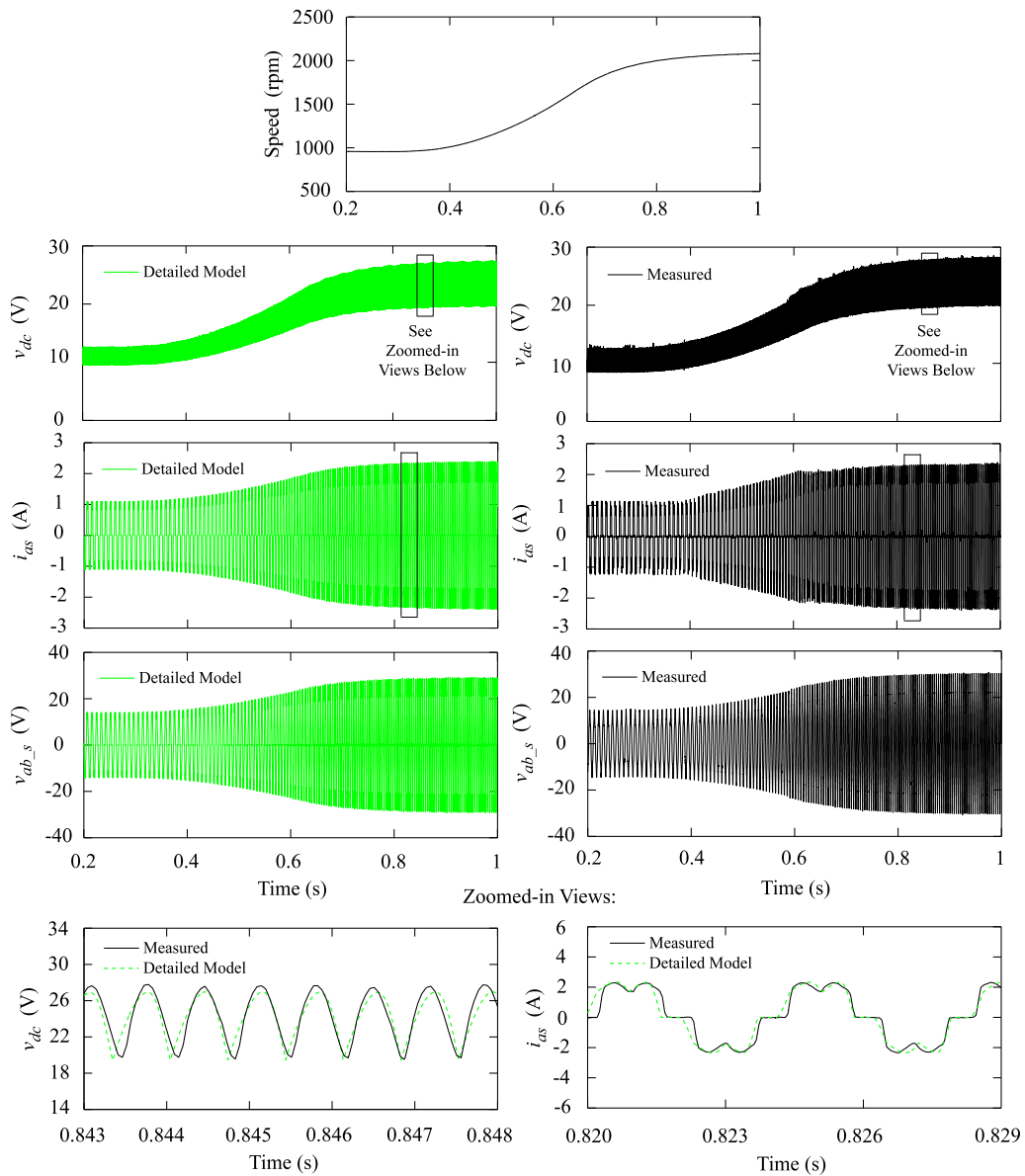


Figure 5.3 Measured and simulated detailed responses to speed increase observed in the dc and ac sides.

5.3.3 Battery Model

To complete the system depicted in Figure 5.1 with the energy storage, the following methodology was considered to model the battery. While the proposed methodology is independent of battery type, a commercial lead-acid battery for automotive application is considered in this paper with the details summarized in Appendix A.4. The battery is represented by its equivalent circuit as depicted in Figure 5.2. It is well understood that the battery open circuit terminal voltage, v_{oc} , and the equivalent internal resistance, r_b , vary significantly depending upon its state of charge [128]. A state-of-charge model is employed here, where v_{oc} and r_b are approximated by polynomial functions of the state of discharge. A similar battery representation has been used previously in the modeling of electric vehicles [129] and [130]. In [130], accurate results were obtained using fifth-degree polynomials

$$v_{oc} = \alpha_0 + \sum_{j=1}^5 \alpha_j (1-Q)^j, \quad (5.5)$$

$$r_b = \beta_0 + \sum_{j=1}^5 \beta_j (1-Q)^j, \quad (5.6)$$

where Q is the relative state of charge (SoC), and the coefficients α_j and β_j are extracted experimentally. The relative SoC is expressed as

$$Q = Q_{init} + \frac{1}{3600 \cdot Q_{max}} \int_0^t i_{bat}(\tau) d\tau, \quad (5.7)$$

where $i_{bat}(\tau)$ is the battery charging current, Q_{init} is the initial relative SoC, and Q_{max} is the battery capacity (Ah). According to (5.7) and Figure 5.2, the current drawn from the battery is simply $-i_{bat}$.

5.4 System Dynamic Average-Value Modeling

5.4.1 Alternator Model in Transformed qd Coordinates and Variables

The developed AVM employs the classical qd rotor reference frame to model the alternator in transformed coordinates and variables. The general theory of qd model of a six-phase machine with two sets of arbitrary shifted stator windings has been set forth in [125]. However, since in the detailed model developed in the previous section, the two sets of windings are aligned, the complexity of the model [125] significantly reduces. In particular, to obtain the transformation matrix for representing the variables in the so-called rotor reference frame, the general reference frame transformation matrix (2.7) is adopted with the angle set to the rotor angle θ_r :

$$\mathbf{K}_s = \frac{2}{3} \begin{bmatrix} \cos \theta_r & \cos\left(\theta_r - \frac{2\pi}{3}\right) & \cos\left(\theta_r + \frac{2\pi}{3}\right) \\ \sin \theta_r & \sin\left(\theta_r - \frac{2\pi}{3}\right) & \sin\left(\theta_r + \frac{2\pi}{3}\right) \\ \frac{1}{2} & \frac{1}{2} & \frac{1}{2} \end{bmatrix}. \quad (5.8)$$

The abc variables for each set of the three-phase windings are transferred into the rotor reference frame. Applying transformation (5.8) to (5.2)–(5.4) and algebraically manipulating the results, the final state model can be compactly expressed as follows:

$$\frac{d\psi_{qs}}{dt} = \omega_b \left(r_s i_{qs} - \frac{\omega_r}{\omega_b} \psi_{ds} + v_{qs} \right). \quad (5.9)$$

$$\frac{d\psi_{ds}}{dt} = \omega_b \left(r_s i_{ds} + \frac{\omega_r}{\omega_b} \psi_{qs} + v_{ds} \right). \quad (5.10)$$

$$\frac{d\psi_{q2s}}{dt} = \omega_b \left(r_c i_{q2s} - \frac{\omega_r}{\omega_b} \psi_{d2s} + v_{q2s} \right). \quad (5.11)$$

$$\frac{d\psi_{d2s}}{dt} = \omega_b \left(r_c i_{d2s} + \frac{\omega_r}{\omega_b} \psi_{q2s} + v_{d2s} \right). \quad (5.12)$$

$$\frac{d\psi'_{fd}}{dt} = \omega_b \left(-r'_{fd} i'_{fd} + v'_{fd} \right). \quad (5.13)$$

Here, ω_b is the base angular frequency, and ω_r denotes the rotor angular speed. Without loss of generality, in (5.9)-(5.13), the flux linkages (λ) and the inductances (L) have been replaced by flux linkages per second (ψ) and the reactances (x), respectively, according to the following relationships:

$$\psi = \omega_b \lambda, \quad x = \omega_b L. \quad (5.14)$$

The expressions for currents are derived from the flux linkage equations as:

$$i_{qs} = -\frac{(\psi_{qs} - \psi_{mq})}{x_{ls}}. \quad (5.15)$$

$$i_{ds} = -\frac{(\psi_{ds} - \psi_{md})}{x_{ls}}. \quad (5.16)$$

$$i_{q2s} = -\frac{(\psi_{q2s} - \psi_{mq})}{x_{l2s}}. \quad (5.17)$$

$$i_{d2s} = -\frac{(\psi_{d2s} - \psi_{md})}{x_{l2s}}. \quad (5.18)$$

$$i'_{fd} = \frac{(\psi'_{fd} - \psi_{md})}{x'_{lfd}}. \quad (5.19)$$

$$x_{aq} = \left(\frac{1}{x_{mq}} + \frac{1}{x_{ls}} + \frac{1}{x_{l2s}} \right)^{-1}. \quad (5.20)$$

$$x_{ad} = \left(\frac{1}{x_{md}} + \frac{1}{x_{ls}} + \frac{1}{x_{l2s}} + \frac{1}{x'_{lfd}} \right)^{-1}. \quad (5.21)$$

$$\psi_{mq} = x_{aq} \left(\frac{\psi_{qs}}{x_{ls}} + \frac{\psi_{q2s}}{x_{l2s}} \right). \quad (5.22)$$

$$\psi_{md} = x_{ad} \left(\frac{\psi_{ds}}{x_{ls}} + \frac{\psi_{d2s}}{x_{l2s}} + \frac{\psi'_{fd}}{x'_{lfd}} \right). \quad (5.23)$$

The torque equation in the rotor reference frame becomes

$$T_e = \left(\frac{3}{2} \right) \left(\frac{P}{2} \right) \left(\frac{1}{\omega_b} \right) \left[\psi_{ds} i_{qs} - \psi_{qs} i_{ds} + \psi_{d2s} i_{q2s} - \psi_{q2s} i_{d2s} \right]. \quad (5.24)$$

The model (5.9)–(5.24) is relatively simple and very convenient to implement. Finally, Figure 5.4 shows the equivalent circuit of the alternator model in qd coordinates. This final model is used for the developed average-value model.

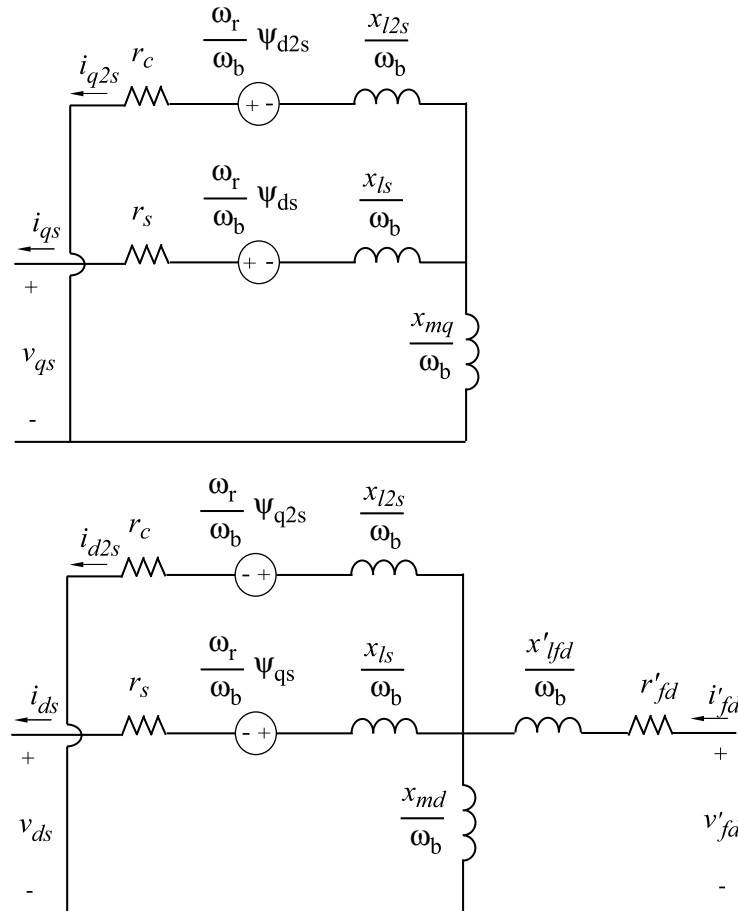


Figure 5.4 Equivalent circuits of the considered alternator model in q and d axes.

5.4.2 Average-Value Modeling of Non-Ideal Rectifier

The parametric approach discussed previously relates the averaged rectifier dc voltage and current, \bar{v}_{dc} and \bar{i}_{dc} , to transformed ac variables $\bar{\mathbf{v}}_{qds}^{rec}$ and $\bar{\mathbf{i}}_{qds}^{rec}$ through (2.24) and (2.25).

For the case of an ideal bridge which was assumed in [70], the first relationship is

$$\left\| \bar{\mathbf{v}}_{qds}^c \right\| = \alpha(\cdot) \bar{v}_{dc}, \quad (5.25)$$

where $\alpha(\cdot)$ is an algebraic function of the loading conditions. However, in low-voltage automotive applications, the losses due to the diode forward-voltage drop can be significant (this is simply because the voltage drop of the two conducting diodes in series, which may be on the order of 1.2 to 1.5V, will be more noticeable in proportion to the output voltage, here about 12V) and it is imperative to take such losses into account. In the case of detailed switching model, the non-ideal diode can be represented by a series connection of an ideal diode, a resistor and/or a constant voltage source in order to account the typically series losses in the bridge. The series losses (the total diode forward voltage drops) would cause an unknown equivalent drop in the output average voltage denoted by $\bar{v}_{eq, drp}$. Considering this

effect, (5.25) can be extended for the case of non-ideal diodes as

$$\left\| \bar{\mathbf{v}}_{qds}^c \right\| = \alpha(\cdot) (\bar{v}_{dc} - \bar{v}_{eq, drp}) = \alpha(\cdot) \left(1 - \frac{\bar{v}_{eq, drp}}{\bar{v}_{dc}} \right) \bar{v}_{dc} = \alpha'(\cdot) \bar{v}_{dc}, \quad (5.26)$$

Here, $\alpha'(\cdot)$ is a new parametric function which also includes the effect of diode voltage drops on the dc bus voltage.

The dc and ac side currents are related similarly. For the case of an ideal bridge:

$$\bar{i}_{dc} = \beta(\cdot) \left\| \bar{\mathbf{i}}_{qds}^c \right\|, \quad (5.27)$$

where $\beta(\cdot)$ is another parametric function of the loading conditions. If it is desired to extend the above equation to include the effects of shunt losses in the rectifier, the parametric

function $\beta(\cdot)$ should be modified to $\beta'(\cdot)$ according to the unknown equivalent shunt current $\bar{i}_{eq,sh}$ as:

$$\bar{i}_{dc} - \bar{i}_{eq,sh} = \beta(\cdot) \left\| \bar{\mathbf{i}}_{qds}^c \right\|, \quad (5.28)$$

$$\bar{i}_{dc} = \beta(\cdot) \left\| \bar{\mathbf{i}}_{qds}^c \right\| + \bar{i}_{eq,sh} = \beta(\cdot) \left(1 + \frac{\bar{i}_{eq,sh}}{\left\| \bar{\mathbf{i}}_{qds}^c \right\|} \right) \left\| \bar{\mathbf{i}}_{qds}^c \right\| = \beta'(\cdot) \left\| \bar{\mathbf{i}}_{qds}^c \right\|, \quad (5.29)$$

Although representing shunt losses may be important for high voltage applications (e.g. HVDC) where the snubbers and voltage balancing circuits cause additional losses, such losses are typically negligible in the low voltage rectifiers due to good insulation and small reverse current of the diodes. Therefore, (5.27) may be considered sufficient for the automotive system considered in this paper.

To complete the model, the angle between vectors $\bar{\mathbf{v}}_{qds}^c$ and $\bar{\mathbf{i}}_{qds}^c$ is expressed based on Figure 2.4, setting the arbitrary reference frame to rotor reference frame:

$$\phi(\cdot) = \arctan\left(\frac{\bar{i}_{ds}^r}{\bar{i}_{qs}^r}\right) - \delta = \arctan\left(\frac{\bar{i}_{ds}^r}{\bar{i}_{qs}^r}\right) - \arctan\left(\frac{\bar{v}_{ds}^r}{\bar{v}_{qs}^r}\right). \quad (5.30)$$

Instead of deriving analytical expressions for $\alpha'(\cdot)$, $\beta'(\cdot)$ and $\phi(\cdot)$, these functions can be extracted numerically from the detailed simulation. For compactness, these functions are expressed in terms of dynamic impedance of the rectifier switching cell defined as

$$z = \frac{\bar{v}_{dc}}{\left\| \bar{\mathbf{i}}_{qds}^c \right\|}. \quad (5.31)$$

A transient study is carried out in which the load resistance is slowly changed in a wide range from 0.1Ω to 100Ω . The numerical functions $\alpha'(\cdot)$, $\beta'(\cdot)$, and $\phi(\cdot)$ together with the impedance, z , are then calculated for each point using (5.26), (5.29), and (5.30). These functions are stored in look-up tables and used in the average-value model implementation.

Using the modified switching model with non-ideal diodes to extract the average-value model parameters, the effects of diode non-idealities and rectifier losses are automatically included into the numerically calculated parametric functions $\alpha'(\cdot)$, $\beta'(\cdot)$ and $\phi(\cdot)$.

To demonstrate the improvement achieved by including the rectifier losses, the parametric functions $\alpha'(\cdot)$, $\beta'(\cdot)$ and $\phi(\cdot)$ have been extracted for both ideal and non-ideal rectifier. The results for both cases are superimposed in Figure 5.5. As this figure demonstrates, the effect of forward voltage drop is more pronounced at heavy loads as the impedance z (or the output dc voltage) decreases. For completeness, the values of parametric functions are also given in Appendix A.4 for the non-ideal rectifier.

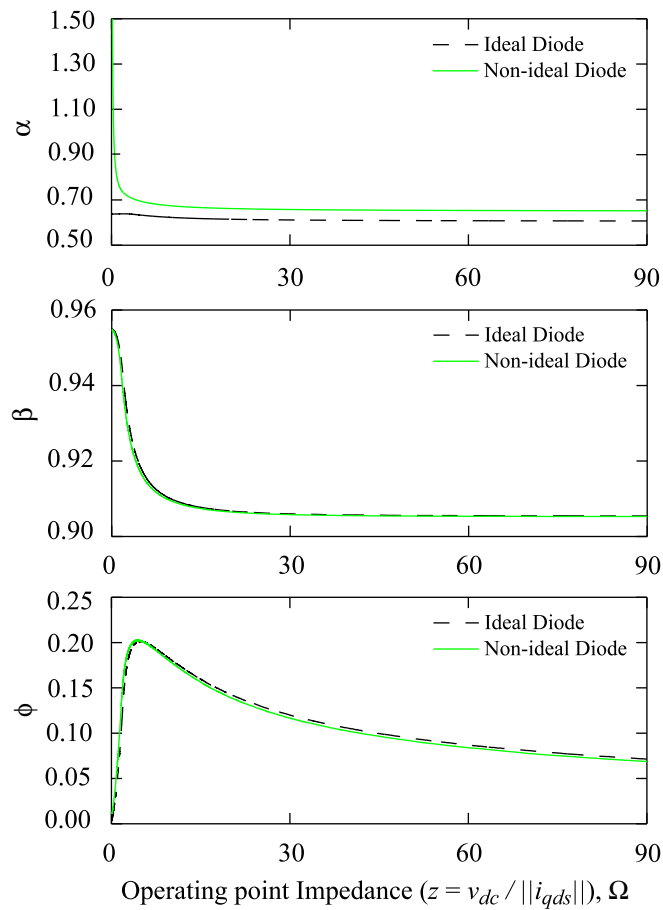


Figure 5.5 Parametric functions considering ideal and non-ideal rectifier diodes.

5.5 Case Studies

The new AVM developed in the previous section has been implemented in Matlab\Simulink [4] and verified in a number of studies presented here. The block diagram of the overall combined model of the vehicular system is depicted in Figure 5.6. This figure also shows the input and output variables of the corresponding subsystems. In the following study, it is assumed that the alternator field winding is supplied from a constant dc source of $v_{fd} = 6.4 V$. Similar to Section 5.2, a resistive load of $R_L = 11.5 \Omega$ is assumed to be directly connected to the dc bus. To verify the considered detailed and the average-value models, the same speed variation as in the studies of Figure 5.3 is assumed here. The corresponding simulation results are superimposed in Figure 5.7. It should be noted that this study has also been considered for verifying the detailed model with the experimental results presented in Figure 5.3. As seen in Figure 5.7, the transient responses predicted by the proposed average-value model precisely follow the averaged behavior of the detailed model (and measured waveforms from Figure 5.3) throughout the whole speed variation region.

In order to demonstrate the improvement achieved by the proposed average-value model with respect to the previously established AVM [70] that assumes an ideal/lossless rectifier, the results predicted by AVM [70] are also provided in Figure 5.7 (right plots). As seen in these plots, the AVM [70] overestimates the dc bus voltage and current because the bridge losses are not considered. The output (dc) power predicted by this model is also significantly higher. At the same time, the proposed AVM predicts non-zero rectifier losses (see Figure 5.7 bottom subplot) and remains in close agreement with the detailed model throughout the transient study.

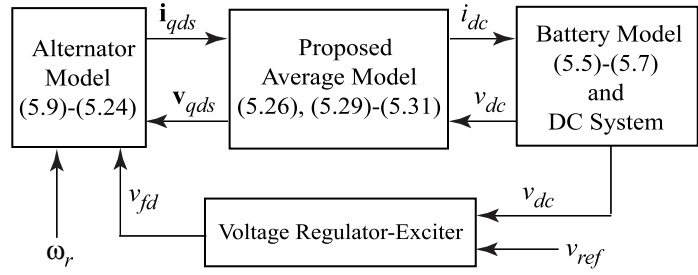


Figure 5.6 Block diagram of the overall combined model depicting subsystems and their inputs and outputs.

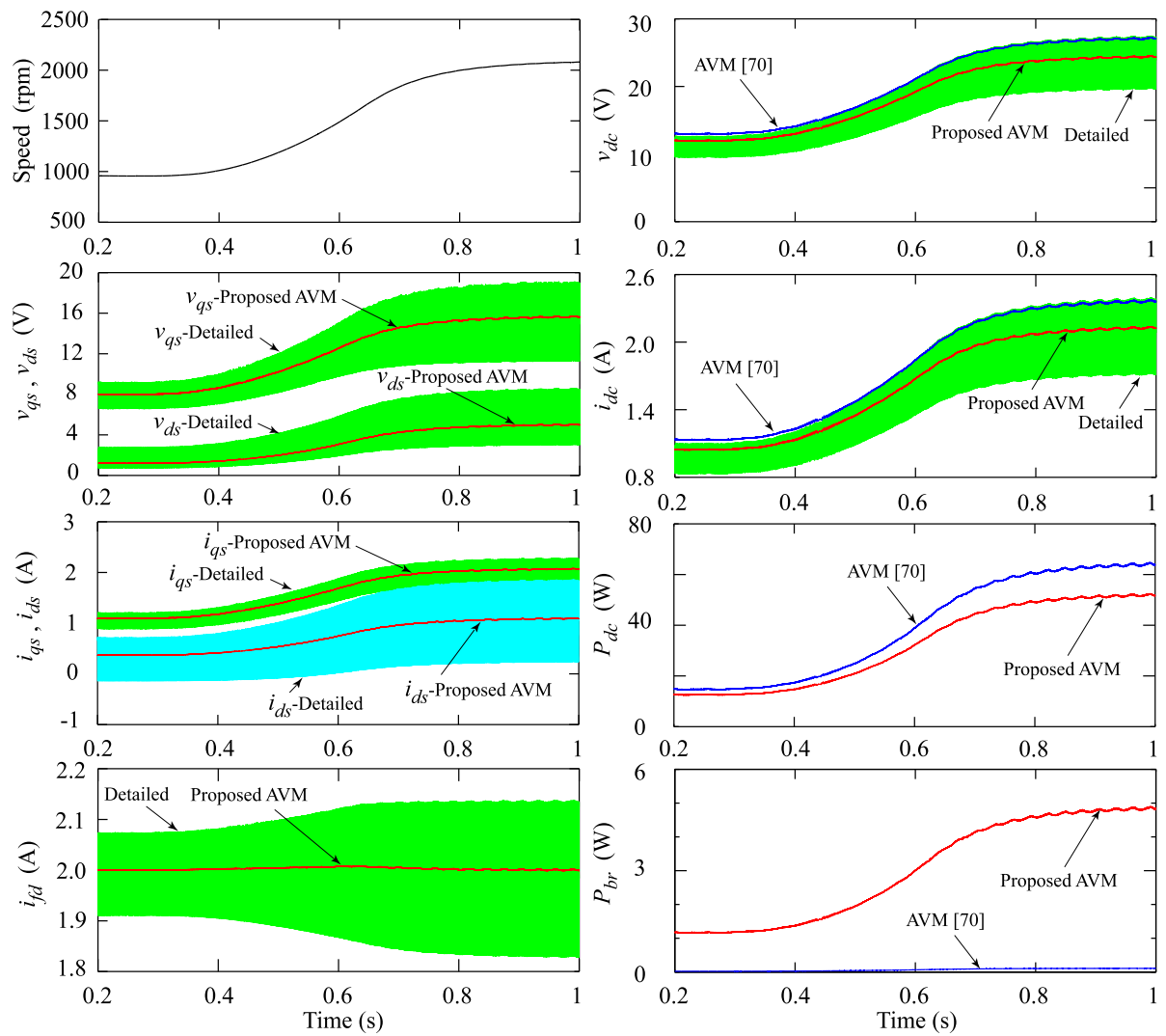


Figure 5.7 System response to the increase in alternator speed as predicted by the detailed and average-value models under fixed excitation.

Next, the voltage regulator-exciter is added to the system to regulate the dc bus voltage. The reference voltage, v_{ref} , is set to 14 Volts. The same speed increase of Figure 5.3 is considered here. Figure 5.8 shows the transient responses in excitation/field current and the dc bus voltage obtained by the detailed and the proposed average-value models as a result of the considered speed increase. As can be seen in Figure 5.8, the transient response of the closed loop alternator-rectifier system is predicted very well by the proposed AVM.

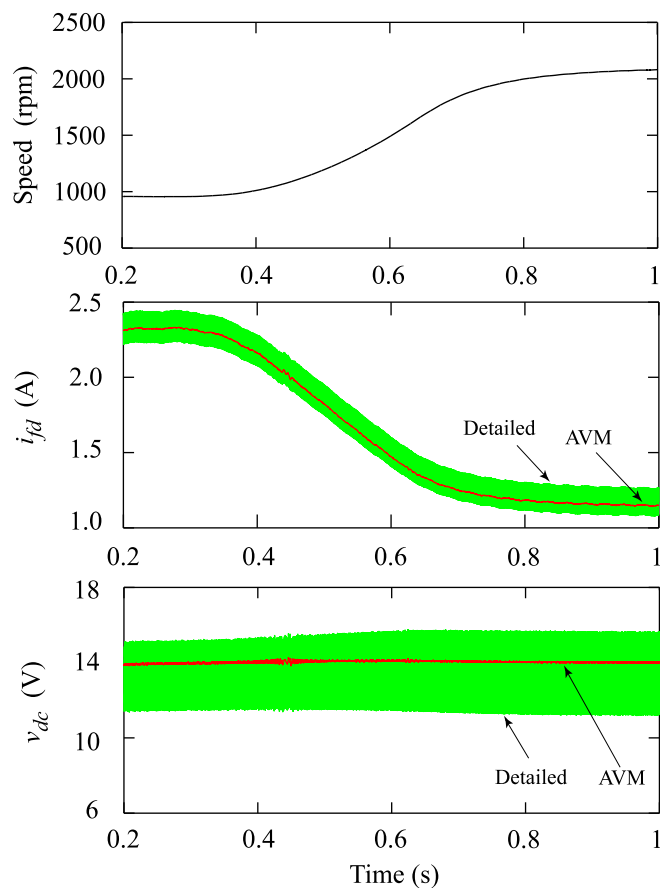


Figure 5.8 Input speed, excitation (field) current and the dc bus voltage predicted by the detailed and the average-value models when the system uses the voltage regulator-exciter.

In the next study, the battery is connected to the dc bus in parallel with a variable resistor that represents the equivalent electric loads in the vehicle. The reference voltage v_{ref} is set

to 13.55 V to maintain the desired charging current of 2.6A into the battery. The value of this current is adjustable and it will determine how fast the battery will charge during the driving of the vehicle. The battery is assumed to have initial SoC of 95%. The study carried out demonstrates the system dynamics during the engine acceleration. For this purpose, the alternator is accelerated from 950 rpm (i.e., the idle engine speed) to 4000 rpm. The corresponding voltage and current waveforms at the dc bus are illustrated in Figure 5.9, together with the battery current and the relative SoC in percent. Overall, an excellent match is observed between the system responses predicted by the average-value and the detailed models, apart from the switching ripple present in the detailed model.

To demonstrate the effects of various losses present in the system and the effectiveness of the proposed AVM in predicting the complete power conversion chain, the alternator input mechanical power, P_m , and the rectifier output dc power, P_{dc} , have also been plotted in Figure 5.9. For better clarity, in the right corner bottom plot, various losses in the system have been superimposed and compared. In this subplot, only the average model results are shown, whereas the detailed model responses are similar and omitted for clarity reason only.

As seen in Figure 5.9, the unique feature of the proposed average model is that it can predict the whole power conversion chain in the system equivalent to using the detailed model. As observed in this study, the amount of losses is significant and consistent with typical Lundell-Alternator-Rectifier systems previously described in the literature [115], [116]. This application also clearly demonstrates the need for inclusion of the losses in the system-level models. Note that even the diode bridge losses are significant since the current drawn from the dc bus can be quite high in such automotive systems.

The numerical efficiency of the proposed model is evaluated next. The computer studies were carried out using Matlab\Simulink software ran on a personal computer (PC) with a 2.4 MHz AMD 3800+ processor. To achieve accurate results with the detailed model, it was found that the variable-step solver ODE15s with a maximum allowable time step of 0.0001s

was needed. To obtain the results of Figure 5.9, the detailed simulation took 10.28s of CPU time requiring a total of 79,512 time steps. The AVM does not have switching and can execute with much larger time steps. With the maximum allowable time step of 0.01s, using the same solver settings, the AVM simulation took 0.14s of CPU time requiring only 1,645 time-steps. This demonstrates almost two orders of magnitude improvement in simulation speed for obtaining essentially identical system-level transient results.

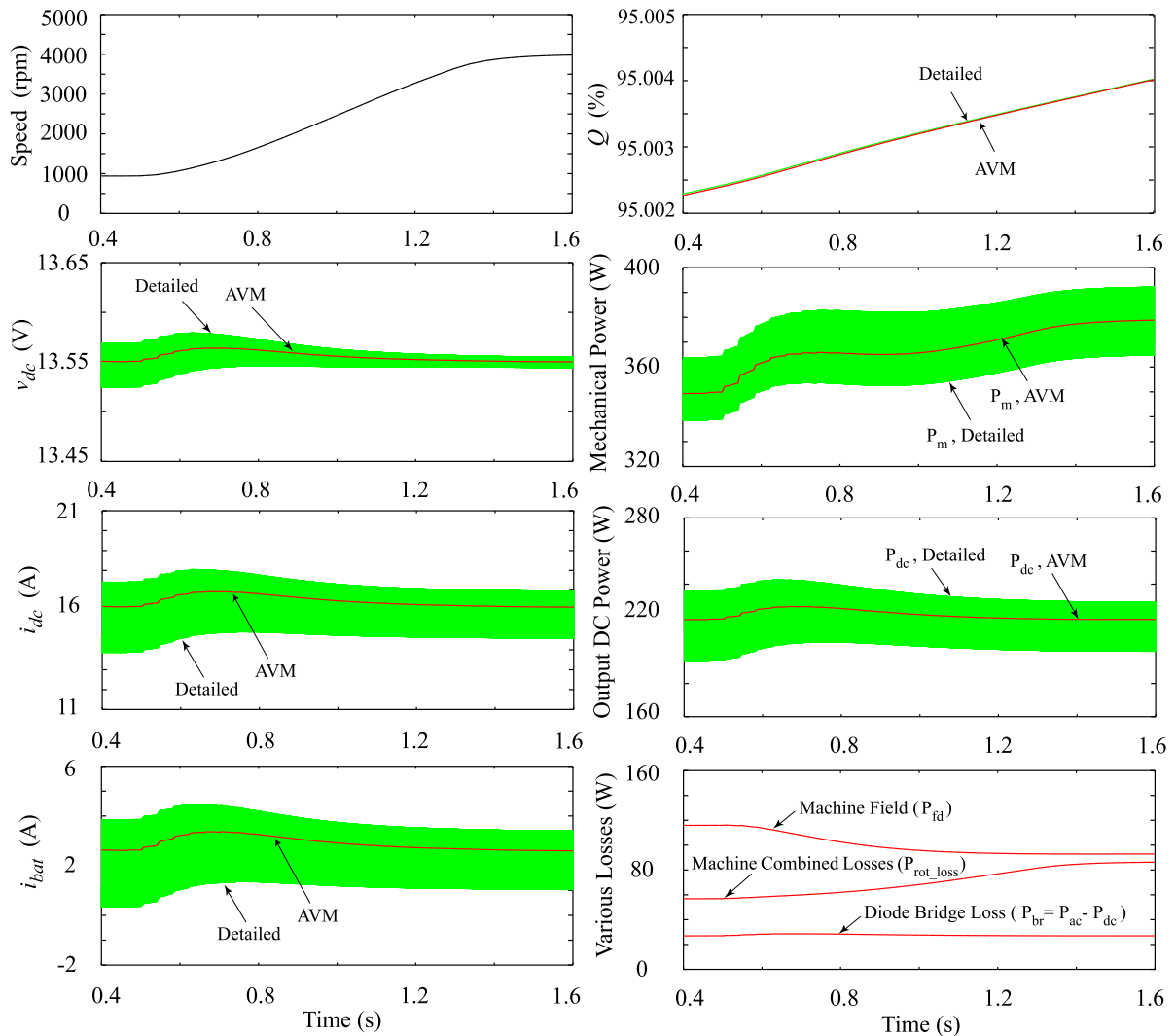


Figure 5.9 System response during the engine acceleration from 950 rpm to 4000 rpm predicted by the detailed and proposed average-value models.

Another very useful feature of the developed AVM is its application to the small-signal analysis of the considered system, which can be achieved very efficiently using numerical linearization (available in all state-variable-based simulation tools such as Simulink [4]). This type of analysis cannot be conveniently performed using the conventional detailed switching model. To demonstrate this feature, the control-to-output transfer function of the system, from the field (excitation) voltage to the dc bus output voltage, has also been extracted using both detailed and average models. Other system-level transfer functions (e.g., from the shaft speed to the output voltage, etc.) can also be similarly obtained by numerical linearization of the developed AVM. A small-signal analysis has been performed around an operating point corresponding to the engine speed of 1520 rpm and the output voltage of 13.55V. The small signal perturbation is then only injected in the field voltage and the speed is kept constant. Figure 5.10 shows the Bode diagrams of the resulting system transfer function. As this figure demonstrates, the average model predicts the small-signal characteristics of the system with a superior accuracy.

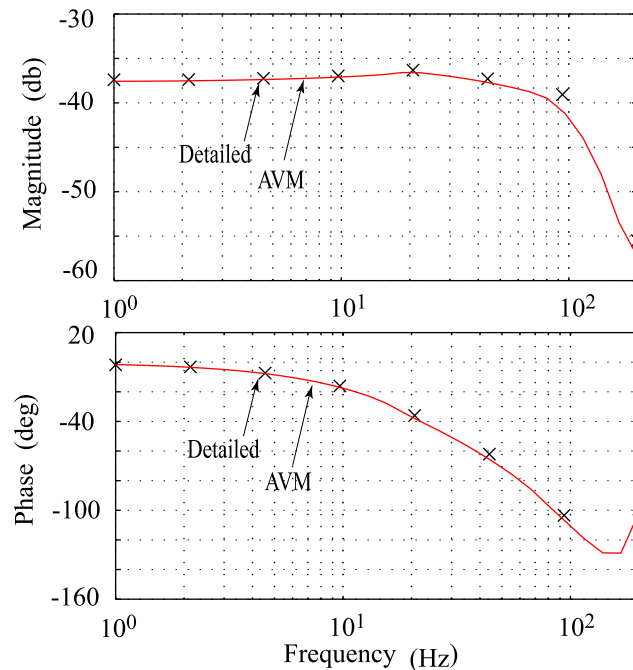


Figure 5.10 System transfer function from the field (excitation) voltage to the dc bus voltage predicted by the detailed and average-value models.

Chapter 6: Generalized Dynamic AVM for High-Pulse-Count Converters

6.1 Introduction

As discussed in Chapter 1, several AVMs for converter systems with the number of pulses more than six have been developed in the literature, most existing models are derived for a specific topology and have a limited range of accuracy. The objective of this Chapter is to develop a methodology that could be applied to any network- or rotating-machine-fed high-pulse-count converter system.

6.2 High-Pulse-Count Converter System Structures

The general structure of a high-pulse-count converter system, wherein the number of phases is considered to be a multiple of three is depicted in Figure 6.1. The most-commonly-used numbers of pulses are 12, 18, and 24, corresponding to 6-, 9-, and 12- phase ac subsystems, respectively. Depending on the application, the system may be fed from a three-phase power network, represented by its Thevenin equivalent, as in Case I, or a single rotating machine (generator) as in Cases II and III. In the first two cases, the three-phase voltages at the input are transformed into multi-phase voltages at the output, using a 3-to-n-phase transformer. Alternatively, in Case III, these multi-phase voltages are directly produced by means of a multi-phase generator. In any case, the resulting multi-phase voltages are fed into several bridge rectifiers that are interconnected at their dc sides through

an optional Inter-Phase Transformer (IPT) followed by an optional dc filter network. The bridges, in general, maybe interconnected in various configurations, i.e., series, parallel, or a series/parallel combination. The overall system ultimately feeds a dc system (load) as depicted in Figure 6.1.

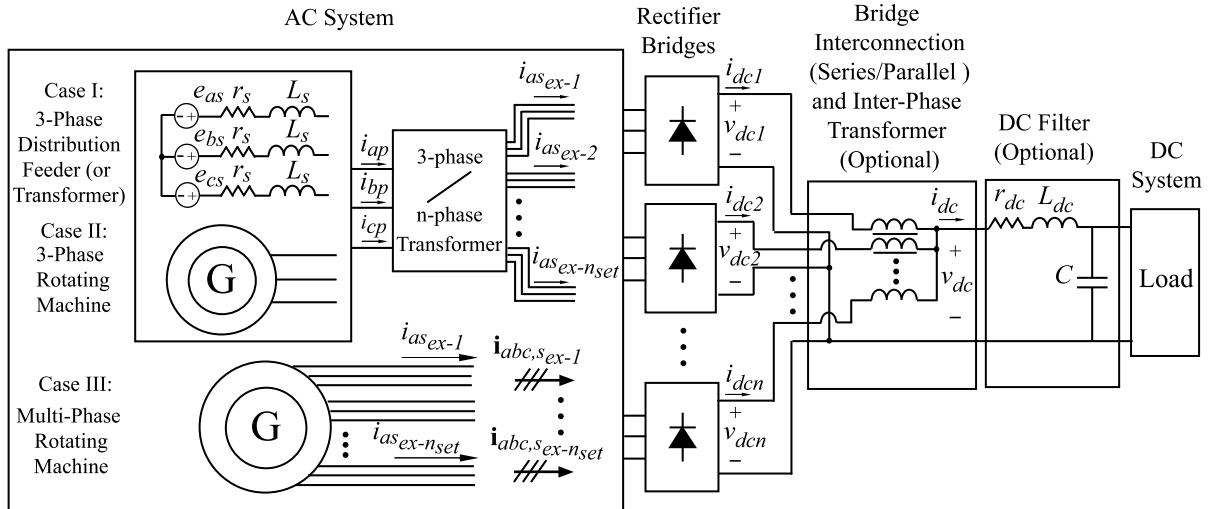


Figure 6.1 Classification of high-pulse-count rectifier systems.

The particular emphasis of this Chapter is on modeling of the multi-phase transformer associated with the first two cases. In the ac subsystem of Figure 6.1, the secondary voltages are divided into several sets of three-phase voltages that are supposed to be equally shifted in phase. In the case of a 6-phase (12-pulse) converter, the two sets of 3-phase voltages at the output are typically required to be shifted by 30 electrical degrees. In Cases I and II in Figure 6.1, such voltages may then be readily obtained using a wye-delta connection on the secondary side of a conventional 3-phase transformer with two sets of secondary windings. The displacement angle of 60 degrees, instead of 30 degrees, is also sometimes considered in 12-pulse converter systems, especially for machine-fed systems [74], i.e., Case III in Figure 6.1.

In converters with higher numbers of pulses than 12, the output 3-phase sets are typically shifted according to the following:

$$\theta_{disp} = \frac{2}{p} 360^\circ = \frac{1}{n_{ph}} 360^\circ = \frac{1}{n_{set}} 120^\circ, \quad (6.1)$$

where p , n_{ph} , and n_{set} are used to denote the number of pulses, phases, and three-phase sets, respectively. In general, the desired shift is obtained using the appropriate interconnection of the windings at the secondary side of a 3-phase transformer with several segments of secondary windings. The terminology used throughout this thesis is that, each of the three-phase groups of windings on the secondary side of such transformer is denoted by “segment” because these windings are interconnected in order to produce the final “sets” of extended secondary windings. However, one of these final sets of extended secondary windings is typically composed of only one base segment. In the simplest and exceptional case of 6-phase transformer discussed above, both final sets are each composed of only one segment of the secondary windings; hence no distinction has to be made between the sets and segments therein. In general, however, the number of segments n_{seg} is equal to or greater than the number of final three-phase sets n_{set} .

For the purpose of discussions, an example 400Hz aircraft power system with the 9-phase (18-pulse) rectifier topology shown in Figure 6.2 and the parameters summarized in Appendix B is considered in this thesis. The presented analyzes, however, can be readily extended to any multiple of three phases. As seen in Figure 6.2, a three-phase source feeds the 3-to-9-phase transformer which in turn is connected to three bridges at the secondary side. The displacement angle between each set of voltages at the secondary side of the transformer is 40 electrical degrees as dictated by (6.1). Without loss of generality, herein the bridges are connected in parallel without an inter-phase transformer and feed the dc system

through an optional capacitor as the dc filter. The dc load is represented by its equivalent resistance denoted by R_L .

Several configurations of the magnetic core and connections may be considered for the 3-to-9-phase transformer of Figure 6.2 [131], [78]. For example, in the configuration depicted in Figure 6.3 [131], the transformer has a conventional three-leg structure with a primary set of windings and five secondary segments of windings. The primary and secondary voltages corresponding to the configuration of Figure 6.3 are illustrated in Figure 6.4 (top diagrams) with the three sets of evenly shifted secondary voltages shown separately (bottom diagrams). In this figure, it is illustrated how the winding connections on the secondary side result in the shifted sets of voltages. According to these diagrams, in order for the secondary voltages to be equal in magnitude and evenly shifted in phase by 40 degrees, it is necessary that [131]:

$$n_{s2} = n_{s5} = n_{s1} \frac{\sin 40^\circ}{\sin 120^\circ} = 0.742n_{s1}. \quad (6.2)$$

$$n_{s3} = n_{s4} = n_{s1} \frac{\sin 20^\circ}{\sin 120^\circ} = 0.395n_{s1}. \quad (6.3)$$

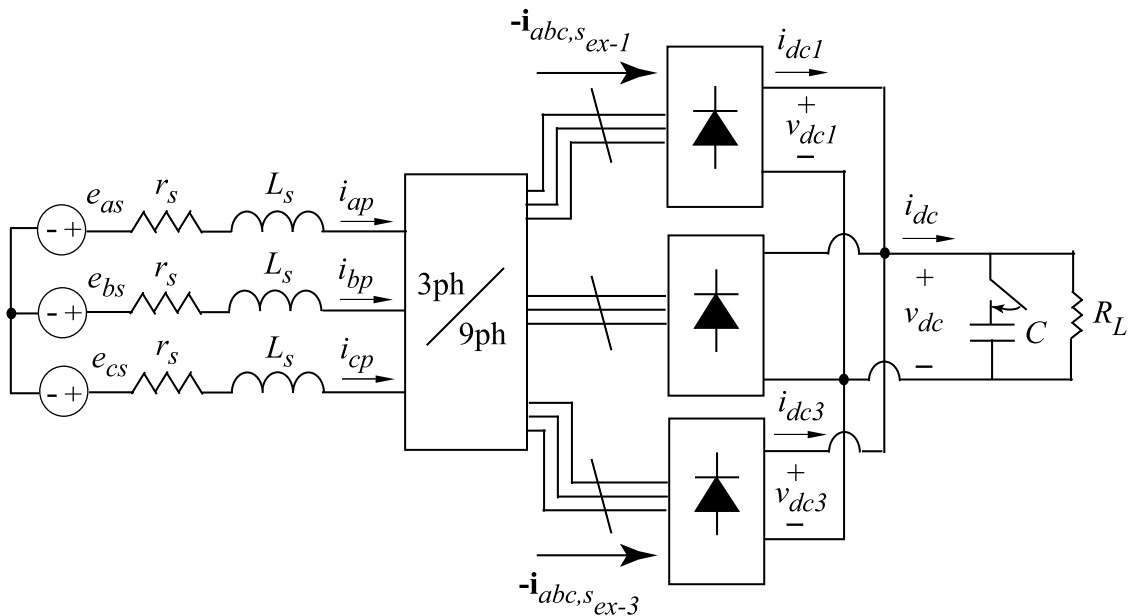


Figure 6.2 Typical 9-phase (18-pulse) rectifier example system topology considered in this Chapter.

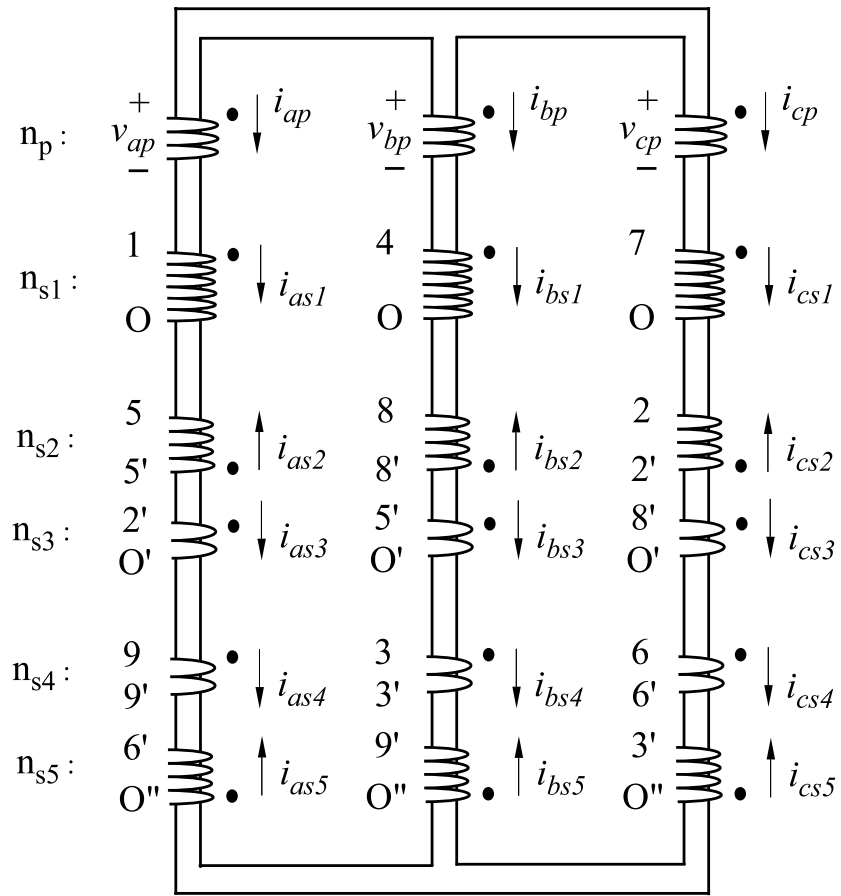


Figure 6.3 Typical 3- to 9-phase transformer structure for the 18-pulse rectifier example system.

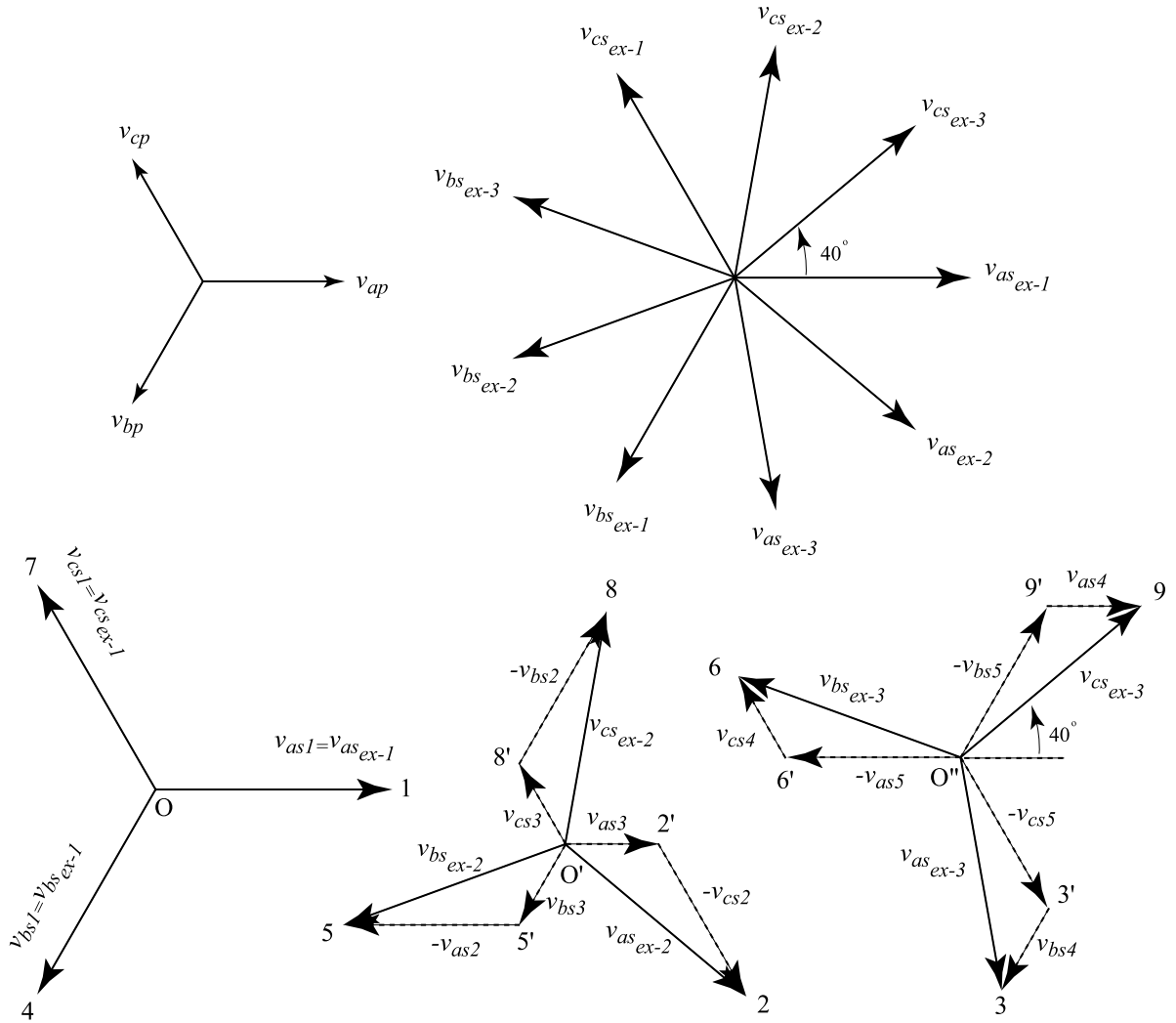


Figure 6.4 Phasor diagrams of the primary and secondary voltages for the 3-to-9-phase transformer of Figure 6.3.

6.3 Multi-Phase Transformer Modeling

6.3.1 Original Interconnected Transformer Model

Let us consider a general case of 3-to- n -phase transformer with a three-leg structure, similar to that depicted in Figure 6.3. The transformer is typically composed of a primary set of windings, specified by the subscript p , and n_{seg} secondary segments of windings denoted by the subscript s_k , $k = 1, 2, \dots, n_{seg}$. Each leg of the transformer corresponds to one

of the three phases a , b , and c , and the three windings within each of the three-phase primary set/secondary segment are assumed identical. This transformer may then be mathematically described by the voltage and flux linkage equations corresponding to the primary set and each of the secondary segments of windings. These equations can be written in a compact matrix form as

$$\mathbf{v}_{abc,p} = \mathbf{R}_p \mathbf{i}_{abc,p} + \frac{d}{dt} \boldsymbol{\lambda}_{abc,p}, \quad (6.4)$$

$$\boldsymbol{\lambda}_{abc,p} = \mathbf{L}_{pp} \mathbf{i}_{abc,p} + \sum_{k=1}^{n_{seg}} \mathbf{L}_{ps_k} \mathbf{i}_{abc,s_k}, \quad (6.5)$$

$$\mathbf{v}_{abc,s_k} = \mathbf{R}_{s_k} \mathbf{i}_{abc,s_k} + \frac{d}{dt} \boldsymbol{\lambda}_{abc,s_k}, \quad k = 1, 2, \dots, n_{seg}, \quad (6.6)$$

$$\boldsymbol{\lambda}_{abc,s_k} = \mathbf{L}_{s_k p} \mathbf{i}_{abc,p} + \sum_{i=1}^{n_{seg}} \mathbf{L}_{s_k s_i} \mathbf{i}_{abc,s_i}, \quad k = 1, 2, \dots, n_{seg}, \quad (6.7)$$

In the above equations, $\mathbf{v}_{abc,x}$, $\mathbf{i}_{abc,x}$, and $\boldsymbol{\lambda}_{abc,x}$ are the vectors including the three-phase voltages, currents, and flux-linkages, respectively, corresponding to the winding x which could be the primary set (p) or any of the secondary segments (s_k). The matrix \mathbf{R}_x is a diagonal matrix including the resistance r_x of the same winding set/segment x . Also, \mathbf{L}_{xx} is an inductance matrix including the values of self- and mutual- inductances among the windings within the same set/segment x , while the matrix \mathbf{L}_{xy} contains the values of mutual inductances between the windings from two different set/segments x and y which can each be the primary set (p) or a secondary segment (s_k).

Due to symmetric properties of the transformers [51], [49]

$$\mathbf{L}_{yx} = (\mathbf{L}_{xy})^T, \quad x, y = p, s_k. \quad (6.8)$$

Some secondary segments may also be chosen to be identical to each other, in terms of the number of turns, etc., as it is the case in the 3-to-9-phase transformer of Figure 6.3. In such cases, a few of the above inductance matrices would be identical.

In order for the transformer detailed model to be implemented according to (6.4)-(6.8), all necessary resistances and inductances have to be established. For each of the windings in any set/segment, the self-inductance includes the magnetizing and leakage parts. The mutual inductance between two arbitrary windings from any set/segment would always include a magnetizing term. However, if these windings are on the same leg of the transformer, an additional leakage term may also be included [49].

Determining the inductance values for the transformer parameters is generally outside the scope of this thesis. These values may be established according to the geometry and magnetic characteristics of the core as well as the number of turns per each winding, and in some cases, the values of all self and mutual inductances are readily available from design [49], [79]. Alternatively, the short-circuit impedances may be extracted from the hardware prototype by performing tests, and the representation of the transformer in terms of resistances and inductances may then be conveniently obtained according to the step-by-step procedure provided in Chapter 6 of [8].

To facilitate the derivation of the transformer models for the purpose of this thesis, several fundamental parameters are defined upon which the inductance and resistance values may be established in a systematic way. Without loss of generality, the self inductance of b -phase primary winding (wound on the middle leg) may be expressed as

$$L_{pp,b} = L_{m,b} + L_{lp,b}, \quad (6.9)$$

where $L_{lp,b}$ and $L_{m,b}$ denote the leakage and magnetizing terms. Some degree of symmetry is always present in the geometry of the core. In the three-leg structure depicted in Figure 6.3, symmetry is present around the middle leg of the transformer (corresponding to phase b). Such symmetry is typically present in all cases, even when the core structure has more

legs, such as the five leg structure considered in [49]. Incorporating this symmetry, for the primary windings on the side legs, phases a and c , the self inductance is equal, and may be expressed in a similar way to (6.9) as

$$L_{pp,a} = L_{m,a} + L_{lp,a}. \quad (6.10)$$

The mutual inductance between the middle-leg primary winding and any side-leg primary windings is denoted by L_{apbp} , and the mutual inductance between the two side-leg primary windings is denoted by L_{apcp} . These values may be readily established as a fraction of $L_{m,b}$ and $L_{m,a}$. For instance, in the three-leg structure of Figure 6.3, clearly we have:

$$L_{apbp} = -\xi_1 L_{m,b}, \quad (6.11)$$

$$L_{apcp} = -\xi_2 L_{m,a}, \quad (6.12)$$

where typically $\xi_1 = 0.5$ but $\xi_2 < 0.5$, since the magnetizing flux in the middle-leg winding is equally divided between the two side-leg windings according to the core symmetry, whereas the magnetizing flux in a side winding sees a lower reluctance for closing through the middle leg compared to the farther side leg.

Using the above fundamental parameters, other inductances may be established using the appropriate turn ratio. In particular, the self inductance of any other winding i may then be expressed as

$$L_{ii,a} = \left(\frac{n_i}{n_p} \right)^2 L_{m,a} + L_{li,a}, \quad (6.13)$$

$$L_{ii,b} = \left(\frac{n_i}{n_p} \right)^2 L_{m,b} + L_{li,b}, \quad (6.14)$$

for the cases when the winding is on the side and middle legs, respectively. The leakage terms in these cases are represented by $L_{li,a}$ and $L_{li,b}$, respectively. Also, n_i and n_p denote the number of turns in the winding i and primary winding, respectively.

Next, in order to establish the mutual inductance values, we consider the mutual inductances between the primary windings (p) and the first segment of the secondary windings (s_1). The values for this type of mutual inductance are denoted by L_{bpbs} and L_{apas} for the cases that both windings are on the middle leg, and on one of the side legs, respectively. The magnetizing parts of these inductances may be readily written in terms of the turn ratio and the primary magnetizing values defined above. However, these inductances also include a leakage term which, in general, is not equal to the leakage of the primary windings since a fraction of the leakage flux solely links an individual winding. Adopting this concept, the mutual inductance between any two windings i and j , in general, has to be written for four cases: *i*) both windings are on the middle leg, *ii*) both windings are on one of the side legs, *iii*) the two windings are each on one side leg, and finally, *iv*) only one of these windings is on the middle leg. Mathematically, for each case we have:

$$L_{ij,bb} = L_{ji,bb} = \frac{n_i n_j}{n_p^2} (L_{m,b} + \xi_3 L_{lp,b}), \quad (6.15)$$

$$L_{ij,aa} = L_{ji,aa} = \frac{n_i n_j}{n_p^2} (L_{m,a} + \xi_4 L_{lp,a}), \quad (6.16)$$

$$L_{ij,ac} = L_{ji,ac} = \frac{n_i n_j}{n_p^2} L_{apcp} = \frac{n_i n_j}{n_p^2} (-\xi_2 L_{m,a}), \quad (6.17)$$

$$L_{ij,ab} = L_{ji,ab} = \frac{n_i n_j}{n_p^2} L_{apbp} = \frac{n_i n_j}{n_p^2} (-\xi_1 L_{m,b}), \quad (6.18)$$

where the coefficients ξ_3 and ξ_4 determine the fraction of the leakage flux linking both windings. Also, (6.12) and (6.11) have been employed for obtaining the last terms in (6.17) and (6.18).

Finally, to establish the winding resistances, the primary winding resistance is defined by r_p . Typically, the resistance of any other winding i is then expressed using the turn ratio as:

$$r_i = \left(\frac{n_i}{n_p} \right)^2 r_p. \quad (6.19)$$

If the number of turns for all windings is known, and the values of the fundamental parameters $L_{m,a}$, $L_{m,b}$, $L_{lp,a}$, $L_{lp,b}$ as well as the coefficients ξ_1 through ξ_4 are specified, all the self and mutual inductances as well as resistance values may be readily established using (6.13)-(6.19), and the transformer model (6.4)-(6.7) can be constructed.

Once the transformer model is established, the next challenge in implementation is the wiring of the transformer at the secondary side. Without loss of generality, we assume that the primary of the transformer is Y-connected. Also, as shown in the case of 9-phase transformer in Figure 6.3, one of the secondary winding segments is typically Y-connected. As a result, the voltages and currents of this segment and those of the primary winding set will be in phase. This segment, s_1 , forms the first set of the final extended secondary windings and its three-phase set of voltages is hence chosen as the reference. For a typical 3-to- n -phase transformer, the $(n_{seg} - 1)$ remaining segments of the secondary windings, are interconnected in order to form the $(n_{set} - 1)$ remaining sets of final extended secondary windings responsible for producing $(n_{set} - 1)$ sets of three-phase voltages that are all equal in magnitude but evenly shifted in phase with respect to the reference set produced by s_1 . Various configurations may be used to achieve such a goal depending on a particular application [131], [78]. Developing such configurations is outside the scope of this research. Regardless, all configurations, if applied correctly, would lead to similar results in terms of producing the above-mentioned sets of voltages.

The above transformer model includes the details of the original interconnected windings of the real transformer and is hence called the original interconnected transformer model. This model is expected to provide sufficient accuracy in most practical cases where the core losses and saturation are not significant. However, the high number of windings as well as

the complicated interconnection among the secondary segments makes this model challenging to implement as well as numerically inefficient. Moreover, this model as is, cannot be conveniently transformed into $qd0$ equivalent circuit for use in the dynamic average model of the system. The ultimate goal of the next sections is to develop a simplified model based on the above detailed representation without loss of generality and accuracy.

It should also be noted that, since typically one of the final extended secondary sets is composed of only one secondary segment, while the other sets include a series connection of more than one segment, in the real transformer, the values of leakage inductance and resistance are not equal among the final extended secondary sets of windings. In practice, this will introduce more asymmetry in the performance of transformer, in addition to the asymmetry imposed by the core geometry. The transformer model developed above, however, is quite general, and can include all these effects.

6.3.2 Analytically-Derived Equivalent Compacted Transformer Model

In order to facilitate the implementation and increase the numerical efficiency of the model, several secondary segment currents may be analytically expressed in terms of other currents, as dictated by the topological structure of the transformer. Thereafter, replacing these equations, the new parameters may be calculated analytically for each extended secondary set of windings. This step results in a simpler model that is easier to implement as well as numerically more efficient, because the interconnected wiring at the secondary side is essentially removed, and the number of windings at the secondary is reduced to the number of sets multiplied by three. Such an approach has been adopted in [49] to simplify a transformer model that produces 12-phase voltages for a 24-pulse converter. The approach significantly depends on a particular configuration of the transformer secondary wiring, and is challenging to generalize. It is, however, beneficial in significantly simplifying the model while completely preserving the generality and accuracy of the model.

To demonstrate this analytically-derived equivalent model, let us consider the example system of 18-pulse converter (Figure 6.2) with the transformer structure of Figure 6.3. The primary winding p and the secondary segments s_1 through s_5 are numbered from top to bottom. According to the topology dictated in Figure 6.3 as indicated by the numberings at the winding ends, we have:

$$i_{as_3} = -i_{cs_2}, \quad (6.20)$$

$$i_{bs_3} = -i_{as_2}, \quad (6.21)$$

$$i_{cs_3} = -i_{bs_2}, \quad (6.22)$$

$$i_{as_5} = -i_{cs_4}, \quad (6.23)$$

$$i_{bs_5} = -i_{as_4}, \quad (6.24)$$

$$i_{cs_5} = -i_{bs_4}, \quad (6.25)$$

The above equations may be written in the following matrix form:

$$\mathbf{i}_{abc,s_3} = \mathbf{T} \mathbf{i}_{abc,s_2}, \quad (6.26)$$

$$\mathbf{i}_{abc,s_5} = \mathbf{T} \mathbf{i}_{abc,s_4}, \quad (6.27)$$

wherein the mapping matrix \mathbf{T} has been introduced as

$$\mathbf{T} = \begin{bmatrix} 0 & 0 & -1 \\ -1 & 0 & 0 \\ 0 & -1 & 0 \end{bmatrix}. \quad (6.28)$$

Next, we consider the voltages across the final extended secondary sets, noting that the first secondary set is directly produced by the s_1 segment. The notation used for the final extended secondary sets is s_{ex-k} , $k=1,2,\dots,n_{set}$. It is clear that, for the example system, n_{seg} and n_{set} are equal to five and three, respectively. According to the topology illustrated in Figure 6.3, we have:

$$v_{as_{ex-2}} = v_{as_3} - v_{cs_2}, \quad (6.29)$$

$$v_{bs_{ex-2}} = v_{bs_3} - v_{as_2}, \quad (6.30)$$

$$v_{cs_{ex-2}} = v_{cs_3} - v_{bs_2}, \quad (6.31)$$

$$v_{as_{ex-3}} = v_{bs_4} - v_{cs_5}, \quad (6.32)$$

$$v_{bs_{ex-3}} = v_{cs_4} - v_{as_5}, \quad (6.33)$$

$$v_{cs_{ex-3}} = v_{as_4} - v_{bs_5}. \quad (6.34)$$

In matrix form, we may write:

$$\mathbf{v}_{abc,s_{ex-1}} = \mathbf{v}_{abc,s_1}, \quad (6.35)$$

$$\mathbf{v}_{abc,s_{ex-2}} = \mathbf{v}_{abc,s_3} + \mathbf{T} \mathbf{v}_{abc,s_2}, \quad (6.36)$$

$$\mathbf{v}_{abc,s_{ex-3}} = \mathbf{T} \mathbf{v}_{abc,s_5} - \mathbf{T}^{-1} \mathbf{v}_{abc,s_4}. \quad (6.37)$$

In the above equation, the inverse of the mapping matrix \mathbf{T} can be written as:

$$\mathbf{T}^{-1} = \begin{bmatrix} 0 & -1 & 0 \\ 0 & 0 & -1 \\ -1 & 0 & 0 \end{bmatrix}. \quad (6.38)$$

It should be noticed that $\mathbf{T}^{-1} = \mathbf{T}^T$.

Considering the currents in the extended secondary windings:

$$\mathbf{i}_{abc,s_{ex-1}} = \mathbf{i}_{abc,s_1}, \quad (6.39)$$

$$\mathbf{i}_{abc,s_{ex-2}} = \mathbf{i}_{abc,s_3}, \quad (6.40)$$

$$\mathbf{i}_{abc,s_{ex-3}} = -\mathbf{T}^{-1} \mathbf{i}_{abc,s_4}. \quad (6.41)$$

Rearranging terms in (6.26), (6.27), (6.39)-(6.41), all secondary segment currents may be written in terms of the extended secondary set currents:

$$\mathbf{i}_{abc,s_1} = \mathbf{i}_{abc,s_{ex-1}}, \quad (6.42)$$

$$\mathbf{i}_{abc,s_2} = \mathbf{T}^{-1} \mathbf{i}_{abc,s_{ex-2}}, \quad (6.43)$$

$$\mathbf{i}_{abc,s_3} = \mathbf{i}_{abc,s_{ex-2}}, \quad (6.44)$$

$$\mathbf{i}_{abc,s_4} = -\mathbf{T} \mathbf{i}_{abc,s_{ex-3}}, \quad (6.45)$$

$$\mathbf{i}_{abc,s_5} = \mathbf{T}^{-1} \mathbf{i}_{abc,s_{ex-3}}. \quad (6.46)$$

In the last equation, the following equation has been employed to simplify the expression:

$$-\mathbf{T}^2 = \mathbf{T}^{-1}. \quad (6.47)$$

The above identity can be proven using (6.28) and (6.38).

Next, (6.42)-(6.46) are substituted into (6.4)-(6.7), and the resulting equations are substituted into (6.35)-(6.37). This results in the following model:

$$\mathbf{v}_{abc,p} = \mathbf{R}_p \mathbf{i}_{abc,p} + \frac{d}{dt} \boldsymbol{\lambda}_{abc,p}, \quad (6.48)$$

$$\boldsymbol{\lambda}_{abc,p} = \mathbf{L}_{pp} \mathbf{i}_{abc,p} + \sum_{k=1}^{n_{set}} \mathbf{L}_{ps_{ex-k}} \mathbf{i}_{abc,s_{ex-k}}, \quad (6.49)$$

$$\mathbf{v}_{abc,s_{ex-k}} = \mathbf{R}_{s_{ex-k}} \mathbf{i}_{abc,s_{ex-k}} + \frac{d}{dt} \boldsymbol{\lambda}_{abc,s_{ex-k}}, \quad k = 1, 2, \dots, n_{set}, \quad (6.50)$$

$$\boldsymbol{\lambda}_{abc,s_{ex-k}} = \mathbf{L}_{s_{ex-k}p} \mathbf{i}_{abc,p} + \sum_{i=1}^{n_{set}} \mathbf{L}_{s_{ex-k}s_{ex-i}} \mathbf{i}_{abc,s_{ex-i}}, \quad k = 1, 2, \dots, n_{set}. \quad (6.51)$$

In general, the new inductance and resistance matrices may be expressed in terms of the original model (6.4)-(6.7). For the example system considered here, after extensive analytical work, these matrices are written as

$$\mathbf{R}_{s_{ex-1}} = \mathbf{R}_{s_1}, \quad (6.52)$$

$$\mathbf{R}_{s_{ex-2}} = \mathbf{R}_{s_2} + \mathbf{R}_{s_4}, \quad (6.53)$$

$$\mathbf{R}_{s_{ex-3}} = \mathbf{R}_{s_2} + \mathbf{R}_{s_4}, \quad (6.54)$$

$$\mathbf{L}_{s_{ex-1}} = \mathbf{L}_{s_1}, \quad (6.55)$$

$$\mathbf{L}_{s_{ex-2}} = \mathbf{T} \mathbf{L}_{s_2 s_2} \mathbf{T}^{-1} + \mathbf{L}_{s_4 s_4} + \mathbf{T} \mathbf{L}_{s_2 s_4} + \mathbf{L}_{s_2 s_4} \mathbf{T}^{-1}, \quad (6.56)$$

$$\mathbf{L}_{s_{ex-3}} = \mathbf{T} \mathbf{L}_{s_2 s_2} \mathbf{T}^{-1} + \mathbf{T}^{-1} \mathbf{L}_{s_4 s_4} \mathbf{T} - \mathbf{T} \mathbf{L}_{s_2 s_4} \mathbf{T} - \mathbf{T}^{-1} \mathbf{L}_{s_2 s_4} \mathbf{T}^{-1}, \quad (6.57)$$

$$\mathbf{L}_{ps_{ex-1}} = \mathbf{L}_{s_{ex-1} p} = \mathbf{L}_{ps_1}, \quad (6.58)$$

$$\mathbf{L}_{ps_{ex-2}} = \left(\mathbf{L}_{s_{ex-2} p} \right)^T = \mathbf{L}_{ps_2} \mathbf{T}^{-1} + \mathbf{L}_{ps_4}, \quad (6.59)$$

$$\mathbf{L}_{ps_{ex-3}} = \left(\mathbf{L}_{s_{ex-3} p} \right)^T = \mathbf{L}_{ps_2} \mathbf{T}^{-1} - \mathbf{L}_{ps_4} \mathbf{T}, \quad (6.60)$$

$$\mathbf{L}_{s_{ex-1} s_{ex-2}} = \left(\mathbf{L}_{s_{ex-2} s_{ex-1}} \right)^T = \mathbf{L}_{s_1 s_2} \mathbf{T}^{-1} + \mathbf{L}_{s_1 s_4}, \quad (6.61)$$

$$\mathbf{L}_{s_{ex-1} s_{ex-3}} = \left(\mathbf{L}_{s_{ex-3} s_{ex-1}} \right)^T = \mathbf{L}_{s_1 s_2} \mathbf{T}^{-1} - \mathbf{L}_{s_1 s_4} \mathbf{T}, \quad (6.62)$$

$$\mathbf{L}_{s_{ex-2} s_{ex-3}} = \left(\mathbf{L}_{s_{ex-3} s_{ex-2}} \right)^T = \mathbf{T} \mathbf{L}_{s_2 s_5} \mathbf{T}^{-1} - \mathbf{T} \mathbf{L}_{s_2 s_4} \mathbf{T} + \mathbf{L}_{s_2 s_4} \mathbf{T}^{-1} - \mathbf{L}_{s_3 s_4} \mathbf{T}. \quad (6.63)$$

The above model is more effective than the original model, but the analytical effort in obtaining it is extensive and highly depends on the wiring of the secondary side. However, the generality of the model, with respect to the original model, is preserved including the asymmetry between the mutual inductances across different transformer legs as well as the asymmetry between the leakage inductance and resistance of the final secondary sets.

The above-mentioned asymmetric properties of the transformer will affect the shape of the secondary voltages causing asymmetric ripple around the average value of the dc side variables. However, in the dynamic average models, due to the averaging over the switching interval, the ripples are averaged out, and the overall effect of these asymmetric properties is less important. Therefore, in the next step, we will consider removing these asymmetric properties while keeping the effects of these features in an average sense. In doing so, the modeling is considerably simplified while maintaining the desired accuracy of the final model. First, we consider the asymmetry in core geometry which results in different mutual inductances among the windings on different transformer legs.

6.3.3 Round Shifted Equivalent Model

Earlier in this Chapter, we assumed a general case wherein the symmetry in the core exists solely around the middle leg. In many cases, additional symmetry either exists in the core, or is approximated in a way that the interactions among the coils on any two of the transformer legs appear identical. In this case, the distinction between the side and middle legs, introduced earlier, no longer has to be made. In other words, self inductance of the primary coils (6.9) and (6.10) are equal to each other, and in (6.11) and (6.12), the coefficients $\xi_1 = \xi_2 = 0.5$. For the sake of dynamic average modeling, even if such symmetry does not exist, the values of $L_{pp,a}$ and $L_{pp,b}$ may be averaged, and used for all the coils. As will be shown later, such averaging provides sufficient accuracy for the purpose of dynamic average modeling. The self inductance of the primary windings is then written as:

$$L_{pp} = L_m + L_{lp}. \quad (6.64)$$

The self inductance of any other winding i may then be expressed as

$$L_{ii} = \left(\frac{n_i}{n_p} \right)^2 L_{pp} = \left(\frac{n_i}{n_p} \right)^2 (L_m + L_{lp}). \quad (6.65)$$

Moreover, in establishing the mutual inductances, no distinction has to be made between the four cases considered earlier in (6.15)-(6.18). The distinction, instead, is made between the two cases where both windings are on the same leg and otherwise. In a compact form, the mutual inductance between any two windings is then conveniently expressed as

$$L_{ij} = L_{ji} = \frac{n_i n_j}{n_p^2} (c_1 L_m + c_2 L_{lp}). \quad (6.66)$$

In the above equation, the coefficient c_1 is equivalent to ξ_1 , ξ_2 , and the coefficient c_2 is equivalent to ξ_3 , ξ_4 . Hence, if both windings are on the same leg, $c_1 = 1$, $c_2 < 1$, and otherwise: $c_1 = -0.5$, $c_2 = 0$.

Employing (6.64)-(6.66), the inductance matrices in the original model (6.4)-(6.7) may be written in the following compact form:

$$\mathbf{L}_{xx} = \left(\frac{n_x}{n_p} \right)^2 L_m \begin{bmatrix} 1+\gamma & -0.5 & -0.5 \\ -0.5 & 1+\gamma & -0.5 \\ -0.5 & -0.5 & 1+\gamma \end{bmatrix}, \quad (6.67)$$

$$\mathbf{L}_{xy} = \mathbf{L}_{yx} = \frac{n_x n_y}{n_p^2} L_m \begin{bmatrix} 1+c_2\gamma & -0.5 & -0.5 \\ -0.5 & 1+c_2\gamma & -0.5 \\ -0.5 & -0.5 & 1+c_2\gamma \end{bmatrix}, \quad x \neq y, \quad (6.68)$$

where γ is the so-called leakage ratio and is defined as follows,

$$\gamma = \frac{L_{lp}}{L_m}. \quad (6.69)$$

It was assumed in deriving the above model for the transformer that the magnetic core has a conventional three-leg structure. The magnetic flux produced by an arbitrary winding on any of these legs is hence divided into two equal portions, according to the magnetic path of the core, resulting in the coefficient c_1 in (6.66) to be equal to -0.5 when calculating the mutual inductance values between the windings on two different legs.

Let us now consider a fictitious three-phase transformer with a round cylindrical magnetic core. This structure has been schematically depicted in Figure 6.5. In this figure, the windings are shown as concentrated ones but in fact, the three-phase windings are assumed to be shifted in space by 120 degrees. The transformer has one primary set and n_{seg} secondary segments of windings similar to (and with the same number of turns as) the three-leg transformer described above. In the assumed equivalent round transformer, the windings corresponding to each of the phases, which appeared on the same leg in the original three-leg transformer, are now wound on top of each other and have the same spatial distribution. The geometry and magnetic properties of the core in the round transformer are assumed to be such that the value of the magnetizing inductance as seen in the primary windings is the same

as that of the original three-leg transformer, L_m . The leakage of the primary winding is also assumed to be equal to L_{lp} . It is also assumed that the portions of leakage flux link various windings in the same way as in the three-leg structure. The mutual inductance between any two windings i and j may then be written as

$$L_{ij} = L_{ji} = \frac{n_i n_j}{n_p^2} (c'_1 L_m + c'_2 L_{lp}), \quad (6.70)$$

where

$$c'_1 = \begin{cases} 1 & i, j \text{ belong to the same phase} \\ \cos\left(\frac{2\pi}{3}\right) & \text{otherwise} \end{cases}, \quad (6.71)$$

$$c'_2 = \begin{cases} c_2 & i, j \text{ belong to the same phase} \\ 0 & \text{otherwise} \end{cases}. \quad (6.72)$$

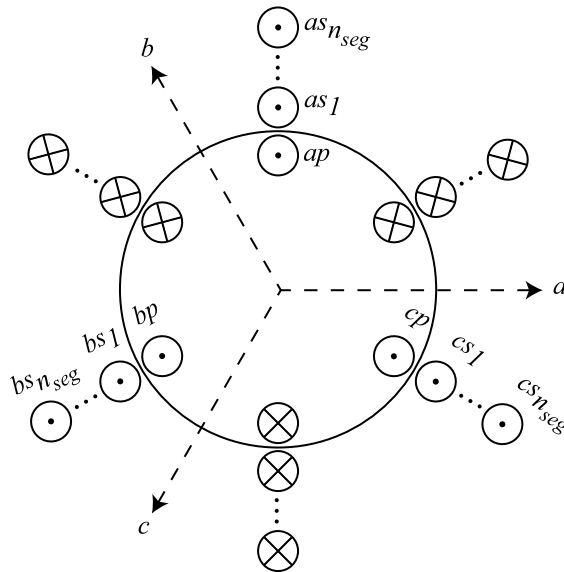


Figure 6.5 Equivalent round transformer model depicting three-phase primary winding set and the equivalent secondary segments.

Since $\cos\left(\frac{2\pi}{3}\right) = -0.5$, the inductances defined by (6.70) – (6.72) would resemble those given by (6.66), and the equivalent round transformer model of Figure 6.5 will correspond to the original three-leg transformer. The mathematical representations of both transformers are hence identical and given by (6.4) – (6.7), (6.67) – (6.69).

In the round transformer of Figure 6.5, it is now assumed that the secondary segments are appropriately connected to result in n_{set} extended sets of the secondary windings. The three-phase currents in the primary are then assumed to be

$$i_{ap} = I_{mp} \cos(\omega_e t + \theta_{0,i}), \quad (6.73)$$

$$i_{bp} = I_{mp} \cos\left(\omega_e t + \theta_{0,i} - \frac{2\pi}{3}\right), \quad (6.74)$$

$$i_{cp} = I_{mp} \cos\left(\omega_e t + \theta_{0,i} + \frac{2\pi}{3}\right), \quad (6.75)$$

where the peak value is denoted by I_{mp} . If the wiring is correct, regardless of the configuration, the three-phase currents in the k -th set of extended secondary windings, s_{ex-k} , are then given by

$$i_{as_{ex-k}} = I_{ms_{ex-k}} \cos(\omega_e t + \theta_{0,i} - (k-1)\theta_{disp}), \quad (6.76)$$

$$i_{bs_{ex-k}} = I_{ms_{ex-k}} \cos\left(\omega_e t + \theta_{0,i} - (k-1)\theta_{disp} - \frac{2\pi}{3}\right), \quad (6.77)$$

$$i_{cs_{ex-k}} = I_{ms_{ex-k}} \cos\left(\omega_e t + \theta_{0,i} - (k-1)\theta_{disp} + \frac{2\pi}{3}\right), \quad (6.78)$$

where $k = 1, 2, \dots, n_{set}$, and the peak value is denoted by $I_{ms_{ex-k}}$. Recalling the principle of Rotating Magnetic Field (RMF) in electrical machines [132], the equivalent RMF corresponding to this set of windings may then be expressed by

$$\vec{B}_{s_{ex-k}}(t) = B_{ms_{ex-k}} \angle \left(\omega_e t + \theta_{0,i} - (k-1)\theta_{disp}\right). \quad (6.79)$$

We then consider a new round transformer identical to the one depicted in Figure 6.5, except the following modification: The extended secondary set s_{ex-k} , including all its segments, has been replaced by a new set of windings, s_{eq-k} . This new set of windings, s_{eq-k} , is similar to, and has the same number of turns as s_1 , but, as shown in Figure 6.6, is spatially displaced with respect to this set by the angle δ_k . In this figure, for the sake of clarity, only the primary set and the two secondary sets s_1 and s_{eq-k} are shown. Moreover, only one side of each winding is illustrated. The equivalent RMF corresponding to this new set of windings is denoted by $\bar{B}_{s_{eq-k}}(t)$ and can be expressed as

$$\bar{B}_{s_{eq-k}}(t) = B_{ms_{eq-k}} \angle (\omega_e t + \theta_{0,i} - \delta_k). \quad (6.80)$$

In order for (6.79) and (6.80) to be equal, the following conditions should be satisfied:

$$B_{ms_{eq-k}} = B_{ms_{ex-k}}, \quad (6.81)$$

$$\delta_k = (k-1) \theta_{disp}. \quad (6.82)$$

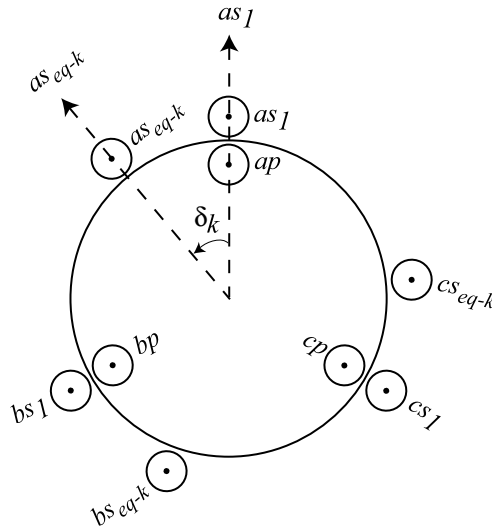


Figure 6.6 The k -th set of extended secondary windings is replaced by its shifted equivalent in the fictitious round equivalent transformer model.

Since the set s_{eq-k} is identical to s_1 , except the displacement, its resistance and leakage inductance would be equal to those of the s_1 set. Moreover, the spatial shift has no effect on the magnitude of the RMF, and for the purpose of satisfying (6.81) it may be assumed that δ_k is equal to zero. In this case, the new structure of the transformer would exactly resemble the one depicted in Figure 6.5, except that s_{eq-k} has different parameters compared to s_{ex-k} . It is concluded that in order for (6.81) to hold, it would suffice that the parameters of the new shifted set s_{eq-k} are made equal to those of the extended secondary set s_{ex-k} . The resulting RMF is then equal in the two cases, and the extended secondary set s_{ex-k} may be replaced by its displaced equivalent set of windings s_{eq-k} . Therefore, the equivalent set will have the same resistance and leakage inductance as the original set and is displaced according to (6.82).

Consequently, all extended secondary sets of windings may be replaced by their equivalent displaced sets. As shown in Figure 6.7, the final round shifted equivalent model for the 3-to-n-phase transformer is then composed of n_{set} sets of equivalent secondary windings that all have the same number of turns n_{s_1} and are evenly displaced by the angle given in (6.1). Note that the values of resistance and leakage inductance for each of these sets are set equal to those of the corresponding extended secondary set in the original configuration, and hence are not symmetric in general.

The final equivalent model of Figure 6.7, similar to the analytically-derived compacted transformer model developed in the previous section, is composed of n_{set} secondary sets of windings. Moreover, the development of the model does not significantly rely on the wiring details at the secondary side. As mentioned before, the n_{set} is typically smaller than the number of segments n_{seg} required in the original transformer. For instance, for the 9-phase

model of Figure 6.3, the total number of windings is reduced from 18 to 12 in the equivalent model of Figure 6.7. The total number of mutual inductances to be defined in this case is $C_2^{12} = 66$, which is significantly smaller than in the previous case, i.e., $C_2^{18} = 153$. For a large number of phases, the equivalent model of Figure 6.7 is hence more convenient to implement in any simulation package and will be computationally more efficient. Moreover, the mutual inductance between any two windings i and j may be determined using the following formula:

$$L_{ij} = L_{ji} = \frac{n_i n_j}{n_p^2} \cos(\theta_i - \theta_j) (L_m + c'_2 L_{lp}), \quad (6.83)$$

where θ_i and θ_j are the position of these windings' axes measured in the positive direction with respect to the primary's phase a axis. Once the values of all self and mutual inductances are established using (6.65) and (6.83), the model may be readily implemented in a suitable software package such as [7]. The great advantages of the round shifted equivalent model are: the simplicity of derivation and implementation; and the significant gain in numerical efficiency while maintaining the same accuracy.

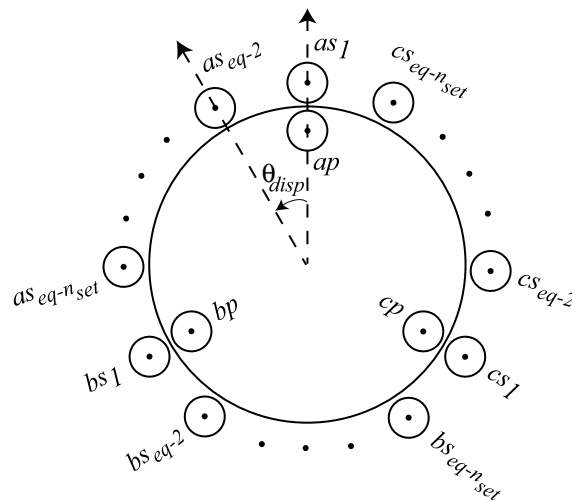


Figure 6.7 Fictitious round shifted equivalent transformer model.

6.3.4 Compensation for Asymmetric Leakages

Although the asymmetry in the core geometry has been averaged in the above model making it more symmetric than the original model and its analytical equivalent, some asymmetry still exists in the model due to the wiring of the secondary side. In particular, recall that one of the final extended secondary sets is typically composed of only one secondary segment, while the other sets include a series connection of more than one segment. Therefore, while replacing the extended secondary sets with their shifted equivalents, the resulting leakage inductances and resistances are not symmetric among the sets. This could be further clarified considering the 9-phase transformer example of Figure 6.3. In this case, the leakage inductance of an arbitrary segment of the secondary, s_k , can be represented in terms of the primary winding leakage as

$$L_{ls_k} = \left(\frac{n_{s_k}}{n_p} \right)^2 L_{lp}. \quad (6.84)$$

The leakage inductances of the final secondary sets are then expressed as:

$$L_{ls_{ex-1}} = \left(\frac{n_{s_1}}{n_p} \right)^2 L_{lp}, \quad (6.85)$$

$$L_{ls_{ex-2}} = L_{ls_{ex-3}} = \left(\frac{n_{s_2}^2 + n_{s_3}^2}{n_p^2} \right) L_{lp} = 0.7069 L_{ls_{ex-1}}, \quad (6.86)$$

where $L_{ls_{ex-k}}$ is used to denote the overall leakage inductance of the final extended secondary set s_{ex-k} , $k = 1, 2, \dots, n_{set}$. Equations (6.2) and (6.3) have been employed to obtain (6.86). Similar expressions may be obtained for the overall resistance of the final extended secondary sets.

The unequal leakage inductances and resistances among the secondary sets in the real transformer will introduce some asymmetry in the system performance. As a result, although

it was intended that the final multi-phase voltages be equal in magnitude and evenly shifted, this would not normally be the case in practice. In many cases, however, the amount of asymmetry may be considered negligible. In general, the symmetric operation is desired, and for this purpose, small additional inductors/resistors may be connected in series to several branches to compensate for the unequal parameters [48]. This procedure is denoted as “compensation” [48]. Alternatively, the number of turns may be slightly adjusted to compensate for this asymmetry.

For the purpose of dynamic average modeling, even if the above compensation techniques have not been employed in practice, the leakages and resistances may be averaged in order to obtain single values for the leakage and resistance of the final extended secondary sets of windings. Therefore, the compensation is done in the transformer model which will be later employed in the AVM.

6.4 Detailed Analysis

The detailed switching models of high-pulse-count converter systems may be constructed in a similar way to the 3-phase (6-pulse) converters in SV-based and NA-based software packages. However, in addition to the switching, the complicated multi-phase transformer module may become the bottleneck in the detailed modeling. The 3-to-9-phase transformer of Figure 6.3, for example, is composed of 18 windings. Each winding is characterized by its resistance and self-inductance. In addition, the mutual inductances between any two windings have to be specified. For this system, the total number of mutual inductances to be defined is therefore $C_2^{18} = 153$.

It is evident that the detailed transformer model is typically composed of a large number of coupled inductors and might be challenging to implement in many simulation software packages. The standard library components in the NA-based software packages such as PSCAD/EMTDC [11] and EMTP-RV [12] do not provide enough flexibility for such

detailed modeling. Among the SV-based programs, the ASMG [7] provides a convenient interface for modeling an arbitrary number of coupled inductors, and this tool has been used for the studies presented in this Section. Once all the self- and mutual-inductances are known, the transformer model may be readily built using the standard syntax of [7], and the windings are interconnected according to the transformer topology, e.g., Figure 6.3.

In order to verify and compare the models developed in the previous Section, these methodologies are demonstrated on the example 18-pulse aircraft power system (Figure 6.2). Three distinct transformer models are considered in the studies. The first and most general (original) model is based on the original configuration of Figure 6.3 and defined by (6.4)-(6.19). This model includes all the details of interconnected segments at the secondary side as well as the asymmetry in the core geometry. These features result in asymmetry among the winding resistances, leakage inductances, and mutual inductances. The second equivalent model is analytically derived from the above original model as described in Section 6.3.2. This model is defined by (6.48)-(6.63) and it preserves all asymmetric features and is completely equivalent to the original model. The only difference between the two is in the number of windings (size of the inductance matrix) and hence the numerical efficiency. It is then expected that the results obtained from these two models will be identical. The third model is the round shifted equivalent model introduced in Section 6.3.3. This model is defined by (6.48)-(6.51), (6.64), (6.65), (6.83), (6.85) and (6.86). The asymmetric properties of the core geometry are averaged in this model. However, the asymmetry among the resistances and leakage inductances of extended secondary sets are preserved.

6.4.1 Detailed Analysis using Uncompensated Transformer Models

For the purpose of verifying the previously developed transformer models, a simple computer study is presented in this Section. Herein, the original leakage inductances and resistances have been used in all transformer models as dictated by the configuration of

Figure 6.3. In the following simulation study, the three-phase source is switched on at $t = 0$ and a resistive load of $R_L = 7 \Omega$ is directly connected at the dc bus. The simulation results are provided in Figure 6.8 and Figure 6.9.

As seen in Figure 6.8 and Figure 6.9, some asymmetry is observed in the secondary side current waveforms in all models due to the asymmetry in transformer core geometry and the secondary windings resistances and leakage inductances according to (6.85), (6.86). Moreover, this asymmetry also translates into additional fluctuation of the dc bus voltage and current as can be seen in Figure 6.8 (first subplot). It is also observed that the original model and its analytical equivalent lead to essentially identical results – which is expected since these models are mathematically equivalent. The primary side currents are superimposed in Figure 6.8 (bottom plot). This plot clearly indicates that asymmetric performance is hardly observed at the primary side, whereas it is typically more visible in the secondary side and dc bus waveforms as seen in Figure 6.8 (top plot) and Figure 6.9. A slight difference between the round shifted equivalent model is due to the fact that the asymmetric core has been replaced with an equivalent symmetric one. However, since asymmetry among the secondary side leakage inductances and resistances are still present in this model, there still exists some asymmetry among the secondary currents as well as some fluctuations of the dc bus current as seen in Figure 6.8 (top plot).

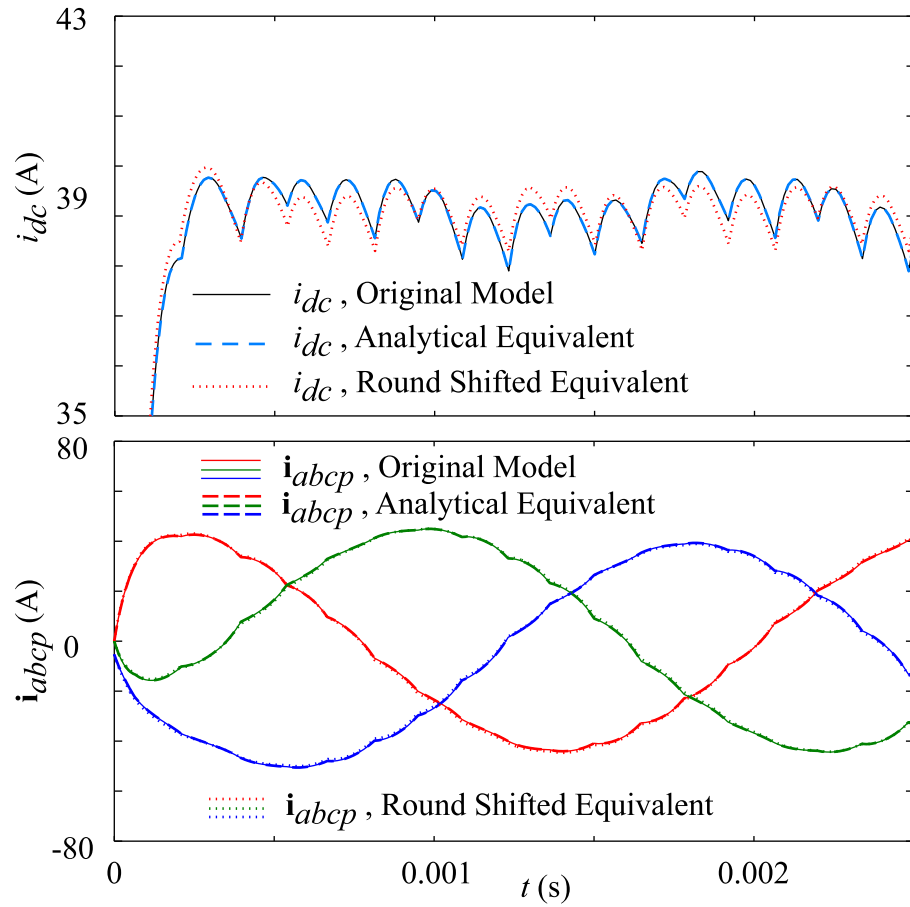


Figure 6.8 Initialization and steady state of the 18-pulse example system as seen at the dc bus and ac primary side currents predicted by various transformer models.

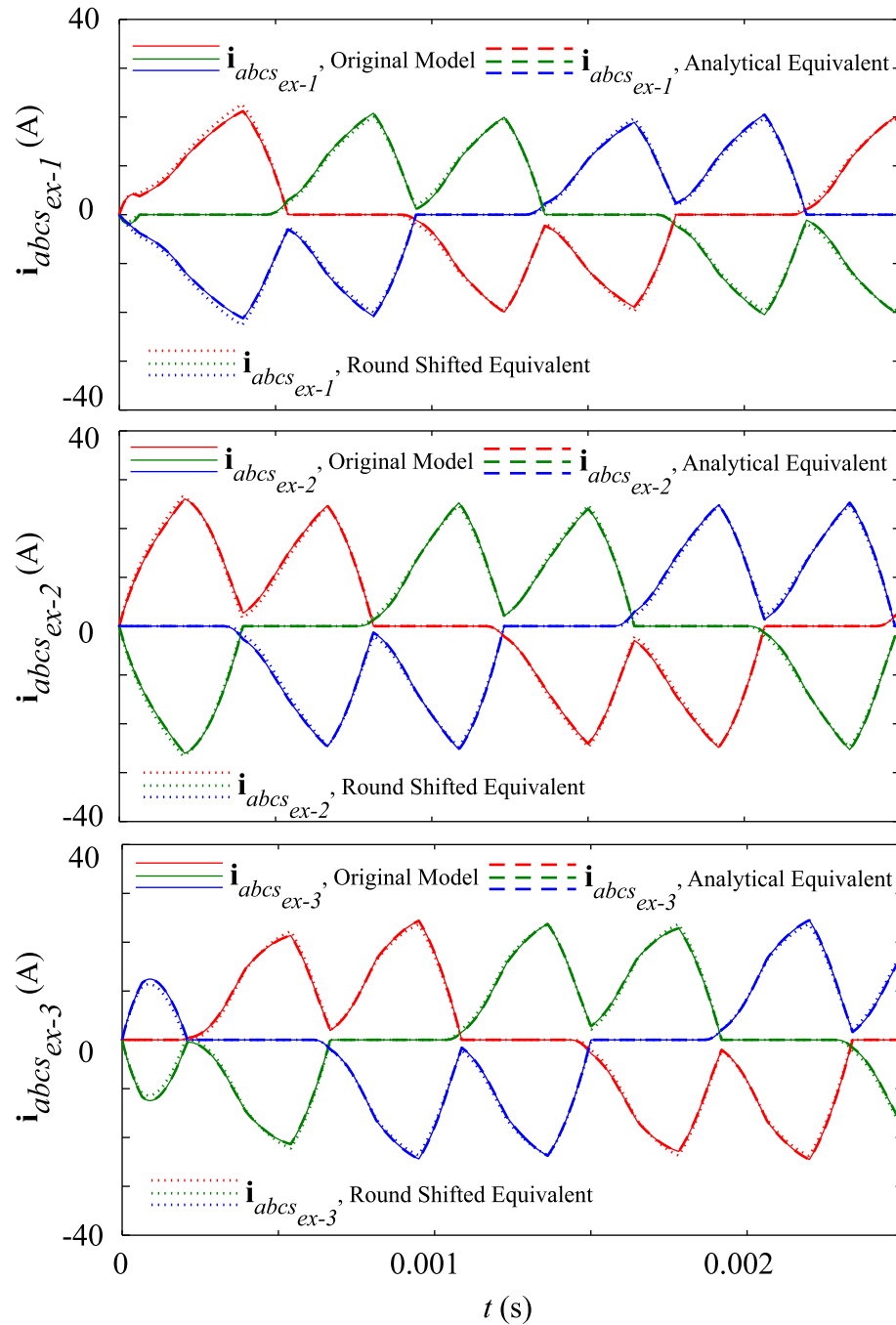


Figure 6.9 Initialization and steady state of the 18-pulse example system as seen at the secondary side currents predicted by various transformer models.

6.4.2 Detailed Analysis using Compensated Transformer Models

In the previously-defined transformer models, the asymmetry among the resistances and leakage inductances may be compensated by connecting small additional resistors and inductors, in series with the second and third extended secondary sets, forcing the overall values to match those of the reference set that has the largest total resistance and leakage inductance. Such compensation is commonly done in practice to achieve symmetric performance. Alternatively, the average values of resistances and leakage inductances may be computed and used for the extended secondary sets. Here, we adopt the former technique.

The resulting currents at the dc side and ac primary sides as predicted by the original and round shifted equivalent models are illustrated in Figure 6.10. The corresponding 9-phase secondary currents are illustrated in Figure 6.11. The currents predicted by the analytical equivalent model are identical to those of the original model. In this case, the responses predicted by the round shifted equivalent model, wherein the asymmetry in the core geometry, leakages and resistances have all been removed, are the most symmetric of all, as expected. The other two models include the asymmetric core properties responsible for the difference observed between the responses of these models and the round shifted equivalent. Comparing the results of Figure 6.10 with Figure 6.8, the previous observation that the primary winding currents are hardly affected by the asymmetric properties is also confirmed. A visible effect of asymmetry, comparing the top plots in these figures, is the detail of the superimposed ripple on the dc bus current. Another visible effect is the reduced magnitude of the currents in the first extended secondary set as seen in Figure 6.9 (top plot).

To better demonstrate the effects of asymmetry, the responses of the system provided by the two extreme cases, corresponding to the uncompensated original model and compensated round shifted equivalent model, are superimposed in Figure 6.12 and Figure 6.13. It is observed in these figures that the asymmetric ripples go around the symmetric ripple, which would imply that the average value of the dc current is also hardly affected by the

asymmetric properties. Furthermore, the ripples will be averaged out in the process of dynamic average modeling. Therefore, the compensation may be done, while developing the AVM, to achieve symmetry and facilitate the analysis.

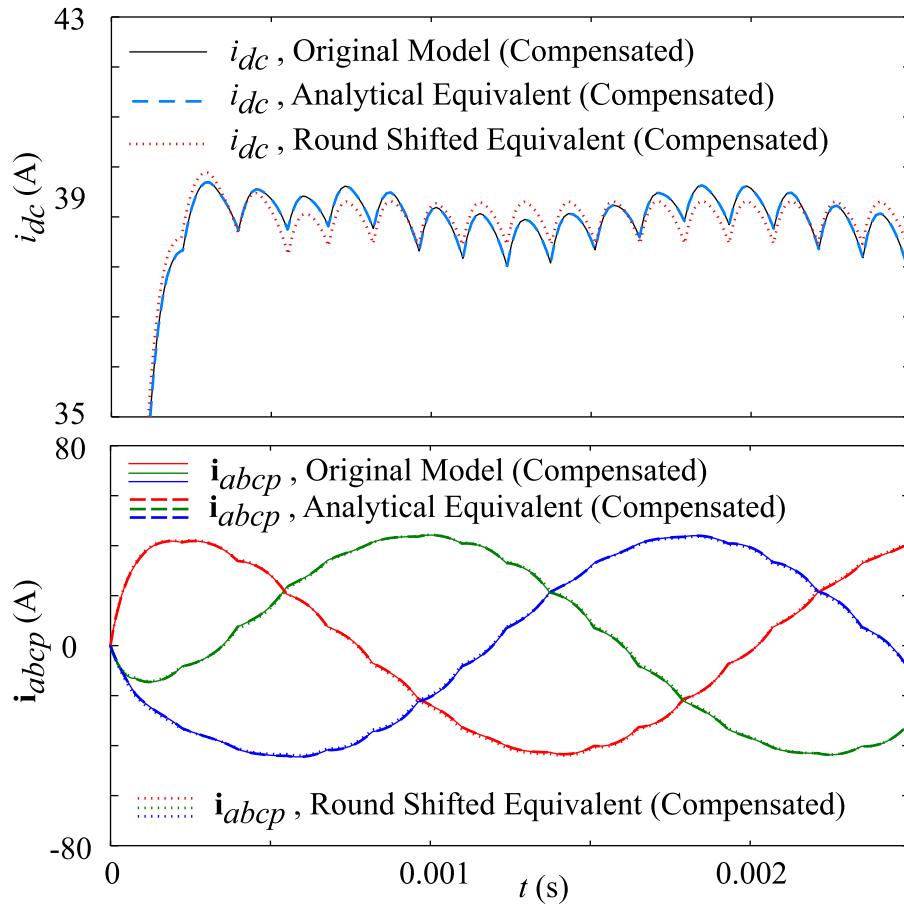


Figure 6.10 Initialization and steady state of the 18-pulse example system as seen in the dc bus and ac primary side currents as predicted by compensated transformer models.

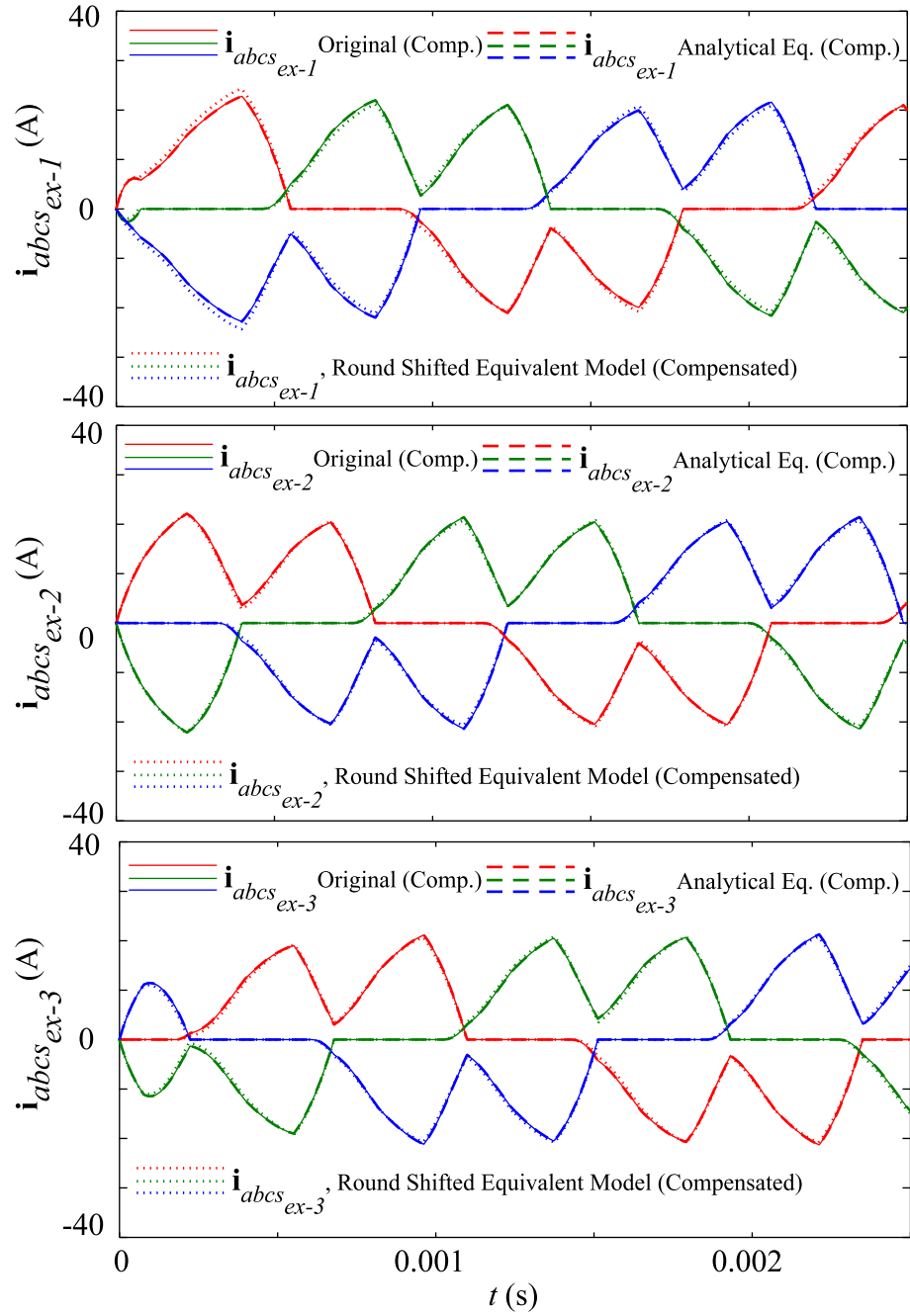


Figure 6.11 Initialization and steady state of the 18-pulse example system as seen in the ac secondary side currents as predicted by compensated transformer models.

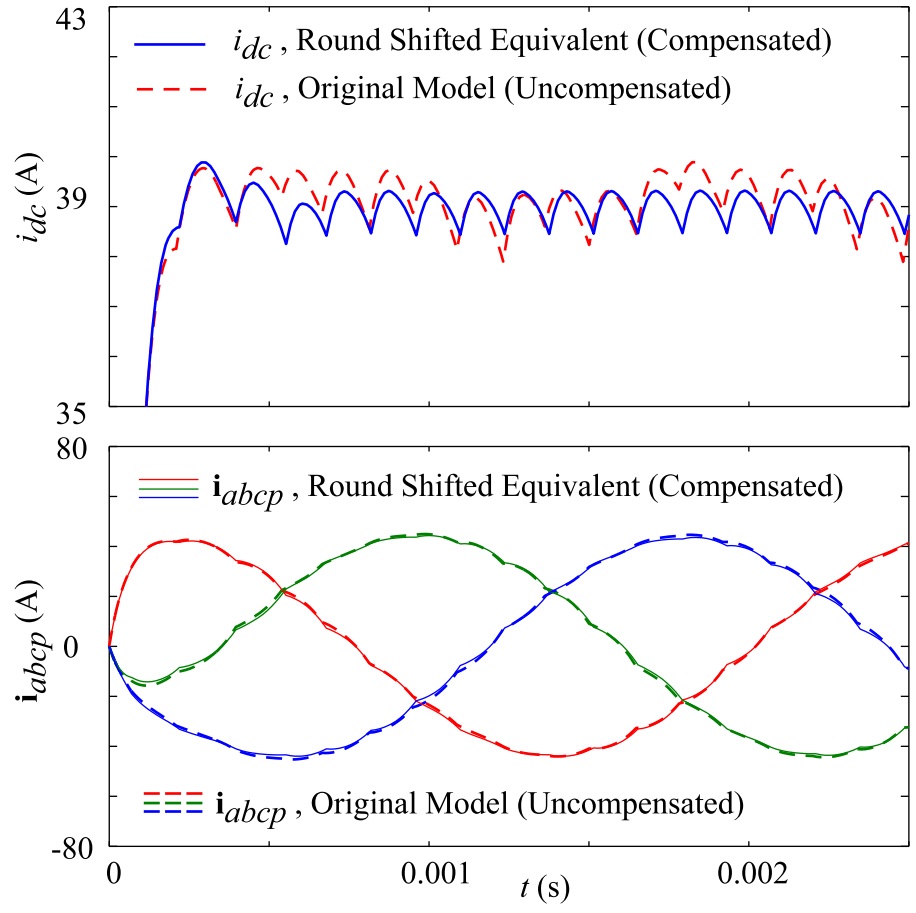


Figure 6.12 Comparison of the 18-pulse example system response as seen in the dc bus and ac primary side currents as predicted by symmetric and asymmetric transformer models.

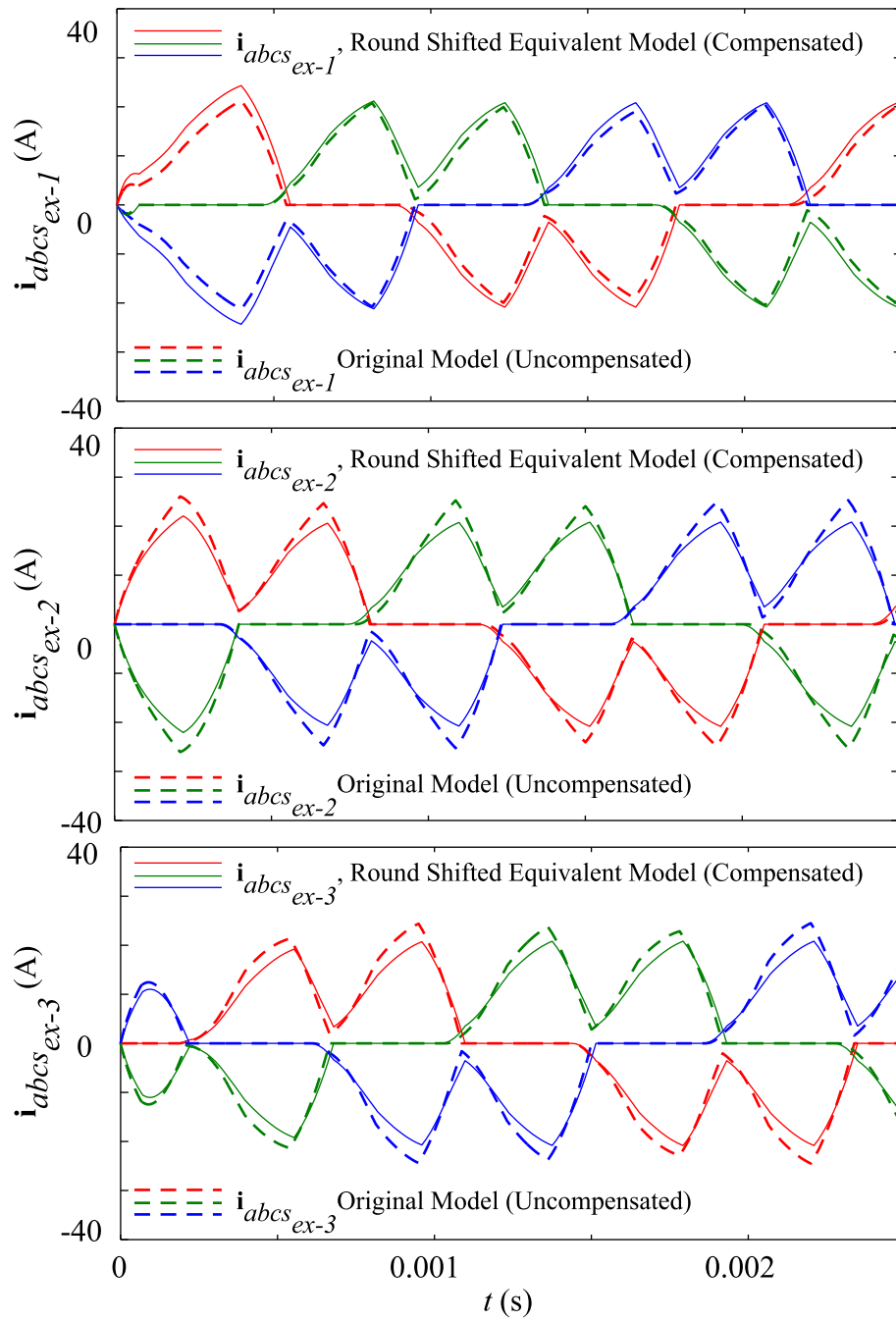


Figure 6.13 Comparison of the 18-pulse example system response as seen in the ac secondary side currents as predicted by symmetric and asymmetric transformer models.

6.4.3 Operational Mode Analysis

A comprehensive study of the operational modes for the 18-pulse converter system may be performed in a similar way to the 6-pulse converter system. In general, in higher-pulse-count systems, two types of commutations are present, namely the inter-phase and inter-bridge commutations. The inter-phase commutation occurs when the current switches from one phase to another within one of the bridges; whereas the inter-bridge commutation corresponds to the transfer of current from one bridge to another. Consequently, in the 9-phase system of Figure 6.2, as the dc load is swept on a wide range from an open-circuit to a short-circuit on the dc bus, various modes of operation are observed which are significantly more complicated as compared to the conventional 3-phase (6-pulse) case.

The mode analysis presented here assumes that the neutral points of the 3-phase primary set and the three secondary sets of the transformer (O, O', O'') are not connected to each other as it is most common practice. If the neutral points of these sets are connected, the complexity of the system increases further allowing for interactions between the bridges. For the most common topological configuration discussed above, 11 modes of operation are summarized in Table 6.1. The corresponding secondary 9-phase currents are shown in Figure 6.14 and Figure 6.15 for Modes 1-4 (DCM type modes) and 5-11 (CCM type modes), respectively. It is evident in these figures that, within each electrical cycle (T_{cycle}), there are 18 equal switching intervals (T_s). Depending on the mode, each switching interval may include one, two, or four subintervals each corresponding to a particular topology determined by the state of all 18 diodes. In these figures, different line strokes (solid, dashed, and dotted) have been used to illustrate each of the three-phase sets corresponding to one of the bridges. Within each set, red, green, and blue colors illustrate the current in each of the phases a , b , and c , respectively.

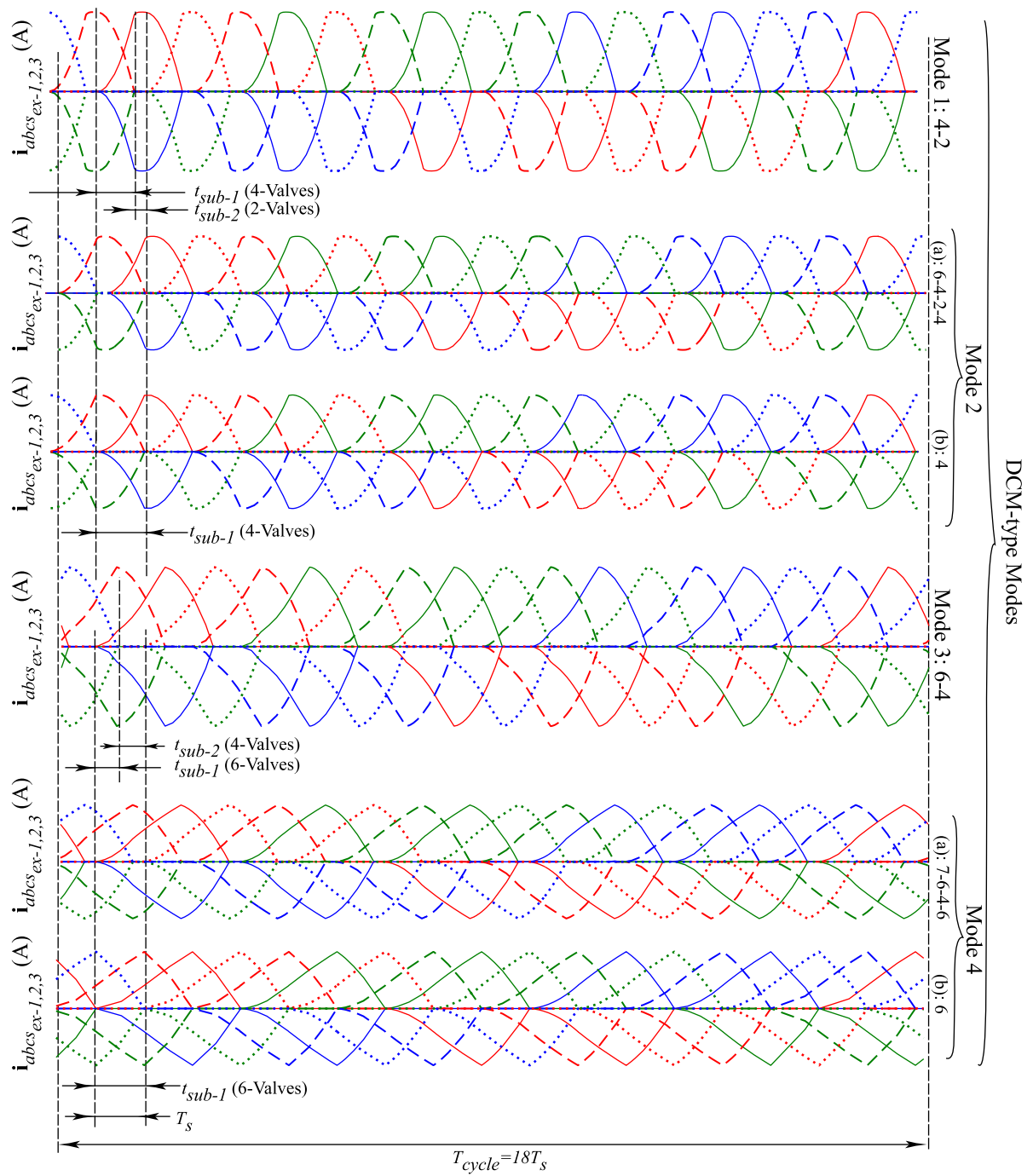


Figure 6.14 Nine-phase ac currents of the 18-pulse converter in DCM-type modes (Modes 1-4).

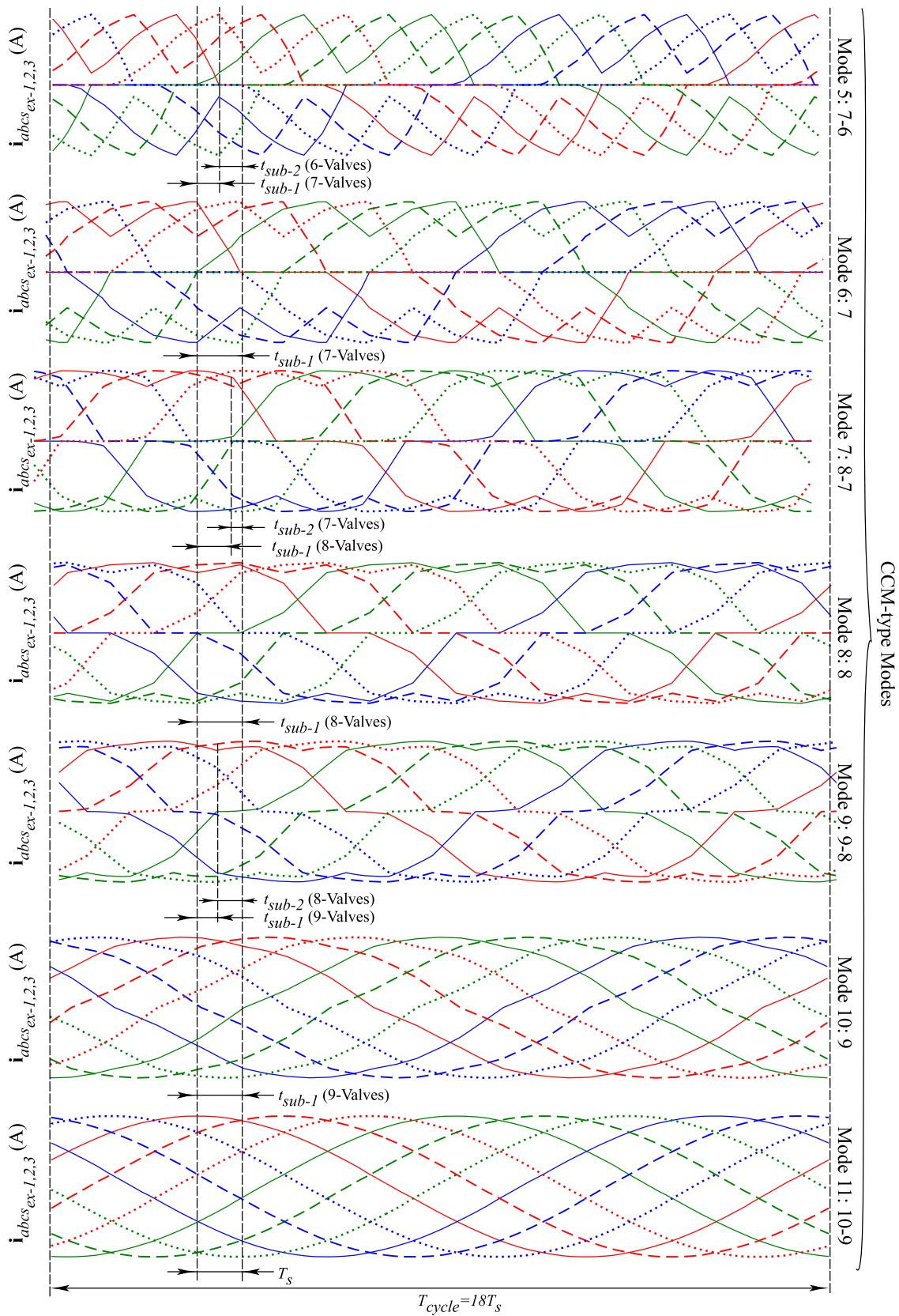


Figure 6.15 Nine-phase ac currents of the 18-pulse converter in CCM-type modes (Modes 5-11).

Table 6.1 Operational modes of the conventional 9-phase (18-pulse) rectifier.

Operational Modes (DCM-Type)	Conduction Pattern	Operational Modes (CCM-type)	Conduction Pattern
1	4-2	5	7-6
2 (a)	6-4-2-4	6	7
2 (b)	4	7	8-7
3	6-4	8	8
4 (a)	7-6-4-6	9	9-8
4 (b)	6	10	9
		11	10-9

For the first mode of operation, two subintervals t_{sub-1} and t_{sub-2} exist within each switching interval T_s resembling a commutation-conduction pattern (4-2 valve) as shown in Figure 6.14 and Table 6.1. For this lightest mode, during the commutation subinterval t_{sub-1} , one pair of diodes is passing the dc bus current to the next pair. After the current commutation is complete, in the next subinterval (conduction subinterval t_{sub-2}), the minimum possible number of diodes (two) is carrying the dc bus current. In this mode, observing the top plot in Figure 6.14, the dotted, dashed, and solid stroke waveforms appear sequentially while moving from the left side to the right. This indicates that inter-bridge commutation is continuously taking place, such that each bridge participates in carrying the overall dc bus current for one third of an electrical cycle. All three sets of three-phase ac currents, corresponding to three bridges, have needle-shape waveforms that are similar to the ac waveforms of the six-pulse converter in DCM operation depicted in Figure 2.3 (a). Therefore, each bridge will output a discontinuous dc current with a needle-shape waveform. Since the dc current provided by each bridge is discontinuous, this mode is categorized as a DCM-type mode. It should be noted, however, that the overall dc bus current is equal to the sum of the dc currents provided by the three bridges (the sum of the positive halves of the ac current waveforms in Figure 6.14), and will be continuous even at very light load. This is a major difference observed between the 6- and 18-pulse systems. However, looking at the 9-

phase ac currents of Figure 6.14, the needle shape waveforms are observed in all Modes 1-4. In all these modes, each of the three bridges has a DCM-type operation although the overall dc bus current remains continuous. We may then call these modes, the DCM-type modes.

As the load is increased, the inter-bridge commutation subinterval becomes longer. The conduction pattern in the next mode of operation depends on the total value of the commutating inductance at the ac side, i.e., source, ac filter if any, and the winding leakage inductance. This value determines the time constant by which the current changes. If this value is large enough, the new diodes will then start to conduct even before there is a chance for the conduction subinterval. As a result, the conduction subinterval t_{sub-2} disappears, and the commutation subinterval t_{sub-1} spans the whole switching interval. This would result in one of the possible Mode 2 operations, i.e., Mode 2(b) or 4-valve. In this type of operation, the inductance smoothes the commutation from the previous diodes to the new ones.

If the overall inductance value is small enough, the time constant may dictate that, within each switching interval, there is enough time for the inter-bridge commutation subinterval to end, and the current can therefore reach its pre-determined maximum value. In this case, it is impossible to force the points corresponding to the turning on of the new diodes and turning off of the old diodes to coincide, although these points move closer together by increasing the load. In other words, the conduction subinterval cannot disappear completely, and the commutation cannot occur precisely at one single point. The new diodes will then have to turn on either after the old diodes have turned off (which is the 4-2 operation), or before this (which will be mode 3 or 6-4 valve operation). However, in this case, at the boundary between these two modes, a transitory mode exists, i.e., mode 2(a), wherein, for a brief subinterval, the new diodes turn on shortly before the inter-bridge commutation interval ends, and turn off immediately after that. Such transitory modes have been also documented for the 12-pulse converter systems [62]. The length of the subinterval during which these two diodes intermittently conduct as well as the peak value of the current during this subinterval is so

small and hence not visible in the plots of Figure 6.14. However, comparing the waveforms for modes 2(a) and 2(b) in this figure, it is clear that in the mode 2(a), or 6-4-2-4 operation, the conduction subinterval exists for a period of time wherein the current has reached the maximum value pre-determined by system parameters. However, in mode 2(b), the 4-valve operation, the peak value of the current occurs at one single point, and the waveforms have a sharp point at which the current starts to decrease. This demonstrates that, due to the long time constant, there has not been enough time for the current to reach the predetermined maximum value corresponding to the conduction subinterval.

During the next mode, two bridges simultaneously carry current in one subinterval t_{sub-2} (4-valve) while the current frequently commutes to a third bridge (6 valve) in the new inter-bridge commutation subinterval t_{sub-1} . The 4-valve subinterval t_{sub-2} is essentially the remainder of the same inter-bridge commutation subinterval that existed in the previous modes, whereas the 6-valve subinterval is the result of a new inter-bridge commutation. As the load increases, the length of the new inter-bridge commutation interval t_{sub-1} increases. The 4-valve subinterval t_{sub-2} becomes shorter, and the two points corresponding to the turning on and off of the old and new pairs of diodes will then approach each other.

A situation, very similar to the transition from Mode 1 to Mode 3, is faced during the transition from Mode 3 to Mode 5. If the overall inductance value is large enough, the 6-valve operation is possible wherein t_{sub-1} spans the whole switching interval, and all three bridges carry the dc bus current during the whole switching interval. Otherwise, the two points corresponding to the turning on and off of the old and new pairs of diodes may not coincide. Since all three bridges are already participating in carrying the dc bus current, the next commutation has to be an inter-phase one. Following the trace of the mode 4(b) waveforms in Figure 6.14, it is observed that the dotted waveforms, which belong to the same bridge, have reached each other from both sides for the 6-valve operation. The bottom

waveforms, reaching each other at the end of the subinterval, are of the same color, green, and correspond to the same diode.

Increasing the load further would make the dc bus current at each of the bridges continuous resulting in the occurrence of the first CCM-type mode of operation. During this Mode (7-6 valve), the subintervals t_{sub-1} and t_{sub-2} correspond to the inter-phase commutation and conduction, respectively. Each bridge is then in fact operating in the CCM-1 Mode of operation discussed previously for the six-pulse converter (Section 2.2). This situation remains the same for the next four operating modes until the point where all ac currents become continuous (Mode 10 or 9-valve Mode). In this Mode, the switching interval T_s is composed of a single subinterval t_{sub-1} wherein three diodes from each bridge are simultaneously conducting which corresponds to all bridges operating in CCM-2 operation. The last CCM mode also includes a subinterval wherein a fourth diode conducts in one of the bridges, and the dc bus is temporarily short-circuited as a result. The pattern in this last mode will hence be 10-9.

It should also be noted that, in the above mode analysis, no inter-phase transformer is considered in the system with the intention to allow maximum interaction between the bridges. An ideal IPT, i.e., the one with infinite magnetizing inductance, in contrast, would force the three bridges to operate independently and hence would only allow certain modes of operation. In particular, only three modes of operation, i.e., modes 5, 10, and 11 of Table 6.1, would appear in this case which correspond to the three modes of operation discussed in Section 2.2 for the 6-pulse system. In other words, similar to the analysis of 12-pulse systems with an ideal IPT [62], such an 18-pulse system may be studied by analyzing one of the 6-pulse bridges with one-third of the load current. Operation of the system with a non-ideal IPT may be understood by analyzing the above extreme cases, as the characteristics of the system, in general, would lie between these two extremes.

Comparing Table 6.1 (for 18-pulse configuration) with Table 2.1 (for 6-pulse configuration), it is evident how increasing the number of pulses generally results in much more complicated switching patterns and a large number of operational modes. These modes depend on many factors including various topological configurations of the system, e.g., neutral points, IPT, etc., parameters of the system, e.g., large or small commutating inductance, etc. Therefore, for the systems with high number of pulses, the operational modes are generally very difficult (or impractical) to establish analytically.

6.5 Dynamic Average Modeling

6.5.1 Reduced-Order Analytical AVM

For the 9-phase (18-pulse) converter system, the best known to us, analytical AVM has been derived in [65] for one operational mode only, and considering the simple case of a voltage-source-fed converter with an ideal phase-shifting transformer. The developed model is an extension of the previously-proposed 6-pulse converter AVM which was briefly reviewed in Section 2.3.1.2 (see AVM-2 therein). In addition to being valid for Mode 5 (7-6 valve) operation only, another limitation is that the model has a reduced-order formulation similar to its three-phase counterpart. Several simplifying assumptions have also been made to facilitate the derivation of this model. The dynamic effects associated with transformer as well as the effects of magnetizing current are neglected. The input voltages are assumed to be a set of nine equally-shifted voltages of the same magnitude. These 9-phase voltages have been seen from the secondary side of the transformer as a balanced ideal 9-phase voltage source and its series impedance. The 9-phase voltages at the secondary side are hence implicitly assumed to be ideal sinusoidal waveforms. This is normally not the case in practice. Such assumptions, in addition to removing the transformer dynamics, remove the

possibility of including the zero sequence at the source-primary connection. The final model is described by a first order differential equation on the dc bus current:

$$\left[\frac{\frac{\pi}{9} - \mu + \frac{9\mu^2}{4\pi}}{\omega_e} r_s + \frac{4\pi - 9\mu}{2\pi} L_s + \frac{\frac{\pi}{9} - \mu}{2\omega_e} r_{dc} + L_{dc} \right] \frac{di_{dc}}{dt} = \frac{18}{\pi} \sin\left(\frac{\pi}{9}\right) \sqrt{2} E \left(1 - \frac{r_s}{\omega_e L_s} \frac{\mu - \sin \mu}{2} \right) - \left(\frac{2\pi - 9\mu}{\pi} r_s + \frac{9}{\pi} \omega_e L_s + r_{dc} \right) i_{dc0} - e_d. \quad (6.87)$$

The qd components of the ac currents are then calculated based on the system state through algebraic equations [65]. In this Chapter, this model is referred to as the AAVM [65]. The results obtained by the proposed generalized methodology introduced in the next Section will be compared with the results obtained from AAVM and with the detailed switching model of the system.

6.5.2 Generalized Dynamic Average Modeling Methodology

It was clarified in Chapter 2 that for the purpose of dynamic average modeling, it is imperative that the ac quantities be represented in the appropriate synchronously rotating $qd0$ reference frame. In the final implementation, the ac sub-system is hence represented in $qd0$ variables. In the case of a network-fed converter system (Figure 6.1 Case I), on the one hand, transforming the voltage source-impedance branches into $qd0$ reference frame is a straightforward procedure. On the other hand, numerous models of the electric machinery are readily available in $qd0$ variables for three-phase [51], six-phase [125] machines, etc. The generalized approach will be defined in a way that the $qd0$ machine model with the desired level of accuracy may be readily employed for modeling the ac subsystem in the case of a machine-fed converter (Figure 6.1 Cases II and III).

Let us now consider the case of voltage-source-fed converter (Figure 6.1 Case I) with a multi-phase transformer such as the 3-to-9-phase transformer configuration of Figure 6.3.

Developing the equivalent model for this configuration and similar multi-phase transformers with a large number of interconnected windings in $qd0$ variables is generally a difficult task, with the most challenging part being the multi-phase transformer. The purpose of this subsection is to develop a $qd0$ equivalent multi-phase transformer model. Once such model is developed, the whole ac subsystem for any of the configurations depicted in Figure 6.1 may be implemented employing this transformer model, the standard voltage source-impedance model in $qd0$ variables, and the desired $qd0$ electric machine models readily available in the literature.

6.5.2.1 Generalized Transformer Model in Transformed Variables

The round shifted equivalent transformer model of Figure 6.7 is more convenient to implement in phase domain compared to the original configuration and its analytical equivalent. However, its main advantage is that it can be conveniently transformed into $qd0$ variables for the purpose of generalized the dynamic average modeling. To demonstrate this point, the voltage and flux-linkage equations are considered for each set of windings in the round shifted equivalent of Figure 6.7:

$$\mathbf{v}_{abc,p} = r_p \mathbf{i}_{abc,p} + \frac{d}{dt} \boldsymbol{\lambda}_{abc,p}, \quad (6.88)$$

$$\boldsymbol{\lambda}_{abc,p} = \mathbf{L}_{pp} \mathbf{i}_{abc,p} + \sum_{k=1}^{n_{set}} \mathbf{L}_{ps_{eq-k}} \mathbf{i}_{abc,s_{eq-k}}, \quad (6.89)$$

$$\mathbf{v}_{abc,s_{eq-k}} = r_{s_{eq-k}} \mathbf{i}_{abc,s_{eq-k}} + \frac{d}{dt} \boldsymbol{\lambda}_{abc,s_{eq-k}}, \quad k = 1, 2, \dots, n_{set}, \quad (6.90)$$

$$\boldsymbol{\lambda}_{abc,s_{eq-k}} = \mathbf{L}_{s_{eq-k}p} \mathbf{i}_{abc,p} + \sum_{i=1}^{n_{set}} \mathbf{L}_{s_{eq-k}s_{eq-i}} \mathbf{i}_{abc,s_{eq-i}}, \quad k = 1, 2, \dots, n_{set}. \quad (6.91)$$

In general, the inductance matrix \mathbf{L}_{xx} may be written as:

$$\mathbf{L}_{xx} = \left(\frac{n_x}{n_p} \right)^2 L_m \begin{bmatrix} 1 + \gamma_x & -0.5 & -0.5 \\ -0.5 & 1 + \gamma_x & -0.5 \\ -0.5 & -0.5 & 1 + \gamma_x \end{bmatrix}, \quad (6.92)$$

where the generalized leakage ratio (asymmetric among different sets) is defined as

$$\gamma_x = \left(\frac{n_p}{n_x} \right)^2 \frac{L_{lx}}{L_m}. \quad (6.93)$$

for set x . In (6.93), L_{lx} denotes the leakage inductance of any of the windings in set x . It can be shown that

$$\gamma_p = \gamma_{s_1} = \gamma. \quad (6.94)$$

$$\gamma_{seq-k} = \gamma \left(\frac{n'_{ex-k}}{n_{s_1}} \right)^2. \quad (6.95)$$

where n'_{ex-k} is an equivalent number of turns that has to be calculated for each set of equivalent secondary windings. Note that all secondary windings have the same number of turns equal to n_{s_1} , but in calculating the leakage inductances and resistances of the windings, the equivalent number of turns n'_{ex-k} has to be used instead of the actual number of turns. For each equivalent secondary set, this number is determined based on the number of turns in each of the participating segments in the corresponding extended secondary set. Typically, if two segments are used per extended secondary:

$$n'_{ex-k} = \sqrt{n_{seg1}^2 + n_{seg2}^2}. \quad (6.96)$$

Employing (6.83), the inductance matrix \mathbf{L}_{xy} between two different sets may also be written as

$$\mathbf{L}_{xy} = \frac{n_x n_y}{n_p^2} (L_m + c'_2 L_{lp}) \mathbf{A}, \quad (6.97)$$

$$\mathbf{A} = \begin{bmatrix} \cos(\theta_{rel}) & \cos\left(\theta_{rel} + \frac{2\pi}{3}\right) & \cos\left(\theta_{rel} - \frac{2\pi}{3}\right) \\ \cos\left(\theta_{rel} - \frac{2\pi}{3}\right) & \cos(\theta_{rel}) & \cos\left(\theta_{rel} + \frac{2\pi}{3}\right) \\ \cos\left(\theta_{rel} + \frac{2\pi}{3}\right) & \cos\left(\theta_{rel} - \frac{2\pi}{3}\right) & \cos(\theta_{rel}) \end{bmatrix}, \quad (6.98)$$

$$\theta_{rel} = \theta_x - \theta_y, \quad (6.99)$$

where θ_x and θ_y are the position of a -phase axes of the sets x and y measured in the positive trigonometric direction with respect to the primary's a -phase axis. Equation (6.99) may be re-written in terms of the displacement angle as

$$\theta_{rel} = (u_x - u_y) \theta_{disp}, \quad (6.100)$$

$$u_p = 1, \quad u_{s_{eq-k}} = k. \quad (6.101)$$

In the next step, all ac variables should be transformed into $qd0$ variables using the appropriate transformation matrix. For this purpose, the three-phase variables at the primary side are transformed using the standard transformation matrix (2.7). The three-phase set of variables corresponding to the secondary set s_{eq-k} are then transformed into $qd0$ variables according to the generalized transformation matrix:

$$\mathbf{K}_{s_{eq-k}}(\theta) = \mathbf{K}(\theta - (k-1)\theta_{disp}). \quad (6.102)$$

Applying these transformations, after some effort, (6.88)-(6.91) may be represented in $qd0$ as

$$\mathbf{v}_{qd0,p} = r_p \mathbf{i}_{qd0,p} + \frac{d}{dt} \boldsymbol{\lambda}_{qd0,p} + \omega \boldsymbol{\lambda}_{dq,p}, \quad (6.103)$$

$$\boldsymbol{\lambda}_{qd0,p} = \mathbf{L}_{pp}^* \mathbf{i}_{qd0,p} + \sum_{k=1}^{n_{set}} \mathbf{L}_{ps_{eq-k}}^* \mathbf{i}_{qd0,s_{eq-k}}, \quad (6.104)$$

$$\mathbf{v}_{qd0,s_{eq-k}} = r_{s_{eq-k}} \mathbf{i}_{qd0,s_{eq-k}} + \frac{d}{dt} \boldsymbol{\lambda}_{qd0,s_{eq-k}} + \omega \boldsymbol{\lambda}_{dq,s_{eq-k}}, \quad k = 1, 2, \dots, n_{set}, \quad (6.105)$$

$$\lambda_{qd0,s_{eq-k}} = \mathbf{L}_{s_{eq-k}p}^* \mathbf{i}_{qd0,p} + \sum_{i=1}^{n_{set}} \mathbf{L}_{s_{eq-k}s_{eq-i}}^* \mathbf{i}_{qd0,s_{eq-i}}, \quad k=1,2,\dots,n_{set}. \quad (6.106)$$

where

$$\lambda_{dq,x} = [\lambda_{dx} \quad -\lambda_{qx} \quad 0]^T. \quad (6.107)$$

The new inductance matrices are now expressed as

$$\mathbf{L}_{xx}^* = \left(\frac{n_x}{n_p} \right)^2 L_m \begin{bmatrix} 1.5 + \gamma_x & 0 & 0 \\ 0 & 1.5 + \gamma_x & 0 \\ 0 & 0 & 1.5 + \gamma_x \end{bmatrix}, \quad (6.108)$$

$$\mathbf{L}_{xy}^* = \frac{n_x n_y}{n_p^2} 1.5 (L_m + c'_2 L_{lp}) \mathbf{I}_{3 \times 3}, \quad (6.109)$$

where $\mathbf{I}_{3 \times 3}$ is the identity matrix. For implementation in a SV-based simulation package, this model can now be conveniently written in a standard state-space form:

$$\frac{d}{dt} \lambda_{qd0,x} = \mathbf{v}_{qd0,x} - r_x \mathbf{i}_{qd0,x} - \omega \lambda_{dq,x}, \quad (6.110)$$

$$\mathbf{i}_{qd0,x} = \frac{1}{L_{lx}} \left(\lambda_{qd0,x} - \frac{n_x}{n_p} \lambda_{qd,m} \right), \quad (6.111)$$

$$\lambda_{qd,m} = L_a \left[\frac{\lambda_{qd,p}}{L_{lp}} + \sum_{k=1}^{n_{set}} \left(\frac{n_{s_{eq-k}}}{n_p} \frac{\lambda_{qd,s_{eq-k}}}{L_{ls_{eq-k}}} \right) \right], \quad (6.112)$$

$$\frac{1}{L_a} = \frac{1}{1.5L_m} + \frac{1}{L_{lp}} + \sum_{k=1}^{n_{set}} \left(\left(\frac{n_{s_{eq-k}}}{n_p} \right)^2 \frac{1}{L_{ls_{eq-k}}} \right). \quad (6.113)$$

In the above equations,

$$\lambda_{qd,x} = [\lambda_{qx} \quad \lambda_{dx} \quad 0]^T. \quad (6.114)$$

The above transformer model is quite general and may be used to represent an arbitrary 3-to-n phase multi-phase transformer. This allows for implementing the round equivalent transformer model in transformed variables with or without any of the previously-discussed

compensation methods for symmetric performance, i.e., additional impedance, adjusting the number of turns, etc. However, in most cases, the transformer is simpler than the above model due to symmetry among different secondary sets. The most common condition is the symmetry among the number of turns:

$$n_{s_{eq-1}} = n_{s_{eq-2}} = \dots = n_{s_{eq-n_{set}}} = n_{s1} = n_s . \quad (6.115)$$

Substituting (6.115) in (6.112) and (6.113) yields

$$\lambda_{qd,m} = L_a \left[\frac{\lambda_{qd,p}}{L_{lp}} + a \sum_{k=1}^{n_{set}} \left(\frac{\lambda_{qd,s_{eq-k}}}{L_{ls_{eq-k}}} \right) \right], \quad (6.116)$$

$$\frac{1}{L_a} = \frac{1}{1.5L_m} + \frac{1}{L_{lp}} + a^2 \sum_{k=1}^{n_{set}} \frac{1}{L_{ls_{eq-k}}}, \quad (6.117)$$

wherein the final turn ratio is defined as $a = \frac{n_s}{n_p}$.

The final model can then be expressed by the equivalent circuit shown in Figure 6.16. In this figure, all secondary quantities have been referred to the primary side using the above turn ratio. In addition to (6.115), the parameters are usually made symmetric among the secondary windings, which results in

$$L_{ls_{eq-1}} = L_{ls_{eq-2}} = \dots = L_{ls_{eq-n_{set}}}, \quad (6.118)$$

$$r_{s_{eq-1}} = r_{s_{eq-2}} = \dots = r_{s_{eq-n_{set}}}, \quad (6.119)$$

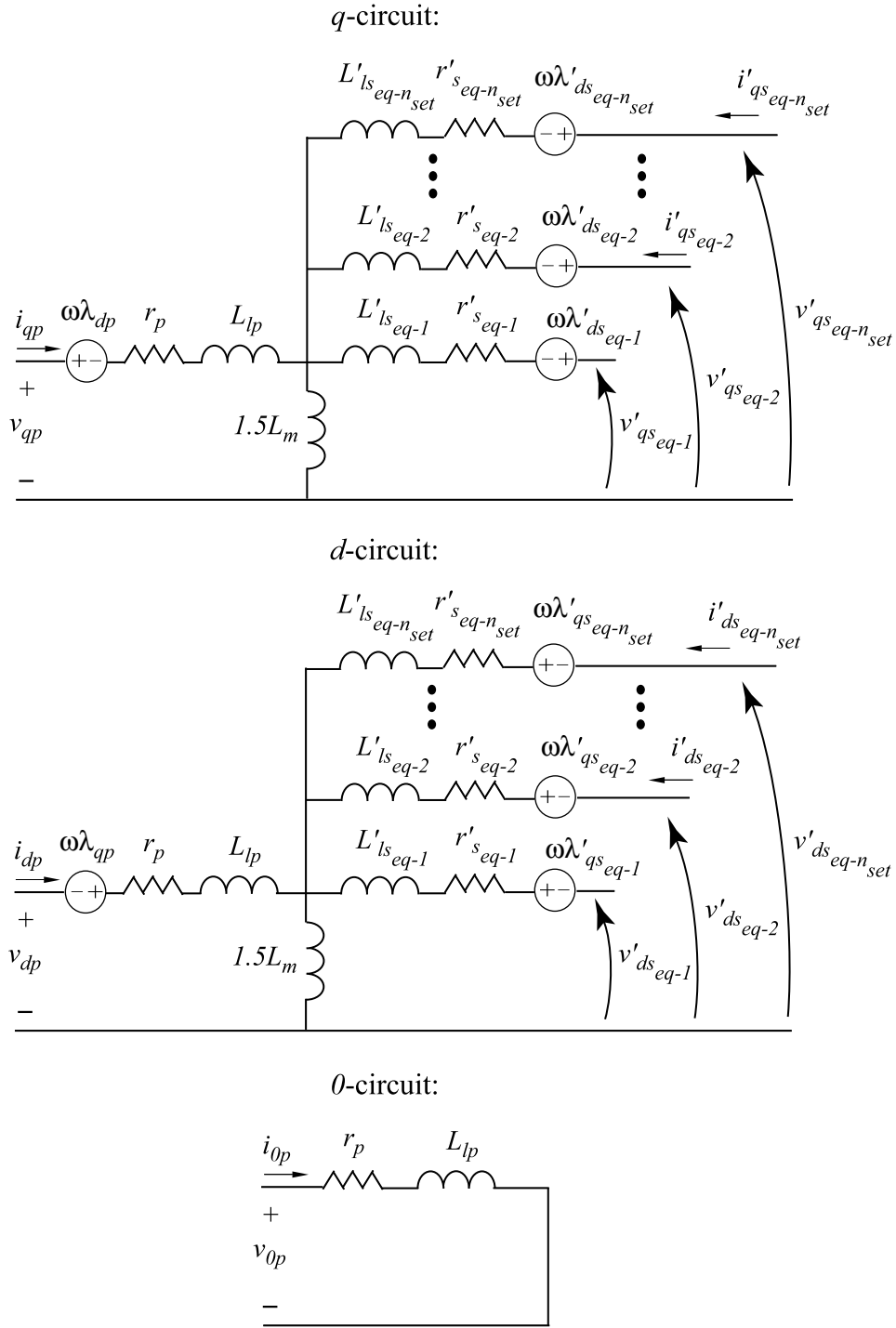


Figure 6.16 Equivalent circuit of the generalized transformer model in transformed qd0 variables.

6.5.2.2 Generalized Rectifier Model

The transformer model developed in the previous Section, feeds n_{set} bridges. The zero sequence is typically not transferred to the secondary and dc sides because the neutral points at the secondary are normally floating with respect to the primary and the bridge. However, the zero sequence may be present at the ac side if the neutral points of the primary windings and the ac source are connected through grounding. The proposed model includes these effects and may be used for asymmetric fault studies as will be presented later.

Adopting the parametric approach, to develop the AVM for the rectifier sub-circuits, two sets of functions are defined that relate the ac and dc variables at the inputs and outputs of each rectifier:

$$W_{v,k}(\cdot) = \frac{\|\bar{\mathbf{v}}_{qd,seq,k}^c\|}{\bar{v}_{dc,k}}, \quad k = 1, 2, \dots, n_{set}, \quad (6.120)$$

$$M_{i,k}(\cdot) = \frac{\bar{i}_{dc,k}}{\|\bar{\mathbf{i}}_{qd,seq,k}^c\|}, \quad k = 1, 2, \dots, n_{set}. \quad (6.121)$$

Also, for the k -th secondary set, the angle between the voltage and current vectors $\bar{\mathbf{v}}_{qd,seq,k}^c$, $\bar{\mathbf{i}}_{qd,seq,k}^c$ may be expressed by:

$$Q_k(\cdot) = \tan^{-1} \left(\frac{\bar{i}_{d,seq,k}^a}{\bar{i}_{q,seq,k}^a} \right) - \tan^{-1} \left(\frac{\bar{v}_{ds,seq,k}^a}{\bar{v}_{qs,seq,k}^a} \right). \quad (6.122)$$

Similar to the case of six-pulse converters discussed in the previous Chapters, the parametric functions (6.120)-(6.122) may be calculated numerically using the detailed simulation or experimental results. It is convenient to express these functions in terms of the generalized dynamic impedance of the k -th rectifier block as

$$Z_k = \frac{\bar{v}_{dc,k}}{\left\| \bar{\mathbf{i}}_{qd,seq,k}^c \right\|}. \quad (6.123)$$

A transient study may be carried out in which the load resistance is slowly changed in a wide range, and the parametric functions $W_{v,k}(\cdot)$, $M_{i,k}(\cdot)$, and $Q_k(\cdot)$, together with the impedance Z_k , are calculated at each operating point for $k=1,2,\dots,n_{set}$ using (6.120)-(6.123), and stored in a look-up table for use in the average-value model implementation.

6.5.2.3 Implementation in SV-Based Simulators

In a SV-based program, the Generalized AVM (GAVM) for a high-pulse-count converter system, with any of the configurations depicted in Figure 6.1, could be conveniently implemented according to the diagram shown in Figure 6.17. For this purpose, the ac subsystem is implemented in transformed $qd0$ variables. The three-phase voltage source-impedance combination and the three- or multi-phase machine models in $qd0$ variables are readily available in the literature. In Case III, the zero sequence is topologically prevented. In Cases I and II, the generalized transformer model in transformed variables developed in Section 6.5.2.1 and depicted in Figure 6.16, is adopted. The final output of the ac subsystem is n_{set} sets of three-phase currents in qd variables. The zero sequence is not transferred to the bridges and the dc side, although zero sequence is generally allowed to exist within the ac subsystem in case of asymmetrical faults. The modules denoted by AVM#1 through AVM# n_{set} include the parametric functions (6.120) through (6.123). The optional subsystem including the inter-phase transformer and the dc filter remain intact with respect to the original detailed model.

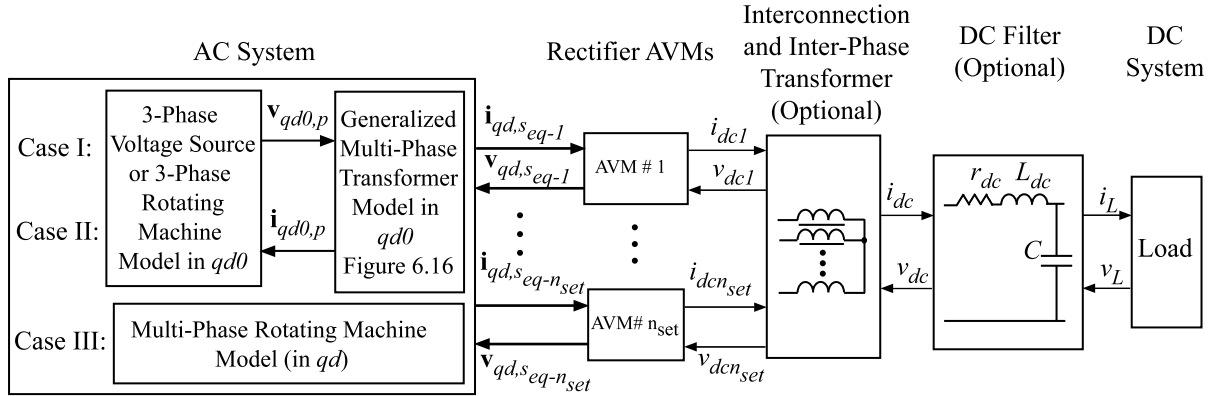


Figure 6.17 Block diagram of the generalized AVM implementation in SV-based simulators.

6.5.3 Generalized Model with Collapsed Transformer

In one of the most-commonly-used configurations of multi-pulse rectifiers, the secondary side windings (with floating neutral points) feed several identical bridges that are connected in parallel at the dc side. In such cases a perfect symmetry is achieved at the secondary side, and in terms of the transformed variables, the voltages and currents of the secondary branches will be equal. The secondary side branches in the equivalent circuit of Figure 6.16 are then effectively connected in parallel. As shown in the simplified equivalent circuit of Figure 6.18, these branches may then be collapsed into one new single secondary branch, with the same voltage, but three times the current. This circuit then represents an equivalent three-phase transformer circuit which is more convenient for implementation.

Using this collapsed equivalent circuit, the secondary side could be represented by one single set of transformed variables in generalized converter reference frame. For this purpose, if the ac subsystem is implemented in arbitrary reference frame, the secondary side variables are transformed into the generalized converter reference frame as:

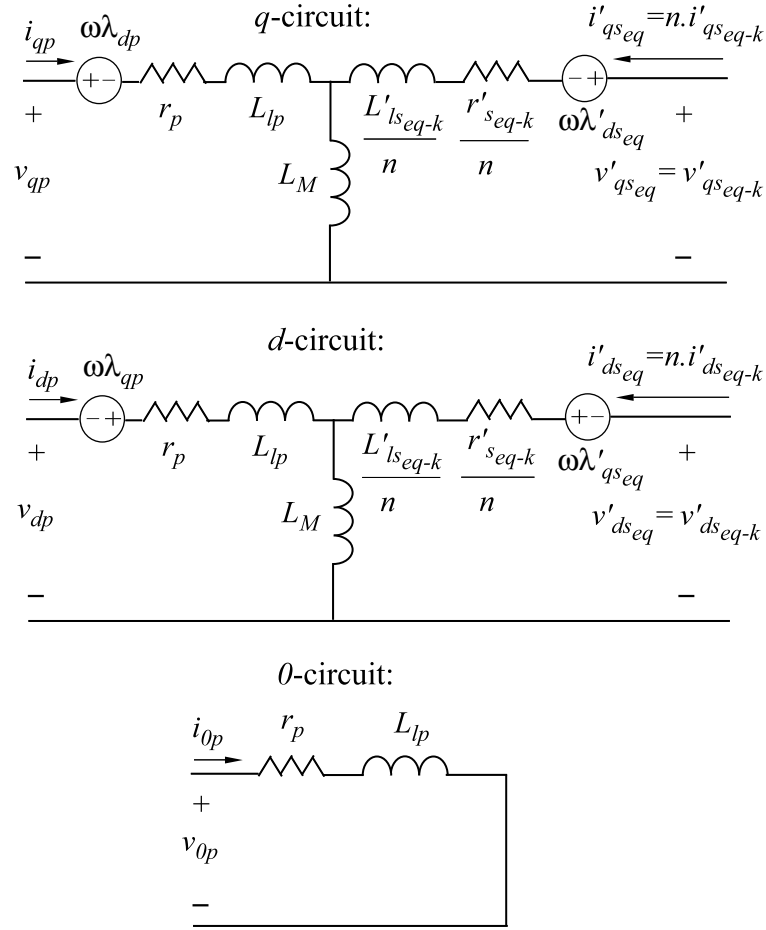


Figure 6.18 Equivalent circuit of the collapsed transformer model in transformed qd0 variables.

$$\mathbf{f}_{qdsdq}^c = \frac{1}{n_{set}} \mathbf{K}_a^c \sum_{k=1}^{n_{set}} \mathbf{f}_{qd, seq-k}, \quad (6.124)$$

$$\mathbf{K}_a^c = \begin{bmatrix} \cos(\phi_c) & \sin(\phi_c) \\ -\sin(\phi_c) & \cos(\phi_c) \end{bmatrix}. \quad (6.125)$$

In (6.124) and (6.125), the angle ϕ_c is the position of the converter reference frame q axis with respect to that of the arbitrary reference frame, and \mathbf{f} is a vector of any network variable, i.e., voltage, current, or flux linkage at the secondary side. Note that, although the qd variables of all secondary sets are equal in perfectly symmetric cases, in (6.124), in order to compute the qd variables of the equivalent set, the qd variables of these sets are

averaged instead of simply choosing one of these sets. By doing so, even if the symmetry among the sets is not perfectly achieved due to any reason, in an average sense, these effects are taken into account in the average model.

The parametric functions are now defined for the single equivalent secondary set as:

$$W_v(\cdot) = \frac{\|\bar{\mathbf{v}}_{qds_{eq}}^c\|}{\bar{v}_{dc}}, \quad \text{and} \quad M_k(\cdot) = \frac{\bar{i}_{dc}}{\|\bar{\mathbf{i}}_{qds_{eq}}^c\|} \quad (6.126)$$

For the equivalent collapsed secondary set, the angle between the voltage and current vectors

$\bar{\mathbf{v}}_{qds_{eq}}^c$, $\bar{\mathbf{i}}_{qds_{eq}}^c$ may be expressed by:

$$Q(\cdot) = \tan^{-1} \left(\frac{\bar{i}_{ds_{eq}}^a}{\bar{i}_{qs_{eq}}^a} \right) - \tan^{-1} \left(\frac{\bar{v}_{ds_{eq}}^a}{\bar{v}_{qs_{eq}}^a} \right). \quad (6.127)$$

These functions are represented in terms of the equivalent dynamic impedance defined as:

$$Z_{eq} = \frac{\bar{v}_{dc}}{\|\bar{\mathbf{i}}_{qd,s_{eq}}^c\|}. \quad (6.128)$$

The high-pulse-count converter system is then conveniently implemented using the equivalent three-phase model as shown in Figure 6.19. This collapsed model requires one single AVM subsystem that relates the dc side and the equivalent secondary side through parametric functions (6.126), (6.127). As seen in this diagram, if desired, the currents in the original secondary sets can be obtained by appropriately scaling the currents in this equivalent set, and applying the generalized inverse qd transformation:

$$\mathbf{K}_{s_{eq-k}}^{-1}(\theta) = \mathbf{K}^{-1}(\theta - (k-1)\theta_{disp}). \quad (6.129)$$

The original multi-phase secondary voltages can also be readily obtained using the above transformation.

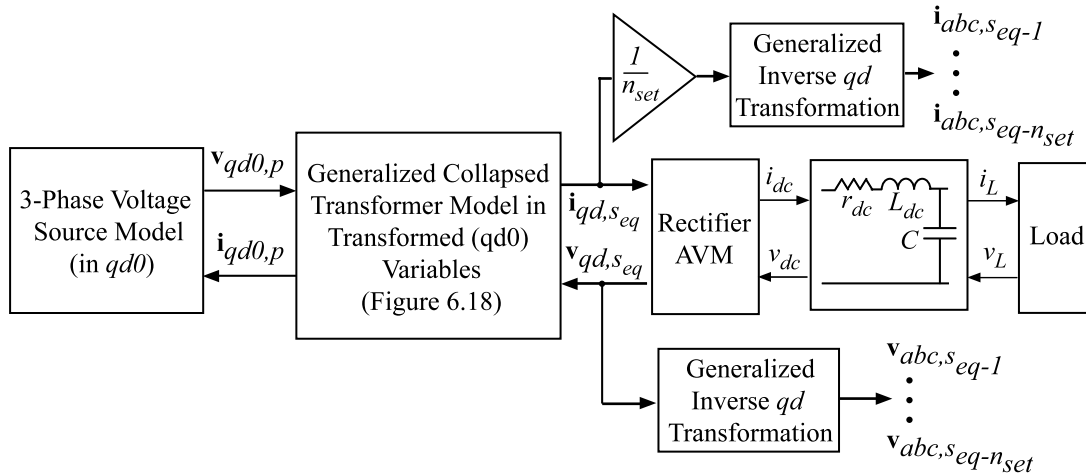


Figure 6.19 Block diagram of the generalized collapsed AVM implementation in SV-based simulators.

6.5.4 Implementation in EMTP-Type Programs

In EMTP-type simulation tools, the ac and dc subsystems may be conveniently implemented using the standard circuit elements that are available as library components. For implementation of the generalized AVM in these packages, it is therefore beneficial to develop the transformer model in phase domain (abc). The generalized transformer model depicted in Figure 6.16 may be rather challenging to implement for the users. The collapsed model of Figure 6.18, however, represents an equivalent single-core three-phase transformer. This model may be implemented using the standard transformer models available in the EMTP-type program libraries.

To further facilitate the model implementation, the collapsed single-core three-phase transformer model may be represented by three separate single-phase equivalent transformers. In the single-core case, different phases are magnetically coupled, whereas in the multi-core case, each phase winding is only coupled to the winding of the same phase. The inductance matrices are hence diagonal matrices in the latter case. The significant

difference between the single-core and multi-core cases arises in presence of the zero sequence.

In order to maintain the validity of the model in presence of the zero sequence, the equivalent diagonalized model for the collapsed transformer may be derived as follows. Considering that all quantities are referred to the primary side, the voltage and flux linkage equations for the collapsed three-phase transformer may be written as

$$\begin{bmatrix} \mathbf{v}_{abc,p} \\ \mathbf{v}'_{abc,s} \end{bmatrix} = \begin{bmatrix} \mathbf{R}_p & 0 \\ 0 & \mathbf{R}'_s \end{bmatrix} \begin{bmatrix} \mathbf{i}_{abc,p} \\ \mathbf{i}'_{abc,s} \end{bmatrix} + \frac{d}{dt} \begin{bmatrix} \boldsymbol{\lambda}_{abc,p} \\ \boldsymbol{\lambda}'_{abc,s} \end{bmatrix}, \quad (6.130)$$

$$\begin{bmatrix} \boldsymbol{\lambda}_{abc,p} \\ \boldsymbol{\lambda}'_{abc,s} \end{bmatrix} = \begin{bmatrix} \mathbf{L}_{pp} & \mathbf{L}_{ps} \\ \mathbf{L}'_{sp} & \mathbf{L}'_{ss} \end{bmatrix} \begin{bmatrix} \mathbf{i}_{abc,p} \\ \mathbf{i}'_{abc,s} \end{bmatrix}, \quad (6.131)$$

$$\mathbf{L}_{pp} = \begin{bmatrix} L_{lp} + L_m & -0.5L_m & -0.5L_m \\ -0.5L_m & L_{lp} + L_m & -0.5L_m \\ -0.5L_m & -0.5L_m & L_{lp} + L_m \end{bmatrix}, \quad (6.132)$$

$$\mathbf{L}'_{ss} = \begin{bmatrix} L'_{ls} + L_m & -0.5L_m & -0.5L_m \\ -0.5L_m & L'_{ls} + L_m & -0.5L_m \\ -0.5L_m & -0.5L_m & L'_{ls} + L_m \end{bmatrix}, \quad (6.133)$$

$$\mathbf{L}_{ps} = \begin{bmatrix} c_2 L_{lp} + L_m & -0.5L_m & -0.5L_m \\ -0.5L_m & c_2 L_{lp} + L_m & -0.5L_m \\ -0.5L_m & -0.5L_m & c_2 L_{lp} + L_m \end{bmatrix}, \quad (6.134)$$

$$\mathbf{L}'_{sp} = \begin{bmatrix} c_2 L'_{ls} + L_m & -0.5L_m & -0.5L_m \\ -0.5L_m & c_2 L'_{ls} + L_m & -0.5L_m \\ -0.5L_m & -0.5L_m & c_2 L'_{ls} + L_m \end{bmatrix}. \quad (6.135)$$

Adding and subtracting $-0.5L_m$ at the right side of (6.131):

$$\begin{bmatrix} \boldsymbol{\lambda}_{abc,p} \\ \boldsymbol{\lambda}'_{abc,s} \end{bmatrix} = \begin{bmatrix} \mathbf{L}_{pp}^* & \mathbf{L}_{ps}^* \\ \mathbf{L}'_{sp} & \mathbf{L}'_{ss} \end{bmatrix} \begin{bmatrix} \mathbf{i}_{abc,p} \\ \mathbf{i}'_{abc,s} \end{bmatrix} - 0.5L_m \mathbf{[1]}_{6 \times 6} \begin{bmatrix} \mathbf{i}_{abc,p} \\ \mathbf{i}'_{abc,s} \end{bmatrix}, \quad (6.136)$$

$$\mathbf{L}_{pp}^* = \begin{bmatrix} L_{lp} + 1.5L_m & 0 & 0 \\ 0 & L_{lp} + 1.5L_m & 0 \\ 0 & 0 & L_{lp} + 1.5L_m \end{bmatrix}, \quad (6.137)$$

$$\mathbf{L}_{ss}^* = \begin{bmatrix} L'_{ls} + 1.5L_m & 0 & 0 \\ 0 & L'_{ls} + 1.5L_m & 0 \\ 0 & 0 & L'_{ls} + 1.5L_m \end{bmatrix}, \quad (6.138)$$

$$\mathbf{L}_{ps}^* = \begin{bmatrix} c_2 L_{lp} + 1.5L_m & 0 & 0 \\ 0 & c_2 L_{lp} + 1.5L_m & 0 \\ 0 & 0 & c_2 L_{lp} + 1.5L_m \end{bmatrix}, \quad (6.139)$$

$$\mathbf{L}_{sp}^* = \begin{bmatrix} c_2 L'_{ls} + 1.5L_m & 0 & 0 \\ 0 & c_2 L'_{ls} + 1.5L_m & 0 \\ 0 & 0 & c_2 L'_{ls} + 1.5L_m \end{bmatrix}. \quad (6.140)$$

The model defined by (6.130), (6.136)-(6.140) can be represented by the equivalent circuit depicted in Figure 6.20. The advantage of the equivalent circuit of Figure 6.20 is that it can be readily defined using most conventional R and L branches that are available in most simulation packages.

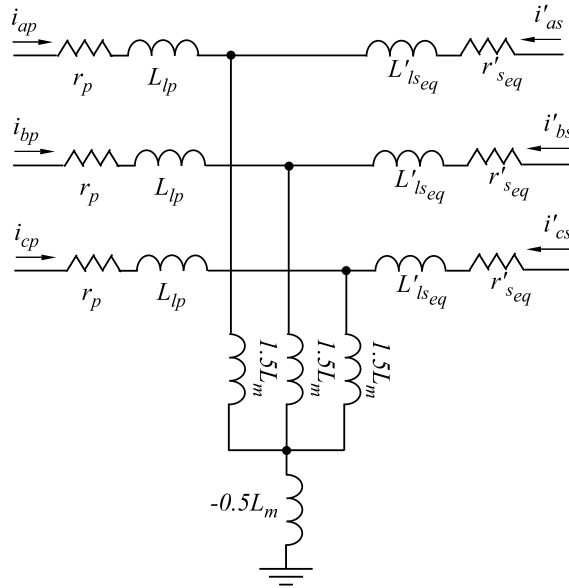
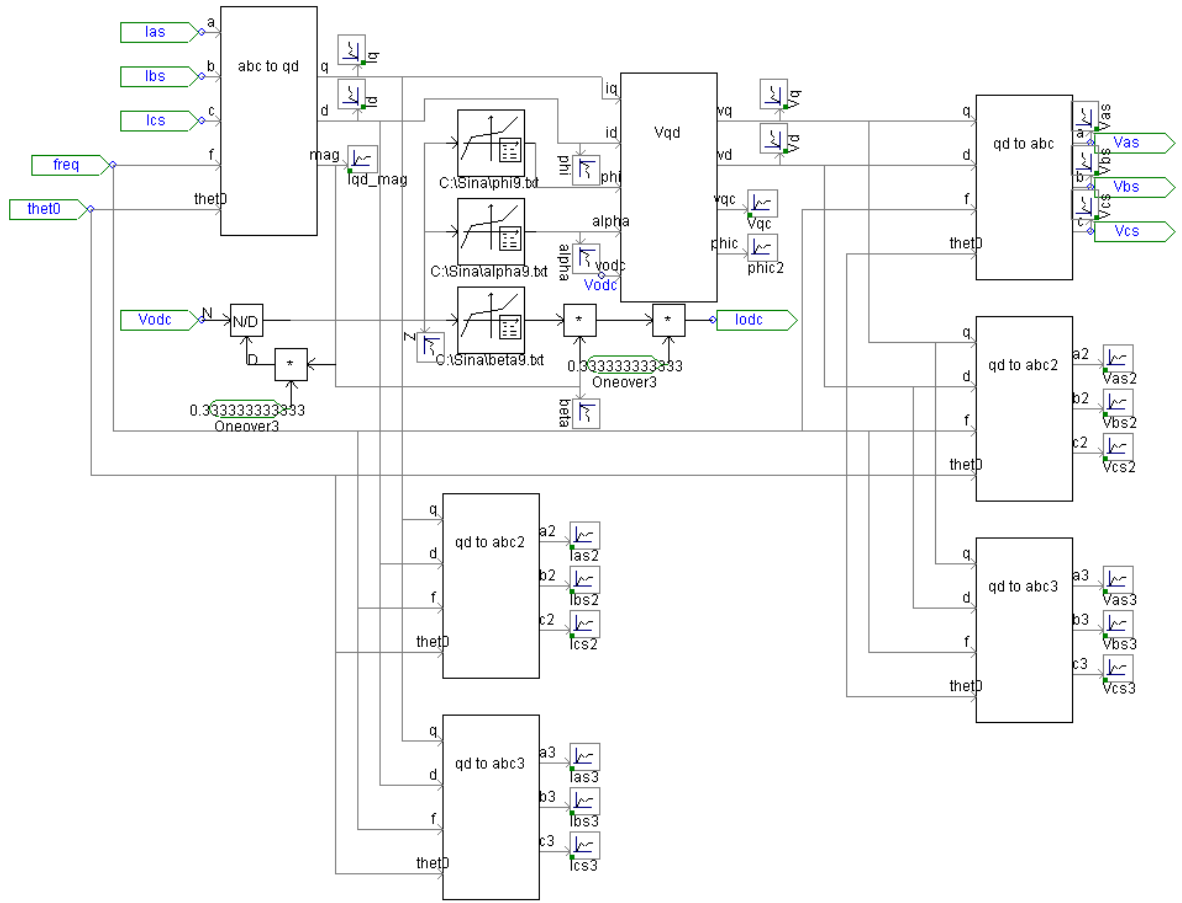


Figure 6.20 Equivalent circuit of the collapsed transformer model in phase (abc) variables.

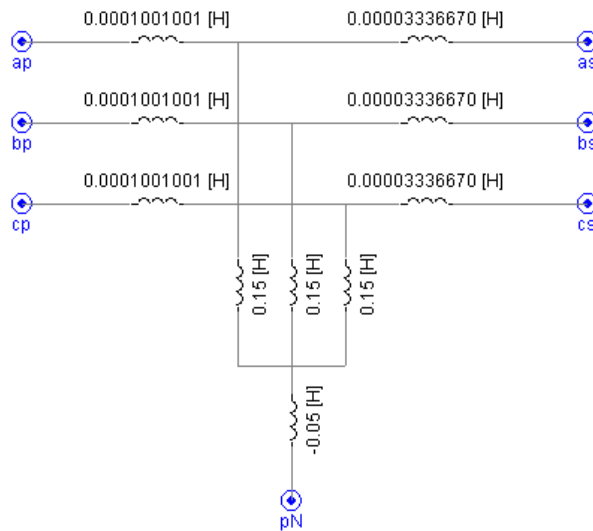
For implementation of the generalized AVM in EMTP-type packages, the interfacing techniques discussed in Chapter 3 have to be employed. Since the model was developed based on the parametric approach, the indirect interfacing technique depicted in Figure 3.9 may be conveniently adopted for this model.

Snapshots of the dynamic average model for the 18-pulse example system implemented in PSCAD/EMTDC [11] are shown in Figure 6.21 and Figure 6.22. Figure 6.21 (a) illustrates the AVM wherein the look-up tables for parametric functions as well as the transformation blocks between abc and qd variables are shown. The whole subsystem of Figure 6.21 (a) forms the PAVM Diode Rectifier block depicted in Figure 6.22 (a). This module is interfaced with the ac and dc subsystems at the input and output ports according to the implementation shown in Figure 3.9 using the dependent sources.

The complicated multi-phase transformer is conveniently represented in phase domain by its collapsed three-phase equivalent model depicted in Figure 6.20. Figure 6.21 (b) shows the contents of the transformer module where the magnetizing branch and leakages are constructed using standard library components. The primary and secondary resistances have been placed outside of this block in Figure 6.22 (a) for the mere purpose of avoiding syntax errors. Finally, the transformer-rectifier combination is encapsulated into a single subsystem-module as shown in Figure 6.22 (b), which can replace the detailed switching sub-circuit of the original high-pulse-count converter system.

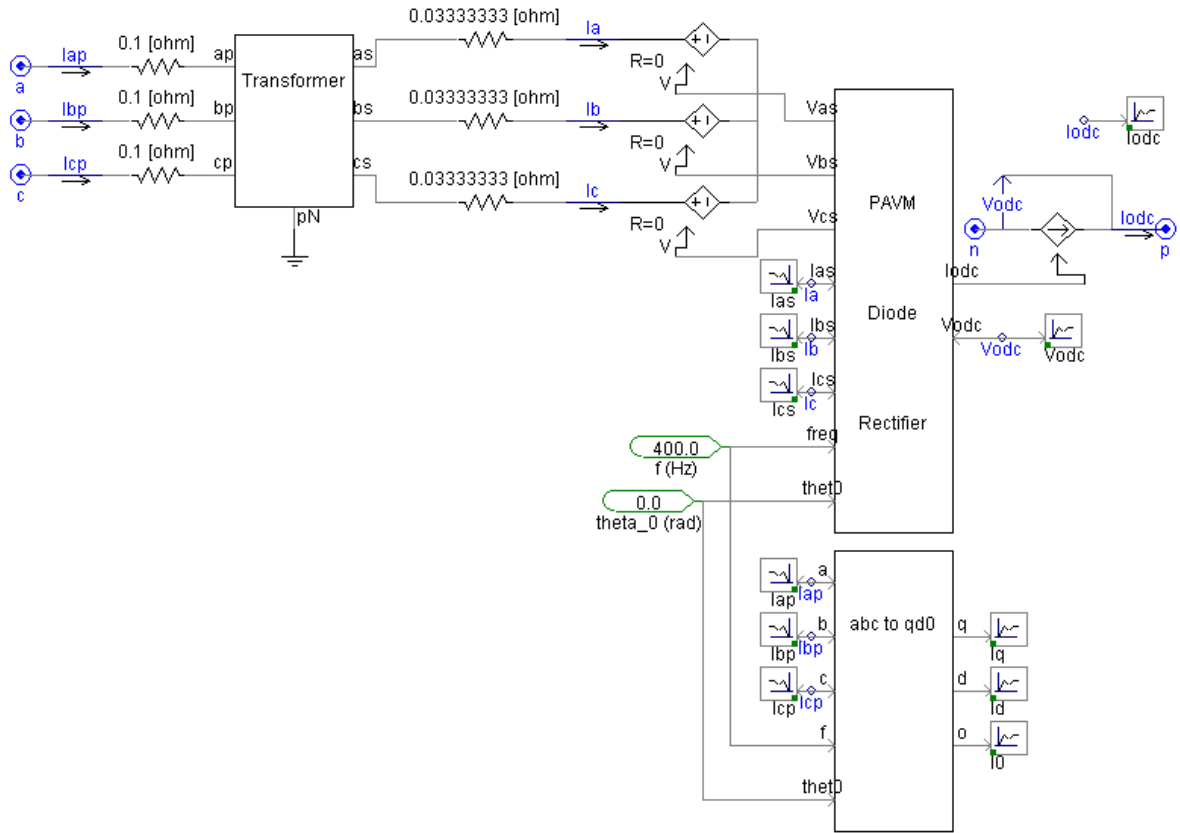


(a)

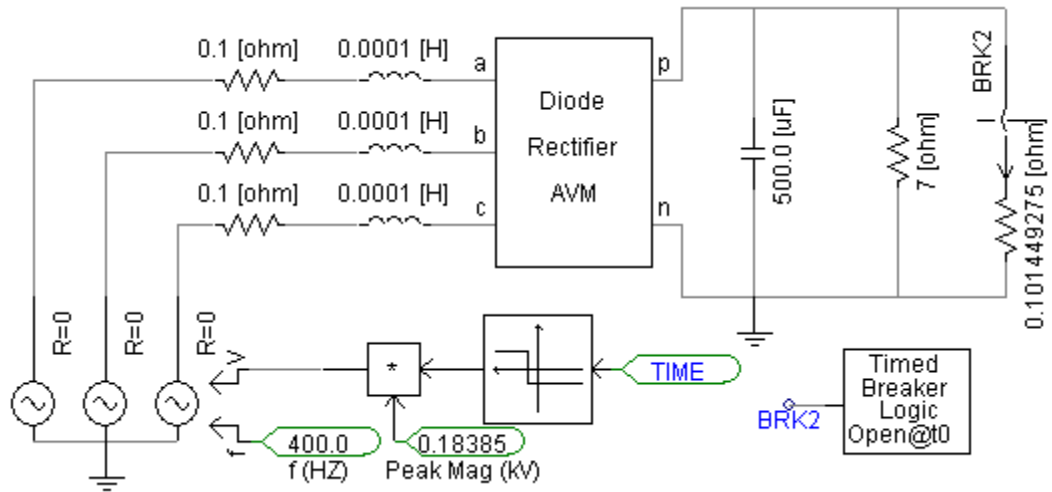


(b)

Figure 6.21 Example of the generalized dynamic AVM implementation in PSCAD: (a) details of the PAVM module; and (b) details of the equivalent-collapsed transformer model.



(a)



(b)

Figure 6.22 Example of the generalized dynamic AVM implementation in PSCAD: (a) interfacing the PAVM and transformer blocks; and (b) AVM module with external ac and dc subsystems.

6.6 Model Verification in Time Domain

In order to investigate the generalized methodology developed in the previous Sections, this methodology is applied to the 18-pulse example system depicted in Figure 6.2 with parameters summarized in Appendix B. The resulting models have been implemented in MATLAB/Simulink [4] and PSCAD/EMTDC [11]. It is generally observed that the results obtained by both simulation packages are essentially identical provided that the time step and solver properties (time step limits and error tolerances) are adjusted appropriately. The responses of the system as predicted by the dynamic average model based on the proposed methodology are compared against a detailed switching implementation of the system together with the reduced-order Analytical Average-Value Model (AAVM) [65] reviewed in Section 6.5.1. These results are compared in time and frequency domains.

6.6.1 Steady-State Analysis

A suitable measure for comparing the detailed and average models in different operational modes is the regulation characteristic of the 18-pulse rectifier system depicted in Figure 6.23. This characteristic may be obtained by varying the load from open circuit to short circuit and recording the dc bus voltage and current. In Figure 6.23, these values, \bar{v}_{dc} , \bar{i}_{dc} , have been normalized by their corresponding maximum values, i.e., open-circuit and short-circuit, as predicted by the detailed model. It is evident that the values of short-circuit current and open-circuit voltage are incorrectly predicted by the AAVM since this model is only valid during Mode 5 (7-6 valve) operation which lies between these two extreme cases (see the boxed region in Figure 6.23). As seen in this figure, the characteristic predicted by AAVM provides an acceptable match with those of the detailed and proposed GAVM in the majority of this region where this model remains valid. The corresponding error is due to idealized representation of the transformer and the existence of other operating modes that are not considered in this model.

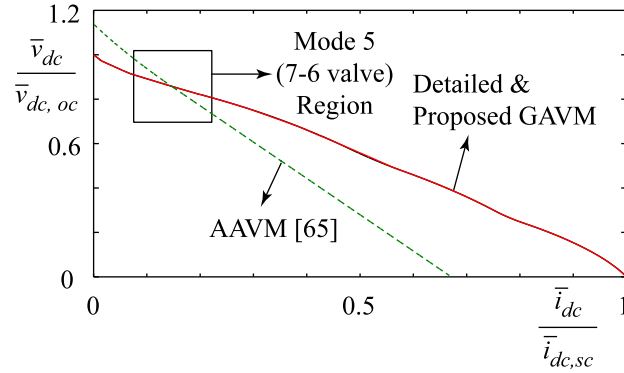


Figure 6.23 Regulation characteristic of the 18-pulse rectifier system as predicted by various models.

6.6.2 Transient Analysis under Balanced Conditions

In order to demonstrate the effect of system dynamic order, time-domain transient studies are considered for two different topologies of this system, i.e., without and with the dc filter capacitor. In the first case, an adjustable resistive load is connected directly at the dc bus. The load is initially set to $R_L = 7 \Omega$. At $t = 2.5 \text{ ms}$, the load is stepped to $R_L = 14 \Omega$. During this transient, the system operation remains in Mode 5 (see Table 6.1) and hence the AAVM [65] remains valid. The corresponding transient responses as observed in the dc bus current and voltage, a -phase secondary s_1 current, and a -phase primary current are shown in Figure 6.24. As seen there, while the AAVM [65] also predicts somehow acceptable results in the first half of the transient, the responses predicted by the proposed model provide a much closer agreement with the detailed model. As explained earlier, in AAVM [65], the dynamics of transformer as well as the magnetizing branch are essentially neglected and the model is hence of lower order. Therefore, it is expected to observe some error compared to the detailed and proposed average models.

In the next study, the load resistance is initially set $R_L = 7 \Omega$. Then, at $t = 3.5 \text{ ms}$, the load is stepped to $R_L = 0.1 \Omega$ which forces the system deep into Mode 10 (9-valve) operation (see Table 6.1). Figure 6.25 illustrates the transient responses of all models as

observed in the dc bus current and voltage, as well as the primary and secondary currents. As seen in this figure, the AAVM fails to predict the transition to Mode 10 and produces erroneous results. However, the proposed model accurately predicts the transient response in the whole region.

For a closer comparison, the three-phase primary currents and the nine-phase secondary voltages and currents as predicted by the detailed and the proposed average model are illustrated in Figure 6.26 and Figure 6.27. The responses of the AAVM are not superimposed on these plots will not provide sufficient accuracy. As observed in Figure 6.26 (top plot), the detailed and average-models essentially provide identical results at the primary side. This is an important observation as it demonstrates that from a system-level point of view, the use of detailed switching model is deemed unnecessary as it does not offer significant additional information with respect to the average model. Moreover, the average model is more efficient than the detailed model especially for the high-pulse-count converter systems with a rather high switching frequency. Executing the detailed simulation is a very time-consuming task in this case as it would require much smaller time steps as the frequency increases. This becomes even more challenging in system-level studies with multiple converters. Recalling the results of Figure 6.25, such a conclusion also applies when the dc sub-system is of particular interest because the ripple on the dc side waveforms is also significantly reduced in high-pulse-count systems.

The results of Figure 6.26 and Figure 6.27, however, demonstrate that the voltages and currents at the transformer secondary side are the only places where the additional information provided by the detailed model is visible (in terms of more accurately predicting the waveform harmonics). The increased simulation efficiency of the average model, in fact, has come at the price of not thoroughly predicting the switching harmonics present in these waveforms as compared to the switching model. However, as seen in these figures, the

secondary voltage and current waveforms predicted by the detailed and average models are very close at light load and heavy load operation, respectively.

Next, a small-signal analysis is performed on the proposed GAVM and AAVM about the operating points in Modes 5 and 10, respectively. Since these AVMs are continuous, obtaining the linear small-signal state-space description of the system from these models becomes an automated and almost instantaneous procedure in many commercial simulation software packages such as Simulink [4]. The resulting eigenvalues of the AVMs obtained for Modes 5 (7-6 valve) and 10 (9-valve) are provided in Table 6.2. The proposed model, in both cases, contains two pairs of complex conjugate eigenvalues and resembles a fourth-order system. The AAVM is a reduced-order model with a single real eigenvalue. These eigenvalues coincide with the transient responses observed in Figure 6.24 -Figure 6.27.

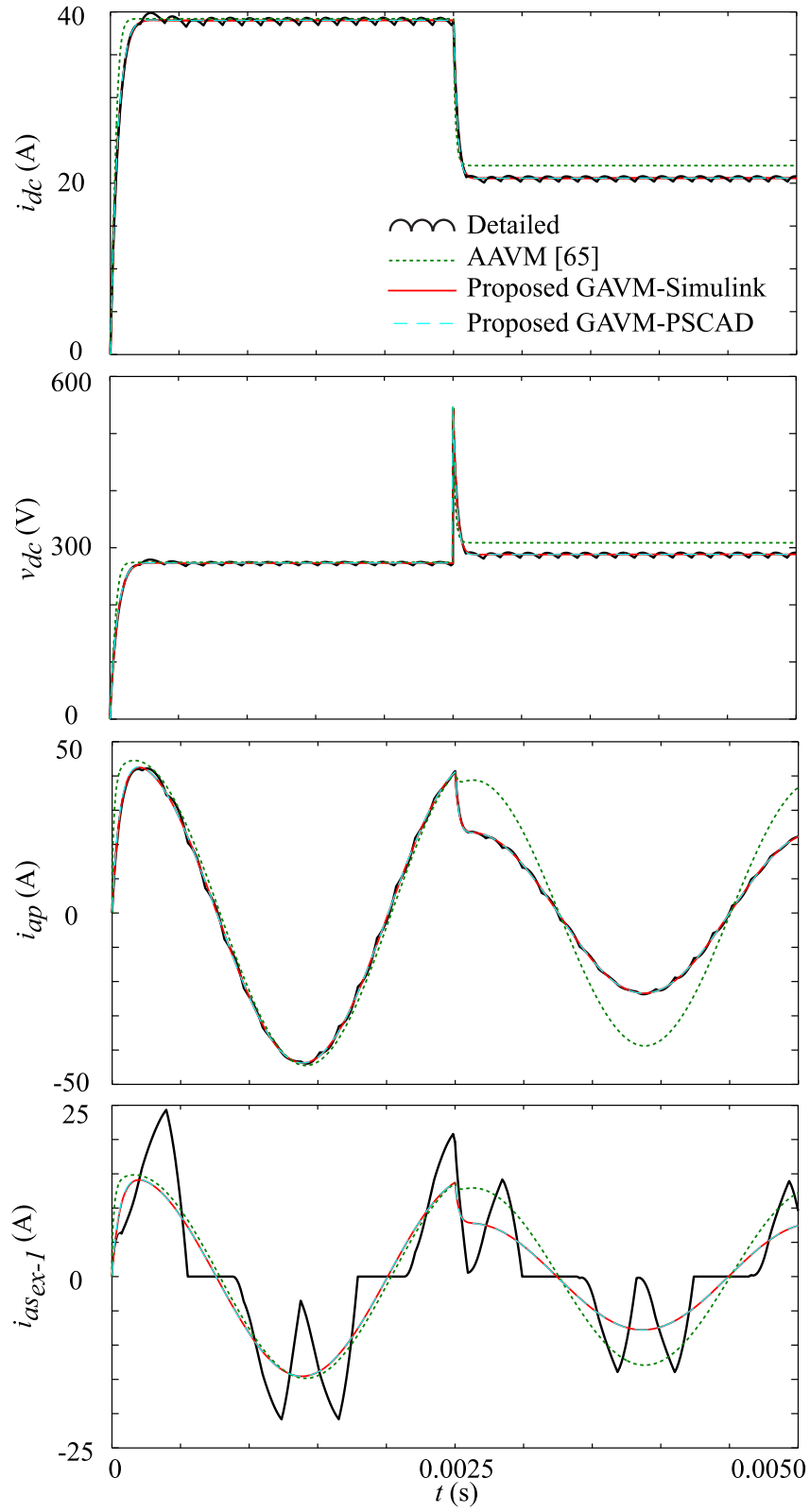


Figure 6.24 Transient response of the 18-pulse rectifier system (without dc filter capacitor) within Mode 5 (7-6 valve) as predicted by various models.

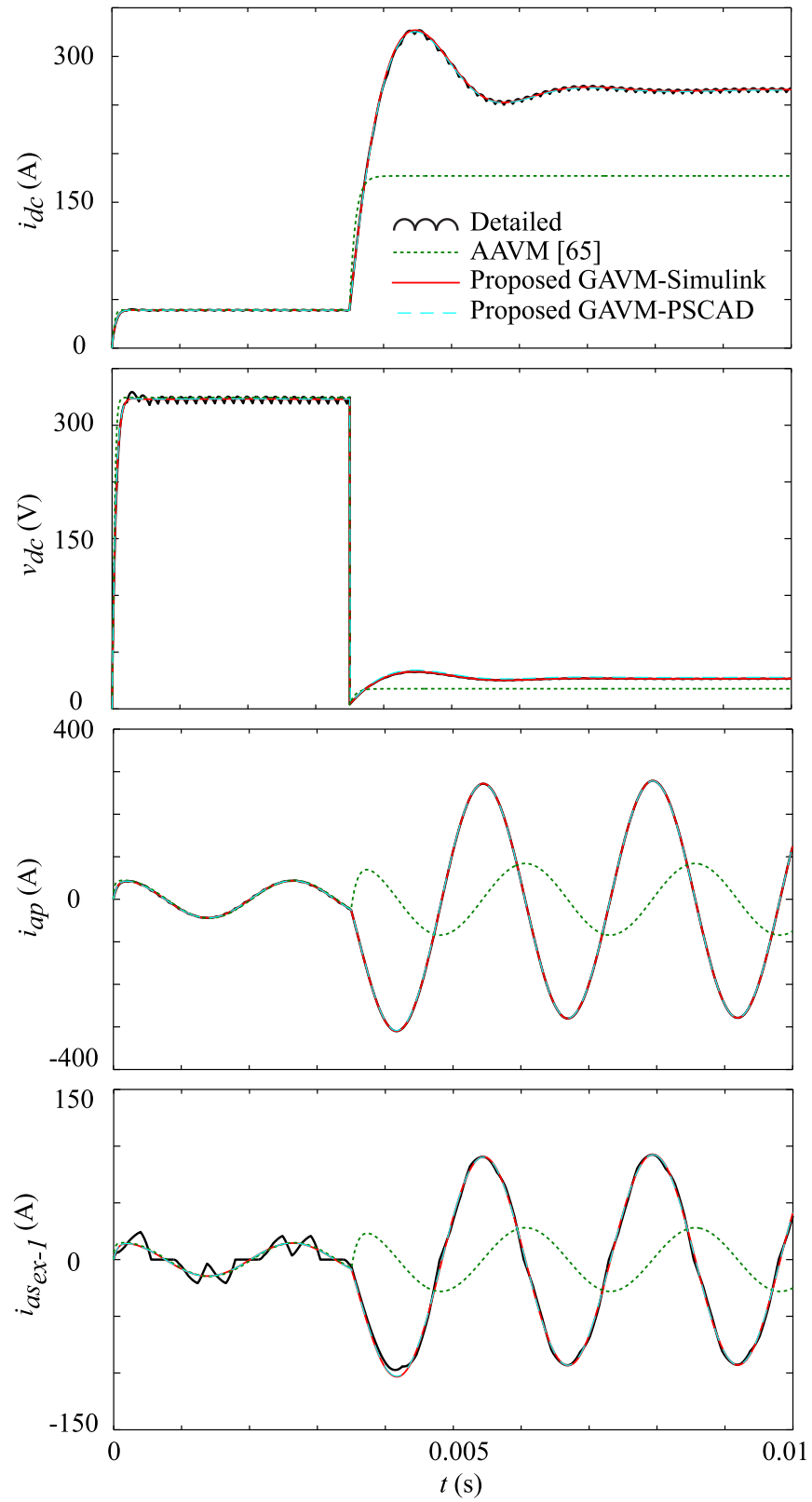


Figure 6.25 Transient response of the 18-pulse rectifier system (without dc filter capacitor) during a transient from Mode 5 (7-6 valve) to Mode 10 (9-valve) predicted by various models.

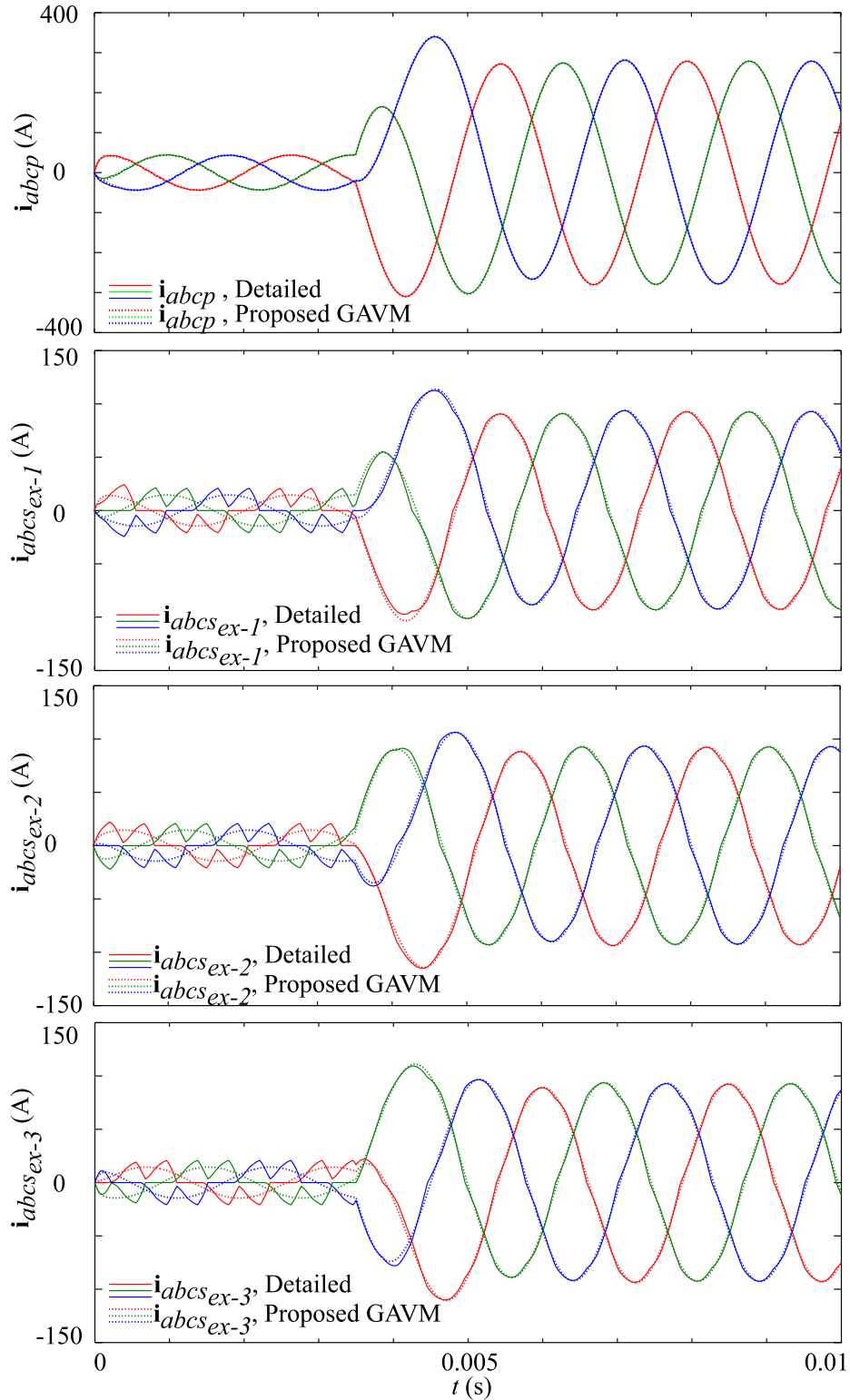


Figure 6.26 Response of the 18-pulse rectifier system (without dc filter capacitor) primary and secondary currents during a transient from Mode 5 (7-6 valve) to Mode 10 (9-valve) as predicted by the detailed and proposed GAVM models.

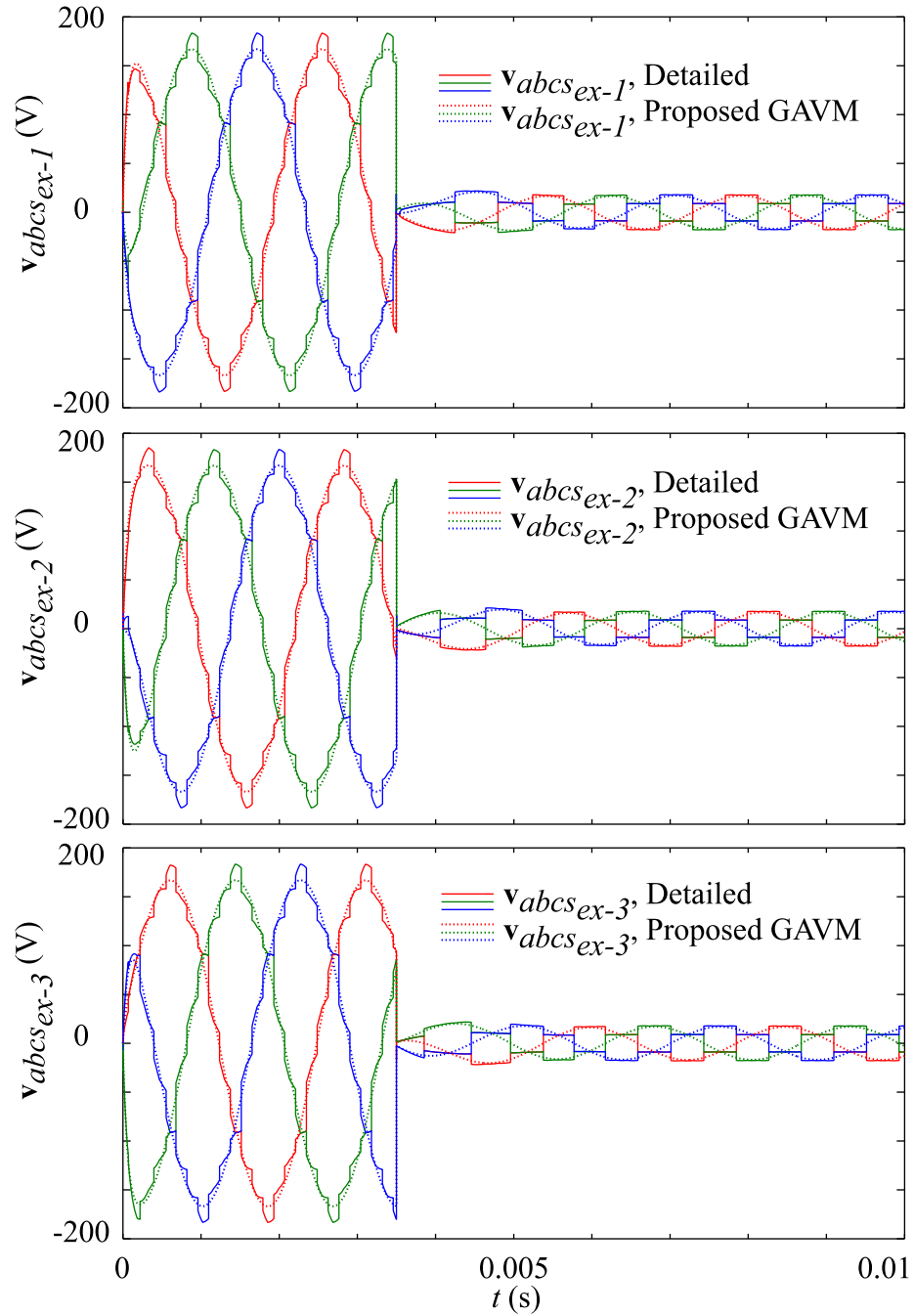


Figure 6.27 Response of the 18-pulse rectifier system (without dc filter capacitor) secondary voltages during a transient from Mode 5 (7-6 valve) to Mode 10 (9-valve) as predicted by the detailed and proposed GAVM models.

Table 6.2 Eigenvalues of the 18-pulse rectifier system (without dc capacitor) in Mode 5 (7-6-valve) and Mode 10 (9-valve) as predicted by AVMs.

Equivalent load	$R_L = 7 \Omega$	$R_L = 0.1 \Omega$
Proposed GAVM	$-1.3 \pm 2513.3j$ $-17006.6 \pm 5994.1j$	$-0.4 \pm 2513.3j$ $-1258.7 \pm 2529.7j$
AAVM [65]	-51262	-12220

Next, the behavior of the system is examined in the presence of dc filter capacitor which results in an increase in the order of the system by one. In the following case study, the load is initially set to $R_L = 10 \Omega$. The load is then stepped up to $R_L = 100 \Omega$ at $t = 5 \text{ ms}$ to force the system into Mode 1 (4-2 valve) operation. The transient responses of all models as observed in the dc and ac sides are illustrated in Figure 6.28. In Figure 6.29, the three-phase primary and nine-phase secondary currents predicted by the detailed and proposed average model have been illustrated for better comparison. Zoomed-in views of the plots of Figure 6.29 are provided in Figure 6.30.

Although the AAVM is mathematically valid for Mode 5 operation, the degraded and reduced-order performance of this model is evident in the first half of this study. In the AAVM as seen in Table 6.3 and Table 6.2, in presence and absence of the dc capacitor, the fifth- and fourth-order system is approximated by its second- and first-order representation, respectively. Moreover, in Mode 1, the AAVM is not valid and leads to erroneous results. The results predicted by the proposed GAVM, however, provide an excellent match with those of the detailed model during the whole transient study.

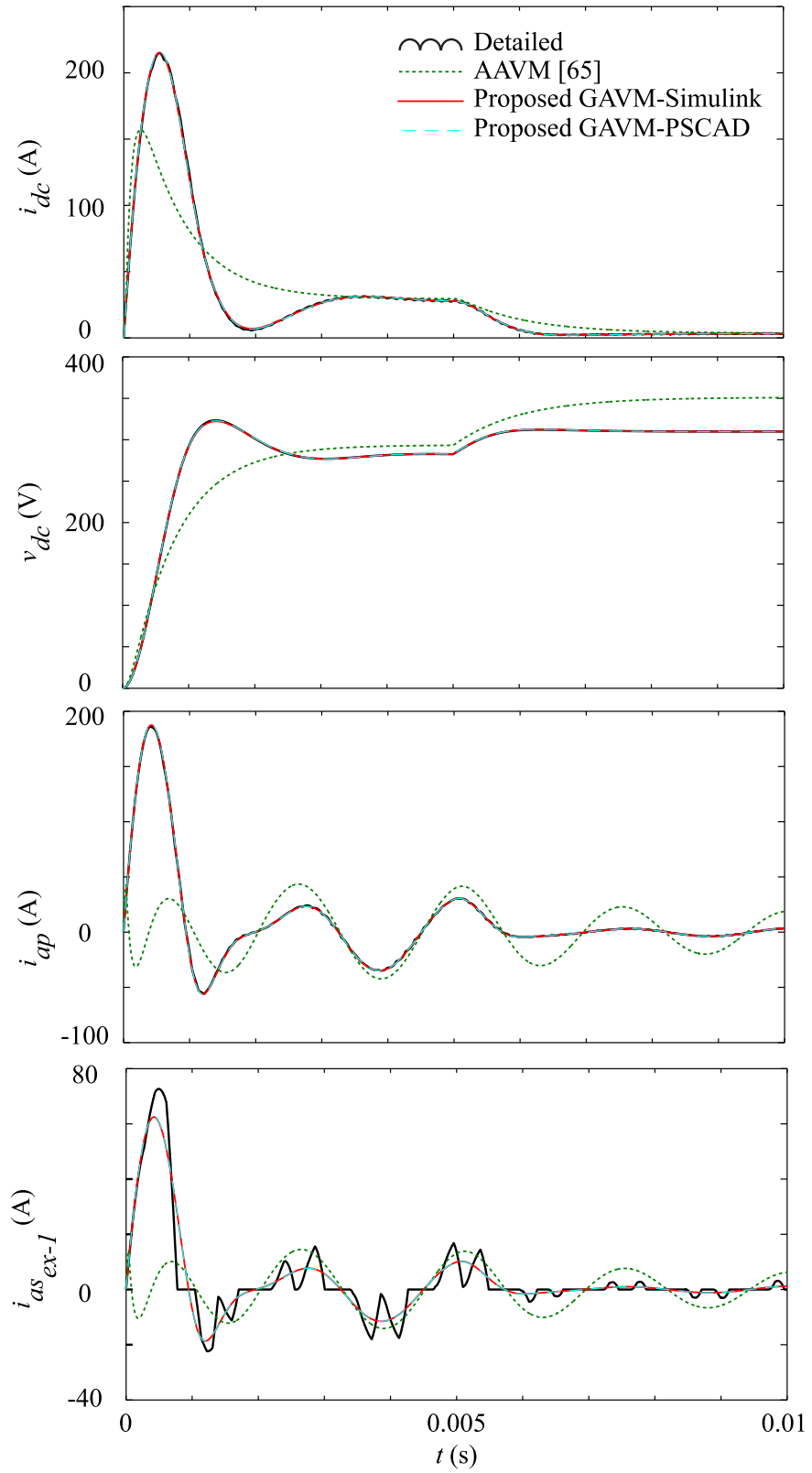


Figure 6.28 Transient response of the 18-pulse rectifier system during a transient from Mode 5 (7-6 valve) to Mode 1 (4-2 valve) in the presence of dc filter capacitor as predicted by various models.

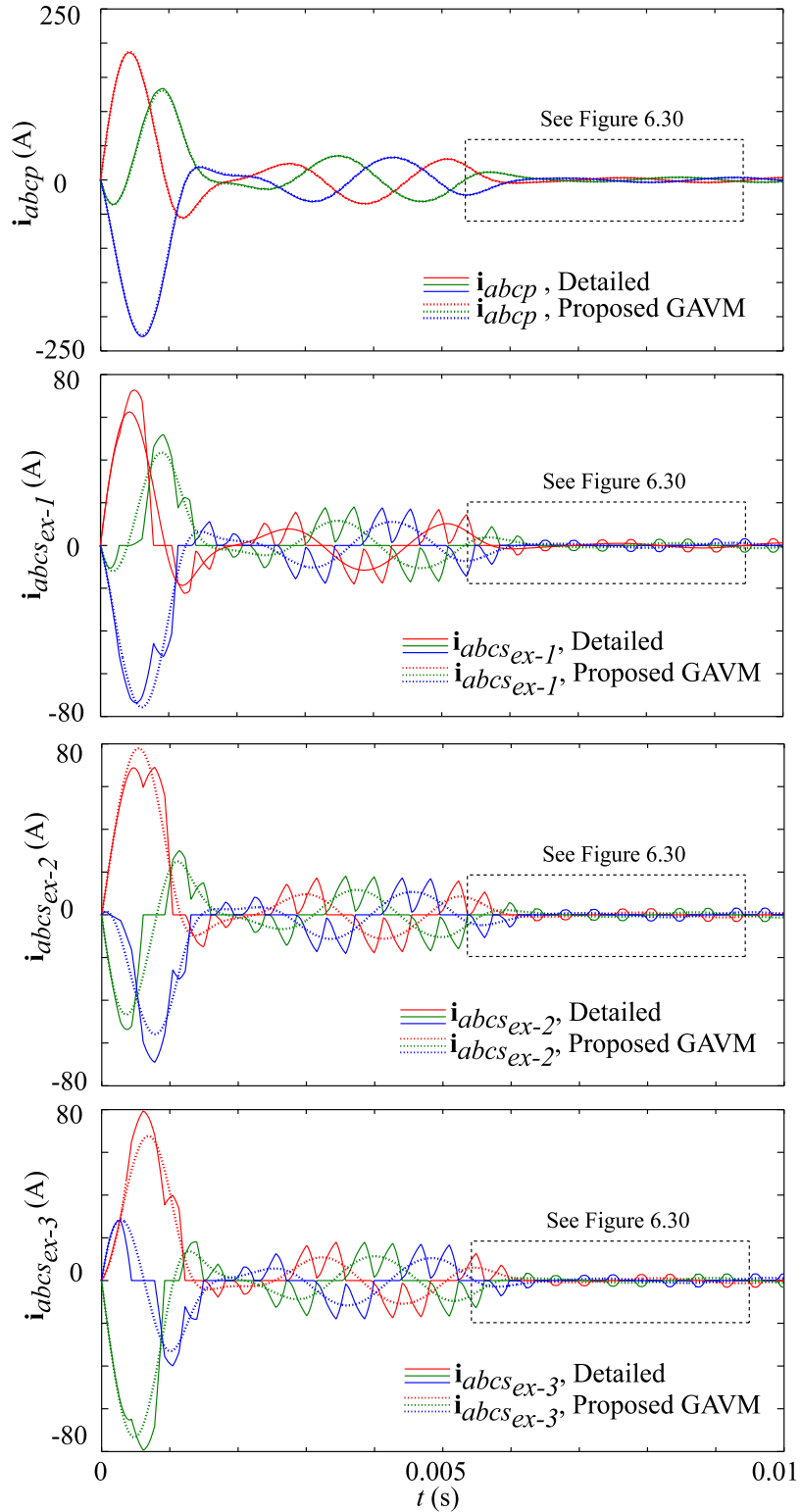


Figure 6.29 Transient response of the 18-pulse rectifier system primary and secondary currents during a transition from Mode 5 (7-6 valve) to Mode 1 (4-2 valve) in the presence of dc capacitor as predicted by detailed and proposed GAVM models.

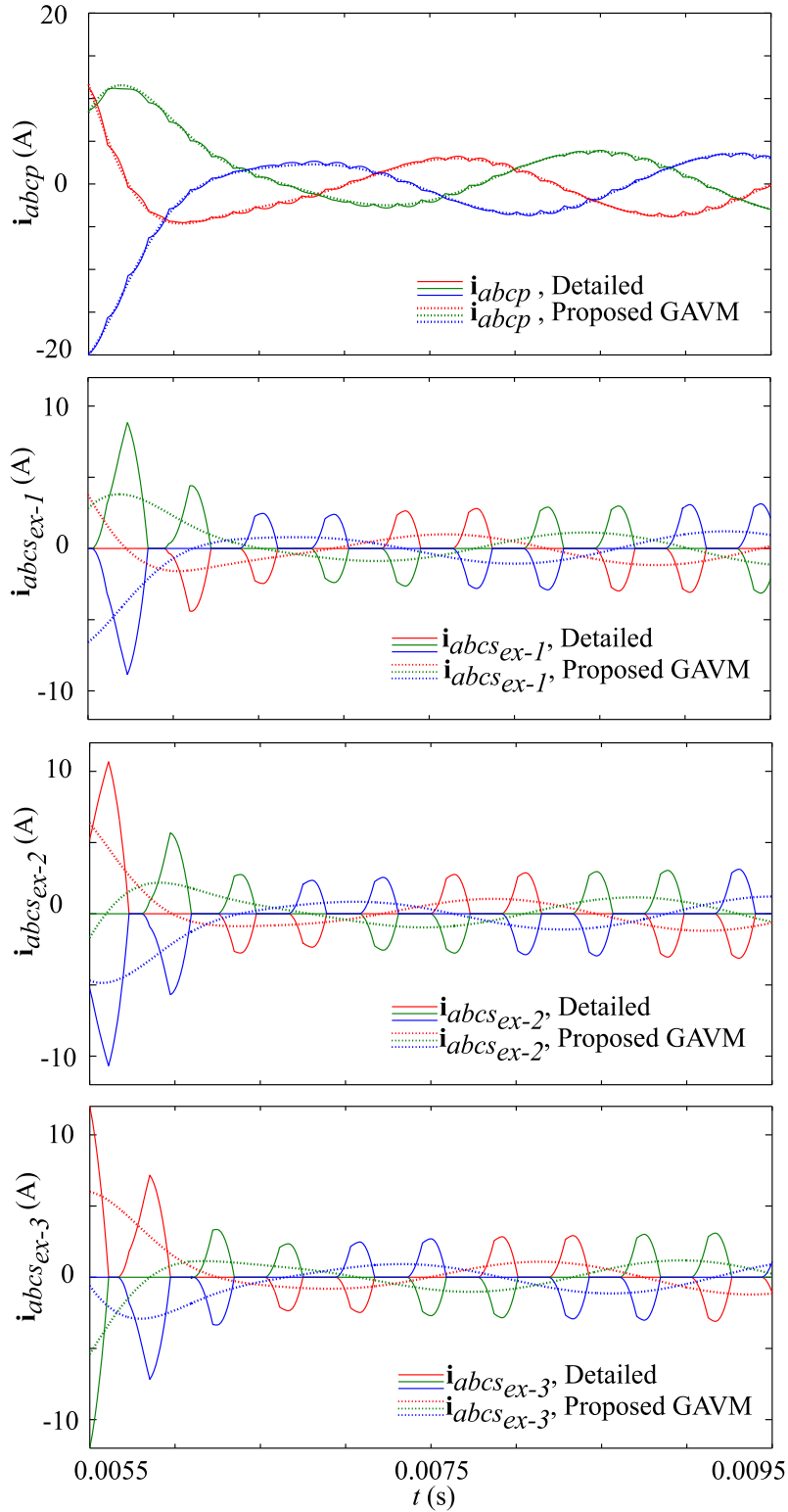


Figure 6.30 Zoomed-in view of the 18-pulse rectifier system primary and secondary currents during Mode 1 (4-2 valve) operation in the presence of dc capacitor as predicted by detailed and proposed GAVM models.

Table 6.3 Eigenvalues of the 18-pulse rectifier system with dc capacitor in Mode 5 (7-6 valve) and Mode 1 (4-2 valve) as predicted by different AVMs.

Average Model	$R_L = 10 \Omega$	$R_L = 100 \Omega$
Proposed GAVM	-22903 $-1 \pm 2513.3j$ $-1144.1 \pm 2039j$	-215475 $-1.2 \pm 2513.3j$ -3369.9 -1354.8
AAVM [65]	-7579.8 -1376.5	-4140.1 -1012.1

6.6.3 Transient Analysis under Unbalanced Conditions

In the following study, the performance of proposed generalized average model is investigated under unbalanced excitation and presence of the zero sequence at the primary side of the transformer. For this purpose, the neutral points of the three-phase source and the transformer primary are both grounded, the dc filter capacitor is added at the dc bus, and the system is started under a balanced three-phase excitation with a load of $R_L = 7 \Omega$ connected at the output. At $t = 0.006 s$, the asymmetry is introduced when the magnitude of one of the phase voltages e_{cs} is reduced by 30 percent. In practice, such a fault may happen as a result of a partial short circuit in one of the phases at the input source. Thereafter, at $t = 0.012 s$, the load is stepped down to $R_L = 0.1 \Omega$ and the simulation is run until $t = 0.018 s$. The dc bus current and voltages as well as the secondary and primary currents predicted by all models are illustrated in Figure 6.31. As seen in this figure, the responses predicted by the proposed GAVM provide a close match with those of the detailed switching model. In addition to neglecting the dynamics of the transformer and the magnetizing current, the results provided by the AAVM are significantly degraded due to the unbalanced input and presence of the zero sequence since this model has been developed assuming a balanced 9-phase source, and hence the zero component is omitted from calculations.

The three-phase ac currents as predicted by the detailed and proposed average models are shown in Figure 6.32 (top plot). As it has been already demonstrated that the AAVM does not provide sufficient accuracy, and this model is considered in Figure 6.32. As seen in this figure, the asymmetric phase currents are accurately predicted by the parametric model during the whole transient. The transformed ($qd0$) primary currents are illustrated in Figure 6.33 (left plots), wherein it is seen that the zero sequence current is predicted accurately by the proposed average model.

The secondary 9-phase currents as predicted by the detailed and proposed average models are also illustrated in Figure 6.32. This figure shows a close agreement between the responses of these models despite a lower level of detail being predicted in the deformed waveforms of the proposed model. This is due the fact that the higher-frequency dynamics have been averaged out in this model. In terms of transformed variables (in qd domain), as seen in Figure 6.33 (right plots), these quantities would be constant in steady state under balanced operating conditions. Under unbalanced excitation, the bridges only see the line voltages, and the zero sequence is hence not transferred to the secondary side. The qd components of these waveforms, however, include some oscillations of the ac line frequency. The superimposed higher-frequency ripple due to switching is averaged out in the proposed model which leads to omission of higher-frequency harmonics of the waveforms. It has been demonstrated that given the valuable gains in terms of numerical efficiency, simplicity, and ease of implementation, such averaging is extremely beneficial. The proposed generalized dynamic average model hence makes a valuable tool especially for simulation of larger systems composed of several converters.

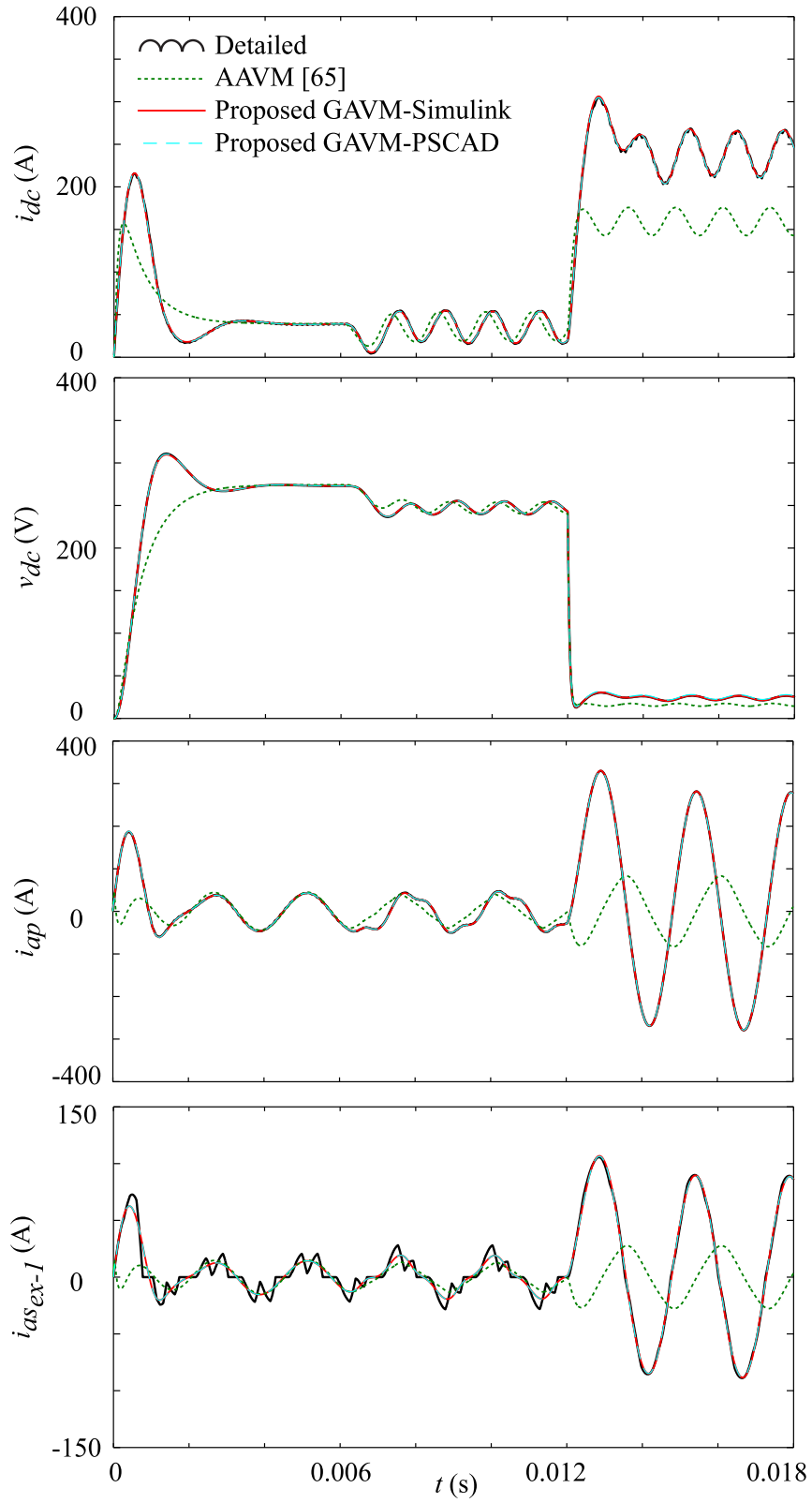


Figure 6.31 Transient response of the 18-pulse rectifier system to a change in the input voltage leading to unbalanced operation in ac side as predicted by various models.

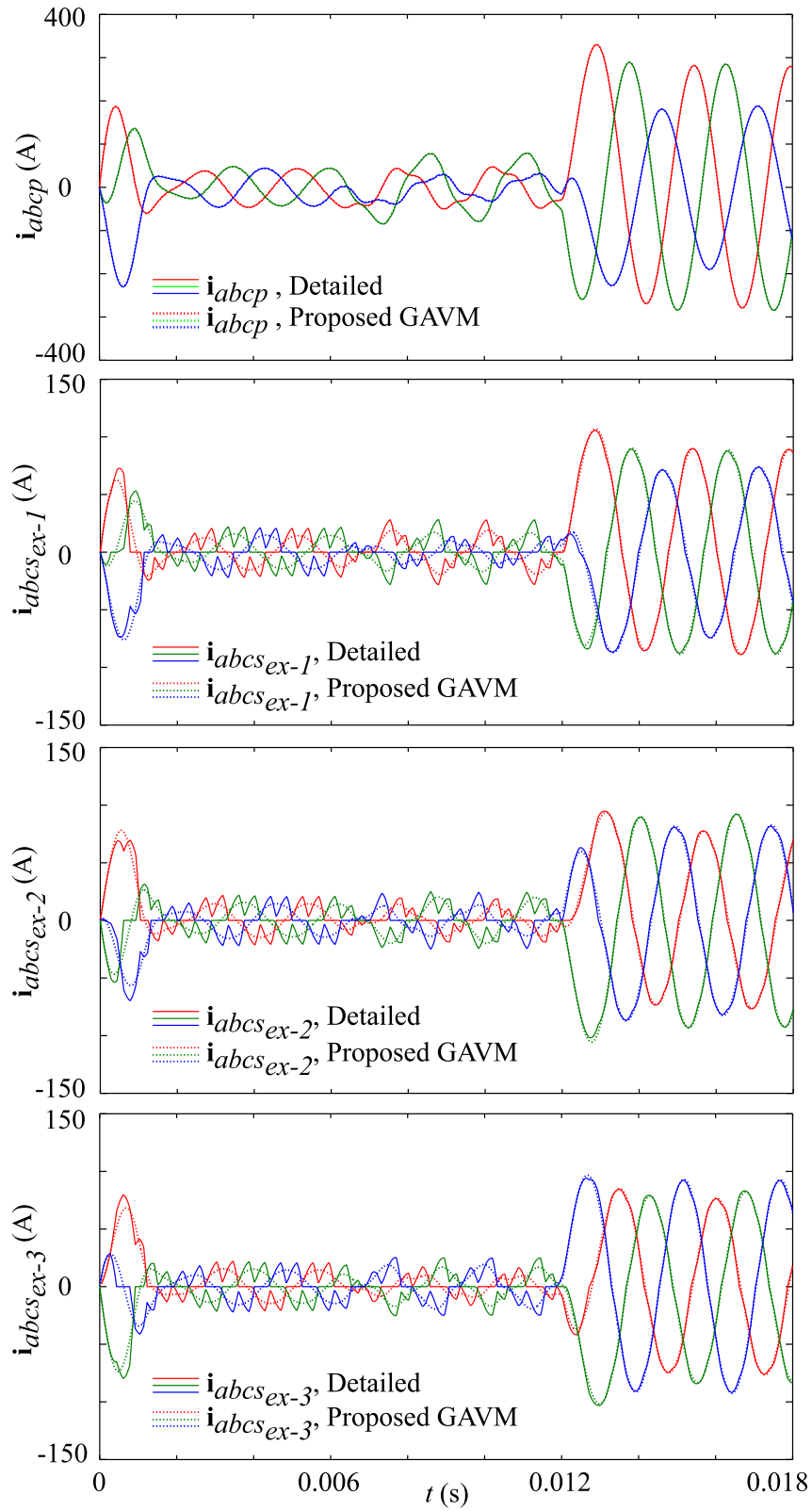


Figure 6.32 Response of the 18-pulse rectifier system primary and secondary currents during a transient leading to unbalanced operation as predicted by detailed and proposed GAVM models.

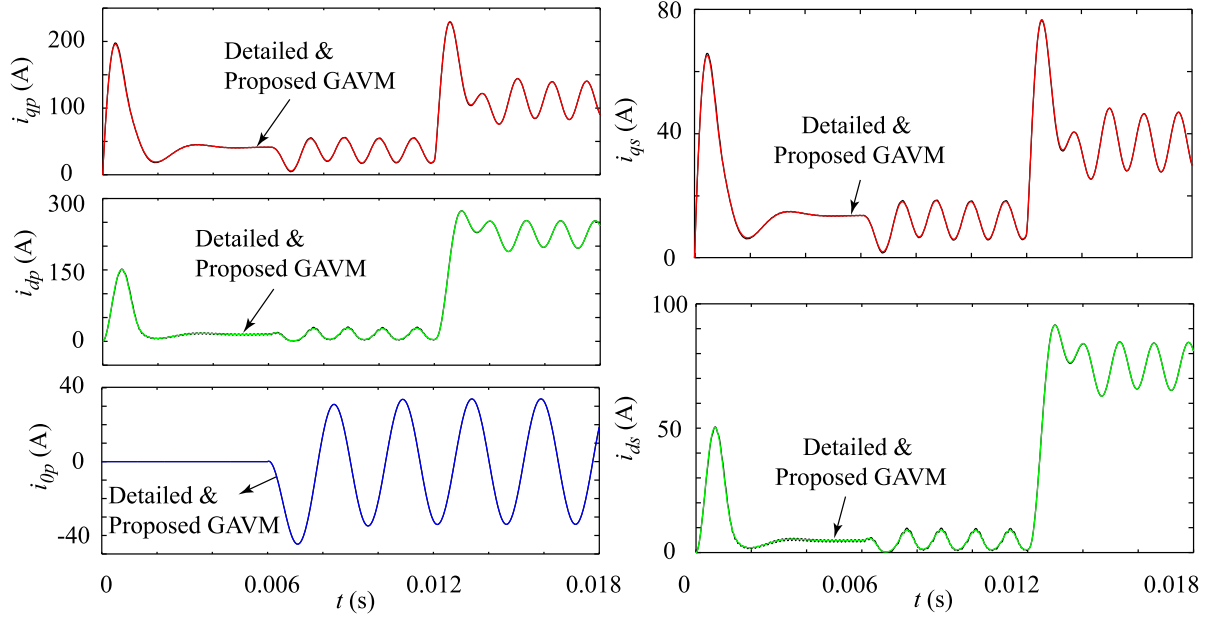


Figure 6.33 Response of the 18-pulse rectifier system primary and secondary currents in transformed $qd0$ variables during a transient leading to unbalanced operation as predicted by detailed and proposed GAVM models.

The transient study presented in this Section has been carried out using Matlab/Simulink [4] and PSCAD/EMTDC [11] run on a personal computer (PC) with 2.83 GHz Intel® Core™2Quad processor. To demonstrate how effective the AVM can be, the time steps taken by the detailed and proposed generalized average-value models are summarized in Table 6.4. In detailed model, the high frequency switching dynamics of 7.2 KHz (18 times the line frequency of 400 Hz) are present even in steady-state. For accurate sampling of these dynamics (using 10 times the frequency rule of thumb [8]), the upper limit of $13.9 \mu s$ must be applied on the time step. Furthermore, to accurately capture the fast transients corresponding to the system startup, the asymmetric fault, and changes in the load, the time step has to be decreased further at least in the vicinity of these transients. In order to achieve accurate results in Matlab/Simulink [4], where the variable-step integration is readily available, it was found that the ODE45 solver can be used with a maximum allowable time

step of $13.9 \mu s$ and the absolute and relative error tolerances of $2e-4$. To obtain the results of Figure 6.31, the detailed simulation required a total of 4,163 time-steps. Dividing the length of study ($18 ms$) by the total number of time steps, on average, the model is therefore run with the time step of $\Delta t = 4.3 \mu s$. This relatively small step size is required in order to capture all the discontinuity events due to high frequency switching of the 18-pulse converter.

The high-frequency switching does not exist in the AVM, and the upper limit on the time step is solely imposed by the ac line frequency of 400 Hz. For accurate sampling of these dynamics (using the approximate 10 times rule) the upper limit of $250 \mu s$ is applied on the time step. Using the variable-step solver ODE23tb with relative and absolute error tolerances of 0.001 and 0.01, respectively, the GAVM required only 169 time-steps. As seen in Table 6.4, on average, the proposed GAVM runs with $\Delta t = 106.5 \mu s$. This time step is about 25 times larger than what was possible in the detailed switching model. In PSCAD, the GAVM would typically require more time steps since the EMTP-type solution uses a fixed time step. Also, the indirect method of interfacing used in PSCAD implementation of the GAVM allows less increase in the time step as compared to the direct interface achieved in the Simulink implementation. It is observed, however, that $\Delta t = 40 \mu s$ can be easily achieved in this case, which demonstrates the improvement of about an order of magnitude compared to the detailed model (precisely 9.3 times).

Table 6.4 Comparison of simulation time steps for different models.

Models	Total Time Steps	Required Δt (μs)
Detailed Model-Simulink	4,163	13.9 (max) 4.3 (average)
Proposed GAVM-Simulink (Directly Interfaced)	169	250 (max) 106.5 (average)
Proposed GAVM-PSCAD (Indirectly-Interfaced)	451	40 (fixed)

6.7 Model Verification in Frequency Domain

In this Section, the detailed and average models are compared in predicting the frequency-domain characteristics of the considered converter system, i.e., the input (ac) and output (dc) impedances. For this purpose, the system is initially assumed to operate in a steady-state defined by a certain fixed load. A small-signal analysis is then considered around this operating point. Based on the discussions in Section 2.5, the small-signal impedance of the system looking into the dc bus is then considered as

$$Z_{dc} = \frac{\hat{v}_{dc}}{-\hat{i}_{dc}}. \quad (6.141)$$

This impedance is in fact the impedance of the three-phase ac network and the 3-to-9-phase transformer module as mapped through the 18-pulse switching converter to the dc side.

The small-signal output impedance characteristics obtained from the detailed and proposed average models, as well as the AAVM for Mode 5 (7-6 valve), corresponding to the quiescent operating point $R_L = 7 \Omega$ (see Table 6.2), are superimposed in Figure 6.34. It is seen that, although the AAVM is mathematically valid for this mode of operation, it cannot accurately capture the impedance characteristics of the system. At the same time, the

proposed model provides an excellent match with the detailed model in portraying these characteristics. This is due to the fact that dynamics of the ac side have been represented in full detail in the proposed GAVM; whereas in the AAVM these dynamics are partly neglected. The impedance characteristics of Figure 6.34 are shown for a range of frequencies below 10 kHz since for the 18-pulse converter with a 400 Hz ac line frequency the switching frequency is 7.2 kHz. As the switching frequency is approached, it is normal to observe some deviation between the detailed and AVM responses. For the whole range of frequencies depicted in Figure 6.34, however, the results demonstrate an excellent match between the detailed and proposed average models.

Evaluating the input impedance of the system looking from the ac side requires special consideration as discussed in Section 2.5. Adopting the approach discussed therein, a small-signal perturbation has been injected in the q -axis around the operating point defined by $R_L = 0.1 \Omega$ (see Table 6.2), which corresponds to Mode 10 (9-valve). The effects of this perturbation is the impedance Z_{qq} , i.e., the first element of the transfer matrix (2.30). The other elements of the impedance characteristics may be obtained in a similar way. The results obtained from the detailed and proposed average models are superimposed in Figure 6.35. The AAVM results are not been shown in this figure since this model is not valid for this mode of operation. It is seen that the results of the proposed GAVM match those of the detailed model with great accuracy.

To demonstrate the effects of adding the dc capacitor to the system, the small-signal ac impedance characteristics in presence of this capacitor are illustrated in Figure 6.36. The impedance Z_{qq} , obtained from the models by means of linearization around the operating point defined by $R_L = 10 \Omega$, corresponding to Mode 5 (7-6 valve) (see Table 6.3) is illustrated in Figure 6.36. It is seen that the proposed model provides a close match with the detailed model as compared to the AAVM. It is also evident that the detailed and proposed

models represent a higher-order transfer function as compared to the AAVM wherein the dynamics of the ac side are partly neglected.

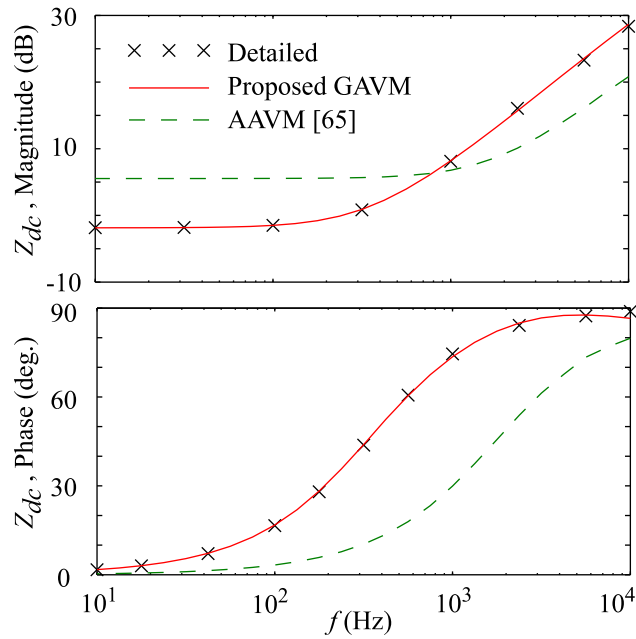


Figure 6.34 Impedance Z_{dc} of the 18-pulse rectifier at dc side in Mode 5 (7-6 valve) without dc capacitor as predicted by various models.

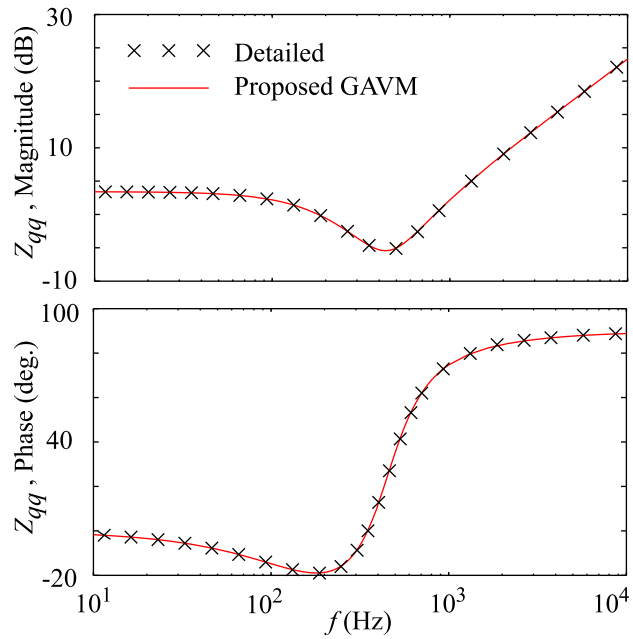


Figure 6.35 Impedance Z_{qq} of the 18-pulse rectifier at the ac side in Mode 10 (9-valve) without dc capacitor as predicted by the detailed and proposed GAVM models.

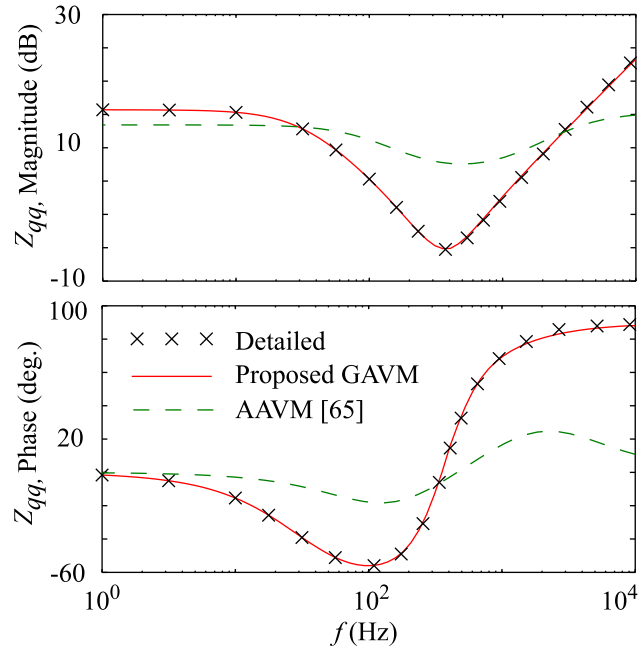


Figure 6.36 Impedance Z_{qq} of the 18-pulse rectifier at the ac side in Mode 5 (7-6 valve) in presence of the dc capacitor as predicted by various models.

Chapter 7: Conclusions and Future Work

7.1 Conclusions and Contributions

The research presented in this thesis leads to more effective modeling of power electronic converter systems. The methodology of developing the so-called dynamic average models (AVMs) for such converters is based on averaging the variables (currents and voltages) within a switching interval and deriving the relationships that govern the dynamics of the system in terms of these averaged variables. The resulting dynamic average models are numerically more efficient compared to the detailed switching models, and hence can execute much faster. This characteristic makes the models suitable for system-level studies of large systems concerned with a large number of power electronic converters. Furthermore, the developed AVMs are suitable for numerical linearization and the respective small-signal analysis.

In particular, a generalized methodology was developed in this thesis that can be applied to an arbitrary high-pulse-count line-commutated converter system in order to develop an average-value model suitable for implementation in both classes of transient simulation programs, i.e., SV-based and NA-based. In Chapter 1, the motivations behind the research and the benefits of dynamics average-value modeling were presented, followed by an in-depth literature review on the dynamic average models available for six-pulse and higher-pulse-count line-commutated converters. The limitations of the available AVMs were then explained, and the goals of the research were outlined.

Chapter 2 presented implementations of analytical and parametric AVMs in state-variable-based simulators. The analysis started with a brief detailed analysis that helped clarify the challenges in developing the AVMs, such as the existence of various operational modes. Since the available AVMs are formulated based on the state variable approach, their implementation in this class of programs is shown to be straightforward.

The contribution of Chapter 3 is the extension of dynamic average modeling approaches to the EMTP-type simulation packages, wherein the indirect and direct methods of interfacing the dynamic average modes are defined. This Chapter mainly addresses **Objective 1** stated in Introduction of this thesis. As the EMTP-type programs are widely used for simulation of large power systems, the dynamic AVMs developed in this Chapter can be utilized in order to achieve significant gains in the simulation time. The results indicate that both indirect and direct methods of interfacing the dynamic average modes with the external circuit-networks provide acceptable results for much larger time steps than were ever possible with detailed model. The indirect interfacing method is generally simpler to implement and requires less analytical derivations. This advantage, however, comes at the price of degraded initialization transient response of the model, and less accuracy at larger time steps (beyond several hundreds of microsecond for typical 60 Hz line frequency). At the same time, the direct interfacing method is shown to remain more accurate in a wide range of time step sizes. Using the time-step of $\Delta t = 1000 \mu s$, which is 20 times larger than the typical EMTP-type time step of $50 \mu s$, the direct method of interfacing still provides a superior level of accuracy as demonstrated by the results of Chapter 3. However, this method requires significant analytical effort to establish the respective Thevenin equivalent circuit.

In Chapter 4, the validity and effectiveness of the developed average models is verified in both classes of simulation software packages. For the first time, it is demonstrated that appropriately-formulated dynamic AVMs can predict the system performance in DCM operation and under unbalanced excitation. The previously-developed models have been

derived assuming only balanced conditions, wherein the effects of asymmetric faults were not investigated. Extensive simulation studies of Chapter 4, carried out on an example six-pulse front-end line-commutated converters system, indicate that all AVMs may provide acceptable results in one mode (CCM-1). The results obtained by various models are also shown to be independent of the software package as long as the respective time step and error tolerances are appropriately chosen. Using the indirect method of interfacing, in PSCAD/EMTDC and EMTP-RV, the increase in the time step size of 4 and 6 times is achieved, respectively. However, using the direct method of interfacing in Matlab/Simulink allows for further improvement (8 times) compared to the typical $50\ \mu\text{s}$ time step.

The contribution of Chapter 5 is the new dynamic AVM for the six-pulse machine-converter system that can accurately predict the entire power conversion chain in the system, as outlined in **Objective 2** of the thesis. The effects of machine and bridge losses are taken into account. The experimental results and simulation studies carried out on an example vehicular power system demonstrate the effectiveness of the developed methodology in predicting the losses and complete power conversion chain in the system, wherein a significant improvement compared to the previously-developed model is also demonstrated. The increase in simulation speed of 73 times is achieved with respect to the detailed model.

The contributions of Chapter 6 include developing the generalized dynamic AVM methodology that can be applied to high-pulse converter systems of various configurations as was the focus of **Objective 3** of this thesis. Such generalized dynamic AVM methodology is developed for the first time and can be applied to an arbitrary voltage source- or machine-fed high-pulse-count converter system. Moreover, all previously-developed AVMs in the literature employ an oversimplified representation of the multi-phase transformer model. In contrast, a novel high-order representation of the multi-phase transformer is developed in Chapter 6 for use in AVMs, as was needed for achieving **Objective 3(a)**. The original transformer model developed in Chapter 6 is capable of representing all the details including

asymmetric properties of the magnetic core and leakages and resistances due to the interconnected configuration. The round shifted equivalent transformer model is more efficient and preserves the model generality and accuracy. A simplified, but effective, collapsed transformer model is also formulated which essentially represents the multi-phase transformer by an equivalent three-phase transformer without loss of accuracy for implementation of generalized dynamic AVMs in the EMTP-type programs.

The generalized AVM developed in Chapter 6 is valid for all operational modes unlike most of the previously-developed models that assume a certain single mode of operation. The developed model also includes the necessary zero sequence and hence remains valid even under unbalanced excitation, which achieves **Objective 3(b)**. Extensive simulation studies are carried out on an 18-pulse high-frequency example aircraft power system in time- and frequency-domains. The presented studies compare the generalized AVM against the detailed switching model of the system as well as the previously-developed analytical AVM for 18-pulse systems. The results demonstrate an excellent match between the responses predicted by proposed generalized AVM and the detailed switching model, wherein a significant improvement in accuracy and range of application as compared to the previously-developed state-of-the-art model is also achieved. The studies verify that the proposed generalized AVM remains valid for all modes of operation, and under balanced and unbalanced excitation.

7.2 Future Work

The research presented in this thesis may be continued in several directions. The following three particular directions are currently under consideration and investigation by other members of the Electric Power and Energy Systems research group at the University of British Columbia, with promising results as outlined below:

1- Formulating the proposed GAVM using the direct interfacing method:

The developed GAVM uses an indirect and less accurate method of interfacing. This method, although simpler, has some accuracy limitations as described in Chapter 3. Extending the approach employing the direct method of interfacing is considered as a future research that would further improve the model numerical efficiency while preserving the good accuracy. This extension may be done similar to the analytical approach formulated in Chapter 3 for direct interface. For this purpose, the dc and ac side equations must be discretized and linearized, such that the final model may be formulated in a Norton or Thevenin equivalent structure similar to Figure 3.8. As demonstrated by the results of Chapter 6, the directly interfaced model in Simulink provides 25 times improvement in time step size compared to about 10 times achieved by indirectly-interfaced model implemented in PASCAD. It is therefore expected that another factor of two to three improvement may be achieved upon accomplishment of this research task.

2- Extending the proposed GAVM to controlled line-commutated converter systems:

Despite the great popularity and range of applications, the uncontrolled converters/rectifiers do not allow bi-directional transfer of power. Extending the approach to the controlled line-commutated converters, i.e., thyristor converters would be of great benefit since this would allow dynamic average modeling of the much

larger class of systems including the HVDC systems. In such converters, the firing angle should be included in the model formulation as an additional control variable.

3- Extending the approach to include the effects of lower frequency harmonics:

In traditional AVMs, the switching harmonics are averaged out and removed from the model. As a result, under balanced excitation, the respective ac variables predicted by the average models appear as purely sinusoidal waveforms. Depending on the application, further accuracy may be desired in predicting the harmonics injected by the converter at the ac side. Such accuracy, for instance, is desired in the system-level analysis concerned with the harmonic filters present in the ac power system. Including the effects of these harmonics into the proposed GAVM will be considered in the future research. Such generalization may be carried out using the multiple reference frame theory [134]. Using this approach, each harmonic may be viewed in the corresponding synchronously rotating reference frame, and the averaging may be carried out for each harmonic term, respectively. The generalized parametric functions may then be defined and evaluated in order to formulate the final desired model. Including a few significant lower-frequency harmonics, e.g., fifth and seventh, may be sufficient for typical power quality and power systems applications.

References

- [1] “ACSLX, *Advanced Continuous Simulation Language, User’s Guide, Version 2.4*,” The AEGIS Technologies Group Inc., 2008. Available: <http://www.acslsim.com>
- [2] EASY5 Engineering Software for the Design, Analysis and Simulation, MSC SimEnterprise, Inc., 2008. Available: <http://www.mscsoftware.com>
- [3] EUROSTAG: Software for simulation of large electric power systems, Tractebel Energy Engineering, 2008. Available: <http://www.eurostag.be> and www.tractebel-engineering.com
- [4] “*Simulink Dynamic System Simulation Software, Users Manual*”, MathWorks Inc., 2008. Available: <http://www.mathworks.com>
- [5] “*SimPowerSystems: Model and simulate electrical power systems, User’s Guide*,” The MathWorks Inc., 2006. Available: <http://www.mathworks.com>
- [6] “*Piecewise Linear Electrical Circuit Simulation (PLECS), User Manual, Version 1.4*,” Plexim GmbH, 2008. Available: <http://www.plexim.com>
- [7] “*Automated State Model Generator (ASMG), Reference Manual, Version 2*,” P C Krause & Associates Inc., 2003. Available: <http://www.pcka.com>
- [8] H. W. Dommel, *EMTP Theory Book*, MicroTran Power System Analysis Corp., Vancouver, BC, Canada, 1992.
- [9] “*MicroTran Reference Manual*,” MicroTran Power System Analysis Corp., 1997. Available: <http://www.microtran.com>
- [10] Alternative Transients Programs, ATP-EMTP, ATP User Group, 2007. Available: <http://www.emtp.org>
- [11] PSCAD/EMTDC V4.0 On-Line Help, Manitoba HVDC Research Centre and RTDS Technologies Inc., 2005.
- [12] Electromagnetic Transient Program, EMTP RV, CEA Technologies Inc., 2007. Available: <http://www.emtp.com>
- [13] R. D. Middlebrook, “Input filter considerations in design and application of switching regulators,” in *Proc. IEEE Industrial Applications Society Conference*, Chicago, USA, Oct. 1976, pp. 91-107.
- [14] M. Belkhat, “Stability criteria for ac power systems with regulated loads,” PhD Dissertation, Purdue University, 1997.
- [15] M. B. Harris, A.W. Kelley, J. P. Rhode, and M. E. Baran, “Instrumentation for measurement of line impedance,” in *Proc. 9th IEEE Applied Power Electronics Conference (APEC’94)*, Orlando, USA, Feb. 1994.
- [16] B. Palethorpe, M. Sumner, and D. W. Thomas, “Power system impedance measurement using a power electronic converter,” in *Proc. 9th International Conference on Harmonics and Quality of Power (ICHQP ’00)*, Orlando, USA, Oct. 2000.

- [17] A. Emadi, A. Khaligh, C. H. Rivetta, and G. A. Williamson, "Constant power loads and negative impedance instability in automotive systems: definition, modeling, stability, and control of power electronic converters and motor drives," *IEEE Trans. on Vehicular Technology*, vol. 55, no. 4, pp. 1112–1125, Jul. 2006.
- [18] Tara, E., Filizadeh, S., Jatskevich, J., et al.: "Dynamic Average Modeling of Hybrid-Electric Vehicular Power Systems," To appear in *IEEE Trans. on Power Delivery*., 2011, 8 pages, (Manuscript ID: TPWRD-00707-2011).
- [19] J. Jatskevich, O. Wasynczuk, E. A. Walters, E. C. Lucas, and Ed Zivi, "Real-Time Distributed Simulation of a DC Zonal Electrical Distribution System," presented at the SAE Power Systems Conference, Coral Springs, FL, USA, Oct. 2002.
- [20] T. L. Skvareniana, S. Pekarek, O. Wasynczuk, P. C. Krause, R. J. Thibodeaux, and J. Weimer, "Simulation of a more electric aircraft power system using an automated state model approach," in *Proc. 31st Intersociety Energy Conversion Engineering Conference*, Washington, USA, Aug. 1996, pp. 133-136.
- [21] C. E. Lucas, E. A. Walters, J. Jatskevich, O. Wasynczuk, and P. T. Lamm, "A Distributed Heterogeneous Simulation of a Representative Aircraft Power System," presented at the SAE Power Systems Conference, Coral Springs, FL, Oct. 2002.
- [22] B. R. Needham, P. H. Eckerling, and K. Siri, "Simulation of large distributed DC power systems using averaged modelling techniques and the Saber simulator," in *Proc. IEEE Applied Power Electronics Conference and Exposition (APEC'94)*, Orlando, USA, Feb. 1994, vol. 2, pp. 801–807.
- [23] K. S. Tam and L. Yang, "Functional models for space power electronic circuits," *IEEE Trans. on Aerospace and Electronic Systems*, vol. 31, no. 1, pp. 288-296, Jan. 1995.
- [24] J. R. Lee, H. H. Cho, S. J. Kim, and F. C. Lee, "Modeling and simulation of spacecraft power systems," *IEEE Trans. on Aerospace and Electronics Systems*, vol. 24, no. 3, pp. 295-303, May 1988.
- [25] J. Morren, S. W. H. de Haan, P. Bauer, J. Pierik, and J. Bozelie, "Comparison of complete and reduced models of a wind turbine with Doubly-Fed Induction Generator," in *Proc. 10th European Conference on Power Electronics and Applications*, Toulouse, France, Sep. 2003.
- [26] J. G. Slootweg, S. W. H. de Haan, H. Polinder, and W. L. Kling, "General model for representing variable speed wind turbines in power system dynamics simulations," *IEEE Trans. on Power Systems*, vol. 18, no. 1, pp. 144–151, Feb. 2003.
- [27] J. G. Slootweg, S. W. H. de Haan, H. Polinder, and W. L. Kling, "Modeling new generation and storage technologies in power system dynamics simulations," in *Proc. IEEE 2002 Power Engineering Society Summer Meeting*, Chicago, USA, vol. 2, Jul. 2002, pp. 868–873.
- [28] J. G. Slootweg, H. Polinder, and W. L. Kling, "Representing wind turbine electrical generating systems in fundamental frequency simulations," *IEEE Trans. on Energy Conversion*, vol. 18, no. 4, pp. 516–524, Dec. 2003.

- [29] C. Abbey, J. Morneau, J. Mahseredjian, and G. Joos, "Modeling Requirements for Transient Stability Studies for Wind Parks," in *Proc. IEEE 2006 Power Engineering Society General Meeting*, Montreal, Canada, Jun. 2006.
- [30] Hee-Sang Ko, J. Jatskevich, G. Dumont and Gi-Gap Yoon, "An advanced LMI-based-LQR design for voltage control of grid-connected wind farm," *Int. J. Electric Power Systems Research*, vol. 78, no. 4, pp. 539–546, Apr. 2008.
- [31] Hee-Sang Ko and J. Jatskevich, "Power Quality Control of Hybrid Wind Power Generation System Using Fuzzy-LQR Controller," *IEEE Trans. on Energy Conversion*, vol. 22, no. 2, pp. 516–527, Jun. 2007.
- [32] A. Tabesh and R. Iravani, "Small-signal dynamic model and analysis of a fixed-speed wind farm - a frequency response approach," *IEEE Trans. on Power Delivery*, vol. 21, no. 2, pp. 778–787, Apr. 2006.
- [33] B. Wu, *High-Power Converters and AC drives*, Piscataway, NJ: IEEE Press/Wiley, 2006.
- [34] K. Lee, V. Blasko, T. M. Jahns, and T. A. Lipo, "Input harmonic estimation and control methods in active filters," *IEEE Trans. on Power Delivery*, vol. 25, no. 2, pp. 953-960, Apr. 2010.
- [35] M. E. Villablanca and J. I. Nadal, "Current distortion reduction in six-phase parallel-connected AC/DC rectifiers," *IEEE Trans. on Power Delivery*, vol. 23, no. 2, pp. 953-959, Apr. 2008.
- [36] K. Lee, G. Venkataramanan, and T. M. Jahns, "Source current harmonic analysis of adjustable speed drives under input voltage unbalance and sag conditions," *IEEE Trans. on Power Delivery*, vol. 21, no. 2, pp. 567-576, Apr. 2006.
- [37] B. Singh, G. Bhuvaneswari, and V. Garg, "Power-quality improvements in vector-controlled induction motor drive employing pulse multiplication in ac-dc converters," *IEEE Trans. on Power Delivery*, vol. 21, no. 3, pp. 1578-1586, Jul. 2006.
- [38] G. W. Chang and S. K. Chen, "An analytical approach for characterizing harmonic and interharmonic currents generated by VSI-fed adjustable speed drives," *IEEE Trans. on Power Delivery*, vol. 20, no. 4, pp. 2585-2593, Oct. 2005.
- [39] M. B. Rifai, T. H. Ortmeyer, and W. J. McQuillan, "Evaluation of current interharmonics from AC drives," *IEEE Trans. on Power Delivery*, vol. 15, no. 3, pp. 1094-1098, Jul. 2000.
- [40] J. Jiang and J. Holtz, "An efficient braking method for controlled ac drives with a diode rectifier front end," *IEEE Trans. on Industry Applications*, vol. 37, no. 5, pp. 1299–1305, Sep. 2001.
- [41] F. Wang, *et al.*, "Analysis and design optimization of diode front-end rectifier passive components for voltage source inverters," *IEEE Trans. on Power Electronics*, vol. 23, no. 5, pp. 2278–2289, Sep. 2008.
- [42] J. G. Hwang, P. W. Lehn, and M. Winkelkemper, "A generalized class of stationary frame-current controllers for grid-connected ac-dc converters," *IEEE Trans. on Power Delivery*, vol. 25, no. 4, pp. 2742-2751, Oct. 2010.
- [43] M. E. Haque, M. Negnevitsky, and K. M. Muttagi, "A novel control strategy for a variable-speed wind turbine with a permanent-magnet synchronous generator," *IEEE Trans. on Industry Applications*, vol. 46, no. 1, pp. 331–339, Jan./Feb. 2010.

- [44] A. Emadi, M. Ehsani, and J. M. Miller, *Vehicular Electric Power Systems: Land, Sea, Air, and Space Vehicles*, Marcel Dekker, Inc., New York, NY, USA, 2004.
- [45] G. W. Chang, H. Wang, G. Chuang, and S. Chu, "Passive harmonic filter planning in a power system with considering probabilistic constraints," *IEEE Trans. on Power Delivery*, vol. 24, no. 1, pp. 208-218, Jan. 2009.
- [46] H. M. Zubi, R. W. Dunn, and F. V. P. Robinson, "Comparison of different common passive filter topologies for harmonic mitigation," in *Proc. 45th International Universities Power Engineering Conference (UPEC '10)*, Cardiff, UK, Aug.-Sep. 2010.
- [47] G. Gong, U. Drofenik, and J. W. Kolar, "12-pulse rectifier for more electric aircraft applications," In *Proc. 3rd International Conference on Industrial Technology*, Maribor, Slovenia, Dec. 2003.
- [48] F. J. Chivite-Zabalza, A. J. Forsyth, D. R. Trainer, "Analysis and practical evaluation of an 18-pulse rectifier for aerospace applications," in *Proc. 2nd International Conference on Power Electronics, Machines and Drives*, Edinburgh, UK, Mar.-Apr. 2004, vol. 1, pp. 338-343.
- [49] E. Walters, O. Wasynczuk, and H. J. Hegner, "Computer modeling of a high-pulse-count ac/dc converter with interconnected multi-legged core transformers," in *Proc. the Naval Symposium on Electric Machines*, Annapolis, USA, Oct. 1998.
- [50] S. D. Sudhoff, "Analysis and average-value modeling of dual line-commutated converter- 6-phase synchronous machine systems," *IEEE Trans. on Energy Conversion*, vol. 8, no. 3, pp. 411-417, Sep. 1993.
- [51] P. C. Krause, O. Wasynczuk, and S. D. Sudhoff, *Analysis of Electric Machinery and Drive Systems*, 2nd ed., IEEE Press/Wiley, Piscataway, NJ, USA, 2002.
- [52] D. Aliprantis, S. D. Sudhoff, and B. T. Kuhn, "A brushless exciter model incorporating multiple rectifier modes and Preisach's hysteresis theory," *IEEE Trans. on Energy Conversion*, vol. 21, no. 1, pp. 136-147, Mar. 2006.
- [53] S. D. Sudhoff and O. Wasynczuk, "Analysis and average-value modeling of line-commutated converter-synchronous machine systems," *IEEE Trans. on Energy Conversion*, vol. 8, no. 1, pp. 92-99, Mar. 1993.
- [54] S. D. Sudhoff, K. A. Corzine, H. J. Hegner, D. E. Delisle, "Transient and dynamic average-value modeling of synchronous machine fed load-commutated converters," *IEEE Trans. on Energy Conversion*, vol. 11, no. 3, pp. 508-514, Sep. 1996.
- [55] J. T. Alt, S. D. Sudhoff, B. E. Ladd, "Analysis and average-value modeling of an inductorless synchronous machine load commutated converter system," *IEEE Trans. on Energy Conversion*, vol. 14, no. 1, pp. 37-43, Mar. 1999.
- [56] M. A. Shrud, A. Bousbaine, A. Elazrag, and N. Benamrouche, "Analysis and simulation of a 42V power system for automotive applications," in *Proc. 44th International Universities Power Engineering Conference (UPEC'09)*, Glasgow, UK, Sep. 2009.
- [57] V. Caliskan, D. J. Perreault, T. M. Jahns, and J. G. Kassakian, "Analysis of three-phase rectifiers with constant-voltage loads," *IEEE Trans. on Circuits and Systems I: Fundamental Theory and Applications*, vol. 50, no. 9, pp. 1220-1226, Sep. 2003.

- [58] V. Caliskan, D. J. Perreault, T. M. Jahns, and J. G. Kassakian, "Analysis of three-phase rectifiers with constant-voltage loads," in *Proc. 30th Annual IEEE Power Electronics Specialists Conference (PESC '99)*, Charleston, USA, Jul. 1999.
- [59] P. Pejovic and J. W. Kolar, "Exact analysis of three-phase rectifiers with constant voltage loads," *IEEE Trans. on Circuits and Systems II: Express Briefs*, vol. 55, no. 8, pp. 743–747, Aug. 2008.
- [60] B. Zhang, "Modeling and analysis of source-commutated five-phase diode rectifier systems," PhD Dissertation, University of Missouri-Rolla, 2004.
- [61] B. Zhang and S. D. Pekarek, "Analysis and average value model of a source-commutated 5-phase rectifier," in *Proc. 35th Annual IEEE Power Electronics Specialists Conference (PESC'04)*, Aachen, Germany, Jun. 2004.
- [62] Y. Tzeng, N. Chen, and R. Wu, "Modes of operation in parallel-connected 12-pulse uncontrolled bridge rectifiers without an interphase transformer," *IEEE Trans. on Industrial Electronics*, vol. 44, no. 3, pp. 344-355, Jun. 1997.
- [63] A. Cross, A. Baghrmian, and A. Forsyth, "Approximate, average, dynamic models of uncontrolled rectifiers for aircraft applications," *IET Power Electronics*, vol. 2, no. 4, pp. 398-409, Jul. 2009.
- [64] A. Baghrmian, A. J. Forsyth, "Averaged-value models of twelve-pulse rectifiers for aerospace applications," in *Proc. 2nd International Conference on Power Electronics, Machines, and Drives (PEMD '04)*, Edinburgh, UK, Mar.-Apr. 2004.
- [65] H. Zhu, "New multi-pulse diode rectifier average models for ac and dc power systems studies," PhD Dissertation, Virginia Polytechnic Institute and State University, 2005.
- [66] H. Zhu, R. P. Burgos, F. Lacaux, A. Uan-zo-li, D. K. Lindner, F. Wang, and D. Boroyevich, "Average modeling of three-phase and nine-phase diode rectifiers with improved ac current and dc voltage dynamics," in *Proc. 31st Annual Conference of the IEEE Industrial Electronics Society (IECON'05)*, Raleigh, USA, Nov. 2005.
- [67] H. Zhu, R. P. Burgos, F. Lacaux, A. Uan-zo-li, D. K. Lindner, F. Wang, and D. Boroyevich, "Evaluation of Average models for nine-phase diode rectifiers with improved ac and dc dynamics," in *Proc. 21st Annual Power Electronics Conference and Exposition (APEC'06)*, Dallas, USA, Mar. 2006.
- [68] S. Rosado, R. Burgos, F. Wang, and D. Boroyevich, "Large- and small-signal evaluation of average models for multi-pulse diode rectifiers," in *Proc. IEEE Workshops on Computers in Power Electronics (COMPEL '06)*, Troy, USA, Jul. 2006.
- [69] I. Jadric, D. Borojevic, and M. Jadric, "Modeling and control of a synchronous generator with an active DC load," *IEEE Trans. on Power Electronics*, vol. 15, no. 2, pp. 303–311, Mar. 2000.
- [70] J. Jatskevich, S. D. Pekarek, and A. Davoudi, "Parametric average-value model of synchronous machine-rectifier systems," *IEEE Trans. on Energy Conversion*, vol. 21, no. 1, pp. 9-18, Mar. 2006.
- [71] J. Jatskevich, S. D. Pekarek, and A. Davoudi, "Fast procedure for constructing an accurate dynamic average-value model of synchronous machine-rectifier systems," *IEEE Trans. on Energy Conversion*, vol. 21, no. 2, pp. 435-441, Jun. 2006.

- [72] J. Jatskevich and S. D. Pekarek, "Numerical validation of parametric average-value modeling of synchronous machine-rectifier systems for variable frequency operation," *IEEE Trans. on Energy Conversion*, vol. 22, no. 4, pp. 1-2, Dec. 2007.
- [73] J. Jatskevich, E. Walters, C. Lucas, and P. T. Lamm, "Average-value model of a high-frequency six-phase generation system," *SAE Trans., Journal of Aerospace*, vol. 113, no. 1, pp. 1854–1861, Nov. 2004.
- [74] J. Jatskevich, and S. D. Pekarek, "Six-phase synchronous generator rectifier parametric average value modeling considering operational modes", *HAIT Journal of Science and Engineering B*, vol. 2, no. 3-4, pp. 365-385, Dec. 2005.
- [75] J. Jatskevich, O. Wasynczuk, E. A. Walters, C. E. Lucas, S. D. Pekarek, and P. T. Lamm, "Automated identification of the operational modes of switched electric circuits," *SAE Trans. Journal of Aerospace*, vol. 109, no. 1, pp. 955–961, Oct. 2000.
- [76] J. Biela, D. Hassler, J. Schonberger, and J. W. Kolar, "Closed loop input current control of a hybrid 12-pulse rectifier," in *Proc. Power Electronics Specialists Conference (PESC'08)*, Rhodes, Greece, Jun. 2008.
- [77] S. Choi, A. R. von Jouanne, P. N. Enjeti, and I. J. Pitel, "Polyphase transformer arrangements with reduced kVA capacities for harmonic current reduction in rectifier type utility interface," in *Proc. 26th Annual IEEE Power Electronics Specialists Conference (PESC'95)*, Atlanta, USA, Jun. 1995.
- [78] S. Choi, P. N. Enjeti, I. J. Pitel, "Polyphase transformer arrangements with reduced kVA capacities for harmonic current reduction in rectifier-type utility interface," *IEEE Trans. on Power Electronics*, vol. 11, pp. 680-690, Sep. 1996.
- [79] J. Jatskevich, O. Wasynczuk, E. A. Walters, and C. E. Lucas, "Continuous state-space modeling of switched electric networks," in *Proc. 2000 IEEE International Conference on Control Applications (CCA '00)*, Anchorage, USA, Sep. 2000.
- [80] J. Pedra, F. Corcoles, and F. J. Suelves, "Effects of balanced and unbalanced voltage sags on VSI-fed adjustable-speed drives," *IEEE Trans. on Power Delivery*, vol. 20, no. 1, pp. 224-233, Jan. 2005.
- [81] M. O. Faruque, Y. Zhang, and V. Dinavahi, "Detailed Modeling of CIGRÉ HVDC Benchmark System Using PSCAD/EMTDC and PSB/SIMULINK," *IEEE Trans. on Power Delivery*, vol. 21, no. 1, pp. 378-387, Jan. 2006.
- [82] S. D. Pekarek, O. Wasynczuk, and H. J. Hegner, "An efficient and accurate model for the simulation and analysis of synchronous machine/converter systems," *IEEE Trans. on Energy Conversion*, vol. 13, no. 1, pp. 42–48, Mar. 1998.
- [83] S. D. Pekarek and E. A. Walters, "An accurate method of neglecting dynamic saliency of synchronous machines in power electronic based systems," *IEEE Trans. on Energy Conversion*, vol. 14, no. 4, pp. 1177–1183, Dec. 1999.
- [84] L. Wang and J. Jatskevich, "A voltage-behind-reactance synchronous machine model for the EMTP-type solution," *IEEE Trans. on Power Systems*, vol. 21, no. 4, pp. 1539–1549, Nov. 2006.

- [85] N. Mohan, T. M. Undeland, and W. P. Robbins, *Power Electronics: Converters, Applications and Design*, 2nd ed., Wiley, Inc., New York, NY, USA, 1995.
- [86] A. M. De Broe, S. Drouilhet, and V. Gevorgian, "A peak power tracker for small wind turbines in battery charging applications," *IEEE Trans. on Energy Conversion*, vol. 14, no. 4, pp. 1630–1635, Dec. 1999.
- [87] K. L. Lian, B. K. Perkins, and P. W. Lehn, "Harmonic analysis of a three-phase diode bridge rectifier based on sampled-data model," *IEEE Trans. on Power Delivery*, vol. 23, no. 2, pp. 1088–1096, Apr. 2008.
- [88] M. Grotzbach and R. Reiner, "Line current harmonics of VSI-fed adjustable-speed drives," *IEEE Trans. on Industry Applications*, vol. 36, no. 2, pp. 683–690, Mar. 2000.
- [89] G. Carpinelli, *et al.*, "Analytical modeling for harmonic analysis of line current of VSI-fed drives," *IEEE Trans. on Power Delivery*, vol. 19, no. 3, pp. 1212–1224, Jul. 2004.
- [90] B. Pilvelait, T. Ortmeyer, and M. Grizer, "Harmonic evaluation of inductor location in a variable speed drive," in *Proc. ICHPS V International Conference on Harmonics in Power Systems*, Sep. 1992, pp. 267–271.
- [91] R. M. Davis, *Power Diode and Thyristor Circuits*, Cambridge University Press, Cambridge, MA, USA, 1971.
- [92] S. D. Sudhoff, B. P. Loop, J. Byoun, and A. M. Cramer, "A new procedure for calculating immittance characteristics using detailed computer simulations," in *Proc. IEEE 38th Annual Power Electronics Specialists Conference*, Orlando, USA, Jun. 2007, pp. 901–908.
- [93] Z. Bing, K. J. Karimi, and J. Sun, "Input impedance modeling and analysis of line-commutated rectifiers," in *Proc. IEEE 38th Annual Power Electronics Specialists Conference*, Orlando, USA, Jun. 2007, pp. 1981–1987.
- [94] J. Sun and K. Karimi, "Small-signal input impedance modeling of line-frequency rectifiers," *IEEE Trans. on Aerospace and Electronic Systems*, vol. 44, no. 4, pp. 1489–1497, Oct. 2008.
- [95] J. Huang, K. A. Corzine, and M. Belkhat, "Small-signal impedance measurement of power-electronics-based ac power systems using line-to-line current injection," *IEEE Trans. on Power Electronics*, vol. 24, no. 2, pp. 445–455, Feb. 2009.
- [96] Y. A. Familant, J. Huang, K. Corzine, and M. Belkhat, "New techniques for measuring impedance characteristics of three-phase ac power systems," *IEEE Trans. on Power Electronics*, vol. 24, no. 7, pp. 1802–1810, Jul. 2009.
- [97] Z. Bing, K. J. Karimi, and J. Sun, "Input impedance modeling and analysis of line-commutated rectifiers," *IEEE Trans. on Power Electronics*, vol. 24, no. 10, pp. 2338–2346, Oct. 2009.
- [98] H. W. Dommel, "Digital computer solution of electromagnetic transients in single- and multiphase networks," *IEEE Trans. on Power Apparatus and Systems*, vol. PAS-88, no. 4, pp. 388–399, Apr. 1969.
- [99] J. Mahseredjian, V. Dinavahi and J.A. Martinez, "Simulation tools for electromagnetic transients in power systems: Overview and challenges", *IEEE Trans. on Power Delivery*, vol. 24, no. 3, pp. 1657–1669, Jul. 2009.

- [100] H. W. Dommel, "Nonlinear and time-varying elements in digital simulation of electromagnetic transients," *IEEE Trans. on Power Apparatus and Systems*, vol. PAS-90, pp. 2561–2567, Nov./Dec. 1971.
- [101] S. M. Chan and V. Brandwajn, "Partial Matrix Refactorization," *IEEE Trans. on Power Apparatus and Systems*, vol. PWRS-1, no. 1, pp. 193–200, Feb. 1986.
- [102] K. Strunz, L. Linares, J. R. Marti, O. Huet, and X. Lombard, "Efficient and accurate representation of asynchronous network structure changing phenomena in digital real time simulators," *IEEE Trans. on Power Systems*, vol. 15, no. 2, pp. 586-592, May 2000.
- [103] L. R. Linares and J. R. Marti, "A resynchronization algorithm for topological changes in real time fast transients simulation," in *Proc. 14th Power Systems Computation Conference (PSCC'02)*, Sevilla, Spain, June 2002.
- [104] K. Strunz, "Flexible numerical integration for efficient representation of switching in real time electromagnetic transients simulation," *IEEE Trans. on Power Delivery*, vol. 19, no. 3, pp. 1276-1283, Jul. 2004.
- [105] M. O. Faruque, V. Dinavahi, and W. Xu, "Algorithms for the accounting of multiple switching events in digital simulation of power-electronic systems," *IEEE Trans. on Power Delivery*, vol. 20, no. 2, pp. 1157-1167, Apr. 2005.
- [106] C. Dufour and J. Belanger "Discrete time compensation of switching events for accurate real-time simulation of power systems," in *Proc. 27th Annual Conference of the IEEE Industrial Electronics Society (IECON'01)*, Denver, USA, Nov.-Dec. 2001.
- [107] V. Dinavahi, M. R. Iravani, and R. Bonert, "Real-time digital simulation of power electronic apparatus interfaced with digital controllers," *IEEE Trans. on Power Delivery*, vol. 16, no. 4, pp. 775-781, Oct. 2001.
- [108] J. R. Marti and J. Lin, "Suppression of numerical oscillations in the EMTP," *IEEE Trans. on Power Systems*, vol. 4, no. 2, pp. 739-747, May 1989.
- [109] J. Lin and J. R. Marti, "Implementation of the CDA procedure in the EMTP," *IEEE Trans. on Power Systems*, vol. 5, no. 2, pp. 394-402, May 1990.
- [110] D.A. Woodford, A.M. Gole, and R.W. Menzies, "Digital Simulation of DC Links and AC Machines," *IEEE Trans. on Power Apparatus and Systems*, vol. PAS-102, no. 6, pp. 1616-1623, Jun. 1983.
- [111] A.M. Gole, R.W. Menzies, H.M. Turanli, and D.A. Woodford, "Improved interfacing of electrical machine models to electromagnetic transients programs," *IEEE Trans. on Power Apparatus and Systems*, vol. PAS-103, no. 9, pp. 2446–2451, Sep. 1984.
- [112] L. Wang, J. Jatskevich, V. Dinavahi, H. W. Dommel, J. A. Martinez, K. Strunz, M. Rioual, G. W. Chang, and R. Iravani, "Methods of interfacing rotating machine models in transient simulation programs," *IEEE Trans. on Power Delivery*, vol. 25, no. 2, pp. 891-903, Apr. 2010.
- [113] J. J. Grainger and W. D. Stevenson, Jr., *Power System Analysis*, McGraw-Hill, New York, NY, USA, 1994.

- [114] M. Heidari, S. Filizadeh, and A. M. Gole, "Support tools for simulation-based optimal design of power networks with embedded power electronics," *IEEE Trans. on Power Delivery*, vol. 23, no. 3, pp.1561 – 1570, Jul. 2008.
- [115] D. J. Perreault and V. Caliskan, "Automotive power generation and control," *IEEE Trans. on Power Electronics*, vol. 19, no. 3, pp. 618-630, May 2004.
- [116] S. C. Tang, T. A. Keim, and D. J. Perreault, "Thermal modeling of Lundell alternators," *IEEE Trans. on Energy Conversion*, vol. 20, no. 1, pp. 25-36, Mar. 2005.
- [117] S. M. Lukic, J. Cao, R. C. Bansal, F. Rodriguez, and A. Emadi, "Energy storage systems for automotive applications," *IEEE Trans. on Industrial Electronics*, vol. 55, no. 6, pp. 2258-2267, Jun. 2008.
- [118] I. Ramesohl, G. Henneberger, S. Kuppens, and W. Hadrys, "Three dimensional calculation of magnetic forces and displacements of a claw-pole generator," *IEEE Trans. on Magnetics*, vol. 32, no. 3, pp. 1685–1688, May 1996.
- [119] S. Kuppens and G. Henneberger, "Numerical procedures for the calculation and design of automotive alternators," *IEEE Trans. on Magnetics*, vol. 33, no. 2, pp. 2022–2025, Mar. 1997.
- [120] H. Bai, "Alternator finite element simulation," Technical Presentation at Delphi Automotive Systems, Troy, MI, USA, Aug. 2000.
- [121] V. Ostovic, J. M. Miller, V. K. Garg, R. D. Schultz, and S. H. Swales, "A magnetic-equivalent-circuit-based performance computation of a Lundell alternator," *IEEE Trans. on Industry Applications*, vol. 35, no. 4, pp. 825-830, Jul./Aug. 1999.
- [122] M. Hecquet and P. Brochet, "Modeling of a claw-pole alternator using permeance network coupled with electric circuits," *IEEE Trans. on Magnetics*, vol. 31, no. 3, pp. 2131-2134, May 1995.
- [123] H. Bai, S. Pekarek, J. Tichenor, W. Eversman, D. Buening, G. Holbrook, M. Hull, R. Krefta, and S. Shields, "Analytical derivation of a coupled-circuit model of a claw-pole alternator with concentrated stator windings," *IEEE Trans. on Energy Conversion*, vol. 7, no. 1, pp. 32–38, Mar. 2002.
- [124] H. Bai, S. Pekarek, J. Tichenor, W. Eversman, D. Buening, G. Holbrook, and R. Krefta, "Incorporating the effects of magnetic saturation in a coupled-circuit model of a claw-pole alternator," *IEEE Trans. on Energy Conversion*, vol. 22, no. 2, pp. 290–298, Jun. 2007.
- [125] R. F. Schniferl and C. M. Ong, "Six phase synchronous machine with AC and DC stator connections, Part I: Equivalent circuit representation and steady-state analysis," *IEEE Trans. on Power Apparatus and Systems*, vol. PAS-102, no. 8, pp. 2685-2693, Aug. 1983.
- [126] J. G. Zhu, S. Y. R. Hui, and V. S. Ramsden "A generalized dynamic circuit model of magnetic cores for low- and high-frequency applications-Part I: Theoretical calculation of the equivalent core loss resistance," *IEEE Trans. on Power Electronics*, vol. 11, no. 2, pp. 246-250, Mar. 1996.
- [127] O. Magdun, A. Binder, and Y. Gemeinder, "Representation of iron core and dielectric losses for calculation of common mode stator ground currents in inverter-fed ac machines," in *Proc. 12th International Conference on Optimization of Electrical and Electronic Equipment (OPTIM)*, Brasov, Romania, May. 2010, pp. 371-376.

- [128] A. Szumanowski and Y. Chang “Battery management system based on battery nonlinear dynamic modeling,” *IEEE Trans. on Vehicular Technology*, vol. 57, no. 3, pp. 1425-1432, May 2008.
- [129] F. E. Wicks and D. Marchionne, “Development of a model to predict electric vehicle performance over a variety of driving conditions,” in *Proc. Intersociety Energy Conversion Engineering Conference*, New York, USA, Aug. 1992, vol. 3, pp. 151-158.
- [130] V. Michael, F. E. Wicks, D. Robertson, and S. Rudin, “Development and application of an improved equivalent circuit model of a lead acid battery,” in *Proc. 31st Intersociety Energy Conversion Engineering Conference*, Washington, USA, Aug. 1996, vol. 2, pp. 1159-1163.
- [131] G. Seguir, *Power Electronic Converters: AC-DC Conversion*, McGraw Hill, Inc., New York, NY, USA, 1986.
- [132] S. J. Chapman, *Electric Machinery Fundamentals*, 2nd ed., McGraw Hill, Inc., New York, NY, USA, 1991.
- [133] R. W. Erickson and D. Maksimović, *Fundamentals of Power Electronics*, 2nd ed., Kluwer, Norwell, MA, USA, 2001.
- [134] P. C. Krause, “Method of multiple reference frames applied to the analysis of symmetrical induction machinery,” *IEEE Trans. on Power Apparatus and Systems*, vol. PAS-87, no. 1, pp. 218–227, Jan. 1968.

Appendices

Appendix A Parameters of the Six-Pulse Converter Example Systems

A.1 Parameters of the 6-Pulse Converter System Considered in Section 3.5

$$\sqrt{3}E = 208 \text{ V}, r_{th} = r_{ac} = 0.05 \Omega, L_{th} = 45 \mu\text{H}, L_{ac} = 50 \mu\text{H}, r_{dc} = 0.5 \Omega, L_{dc} = 1.33 \text{ mH}.$$

A.2 Parameters of the Micro-Wind Turbine System Considered in Chapter 4

PM Synchronous Machine:

$$3\text{-phase, } 2000 \text{ rpm, } 8\text{-pole, } r_s = 0.22 \Omega, L_s = 0.37 \text{ mH}, \lambda'_m = 21 \text{ mV.s}.$$

$$\text{DC Filter: } C_f = 100 \mu\text{F}, L_f = 0 \text{ mH}.$$

$$\text{Boost Converter: } L_b = 11 \text{ mH}, C_b = 4 \text{ mF}.$$

$$\text{Controller: } k_p = 2, k_i = 65, V_{ref} = 28 \text{ V}.$$

$$\text{Pulse-Width Modulator: } V_m = 15 \text{ V}, f_{sw-PWM} = 8 \text{ KHz}.$$

A.3 Parameters of the Front-End Rectifier System Considered in Chapter 4

Parameters of the 3-Phase (6-Pulse) front-end rectifier system considered in Chapter 4:

$$\sqrt{3}E = 480 \text{ V}, f_e = 60 \text{ Hz}, r_{th} = 0.01 \Omega, L_{th} = 500 \mu\text{H}, r_{ac} = 0.091 \Omega, L_{ac} = 9.545 \text{ mH},$$

$$r_{f5} = 0.1 \Omega, L_{f5} = 43.1 \text{ mH}, C_{f5} = 6.53 \mu\text{F}, r_{f7} = 0.05 \Omega, L_{f7} = 26.9 \text{ mH}, C_{f7} = 5.34 \mu\text{F},$$

$$r_{dc} = 0, L_{dc} = 0, C = 500 \mu\text{F}.$$

A.4 Parameters of the Vehicular Power System Considered in Chapter 5

Car Alternator:

3-phase, 14-pole, $N_s/N_{fd} = 0.159$, $r_s = 0.11\Omega$, $L_{ls} = 0.17$ mH, $L_m = 1.45$ mH,

$L'_{fd} = 0.36$ mH, $r'_{fd} = 0.12\Omega$, $r_c = 3.64\Omega$.

Alternator Loss Characteristic:

Speed (rpm)	500	700	900	1100	1300	1500	1700	2100
P_{rot_loss} (W)	9.95	16.86	26.39	35.71	46.29	59.69	71.21	98.96

Battery: Optima 800S, $Q_{max} = 55$ Ah, $v_{oc} = 13.6$ V, $r_b = 0.0192\Omega$, $C_{in} = 10$ mF.

Voltage Regulator: $\tau_1 = 1e-4$, $\tau_2 = 2e-3$, $k_p = 5$, $k_i = 500$.

Parametric Functions for the Non-Ideal Rectifier AVM:

z	0.1	0.5	1	2.5	5	10	20	40	90
α'	1.964	0.9147	0.7882	0.7211	0.6935	0.674	0.662	0.6556	0.652
β'	0.9547	0.9537	0.9508	0.9308	0.9165	0.9094	0.9065	0.9056	0.9053
ϕ	0.0115	0.0305	0.0662	0.1823	0.2021	0.1786	0.1391	0.1020	0.0685

Appendix B Parameters of the 18-Pulse Example System Considered in Chapter 6

3-Phase ac source and dc filter network:

$$V_{rms} = 225 \text{ V} , f_e = 400 \text{ Hz} , r_s = 0.1\Omega , L_s = 100 \mu\text{H} , C = 500\mu\text{F} .$$

Original 3-to-9-phase transformer parameters:

$$r_p = r_{s1} = 0.1 \Omega ,$$

$$r_{s2} = r_{s5} = 0.0551 \Omega ,$$

$$r_{s3} = r_{s4} = 0.0156 \Omega ,$$

$$\mathbf{L}_{pp} = \mathbf{L}_{s_1s_1} = \begin{bmatrix} 85.825 & -64.286 & -17.143 \\ -64.286 & 128.649 & -64.286 \\ -17.143 & -64.286 & 85.825 \end{bmatrix} \text{mH} ,$$

$$\mathbf{L}_{s_2s_2} = \mathbf{L}_{s_5s_5} = \begin{bmatrix} 47.281 & -35.415 & -9.444 \\ -35.415 & 70.873 & -35.415 \\ -9.444 & -35.415 & 47.281 \end{bmatrix} \text{mH} ,$$

$$\mathbf{L}_{s_3s_3} = \mathbf{L}_{s_4s_4} = \begin{bmatrix} 13.386 & -10.027 & -2.674 \\ -10.027 & 20.065 & -10.027 \\ -2.674 & -10.027 & 13.386 \end{bmatrix} \text{mH} ,$$

$$\mathbf{L}_{ps_1} = \begin{bmatrix} 85.714 & -64.286 & -17.143 \\ -64.286 & 128.571 & -64.286 \\ -17.143 & -64.286 & 85.714 \end{bmatrix} \text{mH} ,$$

$$\mathbf{L}_{ps_2} = \mathbf{L}_{ps_5} = \mathbf{L}_{s_1s_2} = \mathbf{L}_{s_1s_5} = \begin{bmatrix} 63.619 & -47.715 & -12.724 \\ -47.715 & 95.429 & -47.715 \\ -12.724 & -47.715 & 63.619 \end{bmatrix} \text{mH} ,$$

$$\mathbf{L}_{ps_3} = \mathbf{L}_{ps_4} = \mathbf{L}_{s_1s_3} = \mathbf{L}_{s_1s_4} = \begin{bmatrix} 33.851 & -25.388 & -6.770 \\ -25.388 & 50.777 & -25.388 \\ -6.770 & -25.388 & 33.851 \end{bmatrix} \text{mH},$$

$$\mathbf{L}_{s_2s_3} = \mathbf{L}_{s_5s_3} = \mathbf{L}_{s_2s_4} = \mathbf{L}_{s_5s_4} = \begin{bmatrix} 25.125 & -18.844 & -5.025 \\ -18.844 & 37.688 & -18.844 \\ -5.025 & -18.844 & 25.125 \end{bmatrix} \text{mH},$$

$$\mathbf{L}_{s_2s_5} = \begin{bmatrix} 47.220 & -35.415 & -9.444 \\ -35.415 & 70.830 & -35.415 \\ -9.444 & -35.415 & 47.220 \end{bmatrix} \text{mH},$$

$$\mathbf{L}_{s_3s_4} = \begin{bmatrix} 13.369 & -10.027 & -2.674 \\ -10.027 & 20.053 & -10.027 \\ -2.674 & -10.027 & 13.369 \end{bmatrix} \text{mH}.$$

Parameters of the analytical equivalent model for the 3-to-9-phase transformer:

$$r_p = r_{s_{ex-1}} = 0.1 \, \Omega,$$

$$r_{s_{ex-2}} = r_{s_{ex-3}} = 0.0707 \, \Omega,$$

$$\mathbf{L}_{pp} = \mathbf{L}_{s_{ex-1}s_{ex-1}} = \begin{bmatrix} 85.825 & -64.286 & -17.143 \\ -64.286 & 128.649 & -64.286 \\ -17.143 & -64.286 & 85.825 \end{bmatrix} \text{mH},$$

$$\mathbf{L}_{s_{ex-2}s_{ex-2}} = \begin{bmatrix} 60.678 & -19.477 & -38.095 \\ -19.477 & 67.385 & -45.474 \\ -38.095 & -45.474 & 84.297 \end{bmatrix} \text{mH},$$

$$\mathbf{L}_{s_{ex-3}s_{ex-3}} = \begin{bmatrix} 67.385 & -19.477 & -45.474 \\ -19.477 & 60.678 & -38.095 \\ -45.474 & -38.095 & 84.297 \end{bmatrix} \text{mH},$$

$$\mathbf{L}_{ps_{ex-1}} = \begin{bmatrix} 85.7143 & -64.286 & -17.143 \\ -64.286 & 128.5714 & -64.286 \\ -17.143 & -64.286 & 85.7143 \end{bmatrix} \text{mH},$$

$$\mathbf{L}_{ps_{ex-2}} = \begin{bmatrix} 46.575 & -89.008 & 40.944 \\ 22.326 & 98.491 & -120.818 \\ -70.390 & -12.665 & 81.566 \end{bmatrix} \text{mH},$$

$$\mathbf{L}_{ps_{ex-3}} = \begin{bmatrix} -12.664 & -70.390 & 81.566 \\ 98.491 & 22.326 & -120.818 \\ -89.008 & 46.575 & 40.944 \end{bmatrix} \text{mH},$$

$$\mathbf{L}_{s_{ex-1}s_{ex-2}} = \begin{bmatrix} 33.864 & -25.452 & -6.723 \\ -25.341 & 50.825 & -25.484 \\ -6.834 & -25.376 & 33.899 \end{bmatrix} \text{mH},$$

$$\mathbf{L}_{s_{ex-1}s_{ex-3}} = \begin{bmatrix} -25.376 & -6.834 & 33.899 \\ 50.825 & -25.341 & -25.484 \\ -25.452 & 33.864 & -6.723 \end{bmatrix} \text{mH},$$

$$\mathbf{L}_{s_{ex-2}s_{ex-3}} = \begin{bmatrix} 61.062 & -62.368 & 1.823 \\ 48.297 & 61.062 & -108.255 \\ -108.255 & 1.823 & 105.844 \end{bmatrix} \text{mH}.$$

Additional resistors and inductors required for compensation (for both above models):

$$r_{comp} = 0.0293 \, \Omega,$$

$$L_{comp,a} = L_{comp,c} = 32.602 \, \mu\text{H},$$

$$L_{comp,b} = 22.822 \, \mu\text{H}.$$

Parameters of the round shifted equivalent model for the 3-to-9-phase transformer:

$$r_p = r_{s_{ex-1}} = 0.1 \Omega,$$

$$r_{s_{ex-2}} = r_{s_{ex-3}} = 0.0707 \Omega,$$

$$\mathbf{L}_{pp} = \mathbf{L}_{s_{ex-1}s_{ex-1}} = \begin{bmatrix} 100.1 & -50 & -50 \\ -50 & 100.1 & -50 \\ -50 & -50 & 100.1 \end{bmatrix} \text{mH},$$

$$\mathbf{L}_{ps_{ex-1}} = \begin{bmatrix} 100 & -50 & -50 \\ -50 & 100 & -50 \\ -50 & -50 & 100 \end{bmatrix} \text{mH},$$

$$\mathbf{L}_{s_{ex-2}s_{ex-2}} = \mathbf{L}_{s_{ex-3}s_{ex-3}} = \begin{bmatrix} 100.071 & -50 & -50 \\ -50 & 100.071 & -50 \\ -50 & -50 & 100.071 \end{bmatrix} \text{mH},$$

$$\mathbf{L}_{ps_{ex-2}} = \mathbf{L}_{s_{ex-1}s_{ex-2}} = \mathbf{L}_{s_{ex-2}s_{ex-3}} = \begin{bmatrix} 76.604 & -93.969 & 17.365 \\ 17.365 & 76.604 & -93.969 \\ -93.969 & 17.365 & 76.604 \end{bmatrix} \text{mH},$$

$$\mathbf{L}_{ps_{ex-3}} = \mathbf{L}_{s_{ex-1}s_{ex-3}} = \begin{bmatrix} 17.365 & -93.969 & 76.604 \\ 76.604 & 17.365 & -93.969 \\ -93.969 & 76.604 & 17.365 \end{bmatrix} \text{mH},$$

Additional resistors and inductors required for compensation (round shifted equivalent model):

$$r_{comp} = 0.0293 \Omega,$$

$$L_{comp} = 29.342 \mu\text{H}.$$